Probing gravity with quantum sensors

- on ground and in space -

D i s s e r t a t i o n

zur Erlangung des akademischen Grades

doctor rerum naturalium
(Dr. rer. nat.)
im Fach Physik

eingereicht an der
Mathematisch-Naturwissenschaftlichen Fakultät
Humboldt-Universität zu Berlin

von
Dipl.-Phys. Vladimir Schkolnik

Präsidentin der Humboldt-Universität zu Berlin:
Prof. Dr.-Ing. Dr. Sabine Kunst

Dekan der Mathematisch-Naturwissenschaftlichen Fakultät:
Prof. Dr. Elmar Kulke

Gutachter:
1. Prof. Achim Peters, Ph.D.
2. Prof. Dr. Oliver Benson
3. Dr. Robert Thompson

Tag der mündlichen Prüfung: 05.10.2016

Abstract

Quantum sensors, such as atom interferometers and atomic clocks are used for high precision and accurate measurements of fundamental constants and the performance of these sensors allows to address fundamental questions in physics. As the only one of the four pillars of our current physical view of the world, gravity can not be combined with the three fundamental interactions of the Standard Model of particle physics. By measuring inertial forces and time, quantum sensors are ideally suited to test the predictions of general relativity.

The sensitivity of atom interferometers scales quadratically with the free evolution time T of the atomic sample. In microgravity, times can be achieved which are not possible on Earth. The use of quantum sensors in space is therefore predestined to improve the accuracy of tests of the Equivalence Principle by several orders of magnitude. To enable such space missions, both an understanding of the underlying operation principles as well as the development of space-qualified technologies are needed.

Additionally, precise and accurate sensors for inertial forces such as acceleration and rotation are required in the field of navigation or geodesy. Such devices based on atom interferometry are commonly used nowadays in the laboratory but mobile versions are still rare. This work contributes to the development of highly sensitive and stable mobile quantum sensors, which enable unprecedented performance.

In the course of this thesis, three measurement comparisons of the gravitational acceleration with the mobile atom interferometer GAIN were performed at different geographic locations. The systems sensitivity of $1.6 \times 10^{-8}\,\mathrm{g}/\sqrt{\mathrm{Hz}}$ is comparable to classical gravimeters based on falling corner cubes while the stability of $5 \times 10^{-11}\,\mathrm{g}$ after $10^5\,\mathrm{s}$ surpasses the one reached by such gravimeters.

With the goal of space-born atom interferometry, a complete and compact laser system for operation of atom interferometry with Bose-Einstein condensates of rubidium on a sounding rocket was designed, qualified and put in operation. Additionally, three sounding rocket payloads were realized to show the technological maturity of the necessary subsystems. Doppler-free laser spectroscopy of rubidium and potassium was used to realize an active optical frequency reference, mandatory for quantum sensor laser systems in space. During the flights the optical laser frequency was compared to an atomic microwave standard via a frequency comb. This measurement represents the first test of the Local Position Invariance in space. These activities pave the way for future deployment of atom interferometry based quantum sensors in space.

The performance achieved on ground combined with the ongoing technological development will enable space-borne atom interferometry with large interferometry times T and thus allow for unprecedented tests of fundamental physics, space geodesy or even gravitational wave detection.

Keywords: quantum sensor, atom interferometry, gravimeter, space, Equivalence Principle

Zusammenfassung

Quantensensoren, wie Atominterferometer und Atomuhren werden zu hochpräzisen und akkuraten Messungen von fundamentalen Konstanten benutzt und die Performance dieser Sensoren erlaubt fundamentale Fragestellungen der Physik anzugehen. Als der einzige der vier Grundpfeiler unserer aktuellen physikalischen Weltsicht, lässt sich Gravitation nicht mit den drei fundamentalen Wechselwirkungen des Standardmodells der Elementarteilchenphysik vereinigen. Durch das Messen von Inertialkräften und der Zeit sind Quantensensoren hervorragend dazu geeignet, die Aussagen der allgemeinen Relativitätstheorie zu testen.

Die Empfindlichkeit von Atominterferometern skaliert quadratisch mit der freien Entwicklungszeit T der atomaren Probe. In Schwerelosigkeit können Zeiten erreicht werden, die auf der Erde unmöglich sind. Die Verwendung von Quantensensoren im Weltraum ist daher prädestiniert die Genauigkeit von Tests des Äquivalenzprinzips um mehrere Größenordnungen zu verbessern. Um solche Weltraummissionen zu ermöglichen, werden sowohl ein Verständnis der zugrunde liegenden Funktionsprinzipien sowie die Entwicklung von weltraumtauglichen Technologien benötigt.

Zusätzlich, werden präzise und akkurate Sensoren die Inertialkräfte, wie Beschleunigung und Rotation messen, für Anwendungen im Bereich der Navigation oder Geodäsie benutzt. Solche auf Atominterferometrie basierende Geräte werden heutzutage häufig im Labor eingesetzt aber mobile Versionen sind noch selten. Diese Arbeit trägt zur Entwicklung von hochempfindlichen und stabilen mobilen Quantensensoren bei die eine noch nie dagewesene Leistung ermöglichen.

Im Rahmen dieser Doktorarbeit wurden drei mobile Vergleichsmessungen der Erdbeschleunigung mit dem Atominterferometer GAIN an verschiedenen geographischen Orten durchgeführt. Die Sensitivität des Systems von $1.6 \times 10^{-8}\,\mathrm{g}/\sqrt{\mathrm{Hz}}$ ist vergleichbar mit klassischen Gravimetern basierend auf fallenden Retroreflektoren während die Stabilität von 5×10^{-11} g nach 10^5 s die von diesen Gravimetern erreichbare sogar übertrifft.

Mit dem Ziel von Weltraumgestützten Atominterferometern wurde ein komplettes, kompaktes Lasersystem für den Betrieb von Atominterferometrie mit Rubidium Bose-Einstein Kondensaten auf Höhenforschungsraketen entworfen, qualifiziert und in Betrieb genommen. Zusätzlich wurden drei Nutzlasten für dein Einsatz auf Höhenforschungsraketen realisiert um die Reife der notwenigen Subsysteme zu zeigen. Insbesondere wurde Dopplerfreie Laserspektroskopie an Rubidium und Kalium verwendet um einen Masterlaser, der für Quantensensor Lasersysteme im Weltraum zwingend erforderlich ist zu stabilisieren. Während der Flüge wurde die optische Laserfrequenz mit einem Frequenzkamm verglichen. Diese Messung stellt einen ersten Test der Lokalen Lorenz Invarianz im Weltraum dar. Diese Aktivitäten ebnen den Weg für den zukünftigen Einsatz von Quantensensoren basierend auf Atominterferometrie im Weltraum.

Die erreichte Leistungsfähigkeit am Boden kombiniert mit der momentanen technologischen Entwicklung wird weltraumgestützte Atominterferometrie mit langen Interferometriezeiten T ermöglichen und noch nie dagewesene Tests der fundamentalen Physik, Weltraumgeodäsie oder sogar Gravitationswellen erlauben.

Schlagwörter: Quantensensor, Atominterferometer, Gravimeter, Weltraum, Äquivalenzprinzip

Contents

1 Quantum sensors for gravity measurements on ground and in space

Present physics is based on two major theories. The Standard Model unifies electromagnetism, the weak, and the strong force [1, 2], while Einstein's general relativity is the theory of gravity [3, 4]. To this moment general relativity passed all tests with flying colours [5, 6] and one of its spectacular predictions, the existence of gravitational waves, was recently confirmed [7]. However, general relativity does not include quantum effects and is therefore incomplete [4, 8]. For this reason a theory that unifies the fundamental forces of the Standard Model with gravity is most promising a quantum theory of gravity [9].

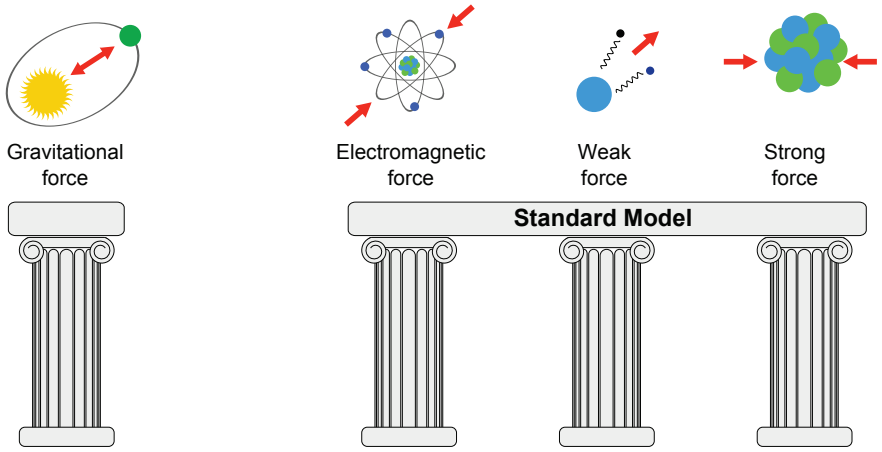

Figure 1.1: The Standard Model of particle physics unifies the fundamental interactions, the electromagnetic, the weak and the strong force (represented by the three connected pillars on the right side). As a quantum theory, the Standard Model is incompatible with the classical theory of Einstein's general relativity (left pillar). Modern physic aim to combine all the four forces in a unified theory.

If general relativity is incomplete, a quantum theory of gravity must violate one or even more of the foundations of general relativity. Some quantum theories of gravity predict such violations at levels which are to date several orders of magnitude smaller than the sensitivity in current experimental tests [8, 10, 11]. General relativity is founded on the so called Einstein Equivalence Principle. Testing this foundations with improved instruments is a promising step towards a quantum theory of gravity [12].

1.1 The missing link: Einstein Equivalence Principle

The Einstein Equivalence Principle (EEP) is the foundation of general relativity and contains three principles: (from [5])

1. "The trajectory of a freely falling test body (one not acted upon by forces such as electromagnetism and too small to be affected by tidal gravitational forces) is independent of its internal structure and composition. This is known as the weak equivalence principle (WEP). In the simplest case of dropping two different test bodies in a gravitational field, the WEP states that the bodies fall with the same acceleration."

2. "The outcome of any local non-gravitational experiment is independent of the velocity of the freely falling reference frame in which it is performed. "

3. "The outcome of any local non-gravitational experiment is independent of where and when in the universe it is performed. "

These principles are pictured in Figure 1.2. The first principle is also called the Universality of Free Fall (UFF), the second is called the Local Lorentz Invariance (LLI) and the third is known as the Local Position Invariance (LPI) [5]. Due to these three principles, a theory of gravity has to be a metric theory which is a theory where the metric tensor alone determines

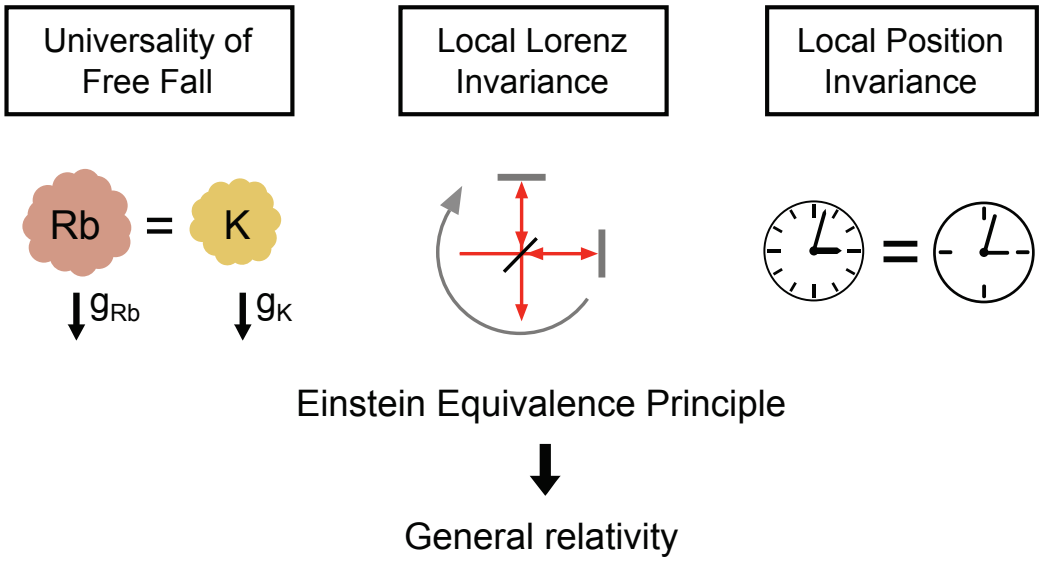

Figure 1.2: The three postulates of the Einstein Equivalence Principle (EEP). The Universality of Free Fall (UFF), represented by two different atomic species as test bodies. The Local Lorentz Invariance (LLI) is represented by a rotating optical Michelson interferometer. The Local Position Invariance (LPI) represented by two internal different clocks that experience the same gravitational redshift (from left to right).

the properties of space-time and its influence on particle trajectories [13]. Some additional requirements on the metric lead to Einstein's theory of gravity [4].

There have been various tests of each EEP postulate [14], but up to now none of them was able to prove a violation. Tests of UFF compare the accelerations g_A and g_B of two different objects A and B (rubidium and potassium atoms f.e. like shown in Figure 1.2) in a gravitational potential. The normalized difference of the two accelerations $2(g_A - g_B)/(g_A + g_B)$ is called the Eötvös ratio η and quantifies a possible UFF violation. UFF has been tested using a rotating torsion balance [15] or by measuring the acceleration of the Moon using a retro reflector located on its surface [16].

LLI was tested in a pioneering experiment by Michelson and Morley in the year 1887 [17] and by a modern version two orthogonal optical cavities interrogated by a laser [18].

LPI tests compare the rate of two internally different oscillators or clocks. For example one clock is based on a magnetic dipole transition and the other one on an electric dipole transition. LPI states that the time displayed by the two clocks is always the same if their position is equal (see Figure 1.2). For the most advanced test of the LPI principle 8 years of data from several atomic fountains and hydrogen masers were compared [19].

Both, time and acceleration, can be measured today with atomic clocks and atom interferometers with very high precision and accuracy. The basic principles of these quantum sensors are presented in the following.

1.2 Quantum sensors for high precision measurements

The term quantum sensor stands for a variety of devices, utilizing the interaction of quantum objects with discrete transition energies with external forces like electromagnetism, acceleration or other physical quantities like pressure or temperature. Quantum sensors can be as simple as one atom with only two energy levels. Another example is an atom-like system, an impurity in diamond called the Nitrogen-Vacancy (NV) colour center for magnetic field sensing [20] or temperature measurements [21]. Here we will use the term quantum sensor for atom interferometers and atomic clocks only, although this expression covers a broad range of sensors.

1.2.1 Atomic clocks

Atomic clocks utilize energy states in atoms as a frequency reference. An oscillator, a microwave or optical field (ω_{RF} and ω_{OPT} in Figure 1.3) interrogates atoms and changes the population between the states depending on the interrogation frequency. The population is detected and an error signal is generated. A feedback loop is used to stabilize the interrogation frequency to the transition frequency [22]. The stability of the atomic transition is transferred to the oscillator, its frequency is divided in the countable range if ω is two high, the number of oscillations are counted and if the absolute frequency is known a time-stamp can be displayed. The operating principle of an atomic clock is shown in Figure 1.3. The unit of time, the second, is defined as the duration of 9 192 631 770 oscillations corresponding to a hyperfine transition

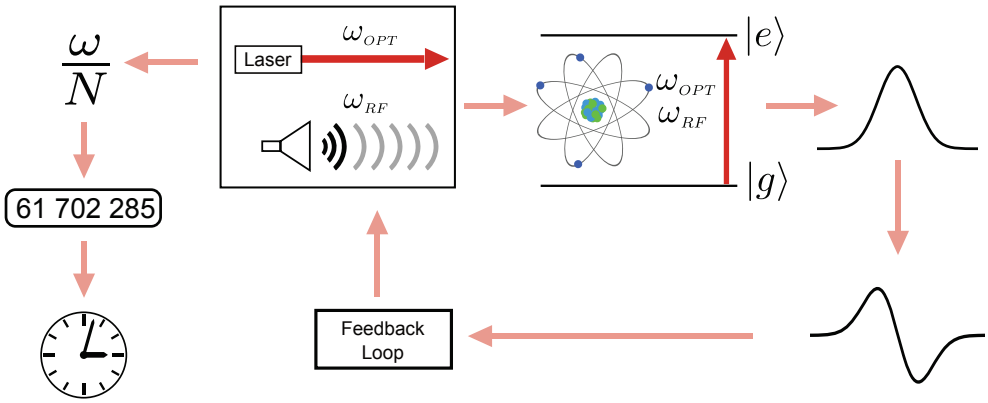

Figure 1.3: The operating principle of an atomic clock. An oscillator in the microwave or optical domain probes an atomic transition. The population in the two states of the atomic sample depends on the oscillators detuning from the atomic resonance and is used to generate an error signal. A feedback loop then stabilizes the oscillators frequency to the atomic resonance. The frequency is divided, the number of oscillation counted and displayed.

in the ^{133}Cs atom [23].

The progress in atomic clocks was accelerated by the invention of laser cooling [24]. Laser cooling and trapping methods allow to create cold clouds of atoms whose motion can be precisely controlled. The low temperature results in a reduced expansion of the atomic cloud. Therefore more atoms contribute to the signal and thus increase the clock's stability [25, 26]. Today, microwave atomic fountains based on laser cooled rubidium and caesium atoms launched upwards against Earth's gravity provide a global clock network [26]. Their almost continuous operation is used for the search of a possible drift of physical constants or acts direct as an LPI test on Earth [19].

A new area of atomic clocks started with the first realization of optical clocks [22]. Here, the oscillator operates at narrow atomic resonances in the optical domain. These clocks already reach frequency instabilities in the order of 10^{-18} [27, 28], and proposed techniques may lead to improvements by an order of magnitude in the near future [29, 30]. This makes and atomic clocks predestined to test general relativity.

A direct consequence of a curved-space time is the gravitational redshift of electromagnetic radiation in a gravitational field [31]:

$$\frac{\Delta\nu}{\nu} = \frac{\Delta U}{c^2}, \tag{1.1}$$

where $\Delta\nu/\nu$ is the relative frequency difference between a clock at rest and a distant clock with a gravitational potential difference ΔU. The LPI states that this redshift is independent of the clock's internal structure [32]. Thus two different clocks at the same position experience the same gravitational redshift. The measurement of the frequency difference of clocks at different gravitational potentials is a direct test of the Equivalence Principle and an improvement in clock performance is followed directly by an improvement in LPI tests. A second type of

quantum sensors, namely atom interferometer, is introduced below.

1.2.2 Atom interferometers

Atom interferometers exploit the wave-particle duality by coherent splitting and recombining matter waves using atom optics elements. A phase difference Φ accumulated between the interferometer paths causes population interference at the interferometer output ports [33]. This is shown in Figure 1.4 a).

The phase difference depends on inertial forces like acceleration and rotation. Electric or magnetic fields also cause phase shifts if the atoms interact with the appropriate field through their electric or magnetic moment. Based on atom-light interactions short pulses of light are used to realize the atom interferometer. During these pulses phase shifts are imprinted by the light field on the atoms, giving the phase contribution in the interferometer. Depending on the interferometer geometry and the states of the atoms, the interferometer can be sensitive to one or several forces at the same time.

An atomic clock can also be seen as an special case of an atom interferometer [35]. The matter wave in the clock is interrogated by the oscillator which imprints a phase on the atoms. If the phase of the oscillator matches the phase of the matter wave, no additional phase is imprinted on the interferometer and one output port remains dark. Phase contributions from inertial forces are strongly suppressed in clock geometries [35].

The first realizations of atom interferometers used solid state gratings or slits as diffraction elements for thermal atomic beams [36, 37]. Advances in laser cooling [24] and coherent atom-light manipulation [38, 39] led to atom interferometers using cold atomic clouds where light pulses are used as beam-splitters and mirrors for the atoms [40]. The combination of

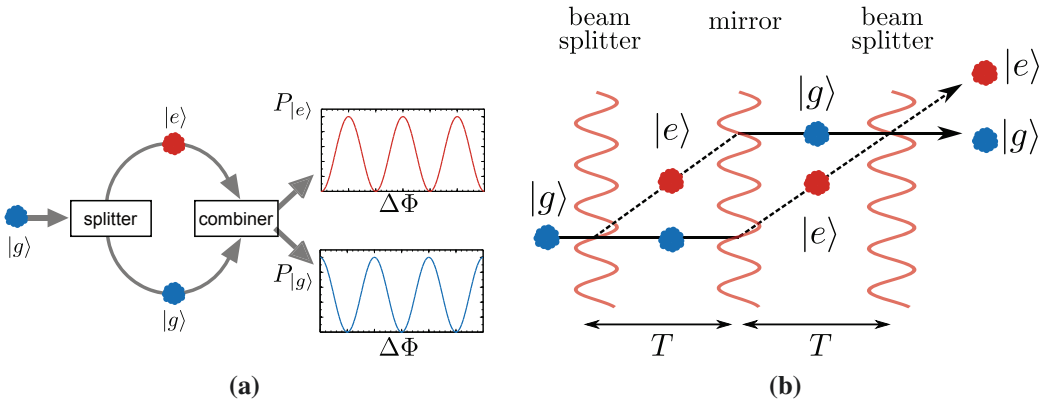

Figure 1.4: The principle of an atom interferometer. (a) A matter wave originally in the ground state $|g\rangle$ is split into a superposition between two states $|g\rangle$ and $|e\rangle$ which travel on two different paths before they are recombined. A phase difference $\Delta\Phi$ accumulated between the two paths causes population oscillation between the two states at the output ports. (b) One realization of an atom interferometer is the Mach-Zehnder configuration where the matter wave is split, redirected and recombined again using light pulses. (Adapted from [34])

the precise control of the laser's light phase used to create the interferometer pulses and the strongly reduced expansion of the atomic sample due to the cooling procedure makes atom interferometers highly sensitive devices for measurements of inertial forces.

Atom interferometers can be used for gravity measurements [41–44], measurements of the gravity gradient [45] and rotations [46]. Moreover, atom interferometry is used for accurate measurements of the fine structure constant [47] and the gravitational constant G [48] and further detection of gravitational waves is proposed [49–51]. Atom interferometers with free falling atoms that measure gravitational acceleration or accelerations in general are of high interest for tests of the UFF. Measuring the differential acceleration between two closely located atomic clouds of two different atomic species, provides a direct test of the Universality of Free Fall.

Figure 1.4 (b) shows a light pulse atom interferometer in the Mach-Zehnder configuration [39]. Like in its optical analog, the input of the matter wave interferometer in free fall is split using a beam splitter-pulse, reflected by a mirror-pulse and overlapped with another pulse again with a free evolution time T between each of the pulses. During the interferometer pulses, an atom can absorb a photon from the light grating or emit one. This changes the atom's momentum, i.e., its external state and also its internal state. The momentum difference leads to different trajectories for each of the two interferometer paths. In presence of gravity the imprinted laser phase on the free falling atoms in both paths is different due to the different locations of the matter wave during the second and third pulse of the interferometer. This causes a phase difference between the two paths

$$\Delta\Phi = \mathbf{k_{eff}} \cdot \mathbf{g} T^2, \tag{1.2}$$

where $\mathbf{g}$ is the Earth's gravitational acceleration and $\mathbf{k_{eff}} \approx 2\mathbf{k}$ the effective wave vector of the light pulses. A theoretical description of cold atom interferometry with light pulses will be given in Chapter 2.

Today, the performance of atom interferometers for measurements of gravity or rotations competes with classical devices or even surpasses them in some areas. While quantum sensors are widely used in laboratories, mobile devices that achieve the performance of lab based setups are still rare. The versatile applications possible with such mobile atom interferometers and clocks on ground are listed below.

1.3 Applications on Earth

Besides their use for tests of general relativity or timekeeping, atomic clocks and atom interferometers can be used for a wide range of applications on Earth. The accuracy of optical clocks reaching some parts in 10^{-18} corresponds to a gravitational redshift caused by a height difference of only 1 cm. Such accurate clocks can therefore be used to determine height differences and to measure the gravitational potential of the Earth. The so called "relativistic geodesy"[52] requires a frequency link to compare the clocks frequency to a reference clock with a known position. Frequency transfer through optical links that meets the requirements for geodesy was recently demonstrated [53]. Besides the need for an optical link, optical clocks need to be

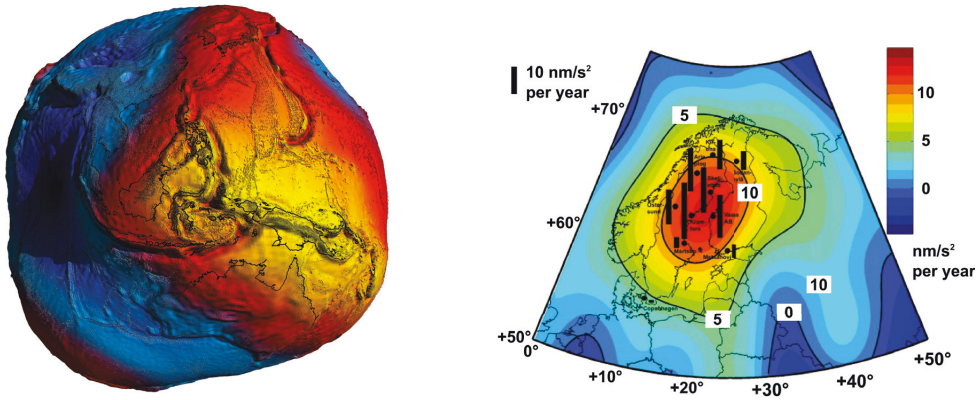

(a) (b)

Figure 1.5: (a) The model of the Earth's geoid measured by GOCE satellite. The colours represent height deviations from an ideal geoid. The scale ranges from −100 m (blue) to 100 m (red). From ESA/HPF/DLR [57]. (b) Gravity changes for Fennoscandia calculated from combined terrestrial (black bars) and satellite measurements. From [58].

portable and robust for the use in geodesy. Several portable optical clocks are currently being constructed [54–56] and the technological development for clocks in space benefits directly from technological developments for ground operation.

Mobile atom interferometers can be used for high precision measurements of Earth's gravity or gravity gradient. This allows to monitor changes of mass variations inside the Earth crust [59]. Mobile atomic gravimeters allow for fast and accurate determination of local gravity values or long term gravity measurements with high temporal resolution. This local gravity measurements, combined with satellite based measurements [58], will improve the determination and prediction of the Earth's geoid, the surface with equal gravitational potential (see Figure 1.5). Gyroscopes based on atom interferometry are sensitive enough to measure changes in the Earth's rotation rate due to seismic activities [60].

The combined measurement of accelerations and rotations in all six degrees of freedom can be used for inertial navigation without the need of additional position information from GPS. The performance of today's commercial inertial navigation solutions can be improved using the in principle accurate and drift-free quantum sensors. A six-axes inertial sensor based on atom interferometry was already demonstrated in the laboratory [61].

The sensitivity of atom interferometers can be improved by increasing the transferred photon momentum or extending the interferometer time T. On Earth, the fundamental limit for the interferometer time is the dimension of the apparatus. This limitation can be overcome in a space environment as presented in the next section.

1.4 Advantages of space-borne operation

Worldwide, tests of the UFF with atom interferometry are proposed, in preparation or already operate on ground. The insight gained in these ground experiments is crucial for planned space missions. Table 1.1 lists current and proposed UFF tests based on atom interferometry and the best classical test as a reference (from [62]). Quantum sensors like clocks and atom interferometers can greatly benefit from microgravity environments, such as a satellite or the International Space Station (ISS). Obviously, the weightlessness in the freely falling reference frame of a space craft allows for unprecedented interferometry times, limited only by the expansion of the atomic cloud.

Experiment	**Species**	**T(s)**	**Accuracy**
Lunar Ranging [16]	Earth/Moon		$1.4\cdot 10^{-13}$
Hannover [63]	^{87}Rb/^{39}K	0.02	$5\cdot 10^{-7}$
Wuhan [64]	^{87}Rb/^{85}Rb	0.071	$3\cdot 10^{-8}$
Hannover VLBAI [65]	^{87}Rb/^{170}Yb	1.3	$[7\cdot 10^{-13}]$
Stanford [66]	^{87}Rb/^{85}Rb	1.34	$[1\cdot 10^{-15}]$
SAI [67]	**^{87}Rb/^{85}Rb or Rb/K**	**1**	$[\mathbf{1\cdot 10^{-12}}]$
STE-Quest [68]	**^{87}Rb/^{41}K**	**5**	$[\mathbf{1\cdot 10^{-15}}]$
QTEST [62]	**^{87}Rb/^{85}Rb**	**10**	$[\mathbf{5\cdot 10^{-16}}]$

Table 1.1: Current and proposed tests of the UFF with atom interferometry. The projected accuracies are shown in square brackets. Space based tests are highlighted bold. The test in the first row is Lunar Ranging, the best classical UFF test in the moment, and is shown as reference. Adapted from [62].

Atom interferometers, as well as atomic clocks based on free expanding atomic clouds [69] can dramatically increase their free evolution time T. Since the resolution of measurements of the acceleration $\Delta a/a$ (or rotation) in atom interferometers follows $\Delta a/a \propto 1/T^2$, and the frequency resolution $\Delta f/f$ in atomic clocks follows $\Delta f/f \propto 1/T$, the sensitivity of these devices highly profit from space operations. This increase in sensitivity requires atomic clouds with very low temperatures and thus low expansion rates. With an increasing size of the atomic cloud the number of detected atoms decreases resulting in a higher noise of the detection process. Expanding atoms can even be lost due to collision with the interior of the vacuum chamber. Other advantages of space operation besides higher sensitivity of quantum sensors are:

- The absence of seismic noise, the limiting factor of many ground based experiments [4]. This is especially important for the study of gravitational waves in space with atom interferometry [70].
- The high gravitational potential difference achievable by satellites on elliptical orbits is a huge advantage for LPI tests with atomic clocks. As can be seen from Equation 1.1,

the gravitational redshift is directly proportional to the potential difference.

- In space, a strong velocity modulation of the spacecraft is possible using high elliptical orbits. This is advantageous for Kennedy-Thorndike experiments, that test a possible velocity dependence of the speed of light [71].
- Atomic clocks in orbit make their signals available to a station on Earth or to other clocks in orbit. A so called master clock in space [72] can provide a reference signal over the globe using satellite links. Clocks with an increase performance will improve the performance of future satellite navigation systems.

The benefits of space operation come along with the high technological challenge for space-borne quantum sensors. All components have to ensure reliable operation over the whole mission lifetime. Besides technological aspects the operation in microgravity differs from the operation on ground. Due to the absence of gravity different parameters in the interferometry sequences are needed. Besides numerical simulations, several microgravity platforms around the globe are used to bring forward technological developments and experience with operation in microgravity environments. These platforms are introduced in the next section.

1.5 Sounding rockets: the next step towards missions in space

To create a ground based microgravity environment several platforms exist. The Novespace zero-g airplane, a modified Airbus starting from Bordeaux, France performs parabolic flights with a free fall time of about 22 s. The standard missions duration is 3 days with one flight per day with 31 parabolas per flight [73]. Another platform is the drop tower in Bremen, Germany [74]. The 122 m long drop tower tube allows for 4.7 s free fall time in the drop mode and 9.1 s in the catapult mode. Before every drop the tower is evacuated allowing only three drops per day.

To extend the microgravity time further, sounding rocket flights are an alternative platform. Several rocket types are available that differ in maximum payload mass and flight apogee. Funded by the DLR space administration, the TEXUS missions use a two stage VSB-30 rocket motor to launch scientific payloads from the European Space Range (ESRANGE) in Kiruna, Sweden [75]. Two TEXUS launches per year in average are performed. The rocket is in free fall several seconds after the separation of the rocket motors. The parabolic trajectory reaches apogees up to 260 km and 6 min of microgravity. Typically four experiments are housed in independent modules. The start of the TEXUS 51 sounding rocket seen from the radar hill, is shown in Figure 1.6.

The advantages of sounding rocket missions come at the price of high mechanical stress on the payload during the launch and the re-entry phase. Successful sounding rocket flights are the next step towards missions in space.

Figure 1.6: The launch of the TEXUS 51 sounding rocket on 23th of April 2015 as viewed from the Esrange radar hill in Sweden, driven by the two stage VSB-30 rocket motor [76]. During the 6 min of microgravity, 4 experiments housed each in their own module were performed.

1.6 Major contributions of this thesis

During my thesis I had the possibility to work on multiple experiments. Here I summarize my contributions to each of them.

- During the work for the mobile atom interferometer GAIN, I prepared and optimized the apparatus and prepared and performed the three presented gravity comparison campaigns together with the other members of the GAIN team. This included the rebuilding of the apparatus after a vacuum break and the redesign of the laser system including the new amplifier module. I worked extensively on the laser system, building, replacing and optimizing its components. I performed the theoretical end experimental work on the wavefront aberrations presented in this thesis.
- For the MAIUS sounding rocket mission, my contributions included the design assembly and integration of the laser system. After the transport to Hannover, Germany I contributed to the operation and optimization of the laser system with the flight electronics. I participated in the qualification process of the flight system in bench and environmental tests.
- For the FOKUS sounding rocket mission my contribution included the design, test and assembly of the rubidium spectroscopy module in a collaboration with Menlo Systems. I performed all the required vibration and qualification tests, integrated the module into the payload and optimized its performance. I participated during the aborted and the actual performed launch campaigns and contributed to their planning. I operated the module during the entire mission including the actual rocket flight. I was involved in

the data analysis with respect to the LPI test. The same contributions apply for the FOKUS Reflight sounding rocket mission.

- For the KALEXUS sounding rocket mission my contribution included the design, assembly and first tests of the complete KALEXUS payload. Afterwards I contributed as an advisor over the whole mission phase and participated during the joint launch campaign with FOKUS Reflight.

1.7 Organization of this thesis

In **Chapter 2** the basic theoretical concepts of atom interferometry are presented. Starting with a two-level system, atom-light interaction is introduced and the evolution of the two-level system is derived. An extension to a three-level system, results in a description of Raman transitions as beam splitters and mirrors for atoms. Different interferometer configurations are presented and the phase evolution of an atom interferometer in a gravitational field is derived. Finally major noise sources of the interferometers phase in a gravimeter configuration are presented.

After the theoretical description of a gravimeter based on atom interferometry, the realization of such an interferometer is presented in **Chapter 3**. First, the experimental setup of the Gravitational Atom INterferometer (GAIN) built at the Humboldt University of Berlin is presented with focus on the laser system. This is followed by a description of the experimental sequence to perform gravity measurements.

Gravity measurement campaigns performed during this thesis are presented in **Chapter 4**. The results of these campaigns are analysed in terms of sensitivity and an overview of the major systematic effects is given. A detailed numerical and experimental evaluation of the effect of wavefront aberrations in an atom interferometer is presented. The possible sensitivity of a future space-borne atom interferometer is estimated.

A demonstrator for future quantum sensors based on atom interferometry in space, MAIUS, is presented in **Chapter 5**. This interferometer based on Bose Einstein Condensates was designed to operate during a sounding rocket flight in winter 2016. The MAIUS mission, including the experimental sequence and the subsystems of the rocket payload are briefly presented. The design, assembly and qualification of the MAIUS laser system is described.

As a milestone towards space operation, the MAIUS frequency reference was duplicated and operated during a sounding rocket flight in April 2015 as a part of the FOKUS mission. The laser frequency was measured against a referenced frequency comb as a prototype test of the Local Position Invariance in the optical domain in space. Two other sounding rocket payloads FOKUS Reflight and KALEXUS were designed build and successfully operated in January 2016. The results of this three campaigns are presented in **Chapter 6**.

Chapter 7 summarizes the results of this thesis and points at possible improvements of the GAIN apparatus. An outlook for future tests of the EEP using atom interferometry and atomic clocks is given.

2 Cold atom interferometry

Quantum sensors are based on the interaction of electromagnetic radiation with the energy levels of a quantum system. This interaction is the basis for understanding the methods used in this thesis. Starting with a simplified model, we derive the dynamics of a two-level system interacting with a microwave or light field. The population oscillation between the two energy levels can then be used to adjust a coherent superposition between them.

Extending the two-level system to a three-level system, the basic principles of atom interferometry with light pulses are introduced and the phase evolution of the atom interferometer in presence of inertial forces is shown. An analysis of the impact of laser phase noise and vibration noise on the interferometer is derived.

2.1 Dynamics of a two-level system

This section adapts the formalism given in [77]. The simplest case of a quantum system is a system with only two energy eigenstates. Although there is usually a multiplicity of energy levels in an atom, the two-level system can be used to understand general properties of atom-light interactions. Furthermore systems with additional energy levels can often be simplified to an effective two-level system.

A two-level system is described by the energy difference $\hbar\omega_{eg}$ between its two states, the the ground state $|g\rangle$ and exited state $|e\rangle$. The photons of the electromagnetic field have an energy $\hbar\omega$ and their detuning from the resonance $\omega - \omega_{eg}$ is introduced as δ (see Figure 2.1). This

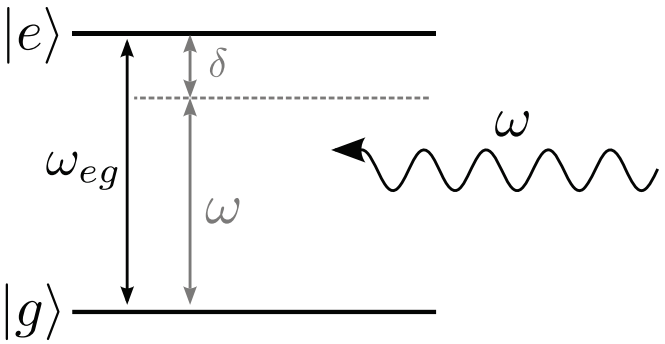

Figure 2.1: A two-level system with a ground state $|g\rangle$ and an exited state $|e\rangle$ with an energy difference $\hbar\omega_{eg}$. A photon with an energy $\hbar\omega$ is detuned by $\delta = \omega - \omega_{eg}$ from the resonance frequency.

two-level system has a time dependent superposition of the two states

$$\Psi(t) = c_g(t)\,|g\rangle + c_e(t)\,|e\rangle \tag{2.1}$$

with time-dependent coefficients $c_g(t)$ and $c_e(t)$. The time evolution of this system is given by the solution of the Schrödinger equation:

$$i\hbar\frac{\partial}{\partial t}\,|\Psi\rangle = \hat{H}\,|\Psi\rangle = (\hat{H}_{\mathrm{A}} + \hat{H}_{\mathrm{int}})\,|\Psi\rangle\,. \tag{2.2}$$

Here $\hat{H}_{\mathrm{A}}$ is the unperturbed Hamiltonian with the eigenenergies $E_g = \hbar\omega_g$ and $E_e = \hbar\omega_e$ of the two states, and $\hat{H}_{\mathrm{int}}$ being the Hamilton operator of the atom-light interaction. We can write

$$\hat{H}_{\mathrm{A}} = \hbar\omega_g\,|g\rangle\langle g| + \hbar\omega_e\,|e\rangle\langle e| \tag{2.3}$$

$$\hat{H}_{\mathrm{int}} = -\mathbf{d}\cdot\mathbf{E}, \tag{2.4}$$

where $\mathbf{d}$ is the electric dipole moment of the atom and $\mathbf{E} = \mathbf{E}(\mathbf{r},t)$ the electric field. In the dipole approximation we neglect the spatial variation of the electric field and write

$$\mathbf{E}(t) = \mathbf{E}_0\cos(\omega t + \phi) = \mathbf{E}_0\left(\frac{e^{i(\omega t+\phi)} + e^{-i(\omega t+\phi)}}{2}\right) \tag{2.5}$$

with the constant phase ϕ. In the basis of the two states the Hamiltonian $\hat{H}$ becomes

$$\hat{H} = \hbar\begin{pmatrix} \omega_g & \Omega_{eg}\left(\frac{e^{i(\omega t+\phi)}+e^{-i(\omega t+\phi)}}{2}\right) \\ \Omega^*_{eg}\left(\frac{e^{i(\omega t+\phi)}+e^{-i(\omega t+\phi)}}{2}\right) & \omega_e \end{pmatrix}, \tag{2.6}$$

where we introduced the resonant Rabi frequency $\Omega_{eg} = -\langle g|\mathbf{d}\cdot\mathbf{E}|e\rangle/\hbar$. This equation is solved by [77]

$$P_e(t) = |c_e(t)|^2 = \left(\frac{\Omega_{eg}}{\Omega_r}\right)^2\sin^2\left(\frac{\Omega_r t}{2}\right) = \left(\frac{\Omega_{eg}}{\Omega_r}\right)^2\frac{1-\cos(\Omega_r t)}{2}, \tag{2.7}$$

$$P_g(t) = 1 - P_e(t), \tag{2.8}$$

for an atom initially in the ground state. The population in the ground $P_g(t)$ and the exited $P_e(t)$ state, oscillates with a frequency proportional to the Rabi frequency $\Omega_r = \sqrt{\delta^2 + \Omega_{eg}^2}$. The presence of the light field gives rise to a shift of the eigenenergies [78]

$$\Delta E_g = -\Delta E_e = \frac{\hbar}{2}(\delta - \Omega_r). \tag{2.9}$$

This shift is called AC Stark shift that can be written in the case of far detuned light ($|\delta| \gg \Omega_{eg}$)

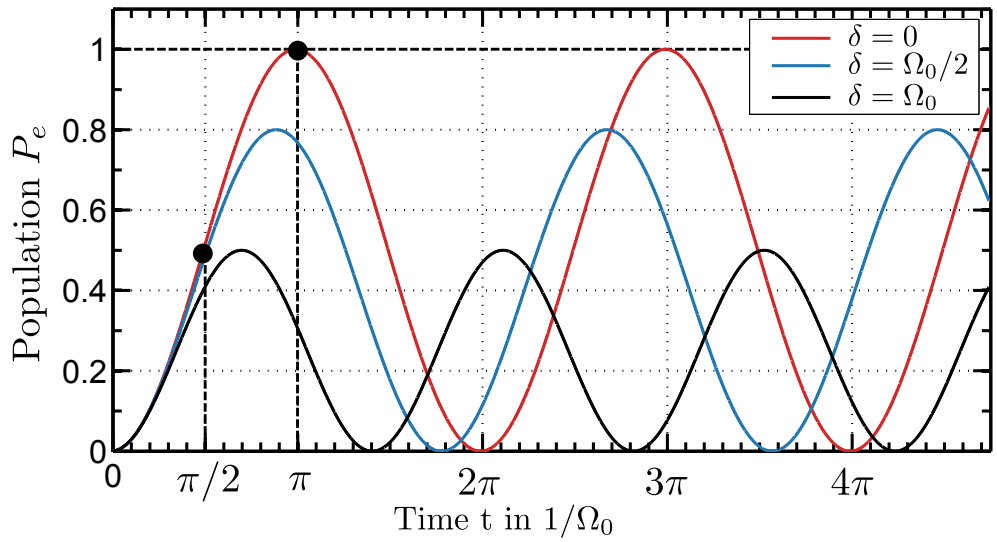

Figure 2.2: Rabi oscillations in a two-level system as a function of the pulse length t and an atom initially in the ground state. The oscillation for three different detunings δ are shown. In the resonant case $\delta = 0$ (red) a complete population inversion is obtained after a π-pulse. For the other detunings $\delta = \Omega_0/2$ (blue) and $\delta = \Omega_0$ (black) the maximum population inversion is reduced.

to

$$\Delta E_g = -\Delta E_e \approx -\frac{\hbar\Omega_{eg}^2}{4\delta}. \tag{2.10}$$

In case of resonant light $\delta = 0$ Equation 2.7 becomes

$$P_e(t) = \frac{1-\cos(\Omega_{eg}t)}{2} \tag{2.11}$$

$$P_g(t) = \frac{1+\cos(\Omega_{eg}t)}{2}. \tag{2.12}$$

The time evolution for different values of the detuning δ is shown in Figure 2.2. This oscillating behaviour can be used to adjust an arbitrary population probability. For the resonant case the population can be inverted by a pulse with the length $\Omega_{eg}t = \pi$ (called π-pulse) if the atom is initially only in one state, while a superposition state with identical amplitudes can be obtained with a pulse length $\Omega_{eg}t = \pi/2$ (called $\pi/2$-pulse).

This description of atom-light interactions includes only the internal degrees of freedom. This is applicable if the frequency of the electromagnetic field is much lower than the momentum spread of the atoms [33] like in microwave atomic clocks. In the case of optical frequencies as in atom interferometers, the description has to be extended to an external degree of freedom. An atom absorbing a photon with a wavelength λ will not only change its internal state, but also its momentum by $\hbar\mathbf{k} = h/\lambda$. The internal and external degrees of free-

dom are now linked to each other and the two states can be written as $|g,p\rangle$ and $|e,p+\hbar\mathbf{k}\rangle$ The momentum and energy conservation for the photon absorption process for the two states with the momentum $\mathbf{p}$ and $\mathbf{p}+\hbar\mathbf{k}$ and kinetic energies

$$\frac{\mathbf{p}^2}{2m} \text{ and } \frac{(\mathbf{p}+\hbar\mathbf{k})^2}{2m} = \frac{\mathbf{p}^2}{2m} + \frac{\hbar\mathbf{p}\cdot\mathbf{k}}{m} + \frac{\hbar^2\mathbf{k}^2}{2m}, \tag{2.13}$$

gives rise to additional terms contributing to the detuning

$$\delta = \omega - \left(\omega_{eg} + \frac{\hbar\mathbf{k}^2}{2m} + \frac{\mathbf{p}\cdot\mathbf{k}}{m}\right), \tag{2.14}$$

namely the one arising from the recoil shift $\hbar\mathbf{k}^2/2m$ of the absorbed photon and the Doppler shift $\mathbf{p}\cdot\mathbf{k}/m = \mathbf{v}\cdot\mathbf{k}$. The interferometer phase $\Delta\Phi$ scales $\propto \hbar\mathbf{k}$, the momentum transferred from the photon as can be seen from Equation 1.2. Transitions with high frequencies are therefore desired for a highly sensitive atom interferometer. The optical transitions in rubidium (e.g. the ^{87}Rb D_2 line whose frequencies can be access easily with available diode lasers) is a suitable choice. The life time of the exited states of this transitions is only 26.24 ns [79], while the free evolution time in modern atom interferometers exceeds 2 s [80].

In contrast, the life time of the hyperfine transition $|F=2\rangle \rightarrow |F=1\rangle$ in ^{87}Rb is $\gg 1$ year, which makes it suitable for atom interferometry. The hyperfine transition in ^{87}Rb is a factor of 5.6×10^4 less sensitive to inertial forces compared to the optical transition (6.8 GHz instead 384 THz). The two photon Raman transition, which transfers the atom from one hyperfine state to the other combines its long life time and thus long free evolution times with the high sensitivity of optical transitions. Raman transitions are introduced in the next section.

2.2 Raman transitions

In this section we closely follow [33, 78]. The principle of Raman transitions using an intermediate level is shown in Figure 2.3. Two counter-propagating ($\mathbf{k_1} \approx -\mathbf{k_2}$) optical fields

$$\mathbf{E}_i = \mathbf{E}_{i,0}\cos(\phi_i) = \mathbf{E}_{i,0}\cos(\mathbf{k}_i\cdot\mathbf{r} - \omega_i t + \phi_{i,0}) \tag{2.15}$$

interact with a three-level system. An intermediate level $|i\rangle$ in this three-level system that is far detuned from the two optical fields with the frequencies ω_1 and ω_2 by the detuning Δ is introduced. From now on we use the the definitions

$$\mathbf{k_1} - \mathbf{k_2} = \mathbf{k}_{\text{eff}} \tag{2.16}$$

$$\omega_1 - \omega_2 = \omega_{\text{eff}} \tag{2.17}$$

$$\phi_1 - \phi_2 = \phi_{\text{eff}} \tag{2.18}$$

In the case of $\Delta \gg \delta$ and $\Delta \gg \gamma$, where γ is the natural line width of the intermediate state

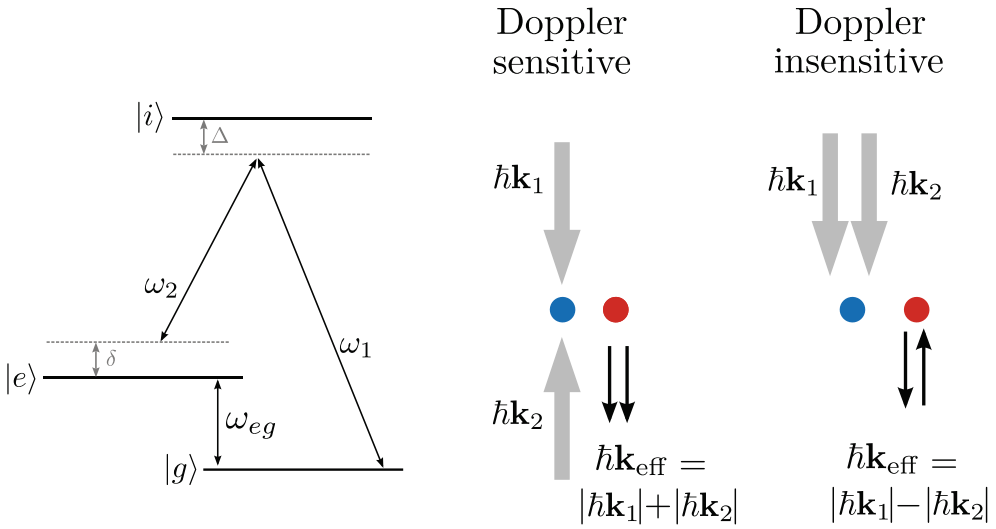

Figure 2.3: (left) Two photon Raman transitions from the ground state $|g\rangle$ to the existed $|e\rangle$ with a long life time using an intermediate level $|i\rangle$. (right) An atom absorbs a photon from one optical field with the wave vector $\mathbf{k_1}$ end emits a photon stimulated by the field with the wave vector $\mathbf{k_2}$. With counter-propagating beams the atoms changes its internal state and gains a momentum of $\hbar\mathbf{k}_{\text{eff}} \approx 2\hbar\mathbf{k_1}$ in this Doppler sensitive transition. In the Doppler insensitive transition with co-propagating beams, the momentum is reduced by a factor of 10^5.

(≈ 6 MHz for transitions of the D_2 line in rubidium), the spontaneous emission from this state and its interactions can be neglected [33, 81]. The previous two-level Hamiltonian has to be extended by the eigenenergy of the intermediate state and the momentum degree of freedom [78]

$$\hat{H} = \hat{H}_A + \hbar\omega_i |i\rangle\langle i| + \frac{\mathbf{p^2}}{2m} - \mathbf{d}\cdot(\mathbf{E_1}+\mathbf{E_2}). \tag{2.19}$$

The Schrödinger equation yields differential equations for the three time dependent coefficients $a_g(t) = c_g(t)e^{-i\omega_g t}$, $a_e(t) = c_e(t)e^{-i\omega_e t}$ and $a_i(t) = c_i(t)e^{-i\omega_i t}$. The coefficients for the intermediate state can be eliminated [82] and the three-level system is transformed to a two-level system. The solution can be written with the following definitions

$$\Omega_{g,n} = -\frac{\langle i|\,\mathbf{d}\cdot\mathbf{E}_n\,|g\rangle}{\hbar}, \quad \Omega_{e,n} = -\frac{\langle i|\,\mathbf{d}\cdot\mathbf{E}_n\,|e\rangle}{\hbar} \tag{2.20}$$

$$\Omega_{\text{eff}} = \frac{\Omega_e^*\Omega_g}{2\Delta} \tag{2.21}$$

$$\Omega_g^{AC} = \frac{|\Omega_{g,1}|^2}{4\Delta} + \frac{|\Omega_{g,2}|^2}{4(\Delta-\omega_{eg})}, \quad \Omega_e^{AC} = \frac{|\Omega_{e,1}|^2}{4\Delta} + \frac{|\Omega_{e,2}|^2}{4(\Delta+\omega_{eg})} \tag{2.22}$$

$$\delta_{12} = (\omega_1 - \omega_2) - \left(\omega_{eg} + \frac{\hbar \mathbf{k_{eff}}^2}{2m} + \frac{\mathbf{p}\cdot\mathbf{k_{eff}}}{m}\right) \tag{2.23}$$

$$\delta^{AC} = \Omega_e^{AC} - \Omega_g^{AC} \tag{2.24}$$

$$\theta_0 = \cos\left(\frac{\Omega_R \tau}{2}\right) + \frac{i(\delta_{12} - \delta^{AC})}{\Omega_R} \cdot \sin\left(\frac{\Omega_R \tau}{2}\right) \tag{2.25}$$

as an oscillation between the ground and exited state:

$$P_e(\tau) = \left(\frac{\Omega_{\text{eff}}^2}{\Omega_R^2}\right) \sin\left(\frac{\Omega_R \tau}{2}\right)^2 = \left(\frac{\Omega_{\text{eff}}^2}{\Omega_R^2}\right) \frac{1 - \cos(\Omega_R \tau)}{2}. \tag{2.26}$$

This effective two-level system also shows Rabi oscillations as a function of the pulse length τ but now with the Rabi frequency of the coupled system

$$\Omega_R = \sqrt{\Omega_{eff}^2 + (\delta_{12} - \delta^{AC})^2} \tag{2.27}$$

which is proportional to the product of the individual Rabi frequencies (in the resonant case). Due to each Raman pulse with a length τ at time t_0 a phase is imprinted on the wave packet depending on the initial and the subsequent state. The phase shifts are shown in Table 2.1.

The phase shift $\pm\phi_{\text{eff}}$ that occurs when the internal and external state are changed is the effective phase (see Equation 2.18). This phase shift depends on the position of the wave packet $\mathbf{k}_{\text{eff}} \cdot \mathbf{r}$ and the effective frequencyω_{eff} and is the origin of the high sensitivity of atom interferometers.

Transition	**Phase shift**
$\|g,\mathbf{p}\rangle \rightarrow \|g,\mathbf{p}\rangle$	$(-\Omega_e^{AC} - \Omega_g^{AC} + \delta_{12})\tau/2 - \theta^0$
$\|g,\mathbf{p}\rangle \rightarrow \|e,\mathbf{p}+\hbar\mathbf{k_{eff}}\rangle$	$(-\Omega_e^{AC} - \Omega_g^{AC} - \delta_{12})\tau/2 - \pi/2 - \delta_{12}t_0 \boxed{-\phi_{\text{eff}}}$
$\|e,\mathbf{p}+\hbar\mathbf{k_{eff}}\rangle \rightarrow \|e,\mathbf{p}+\hbar\mathbf{k_{eff}}\rangle$	$(-\Omega_e^{AC} - \Omega_g^{AC} - \delta_{12})\tau/2 + \theta^0$
$\|e,\mathbf{p}+\hbar\mathbf{k_{eff}}\rangle \rightarrow \|g,\mathbf{p}\rangle$	$(-\Omega_e^{AC} - \Omega_g^{AC} + \delta_{12})\tau/2 - \pi/2 + \delta_{12}t_0 \boxed{+\phi_{\text{eff}}}$

Table 2.1: Phase shifts for a Raman pulse at time t_0 and a pulse length τ for all possible combination of starting and ending states. The boxed phase shift $\pm\phi_{\text{eff}}$ that is imprinted during a state change is the effective phase defined in Equation 2.18 and the source of the high sensitivity in atom interferometers.

2.3 Atom interferometry with light pulses

This section closely follows the introductions given in [33, 83, 84]. With the theoretical tools to understand Raman transitions that transfer momentum to the atomic wave packet, an atom interferometer can be realized. By splitting the wave packet and recombining it again, a phase difference between the interferometer paths manifests in a certain population of the states of the atoms in the output ports of the interferometer. This can be used as a sensitive method to measure the force that caused the phase shift.

2.3.1 Mach-Zehnder interferometer

Various interferometer geometries can be used to sense inertial forces or others like the magnetic field. The most common geometry is the Mach-Zehnder atom interferometer that is the atom optics analog to the optical Mach-Zehnder interferometer. A schematic of which is shown in Figure 2.4.

Here the wave packet is split by the first $\pi/2$-pulse, creating a coherent superposition of the exited and ground state. Due to the momentum transfer the wave packets do not overlap any more after the interferometer time T before being reflected by the π-pulse that acts as a mirror. This reverses the momentum between the superposition, and after an additional time T the atomic wave packet is overlapped, and can be recombined by the last $\pi/2$-pulse. Various interferometer schemes composed by a combination of beam splitter ($\pi/2$-) or mirror π-pulses exist that are sensitive to only one inertial force (f.e. rotation) but suppress the phase contribution due to others (f.e. gravity) [85].

In the last years it was experimentally demonstrated, that the momentum transferred to

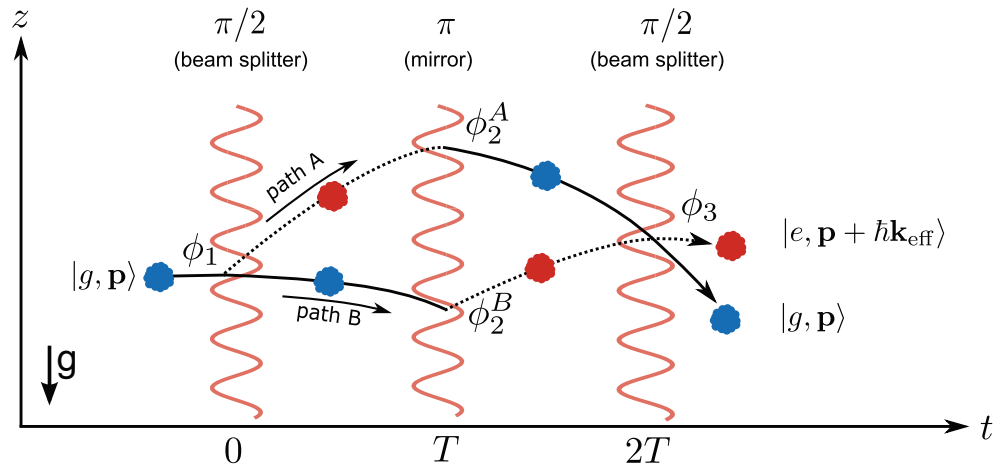

Figure 2.4: A Mach-Zehnder atom interferometer using Raman pulses as beam splitters and mirror. An initial state $|g,\mathrm{p}\rangle$ is split, reflected and recombined in a $\pi/2-\pi-\pi/2$ configuration. The population in the two states $|g,\mathbf{p}\rangle$ and $|e,\mathbf{p}+\hbar\mathbf{k}_{\mathbf{eff}}\rangle$ depends on the phase difference between the two paths A and B.

the atoms and thus the accumulated phase in an atom interferometer can be increased by several orders of magnitude. This was done by successively applying Raman π-pulses to transfer $\mathbf{k_{eff}}$ momentum to atoms in both interferometer paths each pulse. Another successfully demonstrated technique are multi photon Bragg transitions [86].

The sensitivity of atom interferometers to inertial forces scales with the accumulated phase difference between the two arms caused by this forces. Phase contributions caused by gravity in a Mach-Zehnder atom interferometer are presented below.

2.3.2 Phase contributions in a Mach-Zehnder atom interferometer

Since the atomic wave packet is in a superposition of two internal states corresponding to two external momentum states travelling on different trajectories, a phase difference between the two paths will correspond to a population change of the two states after recombination. This phase difference $\Delta\Phi$ can be expressed as a sum of different contributions [33]:

$$\Delta\Phi = \Delta\Phi_{\text{evol}} + \Delta\Phi_{\text{split}} + \Delta\Phi_{\text{laser}}. \tag{2.28}$$

The first term $\Delta\Phi_{\text{evol}}$ corresponds to the free evolution of the atomic wave packet along the two paths. The second term $\Delta\Phi_{\text{split}}$ is caused by the non-perfect overlap of the wave packet and the third term $\Delta\Phi_{\text{laser}}$ is caused by the interaction with the Raman laser field during the pulses.

The phase contribution due to the free evolution of the atomic wave packet can be calculated by solving the Lagrange equation which yields the classical trajectories along the two interferometer arms [84]. The phase contribution $\Delta\phi_{ab}$ for each path is then given by $\Delta\phi_{ab} = S_{ab}/\hbar$ where S_{ab} is the action along the classical trajectory. In the case of a uniform gravity field (i.e. no gravity gradient or terms of higher order), the phase contribution is the same for the two classical trajectories and $\Delta\Phi_{\text{evol}}$ vanishes.

The second contribution $\Delta\Phi_{\text{split}}$ is low and can be neglected under our experimental conditions. For more details see [87].

The third and last contribution $\Delta\Phi_{\text{laser}}$ is the largest one and the main reason for high sensitivity and accuracy in atom interferometers. It originates from the interaction of the atomic wave packet with the interrogating light field as can be seen from the term ϕ_{eff} in Table 2.1. The other terms cancel out in the Mach-Zehnder sequence [78]. In the case of zero effective detuning δ_{12} and zero light shift δ^{AC} the effective phase reduces to

$$\phi_{\text{eff,i}} = \phi_{\text{eff,i}}(z(t_i), t_i) = -\mathbf{k_{eff}}\mathbf{z}(t_i) + \phi_{\text{eff,0}} + \omega_{\text{eff}}(t_i) \tag{2.29}$$

where i corresponds to the i-th pulse and $\phi_{\text{eff,0}}$ is an arbitrary constant phase. The first term is dependent on the position of the wave packet relative to the light field and therefore depends on the classical trajectory of the two interferometer paths A and B (notation as in Figure 2.4). The term $\omega_{\text{eff}}(t_i)$ don't contribute to the interferometer phase in the symmetric Mach-Zehnder sequence if the detuning is constant [88]. The relative probability P_g of finding an atom in the

ground state after the last pulse depends on the phase difference between these two paths and can be written as

$$P_g = \bar{P} - \frac{A}{2}\cos(\Delta\Phi), \tag{2.30}$$

where $\bar{P}$ is the mean population probability and A the peak to peak fringe amplitude (sometimes also called the contrast C). For atoms all initially in the ground state and perfect π and $\pi/2$-pulses, the contrast is unity. In the general case with non-perfect pulses limited by pulse length and/or non-uniform intensity of the Raman beams and decoherence [89] the contrast is reduced. The phase difference between the two paths is then the difference between the imprinted light field phase for each path

$$\Delta\Phi = (\phi_1 - \phi_2^A) - (\phi_2^B - \phi_3), \tag{2.31}$$

where the superscript corresponds to the individual paths as shown in Figure 2.4 and the subscript to the time of the middle of the corresponding pulse. In a uniform gravitational field the classical trajectory is $\mathbf{z}(\mathbf{t_i}) = \mathbf{z_0} + \mathbf{v_0}t_i - \mathbf{g}/2t_i^2$. Using Equation 2.29 together with $t_1 = 0$, $t_2 = T$ and $t_3 = 2T$ the phase contributions calculate to

$$\phi_1 = -\mathbf{k_{eff}}\mathbf{z_0} + \phi_{\mathbf{eff},0} + \omega_{\text{eff}}0 \tag{2.32}$$

$$\phi_2^A = -\mathbf{k_{eff}}(\mathbf{z_0} + \mathbf{v_0}T + \frac{\hbar\mathbf{k_{eff}}}{m}T - \frac{\mathbf{g}}{2}T^2) + \phi_{\text{eff},0} + \omega_{\text{eff}}T \tag{2.33}$$

$$\phi_2^B = -\mathbf{k_{eff}}(\mathbf{z_0} + \mathbf{v_0}T - \frac{\mathbf{g}}{2}T^2) + \phi_{\text{eff},0} + \omega_{\text{eff}}T \tag{2.34}$$

$$\phi_3 = -\mathbf{k_{eff}}(\mathbf{z_0} + \mathbf{v_0}2T + \frac{\hbar\mathbf{k_{eff}}}{m}T - \frac{\mathbf{g}}{2}(2T)^2) + \phi_{\text{eff},0} + \omega_{\text{eff}}2T. \tag{2.35}$$

Here the term $\hbar\mathbf{k_{eff}}/m$ accounts for the recoil velocity due to absorption or emission in the two photon process. Substituting the calculated phase contribution into Equation 2.31 yields

$$\Delta\Phi = \mathbf{k_{eff}} \cdot \mathbf{g}T^2. \tag{2.36}$$

The accumulated phase difference $\Delta\Phi$ and thus the sensitivity of the atom interferometer scales linearly with the effective wave vector and quadratically with the time T between the interferometer pulses. The interferometer phase is also independent of a constant effective frequency ω_{eff} like it is independent of the velocity $\mathbf{v_0}$ (This only holds in a symmetric Mach-Zehnder configuration as recently pointed out in [88]).

The same result can be obtained by measuring the covered distance of a free falling object using three distance measurements spaced by a time T where the ruler scale is given in units of the effective wave vector. This correspondence between the fully classical and quantum mechanical result is remarkable, particularly with regard to the vanishing contribution of the photon recoil. The measured phase can be expressed using the wavelength of the light field and the time T only, without any quantum mechanical contribution. The atomic wave packet

can be seen as a sensor for the local laser field phase and atom interferometry is used as a method for a high sensitively readout of this phase [87].

To account for finite length τ for a Raman $\pi/2$ and 2τ for a π-pulse the equation above is extended to [87]

$$\Delta\Phi = \mathbf{k_{eff}} \cdot \mathbf{g}T(T+2\tau) + \phi_{\text{off}}. \tag{2.37}$$

The additional phase offset ϕ_{off} is added to the last Raman pulse and is used to scan the interferometer phase (see Section 3.4.4).

In the presence of a gravity gradient γ the phase $\Delta\Phi_{\text{evol}}$ due to free evolution does not vanish and needs to be considered. Like in the vanishing case, we can calculate the classical action along the two interferometer paths where the trajectory is now [87]

$$\mathbf{z}(t) \approx \mathbf{z}_0 + \mathbf{v}_0 t - \frac{1}{2}\mathbf{g}t^2 + \gamma t^2(\frac{1}{2}\mathbf{z}_0 + \frac{1}{6}\mathbf{v}_0 t - \frac{1}{24}\mathbf{g}_0 t^2). \tag{2.38}$$

The measured value for g in Equation 2.37 can now be written as

$$g = g_0 - \gamma\left(z_3 + v_{\text{avg}}T - \frac{7}{12}g_0T^2\right) + \mathcal{O}(\gamma^2), \tag{2.39}$$

where z_3 and $v_{\text{avg}} = v_0 + 1/2v_{\text{rec}}$ are the height and the average velocity, during the last Raman pulse and g_0 the gravity value at $z = 0$ respectively. The higher order terms don't contribute at the $\approx 1 \times 10^{-10}$ g level and can be neglected for our targeted accuracy. An in-depth analysis of the gradient's influence including higher orders terms can be found in [87].

The phase contribution due to the interaction with the light field derived above assumed a trajectory collinear to the direction of the light field ($\mathbf{v} \parallel \mathbf{g}$). If this is not the case i.e. when the launch direction of the atomic cloud is not collinear to Earth's gravity, the two interferometer paths will enclose an area and an additional phase contribution [46]

$$\Delta\Phi_{\text{rot}} = 2\mathbf{k}_{\text{eff}} \cdot (\Omega \times \mathbf{v})T^2 \tag{2.40}$$

due to the rotation Ω has to be added to the total interferometer phase. This phase contribution is the atom interferometric Sagnac effect, and can be used just as its classical counterpart for rotation measurements [34]. The influence of the Earth's rotation is actively cancelled in our setup by synchronously rotating the effective wave vector during the interferometer sequence (see Section 3.4.4).

2.4 Sensitivity to noise sources

After deriving the phase contributions for the Mach-Zehnder interferometer geometry in the previous section, we are able to calculate the corresponding gravity value using Equation 2.37. The relative precision $\frac{\Delta g}{g}$ of the determined value is

$$\frac{\Delta g}{g} = \frac{\sigma_\Phi}{\Delta\Phi} = \frac{\sigma_\Phi}{\mathbf{k_{eff}} \cdot \mathbf{g}T^2}, \tag{2.41}$$

with σ_Φ is the uncertainty of the estimated phase. It is the sum of all existing noise sources in the atom interferometer. To analyse the different noise contributions this section introduces the sensitivity function for noise sources in an atom interferometer and applies it to the major noise sources present in GAIN.

2.4.1 Sensitivity function

From the basic interferometer equation $\Delta\Phi = \mathbf{k_{eff}} \cdot \mathbf{g}T^2$ follows that noise imprinted on the effective wave vector $\mathbf{k_{eff}}$, i.e. noise in the difference frequency ω_{eff}, contributes to the interferometer noise. Also vibrations of the effective wave vector add noise to the atom interferometer since accelerations can not be distinguished from the gravitational acceleration g. A quantitative analysis of the influence of these noise sources can be performed using the interferometers sensitivity function $g_s(t)$. It is defined as the change of the interferometer output phase as a function of an infinitesimal phase $\delta\phi$ change occurring during the interferometer sequence

$$g_s(t) = \lim_{\delta\phi\to 0} \frac{\delta\Phi(\delta\phi,t)}{\delta\phi}, \tag{2.42}$$

when the interferometer is working on the fringe slope ($P_e \approx 0.5$). By inserting a phase step into the phase contributions of the three pulses in Equation 2.31 it is clear that a phase step outside the interferometer sequence does not contribute at all ($g_s = 0$). A phase step $\delta\phi$ between the first and second pulse gives

$$\delta\Phi(\delta\phi,t) = -\delta\phi \rightarrow g_s = -1 \tag{2.43}$$

and between the second and third pulse

$$\delta\Phi(\delta\phi,t) = \delta\phi \rightarrow g_s = 1. \tag{2.44}$$

This holds in the case of infinitely short Raman pulses. In the case of finite square Raman pulses the sensitivity function extends to [78]:

$$g_s(t) = \begin{cases} 0 & t < -T - 2\tau \\ \sin(\Omega_R(t+T)) & -T-2\tau < t < -T-\tau \\ -1 & -T-\tau < t < -\tau \\ \sin(\Omega_R t) & -\tau < t < \tau \\ 1 & \tau < t < T+\tau \\ \sin(\Omega_R(t-T)) & T+\tau < t < T+2\tau \\ 0 & T+2\tau < t \end{cases}. \tag{2.45}$$

The sensitivity function is plotted in Figure 2.5. We can calculate the influence of arbitrary

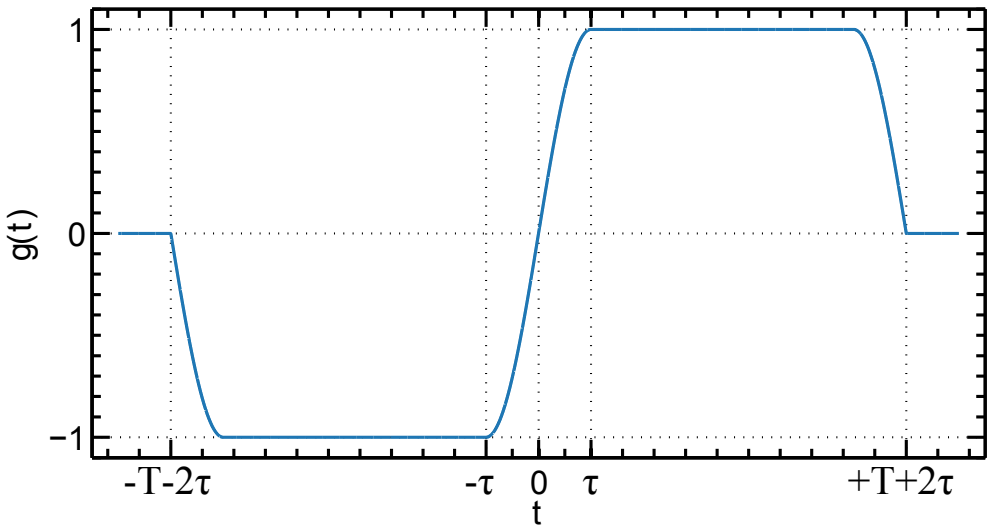

Figure 2.5: The sensitivity function for the Mach-Zehnder interferometer scheme for an infinitesimal phase step at the time t, a $\pi/2$-pulse duration τ and a time T between the pulses.

phase noise $\phi_n(t)$ by integrating Equation 2.42

$$\delta\Phi = \int_{-\infty}^{\infty} g_s(t) d\phi_n(t) = \int_{-\infty}^{\infty} g_s(t) \frac{d\phi_n(t)}{dt} dt. \tag{2.46}$$

2.4.2 Raman phase noise

Raman phase noise is generally measured in the frequency domain instead in the time domain. Therefore we use the Fourier transform of the sensitivity function

$$G(\omega) = \int_{-\infty}^{\infty} g_s(t) e^{i\omega t} dt. \tag{2.47}$$

With a given Raman phase noise power spectral density $S_\phi(\omega)$ we can calculate its influence on the interferometer phase noise $\sigma_{\Phi_{\text{ph}}}$ by integrating over all frequencies [78]

$$\sigma^2_{\Phi_{\text{ph}}} = \int_{0}^{\infty} |H_\phi(\omega)|^2 S_\phi(\omega) d\omega. \tag{2.48}$$

Here we used the relation

$$H_\phi(\omega) = \omega G(\omega), \tag{2.49}$$

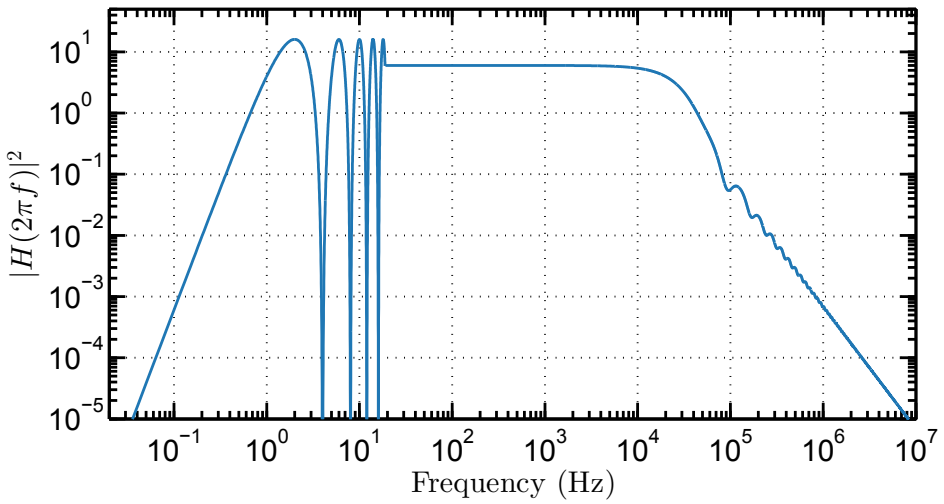

Figure 2.6: The phase noise transfer function for typical experimental parameters $T = 260\,\text{ms}$ and $\tau = 13.5\,\mu\text{s}$. For higher frequencies the average value is plotted.

between the phase noise transfer function $H_\phi(\omega)$ that connects the Raman phase noise with interferometer phase noise, and the Fourier transformed sensitivity function $G(\omega)$ [90].

The written-out transfer function

$$H_\phi(\omega) = -\frac{4\Omega_R\omega}{\omega^2-\Omega_R^2}\sin\left(\frac{\omega(T+2\tau)}{2}\right)\cdot\left(\cos\left(\frac{\omega(T+2\tau)}{2}\right)+\frac{\Omega_R}{\omega}\sin\left(\frac{\omega T}{2}\right)\right) \tag{2.50}$$

is plotted in Figure 2.6 for the experimental parameters $T = 260\,\text{ms}$ and $\tau = 13.5\,\mu\text{s}$. The transfer function shows both a low-pass and a high-pass behaviour. The high-pass frequency is mainly determined by pulse separation time T and increasing T increases the sensitivity function for low frequencies. The low-pass behaviour is mainly given by the pulse length τ and increasing the pulse length reduces the sensitivity function for higher frequencies since Raman phase noise at a frequency ω averages out during a pulse duration $\tau \gg \frac{1}{\omega}$.

2.4.3 Vibrational noise

In our setup the two counter propagating ($\mathbf{k_1} \approx -\mathbf{k_2}$) beams, needed for the velocity sensitive Raman transitions, are realized by launching both beams out of one collimator sitting on top of the vacuum chamber. The beams are retro-reflected on a mirror below the chamber. Vibrations of all components sitting on top are the same for both beams and cancel out. Vibrations of the bottom mirror, however, contribute only to the retro reflected beam and are an additional contribution to phase noise. A displacement δz of the mirror causes a phase shift $\delta\phi \approx \mathbf{k}_{\text{eff}}\delta z$.

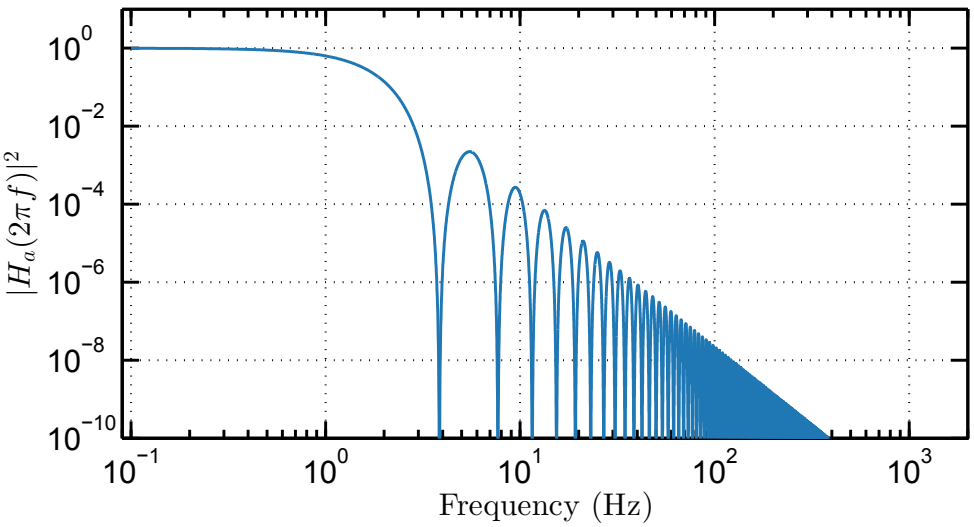

Figure 2.7: The normalized transfer function for vibration noise, evaluated for the experimental parameters $T = 260\,\text{ms}$ and $\tau = 13.5\,\mu\text{s}$

The phase noise due to vibrational noise with a power spectral density $S_a(\omega)$ is then [91]

$$\sigma^2_{\Phi_{\text{vib}}} = \int_0^\infty |H_a(\omega)|^2 S_a(\omega) d\omega, \tag{2.51}$$

where we introduced the transfer function for vibration noise

$$|H_a(\omega)|^2 = \frac{\mathbf{k}_{\text{eff}}{}^2}{\omega^4} |H_\phi(\omega)|^2. \tag{2.52}$$

The normalized transfer function for the experimental parameters $T = 260\,\text{ms}$ and $\tau = 13.5\,\mu\text{s}$ is shown in Figure 2.7. The low pass behaviour is clearly visible. Naturally for a gravimeter, the atom interferometer is most sensitive to low frequencies close to DC, while higher frequencies are attenuated.

The Raman phase noise can be reduced to a degree where it is not the limitation of the interferometer performance, by sophisticated electronic feedback loops and an ultra low noise frequency reference. The vibration noise, however, is the dominating noise contribution. Using an active vibration isolation stage (see Section 3.1.3), a passive isolation stage and correlation with an accelerometer, or a combination of both techniques reduces the influence of vibrational noise. However, until now, only atomic gravimeters placed in an environment with an already very low vibration level (an underground facility f.e. [42]) demonstrated an negligible vibrational noise contribution in combination with an active vibration isolation. Such dedicated measurement sites, where the atom interferometer can operate with its best sensitivity, are not always sites of high interest.

2.4.4 Differential atom interferometers

For measurements of the gravity gradient a differential atom interferometer where two clouds are interrogated simultaneously with the same Raman beams can be used to drastically suppress vibration and Raman phase noise since this both contributions are common mode. By using two clouds separated along the direction of the Raman beam the phase difference between this two interferometers is correlated and can be extracted even under noisy conditions. Such atomic gradiometers have been realized [92] and the gravity gradient contains important information about the mass distribution and can also be used for search of oil, water or other raw materials to name just a few fields of application.

2.5 Summary

This chapter gave an overview of the theoretical foundations of atom interferometry with light pulses. The interferometer phase in the presence of a gravity field was derived and the dominant noise sources were quantitatively analysed. The next two chapters present the realization of an atom interferometer for gravity measurements and its sub components. Long term gravity comparisons with the three most used types of classical gravimeters together with an analysis of present noise sources and possible future improvements are also presented. The outstanding performance on ground allows an estimation of the possible performance for a space based test of the Universality of Free Fall.

3 The mobile atom interferometer GAIN

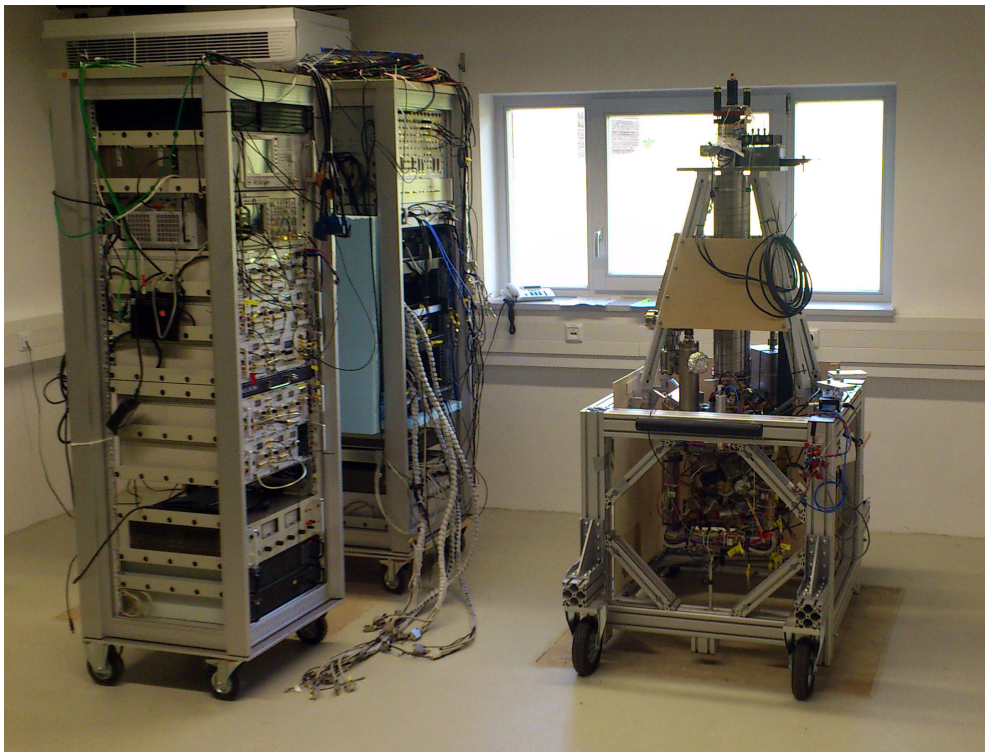

Figure 3.1: The mobile atom interferometer GAIN after transport to the Geodetic Observatory Wettzell. The electronics rack (left), the physics package (right) and the laser system rack (back) are GAIN's three major parts.

With the basic theoretical tools for atom interferometry introduced in the previous chapter, a mobile atom interferometer for gravity measurements is presented. The Gravimetric Atom INterferometer (GAIN) based on an atomic fountain was designed to perform high precision and stable gravity measurements on various sites of interest. This allows for comparisons with other gravimeters to verify GAIN's performance and study systematic effects. The mobility allows for measurements on low vibration sites to reach the gravimeters best possible sensitivity. The insight obtained there is crucial for future tests of fundamental physics with atom interferometry both on Earth and in space.

The experimental setup with focus on the laser system is presented. This is followed by the description of the experimental sequence for gravity measurements. Long term gravity

measurements including comparisons with three types of gravimeters used most today and an analysis of the gravimeter performance during this comparisons is presented in Chapter 4.

The experimental setup of GAIN can be divided into three major parts. The so called *physics package* includes the vacuum chamber with optics mounted into a mobile frame and the vibration isolation underneath. The *laser system* provides laser with sufficient output power for laser cooling, interferometry and a precise control over the laser's frequencies including switching and distribution of the light. As a connection between these two parts, the *control system* provides for the operator the necessary control of most of the parameters that define the experimental sequence and store the measured data. These three parts are presented here.

3.1 Physics package

The physics package is the place where the preparation of the atomic cloud and the experimental sequence is taking place. It can be separated from the laser system and the electronics and is build with only few movable parts. Its task is to isolate the atomic sample from the environment in a well shielded interferometer zone, but also allow for optical access for the laser light to prepare, manipulate and detect the atoms. The physics package was developed by Alexander Senger and a detailed description can be found in his thesis [93]. While being based on previous laboratory set-ups [87], it was built with a high degree of compact, integrated and fixed components. The physic package can easily be transported while maintaining the vacuum pressure and alignment of the optical components.

3.1.1 Vacuum chamber

In GAIN the interferometer time T reaches up to 260 ms and the atoms in the atomic fountain travel more than 1.5 m in the interferometer tube. Collisions with atoms from the residual gas in the vacuum cause atom number loss in the atomic cloud depending on the vacuum pressure. Therefore, the operating vacuum pressure should be in the 10^{-10}–10^{-9} mbar range [94].

The GAIN vacuum chamber is shown in Figure 3.2. The chamber is assembled from several major parts. First, the magneto-optical trap (MOT) chamber (see Figure 3.2), where the atoms are cooled and launched upwards in an atomic fountain. The MOT chamber is connected to the detection area via a flexible joint. The joint is used to adjust the launch direction of the atomic sample. While this can also be done with the balance of MOT beams it is preferred to decouple the adjustment of the launch direction. This allows to adjust the MOT for the coldest temperature and then the direction of the launch without deflecting one thing from the other. The octagon-shaped area (see Figure 3.2) is used for the detection and provides access for an ion getter pump and a titanium sublimation pump. A 75 cm long tube serves as the interferometer region and a three layer shield made from mu-metal around the interferometer region suppresses the magnetic field of the environment present in the tube. The chamber is made of Titanium Grade 5, chosen due to its low magnetic permeability. This helps reducing eddy currents caused by on and off switching of the magnetic field produced by the coils attached to the MOT chamber. The low density of the Titanium Grade 5 also reduces the

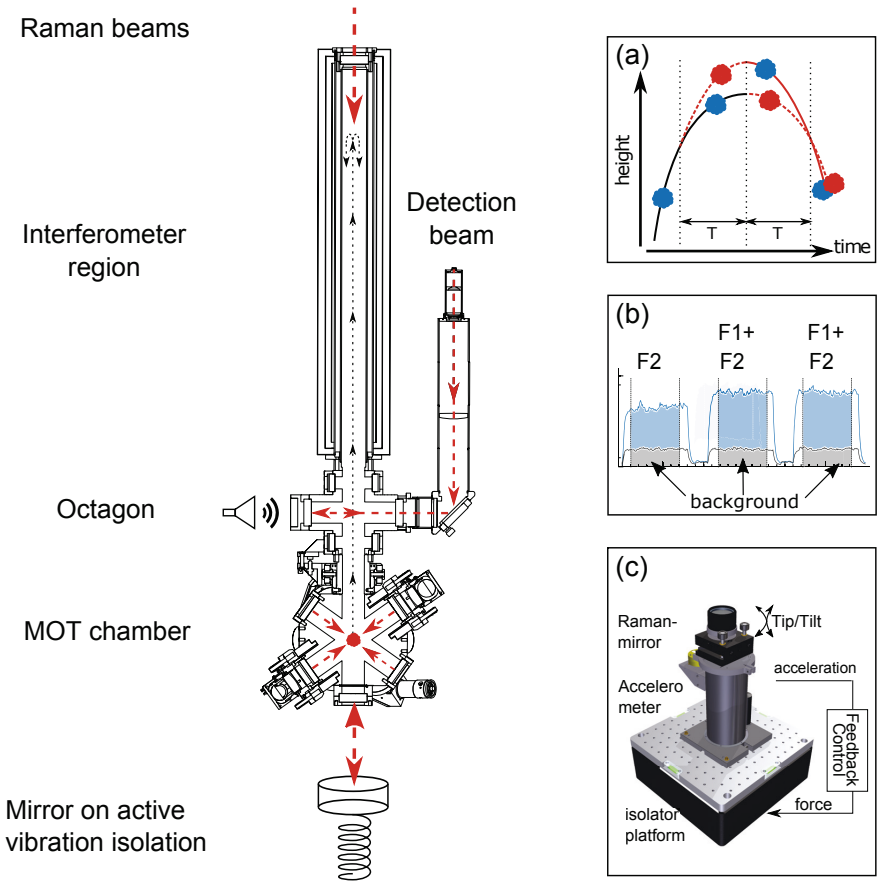

Figure 3.2: Cross-sectional view of the GAIN vacuum chamber (designed by A. Senger [93]). The labelled regions are detailed described in the text. (a) Atoms are loaded in a magneto-optical trap (MOT) and launched in an atomic fountain against gravity. After the Mach-Zehnder interferometer pulse sequence (b) the normalized population of the atoms in the two states is detected. (c) The retro reflecting mirror is sitting on top of the vibration isolator platform. Sub-figure (c) courtesy of Christian Freier.

overall weight of the setup while featuring high stiffness. Windows providing optical access are sealed with indium wires while pumps and tubes are sealed via knife edge copper gaskets that are widely used in UHV applications.

A pressure level below 2×10^{-10} mbar can be reached in our setup. A dispenser [SAES Getters], a compact alkali metal source, releases rubidium when it is heated by an applied current, providing an adjustable rubidium background pressure. As a trade-off between loading time and background vacuum pressure the interferometer usually operates around 7×10^{-10} mbar. The vacuum is maintained by the ion pump and an activation of the titanium sublimation pump is performed only 1-2 times a year mostly after firing the dispensers with a higher current than usual which acts as a cleaning procedure. If disconnected from the power supply for hours, the ion pump reaches the previous pressure values after minutes. This allows to transport

the chamber without a continuous power supply and the operation of the system shortly after power up.

3.1.2 Beam optics

To trap, manipulate and detect the atoms, light is delivered to the chamber via polarization maintaining (pm) optical fibres. The six MOT beams are collimated in custom made telescopes to a $1/e^2$ beam diameter of 30 mm. For a compact design of the MOT telescopes, the beam is folded via a gold coated mirror. The MOT telescopes include a polarizer for further cleaning of the fibre output polarization and a retardation plate to create the desired circular polarization needed for MOT operation. Some percent of the light power are directed on a photo diode via a beam splitter to monitor the power inside each telescope. The telescopes are attached to the vacuum chamber in the so called 1-1-1 configuration with all axes tilted by an angle $\cos\alpha = 1/\sqrt{3}$ to the vertical interferometry axis [93]. Small adjustments of the telescopes' orientation can be made with two fine adjustment screws. A coarse beam adjustment is made by maximizing the power measured behind a small aperture centred on the window opposite to the telescope. Fine adjustment is done by coupling the light from the first telescope into the fibre of the opposite one. However, this method of an almost perfect beam overlap results in an unstable MOT caused by standing waves formed by the opposite beam pairs. To circumvent this, the telescopes are symmetrically inclined in respect to the horizontal plane by one or two turns of the fine adjustment screws while observing the MOT signal. This adjustment procedure is crucial for achieving a low temperature of the atoms in the MOT.

The beams for removal of the atoms in either the F=1 or F=2 state (called blow away beams) are delivered via bare fibres attached to the octagon. The divergence of the beam leaving the fibre is high enough to sufficiently enlarge the beam at the atom's position. The detection beam (see Figure 3.2) is collimated in a lens tube, incorporating a $\lambda/4$ wave plate and an adjustable iris for changing the beam size. The beam is retro reflected on a mirror. As a consequence atoms absorb photons from both directions during the detection and are not immediately pushed away from the detection beam as in case of a beam from one direction (like in the case of the blow away beams).

The Raman telescope [60FC-T-4-M200-37, Schäfter + Kirchhoff GmbH] delivers the interferometer beams to the atoms with highest requirements for beam quality, collimation and alignment. The beam from a polarization maintaining fibre with the numerical aperture $NA = 0.09$ is collimated by a lens with a focal length $f = 200$ mm to a beam with a $1/e^2$ diameter of 29.5 mm. The lens has a flatness specified as better than $\lambda/20$ over the clear aperture. The telescope is fixed to a mirror mount and its angle can be changed through two stepper motors. After passing the vacuum chamber trough two high quality windows (custom assembly [SVI Melles Griot] with a flatness specified better than $\lambda/20$ over the used area) the beam is retro reflected by a mirror and the linear polarization is rotated by 90° by double passing a $\lambda/4$ wave plate. This orients the polarization of the retro reflected beam orthogonal to the incoming beam, resulting in the desired lin$\perp$lin orientation for the Doppler sensitive interferometer. By inserting a $\lambda/4$ wave plate plate in the Raman beam path direct behind the telescope, Doppler insensitive transitions can be introduced. The Raman beams need to be prevented from retro

reflection in this method by blocking the the bottom $\lambda/4$ wave plate and the mirror. A detailed description of the influence of the Raman beam orientation and wavefront aberrations to the measured interferometer phase will be presented in Section 4.4.

3.1.3 Vibration isolation

As already stated in Section 2.4.3 vibration noise of the retro-reflecting mirror transfer into interferometer phase noise according to Equation 2.51. Vibration noise not only degrades the interferometer performance but can also make the phase measurement impossible if the vibration noise exceeds $\pm\pi$ between two consecutive measurements [95].

Therefore, a two stage active vibration isolation platform is used in GAIN. Residual vibrations of an originally passive isolation platform [50BM-10, MinusK] based on mechanical springs and pendulum [81] are measured by a seismometer [CMG-3VL, Guralp] sitting on top (see Figure 3.3). They are used as the input signal of a feed-back loop to counteract the vibrations via two voice-coils that are installed as a modification of the original platform. The data acquisition is performed by a real-time computer system [compactRIO, National Instruments]. Thereby the original resonance frequency of the platform could be reduced from 0.5 Hz to 0.05 Hz providing between a factor of $10-100$ reduction of the amplitude spectral density of the laboratory vibrations in the 0.1 Hz - 50 Hz frequency band [81]. Figure 3.3 shows the performance of the stage. On top of the seismometer the retro-reflecting mirror is mounted on a Tip/Tilt stage realized by two piezo elements [S-330, PI] to control the mirror orientation for Coriolis force compensation (see Section 3.4). This active vibration isolation is based on ideas presented in [96] and was realized during the diploma thesis of Christian Freier [97].

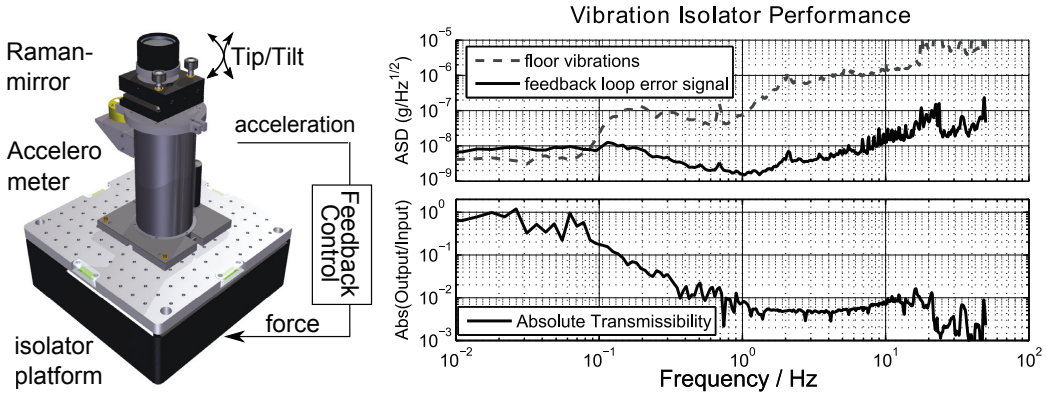

Figure 3.3: (left) A CAD model of the vibration isolation platform. The Raman mirror is mounted in a Tip/Tilt stage on top of the accelerometer which itself is mounted on top of a vibration isolation platform. A feedback loop to reduce the vibrations using built-in voice coils. (right) The acceleration spectral density (ASD) of the floor vibrations (dotted line) and the feedback loop error signal (solid line) are shown in the upper plot. A reduction between a factor of $10-100$ in the 0.1 Hz-50 Hz frequency band is achieved (lower plot). Modified figure, original figure courtesy of Christian Freier.

3.2 Laser system

To trap, launch, select, interrogate and detect the atoms, different laser frequencies are needed. They have to be controllable in their absolute frequency and the light intensity needs to be switched with µs resolution. Additionally, the laser linewidth and frequency stability, including phase noise of the Raman lasers should not limit the interferometer performance. While many different laser set-ups for atom interferometry are build in laboratories on one or more optical tables, compact systems for atom interferometry were rare during the primary design phase of the apparatus. A mobile atom interferometer also needs a mobile laser system to operate outside the lab on different points of interest. These sites are usually operated by the geodesic community to perform gravity measurements. They are mostly accessible by cars and usually contain a dedicated house for operating gravimeters. The temperature in this buildings is generally controlled within 1–2 °C.

This sets the laser system requirements for a mobile atom interferometer. It has to be compact enough to be transported and operated in a standard height room. The impact of the changing temperature has to be reduced to a degree where a gravity measurement can be performed over a period of days with only small interruptions. Especially the laser power at the MOT telescopes need high absolute and relative stability to reduce drifts of the MOT position and avoid frequent realignments. A big part of this thesis was dedicated to the operation and optimization of the laser system including numerous replacements and redesigns of the laser sources. To overcome the limitations of the setup first used, a highly stable fibre coupled tapered amplifier module was designed, built and integrated into the existing setup. This allowed to reduce the complexity of the laser system and simultaneously to eliminate the need of any adjustments in this module over the duration of multiple gravimeter measurements. The GAIN laser system is presented in the next section, including a detailed description of the amplifier module.

3.2.1 Laser system overview

A typical lab setup consists of standard size optics mounted on a heavy optical table. Such a setup is generally to big and to heavy to be used for mobile operation. The laser system of GAIN is therefore based on self-made mounts for the optical components, mounted on a 10 mm × 10 mm drill hole grid. The length of the optical beam paths in the individual modules is kept to a minimum to reduce the effects of thermal drifts. To decouple the optical adjustment of the components from one other, the laser system is divided in multiple modules interconnected with polarization maintaining (pm) fibres. This also minimizes the time needed for replacement of broken components and of realignment after transportation.

To provide the optical frequencies needed for the atom interferometer operation five laser sources shown in Figure 3.4 are used and three additional amplifiers provide sufficient optical power. While the amount of laser sources can be reduced even to only one laser [98] a higher number of laser sources allows for the most flexible interferometer operation and makes advanced or new interferometer sequences easy to implement. Two external cavity diode lasers (ECDL), each amplified by a 1 W tapered amplifier [Eagleyard] are used for the generation of

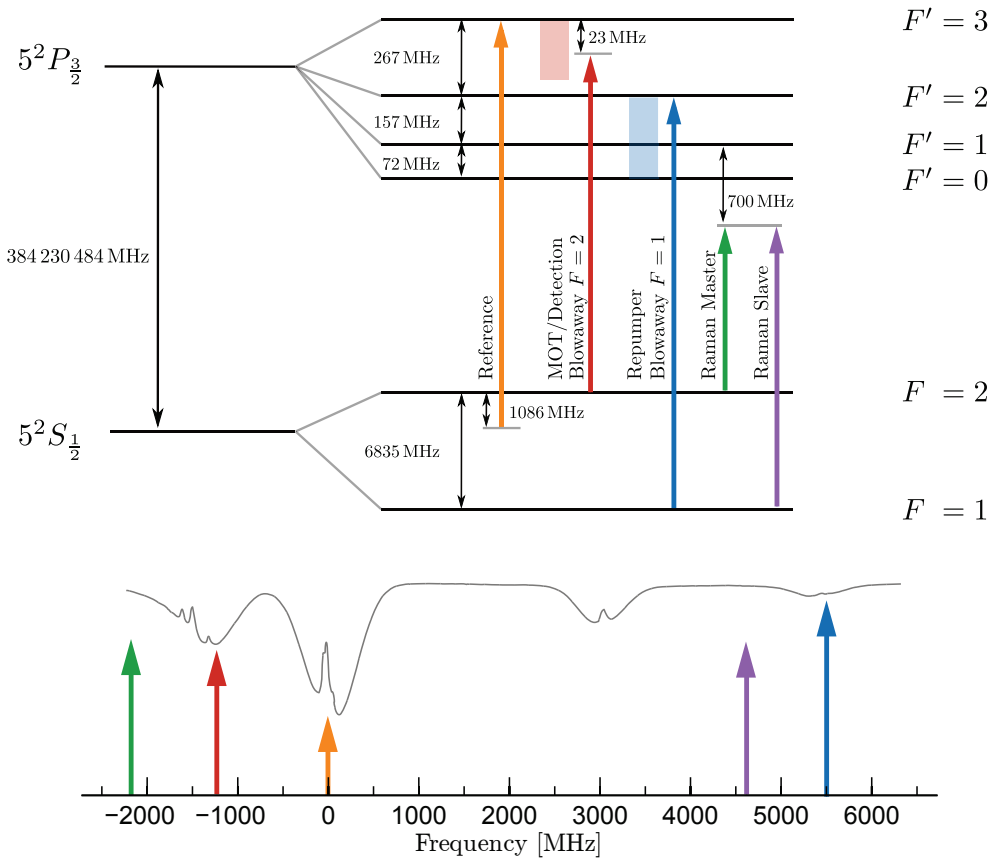

Figure 3.4: (Top) The level scheme of the rubidium D_2 line and the corresponding frequencies of the five laser sources in GAIN. The reference laser is stabilized to the closed ^{85}Rb cooling transition while the remaining four laser are offset locked and perform cooling, repumping, detection and interferometry with ^{87}Rb. The shaded regions represent the tuning range used in the experimental sequence. Frequency data extracted from [79]. (Bottom) Doppler free absorption in rubidium and the involved transitions.

the Raman beam splitter pulses (represented by green and violet arrows in Figure 3.4). Two distributed feedback diode lasers (DFB) [Eagleyard] are used for cooling, repumping, detection and the blow away pulses (red and blue arrows). The light of one DFB diode is amplified by a 2 W [FBH, Berlin] tapered amplifier in a fibre coupled module. The last ECDL (orange arrow) is dedicated as an optical reference for the previous four lasers and is discussed next.

3.2.2 Reference laser

Each laser in the setup has to be referenced to a well known optical frequency. This can be done with a frequency comb or via locking to atomic transitions. While a frequency comb offers a high degree of precision and accuracy, commercial variants are expensive and bulky compared to our laser system. However, Chapter 6 will present a frequency comb developed

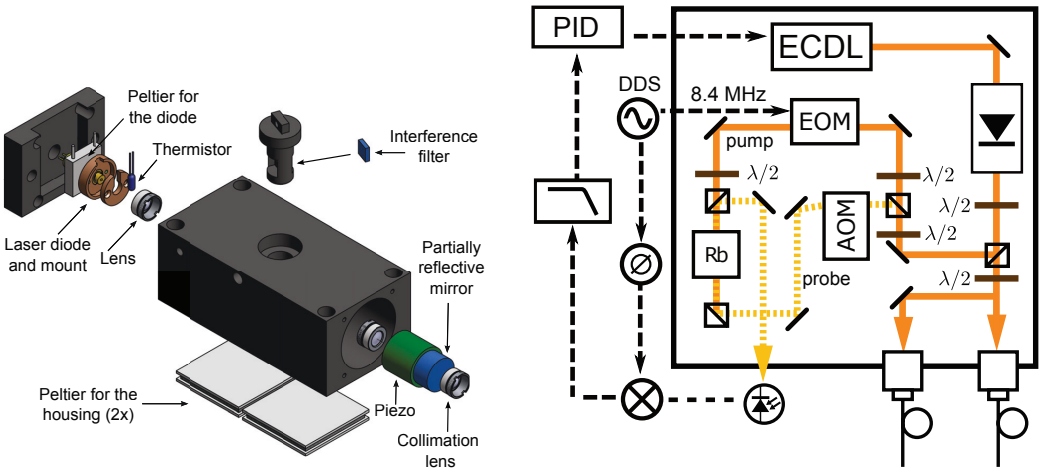

Figure 3.5: (a) An explosion view of the external cavity diode laser used as a reference laser in GAIN. Light emitted by the laser diode is collimated and passes an interference filter to force single mode operation. The beam is then focused on a partially reflective mirror forming the cats eye configuration and is collimated again. Original CAD model by M. Schmidt [78]. **(b)** A schematic view of the GAIN reference module that stabilize the ECDL's frequency using MTS spectroscopy. See the text for more details.

for an operation on sounding rockets that is compact in volume, low in power consumption and offers an automated control of all parameters. Since all frequencies needed in our gravimeter are spread only over 8 GHz we use a stabilised laser as a reference.

For laser stabilization, we employ the modulation transfer spectroscopy (MTS) technique [99, 100] that uses the Doppler free saturation spectroscopy signal [101]. This allows to lock the laser to an atomic transition with sub MHz frequency stability. Compared to the widely used frequency modulation spectroscopy (FMS) [102] where the probe beam is modulated, the MTS signal shows strong features only for the closed transitions. The remaining transitions are highly suppressed due to the non-linear process involved in the MTS signal generation. Additionally, the MTS signal has no derivative of the Doppler broadened absorption in contrast to the FMS technique, resulting in a zero error signal outside the closed transitions and thus a higher long term frequency stability. The MTS technique needs an additional modulator, that can be a phase modulator or an acoustic optical modulator (AOM), in the path of the pump beam. This increases the cost and the experimental complexity of the MTS set-up. However, for GAIN the long term stability of gravity measurements depends on the stability of the effective wave vector $\mathbf{k}_{\text{eff}} \approx 2f_{\text{ref}} \cdot (2\pi/c)$ that needs to be better than the targeted stability of $\approx 5 \times 10^{-11}$ g after 10^5 s at the moment (with the frequency f_{ref} of the reference laser). This requirement is hard to reach with a set-up less complex than the MTS one. For this reason the MTS technique is used to stabilize the GAIN reference laser.

The schematic of the spectroscopy module is shown in Figure 3.5 (b). The reference laser is a in-house constructed [78] ECDL based on the design originally realized at SYRTE [103] and

is shown in Figure 3.5 (a). It uses a commercial laser diode [Sharp GH0781JA2C] that operates around 785 nm without external feedback. To tune the frequency to the desired rubidium transition and to narrow the laser linewidth we use a cavity formed by focusing the beam on a partially reflective mirror. The mirror in this so called cats-eye configuration [103] is mounted on a piezo crystal for fine tuning the cavity length. In this arrangement, the laser would lase in multiple modes all corresponding to the different cavity modes in the laser gain bandwidth. To implement a stronger mode competition, an interference filter with a bandwidth < 0.3 nm is inserted into the cavity. The combination of the cavity and interference filter offers single mode operation resulting in a line width ≈ 50 kHz (FWHM) and an output power of ≈ 50 mW [78]. A mode hope free tunability over the free spectral range (FSR) of the cavity of 1.9 GHz by changing the cavity length with the piezo only is achieved. The laser can be mode hope free tuned by more than 8 GHz [78], when the diode current is adjusted in a fixed ratio to the applied piezo voltage. We chose this linear cavity design because it is less sensitive against misalignments and vibrations compared to the common used Littrow or Littmann design that uses the first order reflection from a grating as a frequency discriminator [103, 104]. Coarse wavelength change is accomplished by turning the interference filter and fine changes are performed by changing the piezo voltage or the diode current without changing the beam path like in the Littrow configuration. This decouples the frequency tuning from the beam pointing that that is sufficient for fibre coupling of the lasers.

About 1 mW light from the reference laser is split off for the spectroscopy lock, while the rest is coupled into two pm fibres for frequency stabilization of the cooling and Raman module. To perform Doppler free spectroscopy, the beam is divided into the pump and probe beam (solid and dashed beams in Figure 3.5 (b)). While the probe beam's frequency is shifted by 80 MHz with an AOM [3080-125, Crystal Technology, Inc] to avoid standing waves in the gas cell, the pump beam is phase modulated by an electro-optical modulator (EOM) [8450-202-300-1, Linos]. The modulated side-bands on the pump beam experience a four wave mixing process with the probe beam in the gas cell. The process is more efficient for closed transitions, leaving a very strong signal on these and small ones on the other transitions [99, 105]. The probe beam is detected by a fast photo diode and the AC-coupled signal is demodulated on a double balanced mixer. The mixed signal is proportional to the derivative of the absorption signal and is used as an error signal for locking the ECDL with self-build PI feedback control. The feedback is divided in a slow path controlling the piezo position and a fast path for the laser diode current. We stabilize the laser 40 MHz below the $|F = 3\rangle \rightarrow |F' = 4\rangle$ ^{85}Rb transition (due to the 80 MHz shift of the probe beam, the zero-velocity class for the probe and pump beam in the gas cell is Doppler shifted by 40 MHz). Typically, operation times in the lab can reach several weeks without the need for relocking the laser, while mobile measurements demands manual intervention on the hardware on a daily basis caused by environmental changes.

3.2.3 Cooling module

The cooling module contains two laser diodes, frequency locked to the reference laser. They are used for cooling, repumping, blow away pulses and detection. The locks are based on a

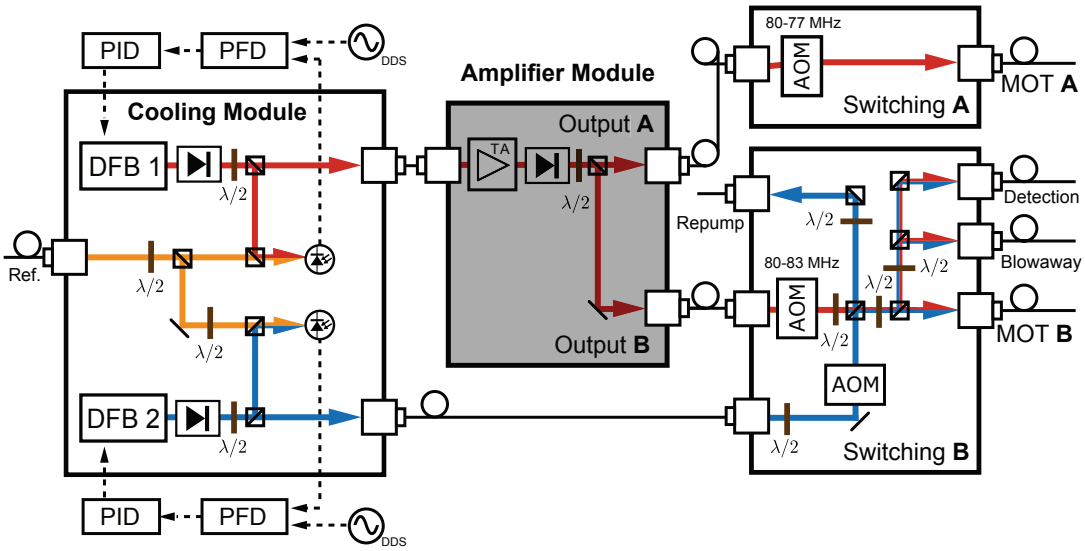

Figure 3.6: A schematic view of the part of the laser system used for generating and switching light for cooling, repumping, blowaway and detection. Light from DFB 1 is stabilized to the cooling transition (red arrow in Figure 3.4) and is amplified (the greyed out amplifier module is described in the next section). Light from DFB 2 is stabilized to the repump transition (blue arrow in Figure 3.4) and both lights are distributed and partially overlapped in the switching modules. Some mirrors are not shown for clarity.

digital phase-frequency-detector (PFD) [HMC440QS16G, Hittite] that detects the phase between the beat frequency and a reference frequency provided by a Direct Digital Synthesizer (DDS). The output of the PFD contains pulses with a length proportional to the phase difference. By low pass filtering the output, one gets a dc signal proportional to the phase difference. This signal is fed into a feedback loop similar to the one used for the reference laser. The offset frequencies for cooling are $\approx 1000\,\mathrm{MHz}$ and $\approx 5080\,\mathrm{MHz}$ for the repumping laser. The laser type used in the cooling module is a DFB diode laser [EYP-DFB-0780-00080] with a feedback grating directly imprinted into the diode gain structure. These diodes have a linewidth of about 1 MHz and offer large mode-hop free tuning up to 100 GHz [106]. We choose these diodes due to their robustness and compact size. The larger line width compared to ECDLs is not a limitation in this setup since cooling and repumping requires a line width smaller than the natural transition for rubidium of $\approx 6\,\mathrm{MHz}$.

Light from each DFB diode laser is collimated by a lens with a focal length of 3.1 mm [C330TMD-B, Thorlabs] and passes a double stage 60 dB optical isolator [I-80-U-2, Isowave] to protect the the DFB diodes from optical feedback. DFB diode lasers are very sensitive to optical feedback and tend to operate multi mode without optical isolation. Optical feedback from the rear facet of one tapered amplifier in the first GAIN laser system generation caused unstable multi-mode operation of the amplified DFB diode. In addition to the 60 dB optical isolator another 35 dB isolator was placed into the beam path to stop this effect. A small part of the light, $\approx 2\,\mathrm{mW}$ from each diode, is individually overlapped with light from the reference

laser and focussed on a fast photodiode [Hamamatsu, G4176-03] to generate a beat signal for each of the two lasers. The beat signals are then amplified, the repump beat frequency is divided by a factor of 8 by a pre-scaler [HMC363S8G, Hittite]. Each beat signal is divided by a factor of 32 and 10 for the repump and the cooling, respectively, in the adjustable internal prescalers of the PFD to obtain a frequency in the working range of the PFD for error signal generation.

The remaining light from each laser is coupled into polarization maintaining fibres. The light from the DFB 2 laser, stabilized 5080 MHz above the reference laser frequency, is used for repumping and the F=1 blow away and is sent directly to the switching B module (see Figure 3.6). Light from DFB 1 is used for cooling, detection and the F=2 blow away and is amplified in the amplifier module (see Section 3.2.4) before it is also sent to the "switching B" and additionally to the "switching A" module, as can be seen in Figure 3.6. Both modules are used for overlapping the cooling and repumping light and fast switching with the help of AOMs.

Additionally, they also produce the needed frequency detuning between the three upper MOT beams (MOT B beams) and the three lower (MOT A beams) of 3 MHz each. The commonly used approach for doing this is the use of an AOM in the double pass configuration, which is less sensitive to the angle deviations imprinted by the AOMs frequency change. This was also the procedure used in the old setup (up to the summer 2013) and had major drawback of frequently needed complete realignment due to long beam paths in the setup. Each switching module now uses an AOM in a single pass configuration for the 3 MHz detuning. Using a collimator and coupler with a short focal length of 2 mm [60FC-4-A2-02 and 60SMS-1-4-A2,Schäfter + Kirchhoff] the 3 MHz detuning decreases the power coupled into a pm fibre by only 5 %. A quantitative analysis of the efficiency of the switching modules can be found in [81]. After passing through the switching module, the light for detection, the $|F = 1\rangle$ and the $|F = 2\rangle$ blowaways and additional repumper light is coupled into pm fibres (see Figure 3.6). The light in the outputs MOT A and MOT B of the switching modules is sent each to a 1

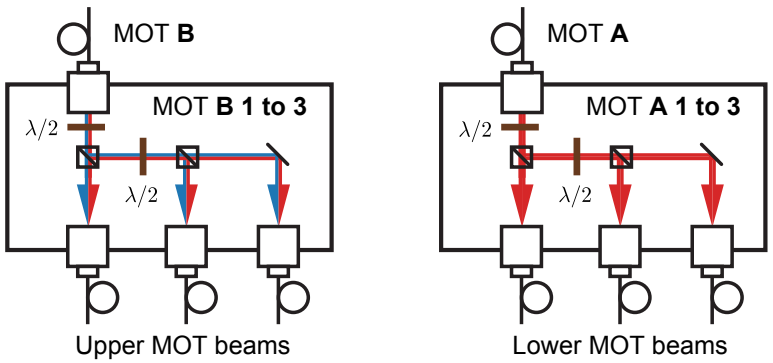

Figure 3.7: 1 to 3 distribution modules for the two MOT beam triplets. Fibre coupled light from the outputs MOT A and MOT B from each switching module is distributed into three fibre coupled outputs each. The ratio between the beams is adjusted with a combination of $\lambda/2$ wave plates and polarizing beam splitters.

to 3 distribution module containing two polarizing beam splitter and two $\lambda/2$ wave plates in fine adjustment rotation mounts [PRM05/M, Thorlabs]. The three outputs of each module are coupled into pm fibres. These distribution modules are shown in Figure 3.7.

3.2.4 Amplifier module

The output for atom cooling, trapping and launching is amplified in a dedicated module containing a tapered amplifier. The tapered amplifier (TA) is a laser diode where both, the front and rear facet are anti-reflective (AR) coated. Thus it can not operate in the lasing mode without additional feedback, but amplifies laser light that is coupled into the gain region. After a narrow ridge wave guide (RW) section the gain region is expanded into a tapered section with a larger area that allows for higher output powers and prevents the TA from destruction due to high optical intensity. The highly asymmetrical exit facet with dimensions of 3 µm in the short direction (called fast axis) and 210 µm in the long direction (called slow axis) complicates the collimation and emits a highly elliptical beam profile.

The first realisation of the GAIN cooling laser system [78] used two tapered amplifiers for cooling. One for the lower MOT triplet called TA-A and one for the upper one called TA-B. The output power of the amplifiers was 1 W each, but only 300 mW and 330 mW for TA-A respectively TA-B could be fibre coupled. The low fibre coupling efficiency results from losses due to an optical isolator of $\approx$ 18 % and a non optimal collimation of the tapered amplifier output. The collimation is a complex task for output beams with a high astigmatism, that is also depending on the operation current of the tapered amplifier. The previous approach was to collimate the fast axis with a short focal lens only and the slow axis with a combination of a short focal lens and a cylindrical lens, where the lens position was determined by focusing the beam on a distant screen. This procedure however, is not precise enough to remove the astigmatism and results in a non-optimal fibre coupling efficiency.

To increase the available power, the TAs were replaced by 2 W versions later. The output power ex-fibre increased to 580 mW for TA-A and 460 mW for TA-B. The higher total power, however, is not the only parameter of importance. The power ratio between the lower and upper MOT beam triplet, the total power in the 3 lower MOT beams divided by the total power in the 3 upper MOT beams (according to Figure 3.7) is crucial for the position and temperature of the atomic cloud in the MOT and should be as constant as possible to avoid frequent readjustments. When using two amplifiers, the drift in fibre coupling due to misalignment of the optical components or the holder for the TA chip are in general not common mode and the power ratio changes with time. In the previous set up this resulted in frequent realignments of the module on a daily basis.

During this thesis, a new amplifier module was designed, built and implemented in the GAIN laser system. This module is shown in Figure 3.8. Various mounts for the amplifier chip were designed and tested with respect to the possibility of precise alignment. The size of the mount and long term stability of the shape and position of the beam output were also evaluated for the mobile GAIN laser system. The new amplifier module contains one tapered amplifier instead of the previous two, while delivering almost the same amount of laser light via optical fibres. Additionally, the absolute power stability is superior over the original set-up due to

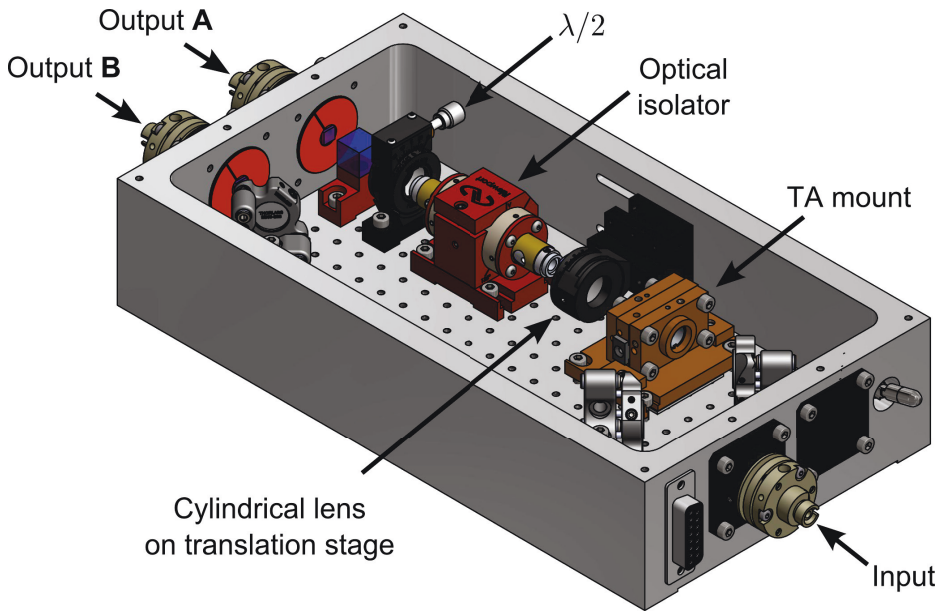

Figure 3.8: CAD drawing of the amplifier module developed and used for static and mobile gravity measurements with GAIN. It has one fibre coupled input from the light of DFB 1 in the cooling module. The light is coupled into the rear facet of the TA and collimated again. The light passes an optical isolator and is split into two paths with an adjustable power ratio. The light is coupled into the fibres of output A and B.

the new amplifier mount and minimized beam paths which are less sensitive to temperature changes and mechanical strain. In addition the relative power between the two MOT beam triplets derived from the single TA is more stable because changes in the TA's output power are common mode in both outputs. A quantitative analysis of the stability performance is given in Section 3.2.4.

Amplifier mount

First, an improved version of the mount for the tapered amplifier diode was designed together with Christian Freier. The main changes to the previous one include the removal of adhesives, that slowly coat the amplifiers facets with their outgassing products and lead to a failure in the end. The duration of this process can be as short as several months. Glued components also show a significant ageing behaviour and temperature drift that causes misalignment. The new mount for the tapered amplifier is shown in Figure 3.9. The amplifier chip is integrated on a C-mount package. A borehole in the middle is used for mounting the C-mount to the amplifier holder (as shown in Figure 3.9 (a)), while a piece of indium foil under the lower surface of the C-mount provides good thermal connection without compromising mechanical stability. The amplifier mount is made from copper due to its high thermal conductivity and the heat produced by the TA-chip is efficient removed using a Peltier element under the mount. A thin thermally conductive foil [U 90 KERATHERM, Kerafoil] on both sides of the Peltier is used

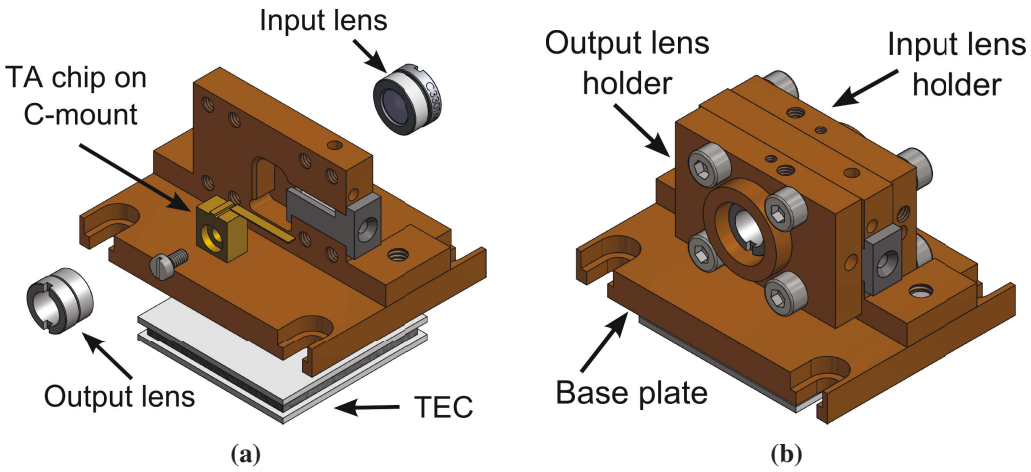

Figure 3.9: (a) Explosion view of the tapered amplifier mount. The tapered amplifier chip on the C-mount is screwed to the amplifier mount made from copper for sufficient heat transfer using a Peltier element (TEC). (b) Two lenses for collimation of the TA's input and output are placed in a thread of the lens holder. After the final adjustment of the lens's position the holder is fixed with screws.

instead heat sink paste to minimize outgassing.

The lenses used to collimate the input (2.75 mm focal length [C390TME-B, Thorlabs]) and output (3.1 mm focal length [C330TMD-B, Thorlabs]) beam are each mounted into the threads of the lens holders. The threaded lenses allow to adjust the distance to the TA chip and are locked via set screws afterwards. The position plates themselves are screwed to the main holder. To collimate the input beam, which is equivalent to focus an input beam into the amplifier, the lens is positioned such that the size of a spot on a distant screen is minimized and as symmetrical as possible.

The same procedure is applied for the amplifiers output, but due to the high astigmatic beam only the fast axis can be collimated with the output lens in the mount. The resulting spot on a screen reveals a line shaped form. To decouple the amplifier from the preceding module it is seeded by light coming out of an optical fibre. The maximal overlap between the amplifiers input mode and the fibre mode is achieved by coupling the TA rear facet output back into the seed fibre. A fibre coupler using a lens with a focal length of 7.5 mm [60SMS-1-4-A7.5-03, Schäfter + Kirchhoff] was found to achieve the best coupling efficiency.

The collimation of the slow axis of the front output to obtain a symmetrical beam shape is performed with a cylindrical lens with a focal length of 25 mm. The lens is mounted on a rotation mount [RSP05/M, Thorlabs], that is installed on a small translation stage [DS25-X, Newport]. Both mounts can be fixed in their positions by set screws after the optimization of the collimation.

Figure 3.10 shows the beam profile of a 2 W tapered amplifier recorded with a CCD camera for different camera distances. For small distances the beam profile contains a superposition of higher order spatial modes due to the highly asymmetrical exit facet (3 µm $\times$ 210 µm).

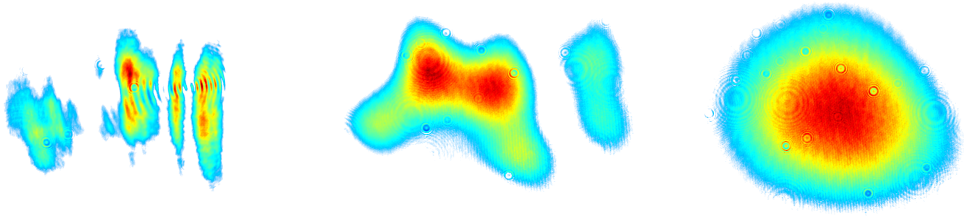

(a) **(b)** **(c)**

Figure 3.10: The evolution of the collimated beam profile originating from a tapered amplifier for different distances from the beam origin. **(a)** The beam profile in 26 cm distance. Due to interference of multiple modes the beam profile has no similarity with a Gaussian at all. **(b)** In 175 cm distance, the beam profile looks cleaner and a continuous intensity distribution contains most of the power in the beam. **(c)** At 340 cm almost all higher modes diverged away and an almost pure Gaussian mode remains.

However, 59 % of the power in this beam can be coupled into a single mode fibre. This can be explained by analyzing the spatial beam profile at distances where the higher order modes disappear due to their higher divergence compared to the Gaussian mode and almost a pure Gaussian mode is present. This demonstrates that by looking at the intensity distribution of the TA output at short distances like the distance in Figure 3.10 (a), an optimal beam collimation is very hard to recognize. An accurate position of the cylindrical collimation lens optimizes the beam collimation.

First the TA beam is coupled into a fibre at the output B (shown in Figure 3.8) by means of the adjustable mirror mount in front of the fibre coupler. The coupling is optimized by successively changing the distance of the cylindrical lens from the output facet and optimizing the coupling with the fibre coupler and a mirror after each change. The output A is directly coupled into a coupler without an additional mirror. After this procedure a coupling efficiency of 59 % is achieved.

Amplifier module performance

Considering a loss of 17 % due to the optical isolator [ISO-04-780-MP, ISOWAVE], a total power of 975 mW ex-fibre was achieved. This power from a single amplifier is only 7 % lower than in the previous setup using two 2 W amplifiers and reduces its complexity. In addition, the stability of the absolute power and more importantly, the stability of the power ratio ($\approx$ 0.85) between the two outputs A and B was improved. A measurement of the power ratio fluctuations between output A and output B for a period of 7 days is shown in Figure 3.11.

The fluctuations of the power ratio are 0.44 % during the 7 day period. This is almost a factor of 5 better then the 2.0 % fluctuations over the period of one day in a setup using two separate amplifiers [107]. The setup in [107] is very similar to the previous GAIN cooling module and we assume comparable fluctuations. During the measurement period the total output power showed fluctuations below 3 %.

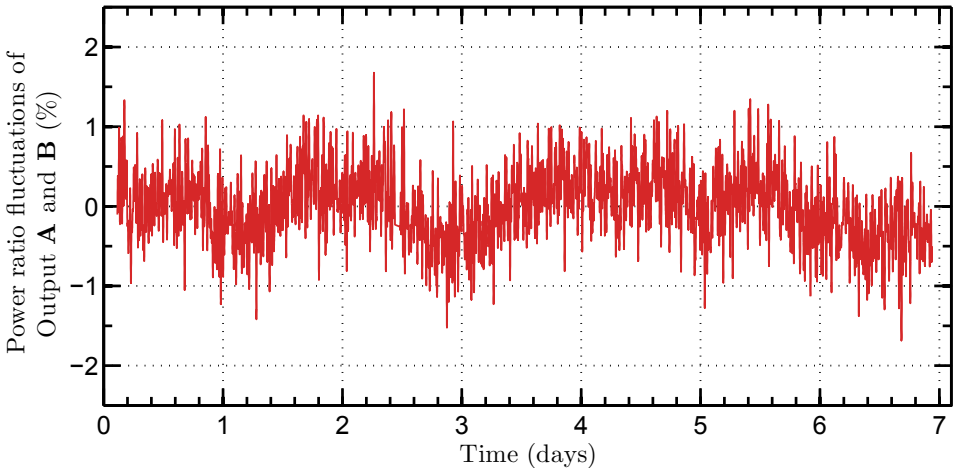

Figure 3.11: A measurement of the fluctuations of the power ratio (output A)/(output B) of the amplifier module for a period of 7 days. This power ratio is crucial to the position and temperature of the atomic cloud in the MOT. The rms fluctuations are 0.44 % during the whole time of the measurement. The total power showed fluctuations below 3 % level during this time.

The amplifier module simplifies the GAIN laser system and minimizes its maintenance time. After a transport of the whole apparatus to the Geodetic Observatory Wettzell (see Section 4.1.3), the total power in the module dropped by only 2 % which allowed for an immediate operation. And the module operates now for almost two years without noticeable change in power and without any need for readjustments.

3.2.5 Raman module

The laser light needed to perform the Raman transitions for velocity selection and interferometer pulses is generated in the Raman module. To induce Raman transitions between the two hyperfine ground states of ^{87}Rb, a fixed phase relation of the two laser fields separated by the hyperfine splitting of ≈ 6.835 GHz is required. Residual phase noise will be imprinted on the interferometer phase (see Section 2.4.2) and has to be minimized. In contrast to the cooling module, the Raman module is based on two ECDLs which have a smaller line width and thus lower free running phase noise than DFB diode lasers. A layout of the Raman module is shown in Figure 3.12.

Light from two ECDLs is amplified by two separate 1 W tapered amplifiers, overlapped and fibre coupled both to a polarization maintaining fibre because both Raman frequencies in our setup are launched from one collimator on top of the vacuum chamber (see Figure 3.2). Before overlapping the beams, light from each TA passes a rubidium vapour cell to absorb the spontaneous emission from the amplifier. The high intensity stimulated emission saturates the rubidium vapour and is almost unaffected while spontaneous emission (amplified or not) is absorbed. Both laser fields are then overlapped on a polarizing beam splitter resulting in an orthogonal polarization of the fields. A second polarizing beam splitter projects both beams

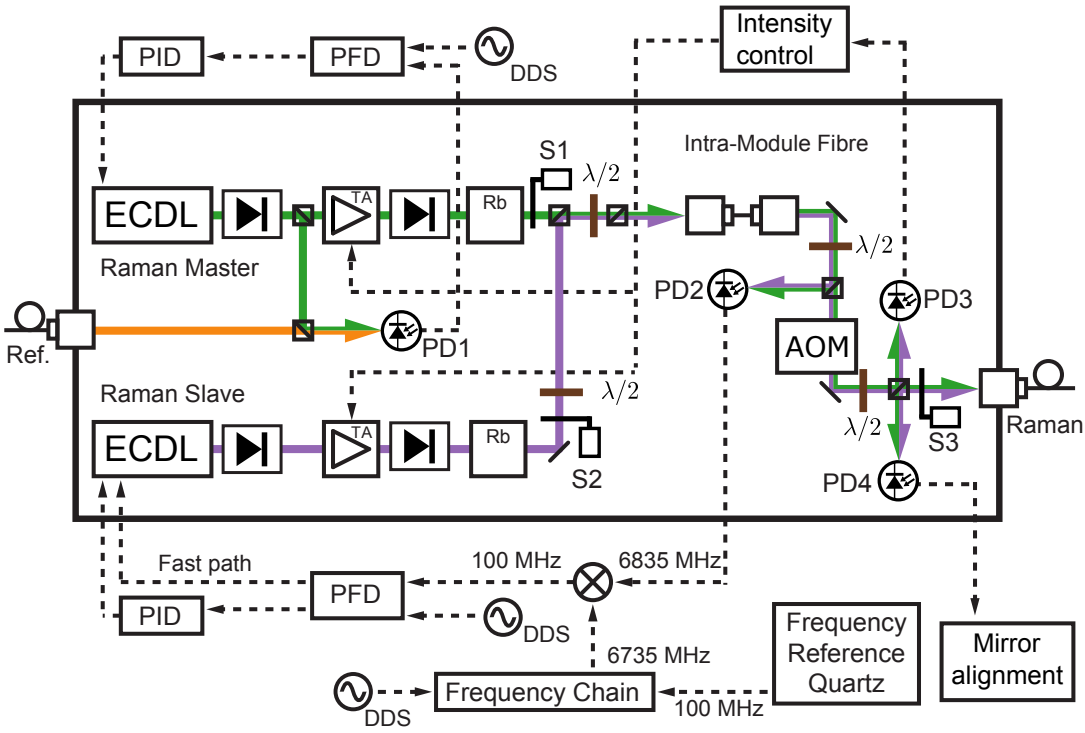

Figure 3.12: Schematic of the GAIN Raman laser module. Light from two ECDLs Raman Master and Raman Slave is separate amplified and overlapped afterwards in an optical intra module fibre. Raman Master is stabilized to the reference laser with PD1. After the intra module fibre a fraction of the light is used to generate the beat signal for the Raman phase lock (PD2). The shaping of the Raman pulses is performed with the AOM. PD3 is used for stabilization of the ex-fibre output power of each TA and PD4 is used for alignment of the retro-reflecting mirror. Some mirrors are not shown for clarity.

onto the same polarization axis while a wave plate adjusts the power ratio between them. Using the same polarization for the two Raman beams reduces the available laser power by a factor of ≈ 2, but reduces at the same time the phase noise caused by the small difference in the optical path for the two orthogonal polarizations in an optical fibre [91]. Every noise caused after this element is common to both frequencies and does not affect their phase relation. Additionally the intra-module fibre assures a constant spatial wavefront on the photo diode independent of the wavefront fluctuations of the individual amplifiers.

After the fibre the guided light is collimated and passes an AOM [3080-125, Crystal Technology, Inc] for fast switching and pulse intensity shaping of the Raman pulses. A shutter in front of the Raman fibre (S3 in Figure 3.12) prevents spurious light from entering except during the Raman pulses. The Raman Master ECDL is offset stabilized to the reference laser light coming from a separate optical fibre (PD1 in Figure 3.12) by overlapping it with a fraction of the Raman Master prior to amplification. The stabilization scheme is similar to one used for the cooling and repumping lasers. But due to the phase stability required for the Raman Slave

laser, a more sophisticated phase locking scheme is used. To stabilize the Raman Slave in phase and frequency with respect to the Raman Master laser, a low noise phase reference and larger locking bandwidth is needed. The ultra low noise 6800 MHz reference is generated by a frequency chain developed at SYRTE [91] that uses a dielectric ring oscillator (DRO) that is phased locked to a harmonic of a commercial ultra low phase noise quartz oscillator [DLR 100, Spectra Dynamics]. After the intra-module optical fibre a small fraction of the overlapped light is focused on a fast photo diode (PD2 in Figure 3.12).

The phase locked loop is based on a low noise digital PFD [MC100EP140, On Semiconductors]. The error signal is split into a low and a high frequency part which is directly connected to a printed circuit board (PCB) for fast modulation of the laser diode current. On this board, a N-channel FET acts as a voltage to current converter for the laser diode. The cable length in this feedback path is less than 1 m in total. This minimizes phase shifts in the cables as well RF pick up. To improve the bandwidth of the feedback circuit even further for high frequencies, a lag-lead compensation is included in the circuit. The achieved bandwidth for this phase lock reaches 4 MHz [108].

To stabilize the relative power of the two Raman frequencies, the power from each tapered amplifier is measured on a photo diode placed after the intra-module fibre (PD3 in Figure 3.12). Two shutters (S1 and S2 in Figure 3.12) are used to independently block the beam of the tapered amplifiers. Thus the fibre coupled power of only one of the amplifiers is measured by the photo diode. A digital feed back loop adjusts the output power of each amplifier to a reference value using the injection current of the amplifiers. During this process the phase locked loop is interjected using a sample and hold circuit (see [81] for more details).

3.3 Control of experimental parameters

To perform the experimental sequence, precisely timed outputs and inputs with a per shot jitter less than 3 ns and an accuracy of $\approx$ 50 ps are required [93]. In GAIN, a commercial computer system [PXI-8196, National Instruments] is used to generate analogue and digital channels with the required timing. The included field programmable array (FPGA) can be addressed using the Labview [National Instruments] development environment. I/O-boards [DAQ 6259 and DAQ M 6229, National Instruments] provide 32 16-bit analogue and 64 digital [93] channels. They control the whole experiment except the vibration isolation platform, which has an independent control system. An in-depth analysis of the control system and its performance can be found in [93].

A graphical interface allows the definition of values and timing of the I/O channels by the user in a list, which is transferred to the FPGA. This list can be changed manually or from one experiment cycle to the next using an arbitrary numerical equation. This allows for parameter scans or more complex measurement sequences. The experimental sequences can be stored, loaded again and modified. All data taken during a sequence is stored in a *MySQL* database on a server for data analysis. For a more complete description of the database structure see [81].

3.4 Experiment sequence

This section presents the steps of the experimental sequence. Starting with the preparation of the atomic sample, the state and velocity selection of the sample, the interferometry pulses and the state selective detection are presented.

3.4.1 Preparation of the atomic sample

The sequence starts with loading atoms from the thermal background gas into the magneto-optical trap. After typical times of 595 ms, approximately 5×10^8 atoms are loaded into the MOT. To launch the atoms upwards and to cool them down we use the moving molasses technique [109]. After switching off the MOT coils and waiting for 5 ms for eddy currents to decay, we detune the three upper MOT-beams to the red and the lower one to the blue by the same amount. We realize this by changing the frequency of the AOMs for the upper and lower beam triple individually. The MOT beams are arranged in the 1-1-1 configuration, where the beam axes are inclined by $\cos(\alpha) = 1/\sqrt{3}$ in respect to the vertical axis. In our setup the AOM detuning Δ_{AOM} is 3 MHz and the atoms are launched with a velocity

$$v = \lambda \cdot \frac{\Delta_{AOM}}{\cos(\alpha)} \approx 4.05\,\mathrm{m/s}. \tag{3.1}$$

The detuning results in a moving frame of the MOT beams and the atoms are accelerated until they are in rest in the moving frame of the MOT beams. After launch we adiabatically ramp down the RF power of the AOM amplifier used for the cooling beams in each switching module. To ensure that the cloud contains only atoms in the F=2 state we switch off the repump light a few ms later. The temperature, as well as the form and position of the atomic cloud in the MOT is strongly dependent on the MOT beam balance and the residual magnetic field in the MOT region [110], that is compensated with three pairs of coils. The exact current values of the compensation coils and the beam balance is optimized for the coldest temperature. With this molasses cooling technique we achieve a cloud temperature of $\approx 3\,\mu\mathrm{K}$.

Assuming a Gaussian velocity distribution of the clouds temperature T, the velocity distribution has a width σ_v ($1/\sqrt{e}$) of [111]

$$\sigma_v = \sqrt{\frac{T \cdot k_B}{m}} \tag{3.2}$$

with the ^{87}Rb atomic mass m and the Boltzmann constant k_B. With the temperature of our cloud after launch of 3 µK the width of the velocity distribution σ_v is 1.7 cm/s.

The velocity distribution results in a width of the Doppler shift σ_f of the Raman resonance frequency $\sigma_f = \sigma_{\mathbf{v}} \cdot \mathbf{k}_{\mathrm{eff}}/(2\pi)$. This width in the frequency domain corresponds to a width $\sigma_t = 1/(2\pi\sigma_f)$ in the time domain. For our temperature of 3 µK the width $\sigma_f =$ is 43.4 kHz and $\sigma_t =$ is 3.7 µs. The relatively low power for our Raman pulses corresponds to a low Rabi frequency (see Equation 2.27) and such $\pi/2$- or π-pulses would address only a narrow frequency and thus velocity distribution. This fact would limit the contrast of the interferometer

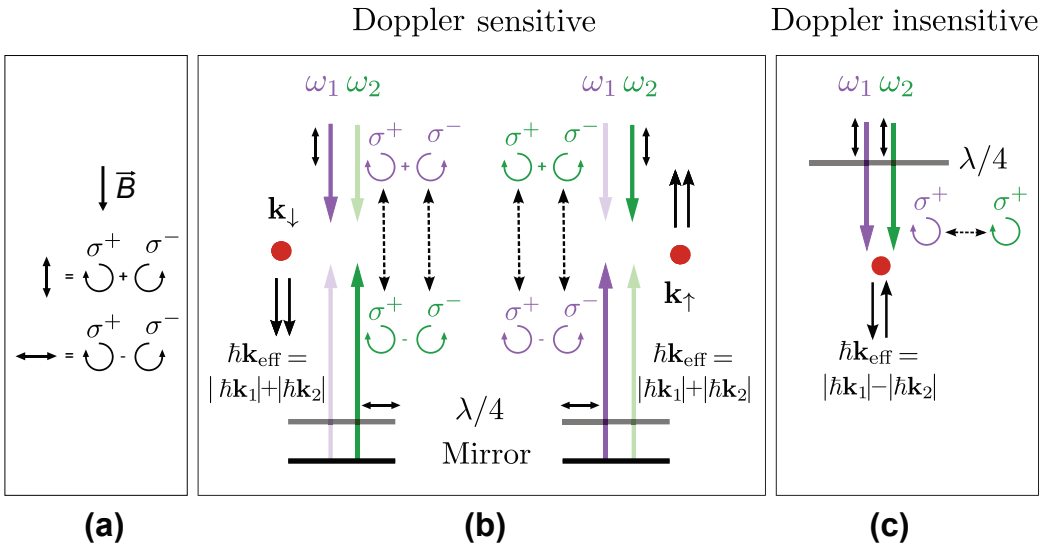

Figure 3.13: Possible Raman transitions in the GAIN setup. (a) The two orthogonal linear polarizations decomposed into circular ones in the presence of the applied magnetic field $\vec{B}$. (b) Only $\sigma^+\sigma^+$ and $\sigma^-\sigma^-$ light can drive the desired Raman transitions in our setup. In the Doppler sensitive case, the Doppler shift allows only one beam combination depending on the detuning called $\mathbf{k}_\downarrow$ or $\mathbf{k}_\uparrow$. (c) The Doppler insensitive case can be realized with an inserted $\lambda/4$ and no retro reflection. See text for more details.

and makes a careful analysis of the systematics effects much harder, because one has to average over the whole vertical momentum distribution [87]. Additionally, we want to have all atoms in the m_F=0 magnetic sub-state to suppress the first order Zeeman shift. Both tasks can be accomplished at the cost of atom number by a low intensity and thus long duration Doppler sensitive Raman π-pulse (see Figure 2.3).

Due to the selection rules and the corresponding Clebsch–Gordan coefficients, only Raman beams with the same helicity, i.e., $\sigma^+\sigma^+$ or $\sigma^-\sigma^-$ can drive two photon Raman transitions between the same magnetic sub states ($\Delta m_F = 0$), like the magnetically insensitive and desired F=1, m_F=0 to the F=2, m_F=0 transition. Here σ^+ light is defined as light that drives a single photon $\Delta m_F = +1$ transitions when being absorbed and σ^- drives $\Delta m_F = -1$. With a constant direction of the vertical magnetic field that is applied inside the interferometer zone. Raman light with the same circular polarisation from the point of view of the Raman beam direction changes from σ^+ to σ^- when being retro reflected and double passes the $\lambda/4$ wave plate.

In GAIN, both Raman beam frequencies propagate through the interferometer zone in the same linear polarization and are retroreflected on a mirror. A $\lambda/4$ plate in front of the mirror rotates the linear polarization of the reflected beams by 90° relative to the incoming beams. A decomposition of the linear polarizations into circular ones is shown in Figure 3.13 (a).

Doppler sensitive Raman transitions where an atom absorbs a photon from a beam with one frequency and emits a photon into the counter propagating beam with another frequency are driven by $\sigma^+\sigma^+$ and $\sigma^-\sigma^-$ light. This is indicated in Figure 3.13 (b) where the dashed

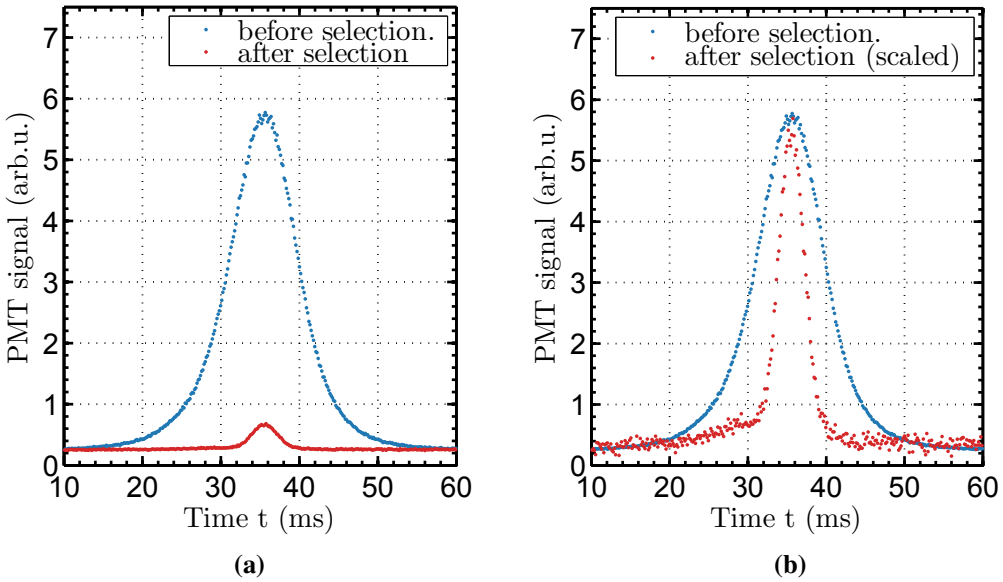

Figure 3.14: Fluorescence signal from the launched atoms detected by the PMT before (blue dots) and after (red dots) the velocity selection pulse. (a) After the velocity selection the the atom number is reduced by about a factor of 50. (b) The signal of the atoms after the selection is scaled to the original signal. A narrower distribution (along the launch axis) after the selection is visible.

arrows indicate the transitions involved in the Raman transitions. With the detuning caused by the Doppler shift only one beam pair is resonant and called $\mathbf{k}_{\downarrow}$ or $\mathbf{k}_{\uparrow}$. The other beam pair is not resonant and is show half transparent.

Without the retro reflecting mirror and the $\lambda/4$ wave plate Doppler insensitive transitions can be realized on our setup when a $\lambda/4$ wave plate is placed direct after the collimator as shown in Figure 3.13 (c). A detailed calculation of the allowed transitions and their probabilities can be found in [94].

The velocity selection pulse with a width of 12 µs transforms a velocity distribution with a width of 5.2 mm/s corresponding to a temperature of 280 nK in the vertical direction (z-axis) of the Raman beams to the F=1, m_F=0 state [81]. A strong magnetic field during this pulse ensures that only atoms in the m_F=0 state are resonant to the applied light pulse and perform the transition. The remaining atoms in the F=2 state are removed by a blow away pulse resonant to the closed cooling transition.

The temperature of the atomic cloud in the x and y axis remains unchanged and leads to an increase of the cloud diameter by 2.6 cm/s. When the atoms reach the detection area $\approx$ 778 ms at the way down of their parabolic flight the cloud is larger than the area of our detection and results in reduced signal and thus higher detection noise. Reducing the velocity distribution of the cloud using techniques like Raman sideband cooling [112] or evaporation increases the total atom number due to lower expansion and the reduced loss during velocity selection.

Figure 3.14 (a) shows a time of flight (TOF) signal of the atomic cloud before and after the velocity selection process detected by the photo multiplier tube (PMT). In Figure 3.14 (b)

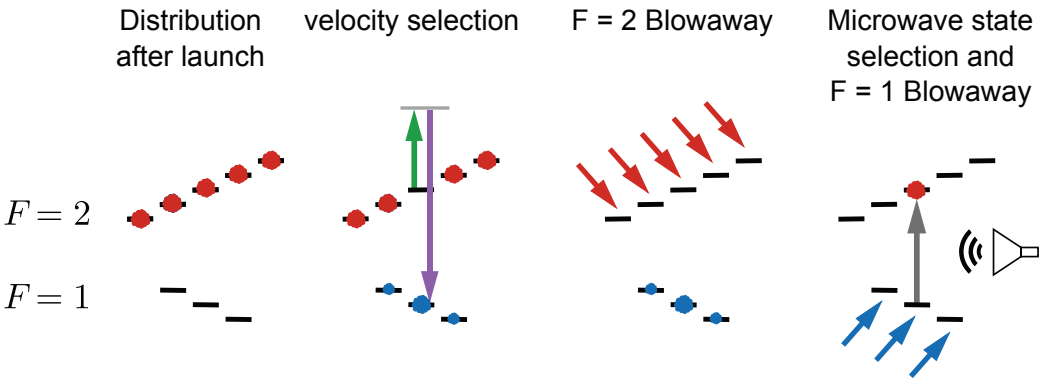

Figure 3.15: State selection of the atomic sample after launch. A long velocity selective Raman pulse, transfers a narrow transversal velocity distribution from the $|F = 2, m_F = 0\rangle$ to the $|F = 1, m_F = 0\rangle$ state. The remaining atoms are removed by a blow away pulse. A combination of a microwave and a second blow away pulse remains residual atoms in the $|F = 1\rangle$ state and completes the selection process.

both signals are scaled to the same amplitude. A reduced TOF signal width of the cloud shows a reduction in width of the velocity distribution. After the velocity selection, a microwave π-pulse is applied to the atoms and transfers atoms from the F=1, m_F=0 state to the F=2, m_F=0 state. A second blow away pulse resonant to the F=1 transition removes atoms in this state. This selection procedure step is necessary to remove atoms that have been pumped to the m_F=1 or m_F=-1 magnetic sub-states during the velocity selection pulse. Now the cloud is in a magnetic insensitive sub-state and enters the magnetically shielded interferometry zone with a narrow velocity distribution. The state selection process is visualized in Figure 3.15. The preparation procedure takes about 62 ms from launch to final blowaway after the microwave state selection.

3.4.2 Detection

The detection of the atomic population in their respective internal states has to be performed by a state selective method where the detection resolves the different internal states of the atoms or their different external states that are coupled through the Raman interferometry pulses. The external state detection method uses the spatial separation of the clouds in the detection zone due to their different momenta 128 ms after the last Raman pulse. The velocities of the two states differ by the two-photon recoil velocity $v_r = \hbar k_{\text{eff}}/m \approx 11.8\,\text{mm/s}$ separating them by 1.5 mm in the detection zone of the GAIN setup and the two states still overlap and is not used in GAIN. However, this method can be used in atom interferometers with ultra cold sources like in MAIUS (see Chapter 5) or large-momentum transfer. The internal state labelling in GAIN is used for separate detection of each state independent of the overlap of the cloud.

During their parabolic flight against gravity the atoms pass the detection zone (shown in Figure 3.2) twice. Falling down after the interferometer sequence the atoms pass the detection zone and are illuminated by three short detection pulses detuned close to the $|F = 2\rangle \rightarrow$

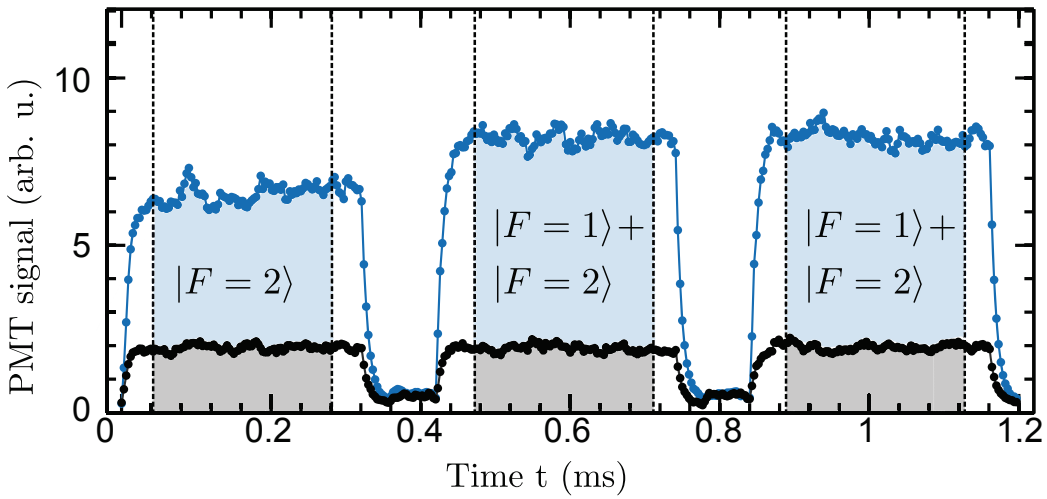

Figure 3.16: The GAIN state selective detection scheme. The fluorescence signal emitted by atoms during the first pulse close detuned to the $|F=2\rangle \rightarrow |F'=3\rangle$ resonance is detected. After a $|F=1\rangle \rightarrow |F'=2\rangle$ pulse all atoms are in the $|F=2\rangle$ state and this signal of the total atom number is detected just as in the first pulse to normalize the atomic population. The rising and falling edges of the signals (dotted lines) are excluded from the analysis.

$|F'=3\rangle$ transition. Atoms pumped in the excited state by the pulse fall in the ground state emitting a photon and repeat this cycle for the pulse duration. The emitted photons are collected by an achromatic lens pair on a photomultiplier tube [PMT R10699, Hamamatsu] and the emitting electrons are amplified with an adjustable factor up to 10^7.

The PMT signal of the first detection pulse is proportional to the number of atoms in the $|F=2\rangle$ state. The detection beam is retroreflected to create a standing wave for atoms to reduce the total transversal momentum gained by the detection photons (Figure 4.16 in Chapter 4 shows the layout of our detection area). This ensures that the atoms are not blown away in the detection process. Between the pulses, light resonant to the $|F=1\rangle \rightarrow |F'=2\rangle$ transition is used to repump all atoms to the $|F=2\rangle$ state. The number of photons collected during the second and third detection pulse are therefore proportional to the total number of atoms in both states $|F=2\rangle$ and $|F=1\rangle$.

After the atoms left the detection region, another set of three pulses with the same timing is applied. The collected photons from stray light and florescence from atoms in the background gas (black dots in Figure 3.16) are used as a reference signal and are subtracted from the first set of pulses (blue dots in Figure 3.16). A typical detection signal is shown in Figure 3.16. The normalized population in the exited state $P_{|F=2\rangle}$ is calculated by numerical integration of the individual detection signals without the rising and falling edges first, and by subtracting the background signal from the total PMT signal that is proportional to the atom numbers $N_{|F=1\rangle}$ and $N_{|F=2\rangle}$ in each of the two states. The normalized population is calculated then by

$$P_{|F=2\rangle} = \frac{N_{|F=2\rangle}}{N_{|F=1\rangle} + N_{|F=2\rangle}}. \tag{3.3}$$

The third pulse in every detection set can be used in the future for diagnosis of the detection timing [81]. Without this normalization scheme a pulse containing light with both frequencies ($|F=2\rangle \rightarrow |F'=3\rangle$ and $|F=1\rangle \rightarrow |F'=2\rangle$) detects the total atom number in the detection area. Such time of flight measurements are shown in Figure 3.14.

3.4.3 Interferometry

During the interferometer sequence, composed of multiple Raman pulses, the Raman frequency $\omega_{\text{eff}} = \omega_1 - \omega_2$ is chirped with $\omega_R(t) = \omega_{R_2} + \alpha_\omega t$ to compensate for the Doppler shift induced by gravity (see Section 3.4.4). To find the right frequency ω_{R_1} only one Raman pulse with a length shorter than a π-pulse is applied at the position and time of the last $\pi/2$-pulse in the complete interferometer. Its frequency is scanned and the normalized population of the transferred atoms is detected. The frequency of the maximum transition probability at the time of the pulse is used for the interferometer. Figure 3.17 shows a frequency scan of the last Raman pulse with the obtained transition probability.

After the transition frequency is determined, the right pulse length for the Raman pulses needs to be adjusted. A scan over the Raman pulse length is shown in Figure 3.18. From this scan the length of a π-pulse is calculated to be 27 µs and the length of a $\pi/2$-pulse is 13.5 µs.

The pulse length $\tau_\pi = \pi/\Omega_R$ is a function of the Raman beam intensity and the detuning Δ with $\Omega_R \propto 1/\Delta$ and the pulse length addresses velocity distribution width $\sigma_v \propto 1/\tau$ (see Section 3.4.1). From this fact a very short high intensity pulse is desired to address all atoms after the velocity selection. This would suggest to minimize the detuning Δ but this however increases the fraction of atoms lost due to spontaneous emission [82], limiting the interferometer contrast

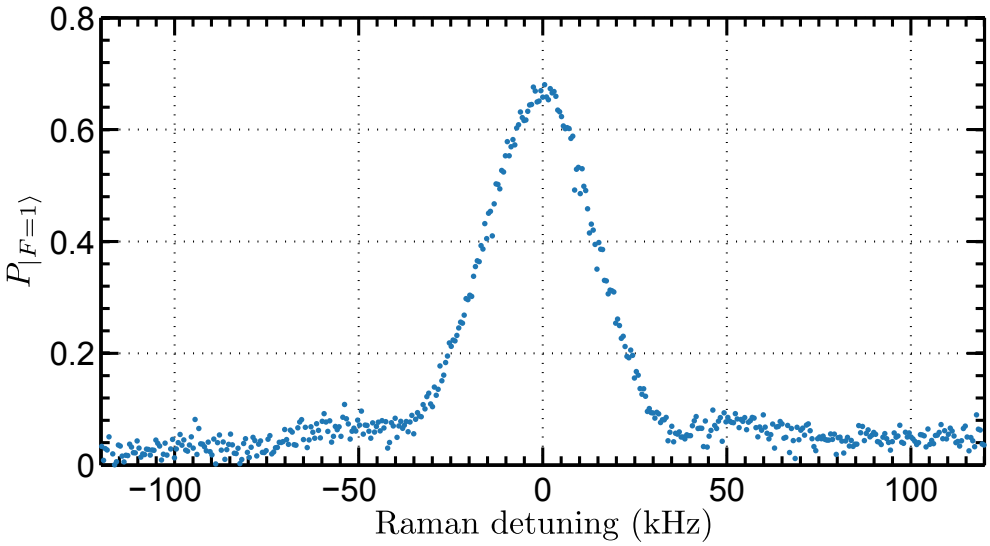

Figure 3.17: A scan of the effective Raman frequency $\omega_{\text{eff}} = \omega_1 - \omega_2$ (shifted by the resonance frequency) while applying a Raman π-pulse. The maximum population transfer from the F=1 to the F=2 state occurs when the frequency is tuned to the resonance.

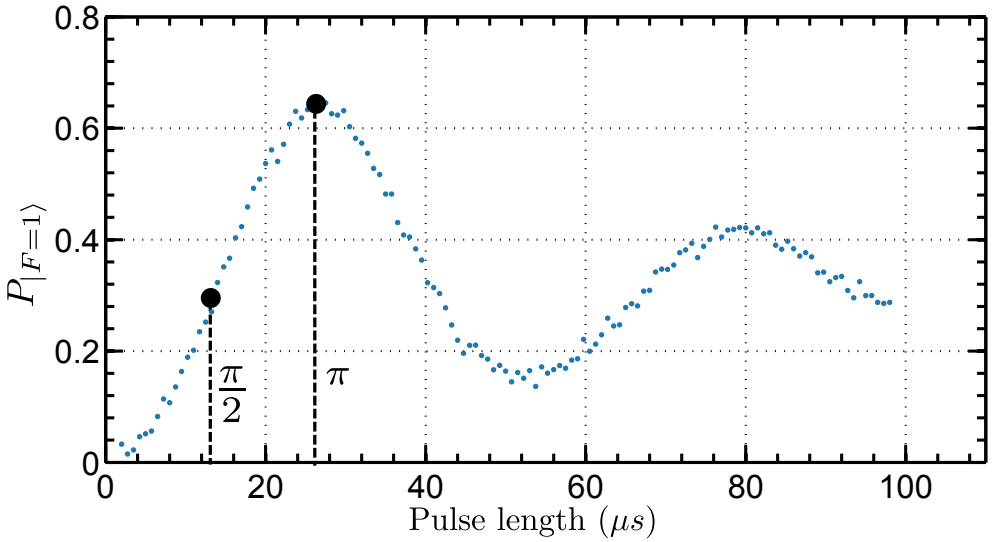

Figure 3.18: A scan of the Raman pulse length. The pulse length resulting in the maximum transition probability (π-pulse) and the $\pi/2$-pulse are indicated.

[113]:

$$\frac{-\delta N}{N} \approx 2\pi\frac{\Gamma}{\Delta}. \tag{3.4}$$

The loss due to the spontaneous emission decreases also with the detuning, so a trade-off between atom loss and high Rabi frequency, i.e. short pulse length leads to a detuning of $\Delta \approx 700\,\mathrm{MHz}$ for the optical power available in GAIN.

This detuning is not large enough when using large momentum beam splitters with multiple Raman pulses to increase the interferometers sensitivity. High power laser sources are then needed allowing for large detunings to achieve high contrast [114].

A $\pi/2 - \pi - \pi/2$ or Mach-Zehnder interferometer can be realized by applying a pulse sequence spaced by the free evolution time T. By changing the phase of the DDS frequency used as reference to phase lock the DRO as described in Section 3.2.5, the interferometer phase can be scanned.

3.4.4 Gravity measurement procedure

After the parameters for the atom interferometry sequence are set (see the previous Section 3.4.3), the necessary steps for a gravity measurement can be performed. Before a value of the gravitational acceleration $g \propto \Delta\Phi$ can be determined, the absolute phase of the interferometer has to be known with an accuracy of 2π. Additionally, the Doppler shift experienced by the atoms during free fall will shift a fixed Raman frequency (see Figure 3.17) out of resonance in $\approx 10\,\mathrm{ms}$. Both facts can be tackled by chirping the difference frequency of the two Raman lasers and compensating the Doppler shift.

Chirp rate determination

Chirping the frequency difference between the Raman lasers imposes an additional phase shift

$$\Delta\Phi_{\text{chirp}} = \alpha_\omega T^2 \tag{3.5}$$

in the interferometer with a sign opposite to the phase shift induced by gravity. When both phases are equal, the total interferometer phase is zero and independent of total interferometer time T

$$0 = (\mathbf{k}_{\text{eff}}\mathbf{g} - \alpha_\omega)T^2 \Leftrightarrow \alpha_\omega = \mathbf{k}_{\text{eff}}\mathbf{g}. \tag{3.6}$$

This fact can easily be understood in the falling frame of the cold atoms. The wavefront seen by the atoms remains constant due to the chirping that cancels the acceleration and no phase is accumulated at all. The gravity measurement is thus reduced to a determination of the exact chirp rate which is generated in the DDS. This DDS itself is referenced ultimately to a GPS signal that is several orders of magnitude more accurate than needed in GAIN.

This is similar to a method used for velocity measurements, where the velocity of a test car is measured by matching its velocity to the velocity of a probe car. A scan of the chirp rate α_ω for different interferometer times T is shown in Figure 3.19. The obtained interferometer fringe gives information about the interferometer contrast and noise. In our interferometer scheme two Raman beams enter the interferometer tube from the top and are reflected from

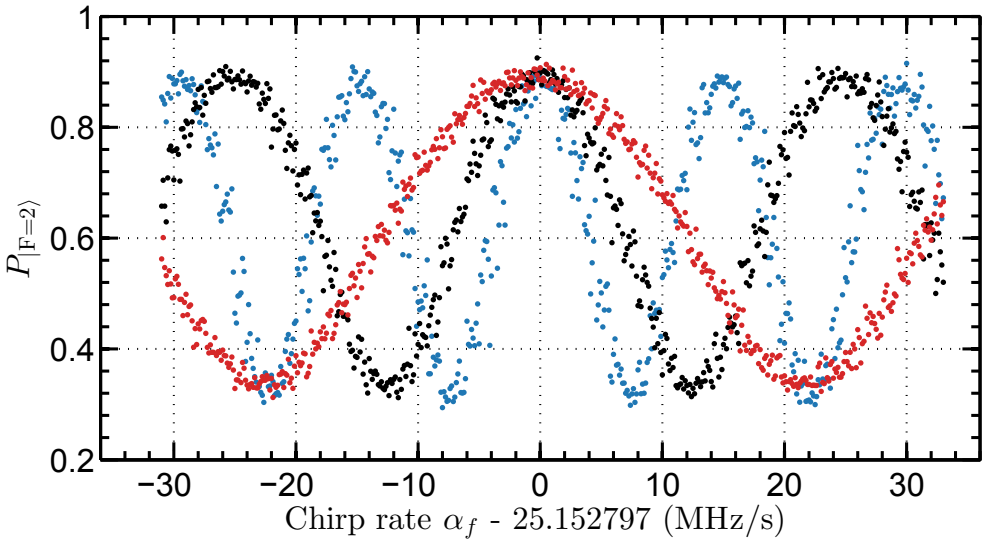

Figure 3.19: The normalized population in the F = 2 state as a function of the frequency chirp α_f for different interferometer times T = 150 ms (red), T = 200 ms (black) and T = 250 ms (blue). For the chirp rate corresponding to the Doppler shift during the free fall the normalized population has a maximum independent of the interferometer time T. The corresponding interferometer fringe is called central fringe.

below the bottom window. Thus two possible effective wave vectors are possible (see Figure 3.13 (b)). One pointing upwards, the so called $\mathbf{k}_\uparrow$ configuration and the downward pointing $\mathbf{k}_\downarrow$ configuration. By changing the sign of the chirp rate α_ω we can switch between both configurations.

Although a gravity value can be obtained by the chirp rate alone, provided its deviation doesn't reach a phase difference larger than $\pm\pi$, we use a more suitable scheme described in detail in the next section.

Gravity value evaluation

Gain operates in a continuous mode launching atoms every 1.5 s. Every 20 min an interferometer fringe is scanned with a resolution of 32 points equally spaced over 2π for both, the $\mathbf{k}_\uparrow$ and the $\mathbf{k}_\downarrow$ configuration. A sinusoidal fit determines the fringe contrast and amplitude that are used to calculate the position of the slopes. Successive measurements jumping between both fringe slopes and both wave vector configurations are performed for the rest of the cycle. A slow software feedback loop adjusts the chirp rate to ensure that the measurement is performed on the slopes only. This scheme was adopted from atomic fountain clocks, where the local oscillator is locked to the central fringe formed by an Ramsey interferometer [26]. The phase offset ϕ_{center} from the exact central fringe is then fitted to the interferometer points. The gravitational acceleration g is then calculated from the chirp rate α_ω, the additional phase offset ϕ_{off} of the last Raman pulse and ϕ_{center} using the Equation

$$0 = (\mathbf{k_{eff}} \cdot \mathbf{g} - \alpha_\omega)\, T(T + 2\tau) + \phi_{\text{off}} + \phi_{\text{center}}. \tag{3.7}$$

The obtained gravity data is corrected by the effect of the atmospheric pressure

$$\Delta g_{\text{atm}} \approx 0.3\,\mu\text{Gal} \cdot (p - p_0), \tag{3.8}$$

where p is the air pressure at the measurement site and p_0 the normal atmospheric pressure [115]. The effect of the Earth's tides (together with the ocean loading effect) on the local gravity value is calculated with the free software package Tsoft [116]. This software uses a set of predetermined tidal parameters and a theoretical model to predict the local tides. Tsoft can also be used to analyse and compare gravity data. The tidal parameters for the measurements sites described in the next chapter can be found in [81].

Raman orientation and intensity control

In addition to the previous steps, the orientation of the Raman beams in respect to the gravity vector has to be adjusted. The gravimeter phase Φ is proportional to the projection of the two vectors $\mathbf{g} \cdot \mathbf{k_{eff}}$ ($\Phi = \mathbf{g} \cdot \mathbf{k_{eff}} T^2$) so for a small deviation θ of the direction of the Raman beams from the direction of the gravitational field the measured value is $g_m = g \cdot \cos\theta = g(1 - \theta^2)$. For a relative accuracy $\Delta g/g$ of 1×10^{-10}, this angle has to be known better than 1×10^{-5} rad.

Fluctuations of the Raman beams orientation also decreases the sensitivity of the gravimeter. The collinearity is ensured by a two step process. As a first step, the piezo driven mirror

sitting on top of the vibration isolation stage (see Section 3.1.3) is used for coupling the reflected Raman beams back into the Raman fibre by monitoring the back coupling on PD4 in Figure 3.12. Short light Raman pulses during the MOT phase are used for active back coupling during the whole sequence. This autocollimator technique guarantees that both, the incoming and the retroreflected, beams are collinear all the time. As a second step, the angle θ of the Raman beams in respect to gravity has to be determined. This is done by a controlled displacement of the Raman telescope during the first hour of a gravity measurement and fitting the corresponding change in gravity. The origin of the parabola corresponds to a vanishing angle θ. The orientation of the telescope is then adjusted to the calculated value and two tilt meters measure its residual displacements for post correction [81]. A more detailed description can be found in the thesis of Christian Freier [117] who essentially contributed to this method.

Fluctuations in the absolute power in each Raman beam change the effective Rabi frequency and changes in the power ratio induce phase shifts due to the AC Stark shift (see Chapter 2). Therefore, the individual powers of the Raman beams and thereby their ratio are stabilized using a monitor photo diode (see Section 3.2.5). The stabilized powers are 54.2 mW for the Raman Master and 31.6 mW for the Raman Slave (cf. Figure 3.4). The ratio of 1.72 to 1 was chosen to just cancel the AC Stark shift (see [81] for more details and a quantitative analysis).

Coriolis effect compensation

The atom interferometer is further sensitive to rotations if they act perpendicular to the area spanned by the interferometer [118]. This Coriolis effect caused by the rotation of the Earth around its axis and a perpendicular velocity component of the atoms calculates to

$$\Delta g = 2\frac{\mathbf{k_{eff}}}{|\mathbf{k_{eff}}|} \cdot (\mathbf{v} \times \mathbf{\Omega}), \tag{3.9}$$

where $\mathbf{\Omega}$ is the rotation vector of the Earth with the magnitude of $73\,\mu\mathrm{rad/s}$ and $\mathbf{v}$ the mean velocity of the atomic cloud. To compensate for this additional phase shift we counter rotate the effective wave vector $\mathbf{k_{eff}}$ against the Earth's rotations during the interferometer sequence, thus cancelling the Earth's rotation in the inertial frame of the atoms moving transversally to the Raman wave front as demonstrated by [80, 118]. The compensation of the Coriolis effect in our setup using the piezo driven retro reflecting mirror has been implemented by Christian Freier [117].

This section presented the major steps needed to measure gravitational acceleration with the mobile atom interferometer GAIN. The results of such long term gravity comparisons with the three most used types of gravimeters on three different measurement sides are presented in the next chapter.

4 Measuring gravity on Earth's surface with GAIN

The previous chapter presented the setup of the Gravimetric Atom INterferometer GAIN and the experimental sequence for an atom interferometry based gravity measurement. Three long term gravity comparison measurement campaigns were conducted during this thesis. This chapter presents the results of these gravity measurements, followed by an analysis of the gravimeter's noise sources and systematic effects. A detailed analysis of the major systematic effect, the impact of wavefront aberrations in our atom interferometer is performed.

4.1 Gravity measurements and comparisons with classical gravimeters

The performance of GAIN has been evaluated in three long term gravity measurement campaigns. Using a theoretical model, the biggest temporal change in gravity caused by tides (see Section 3.4.4) can be subtracted from the measurement to give access to residual gravity signals in the order of some µGal. The µGal is a unit widely used in geodesy and corresponds to $10^{-8}\,\mathrm{m/s^2}$ or $\approx 10^{-9}\,\mathrm{g}$. This allows to analyse the long term stability of GAIN. Simultaneous gravity measurements with other gravimeters can be used for a direct evaluation of GAIN's performance. Small gravitational signals can only be revealed in a direct comparison. These signals caused by changes in the mass distribution of the surrounding area (underground water storage and men made constructions f.e.) or a non-suitable tidal parameters can thereby be distinguished from an experimental drift present in one of the gravimeters. Three state-of-the-art and widespread gravimeter types today were compared against GAIN. Each of these comparisons was performed on a different measurement site which is only possible due to GAIN's mobility.

The first campaign included a comparison with a spring type relative gravimeter, namely the gPhone-98 [119]. Followed by a comparison with the workhorse in absolute gravity measurements, the falling corner cube gravimeter FG5X-220 [120]. Each on a different site in our physics building in Berlin, Adlershof. The third measurement campaign included a gravity comparison with the superconducting gravimeter SG-30 [121]. This campaign was carried out in the Geodetic Observatory Wettzell, in the Bavarian Forest. Each gravity comparison and the operation principle of the corresponding gravimeter is presented below. An extensive presentation of state-of-the-art gravimeters can be found in various textbooks written for the geodetic community [115, 122]. The presented gravity comparisons were accomplished together with Matthias Hauth and Christian Freier.

4.1.1 Berlin campaign I: GAIN vs. mechanical spring gravimeter

Gravimeters based on a mechanical spring most often made of a metal-alloy are widely used in relative gravimetry due to their compactness and low maintenance operation. Because of their intrinsic drift (see below), they are mostly utilized for connection of different measurement locations to a nearby gravity reference point. Their low mass makes this gravimeter type predestined for measurements of gravity gradients by a fast relocation of the device. A picture of a spring gravimeter developed by Micro-g LaCoste is shown in Figure 4.1.

Long term gravity recordings are also often performed with spring type gravimeters since their mainly linear drift can be subtracted from the measurement. The spring gravimeter [gPhone-98, Micro-g LaCoste] from the Institut für Erdmessung (IfE) in Hannover was used for the first gravity compassion with GAIN. This gravimeter type was specifically built for such long time gravity recordings [123] and is shown in Figure 4.1.

The underlying principle of this gravimeter is shown in Figure 4.2 (a). A system consisting of a mass m and a spring placed in a gravitational field will form a steady state that fulfills Hooke's law

$$mg = k\Delta l. \tag{4.1}$$

Here $\Delta l = l - l_0$ is the elongation of the spring from the position without a load and k the spring constant. Measuring the difference in length Δl gives direct access to the gravity. While being very simple, this method is not able to accurately measure changes in gravity. A change of the gravitational field in the order of 10 µGal corresponds to a displacement of only 1 nm [115] for typical values of k and m. This small displacement can only be measured with sophisticated and complex measurement assemblies (optical interferometers f.e.) and is very sensitive to changes in environmental temperature and pressure.

An increase of the sensitivity by more than 3 orders of magnitude can be achieved by using

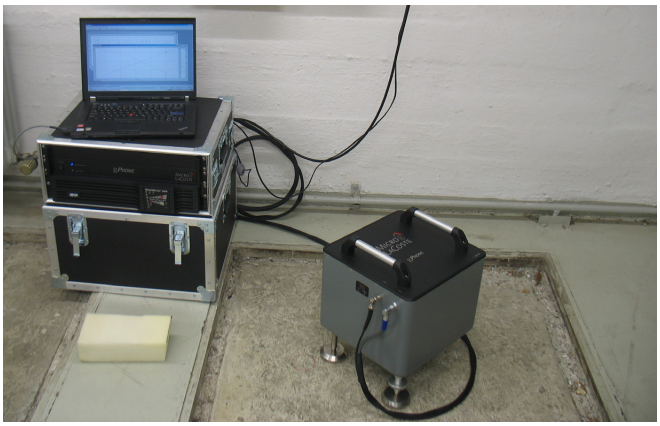

Figure 4.1: The gPhone-98 from the Institut für Erdmessung (IfE), Hannover during a gravity measurement campaign (on the right side). The electronics for control and data evaluation are on the left. Figure courtesy of Manuel Schilling.

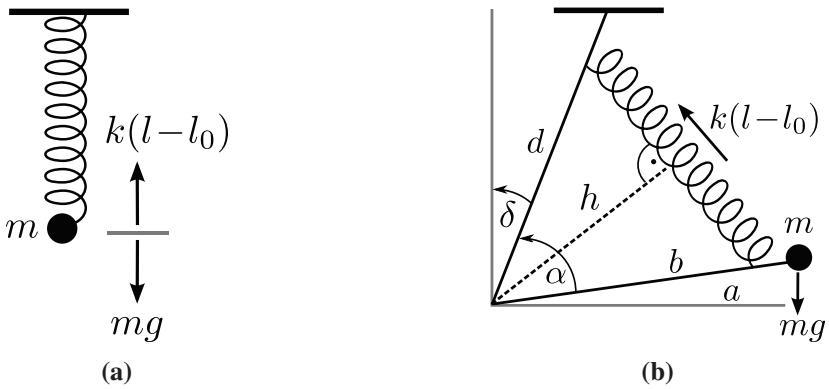

Figure 4.2: (a) A system with a mass m and a spring constant k under influence of gravity g. (b) A general lever spring system (Figure adapted from [115]). See the text below for more details.

the so called general lever spring balance. Here the spring is elongated under an adjustable angle by an additional lever like shown in Figure 4.2 (b). The steady state of the system can be now written as

$$mga\sin(\alpha+\delta) = k\Delta l b\frac{d}{l}\sin\alpha. \tag{4.2}$$

To maximize sensitivity, the device is operated with $\alpha+\delta = 90^\circ$ and $\alpha \approx 90^\circ$ where a change of the gravitational field in the order of 10 µGal now corresponds to a displacement of 2 µm. This is an improvement in sensitivity by a factor of 2000 [115].

As can be seen from Equations 4.1 and 4.2, a change of the spring constant or the length of the spring itself will lead to a change in the measured gravitational value. This changes occur due to ageing of the device. Although spring gravimeters are internally temperature and pressure stabilized, environmental changes still affect them to a certain degree. Spring lever gravimeters from the type gPhone show typically mostly a linear drift in the order of 10 µGal per day after a settlement period of some weeks. Higher order drifts are also present and can not be discerned from small gravitational signals that are therefore undetectable and exclude spring gravimeters from the application in fields where small signals of the order of some µGal or less have to be detected like hydrology, volcanology and others [115].

The comparison between the gPhone-98 gravimeter and GAIN was carried out in December 2012 in Berlin, Adlershof. The position of GAIN was unchanged and situated in a laboratory on the second floor of the physics institute's building. The gPhone-98 gravimeter was operated by the Institut für Erdmessung (IfE) and was placed under an optical table roughly 2 m away from GAIN. To reduce the characteristic drift of spring gravimeters quoted above, the gPhone-98 was operated for several weeks before the actual comparison started. The joint gravity measurement was performed over 4 days during which the gPhone-98 operated continuously and GAIN had only few data gaps due to readjustments. To the time of this comparison neither the power stabilization for both Raman beams nor the amplifier module were implemented in the setup.

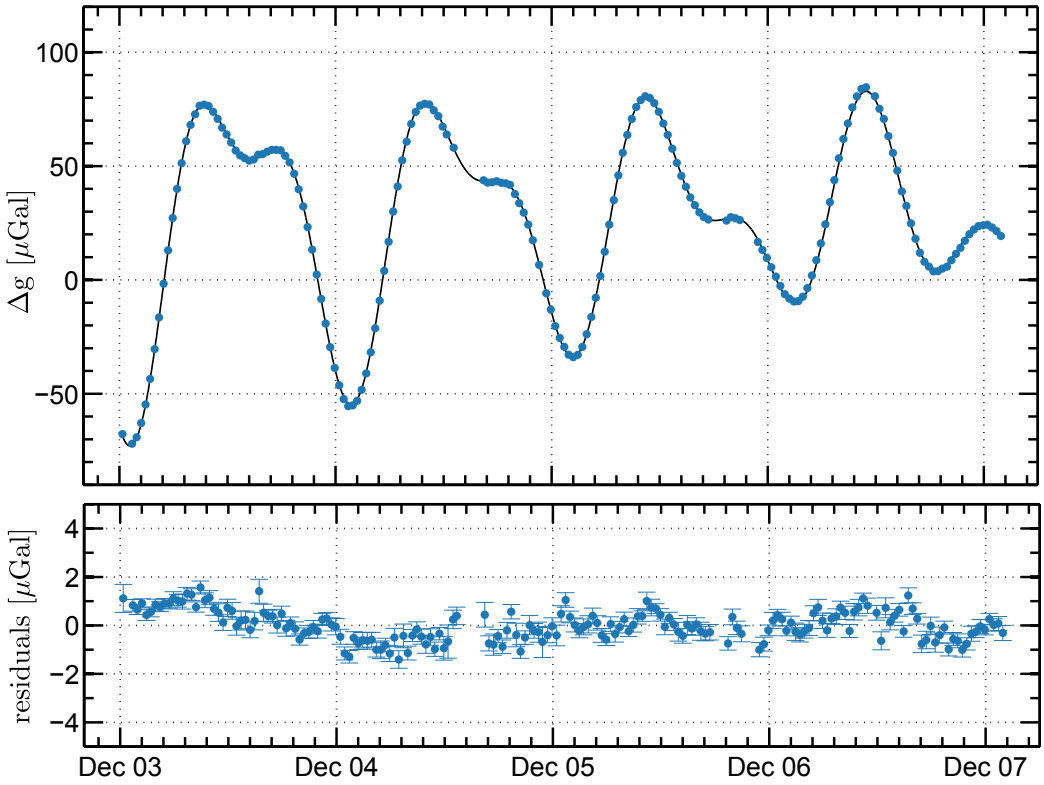

Figure 4.3: Gravity measurements performed with GAIN during the gravity comparison with the gPhone-98 in December 2012 (top) and the predicted local tides (black line). The gravity data are corrected for the atmospheric mass variations. The residuals after correcting the top data for the tidal effect (bottom). Each data point is averaged for 30 min. 1 µGal = 10^{-8} m/s^2.

The results of the gravity recordings are shown in Figure 4.3. Each data point is averaged for 30 min. Almost continuous gravity data was recorded. After correcting for tidal effects and atmospheric mass variations, the remaining signal shows gravity variations smaller than 2 µGal. No drift at the 1 µGal level is visible in the data.

The comparison with the gPhone data is shown in Figure 4.4. A linear drift of 10.2 µGal per day was determined for the gPhone by the operators. This was done by a linear fit of the gravity data corrected by tides and air pressure after several weeks of operation. One can see an increased variation in the order of 4 µGal for the gPhone during day time and a smaller variation (in the order of 1 µGal) during the night hours. This is most likely due to the increased vibration level caused by people in the university building and vehicles passing by. Such a dependence is not visible for the GAIN data, which show no increase of gravity value scatter during day time. To summarize, gravity data recorded by GAIN shows similar gravity variations as the gPhone during night hours and lower variations during day time for an averaging time of 30 min with the advantage of a drift free operation.

The stability of gravimeters can be expressed in terms of the Allan deviation (ADEV) $\sigma_y(\tau)$.

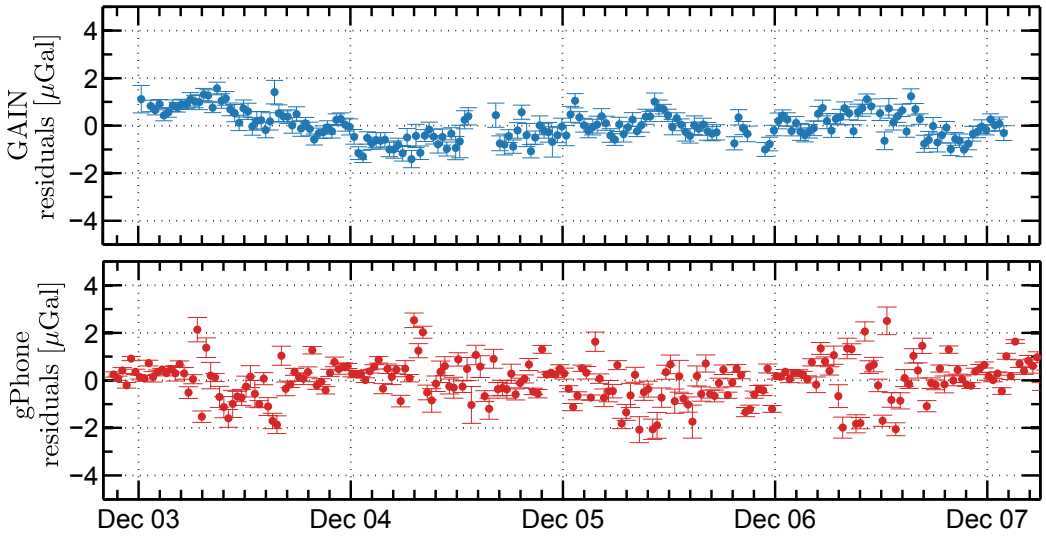

Figure 4.4: The gravity residuals during the comparison with the gPhone. GAIN residuals (blue) and gPhone residuals (red) after correcting for tidal, atmospheric effects and a linear drift of 10.2 µGal per day for the gPhone. Each data point is averaged for 30 min. 1 µGal = 10^{-8} m/s^2.

The two-sample Allan variance

$$\sigma_y(\tau)^2 = \frac{1}{2}\left\langle (y_{i+1} - y_i)^2 \right\rangle = \frac{1}{2(\mathrm{M}-1)} \sum_{i=0}^{\mathrm{M}-2} (y_{i+1} - y_i)^2 \tag{4.3}$$

represents the variance of a gravity measurement averaged for an observation time τ, where y_i is the relative gravity value obtained for this averaging time [124]. M is the number of the data points available after averaging. Figure 4.11 shows the modified Allan deviation (MDEV) [125] for GAIN gravity data taken during the gPhone comparison. The Allan deviation reveals white noise on the order of $1.5 \cdot 10^{-8}\,(\Delta g/g) \cdot 1/\sqrt{\tau}$ between 5 s and 5×10^3 s averaging time.

After 10^4 s the instability reaches a noise floor around $\approx 5 \times 10^{-10}$ g. This behaviour is most likely caused by power ratio drifts of the MOT and Raman beams and was improved after implementing the new amplifier module and Raman power stabilization (see the results of the gravity campaigns presented next).

4.1.2 Berlin campaign II: GAIN vs. falling corner cube gravimeter

After the comparison with the gPhone-98 spring gravimeter in December 2012, a comparison with an absolute gravimeter 6 month later was performed. Modern absolute gravimeters use a free falling test body to determine the gravity value acting upon it, by measuring its position as a function of time [120]. A trihedral prism, often called corner cube, is used as a retro-reflector in one arm of a Michelson type laser interferometer. The free falling corner cube induces a path length change in the interferometer arm. The phase change produces interference fringes after both arms are overlapped on a photo detector. The retro reflector of the second arm is mounted

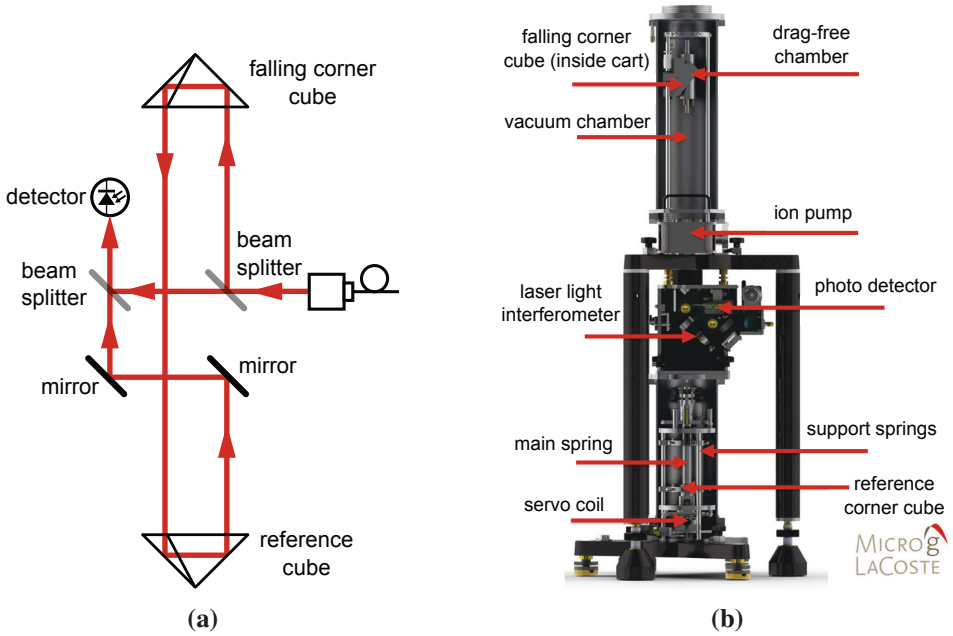

Figure 4.5: (a) The optical beam path in a falling corner gravimeter. A Michelson type interferometer with the falling corner cube in one arm is used to measure the cube's trajectory. (b) An assembled FG5 (modified, originally from Micro-g LaCoste).

on a vibration isolation called "super spring"[126] and serves as the inertial reference, similar to the one used in GAIN.

Figure 4.5 (a) shows a scheme of the optical beam path forming the falling corner cube interferometer. The interferometer fringes manifest in an intensity change on the photo detector and are digitized for post processing. The falling corner cube is located in a vacuum chamber to reduce air drag and can be elevated after the impact by a motorized lift. A commercial iodine stabilized He-Ne laser and a GPS referenced atomic clock provide accurate time and length references. From these references an accurate gravity value can be calculated by fitting the time dependent distance of the corner cube to the one predicted by theory including the gravity gradient [115]. Due to the mechanical recoil of the corner cube during the impact and the corresponding residual vibrations, typically one drop is performed every 10 s .

To reduce the mechanical wear and tear in the gravimeter a measurement is usually composed of 50 drops in the beginning of every hour, like typical used in other campaigns. Although continuous drop rates as high as 3 s were reported for an operation time of several days [127]. The dropping chamber, super spring, laser and electronics can be transported in individual cases allowing for measurements even on sites not accessible by car. However, optimal performance of the falling corner cube relies on low vibration environments. Remote locations and thick concrete pillars are recommended by the manufacturer [128] and most measurements are performed in dedicated buildings. Figure 4.5 (b) shows an assembled FG5.

The comparison with the falling corner cube gravimeter FG5X-220 took place in June

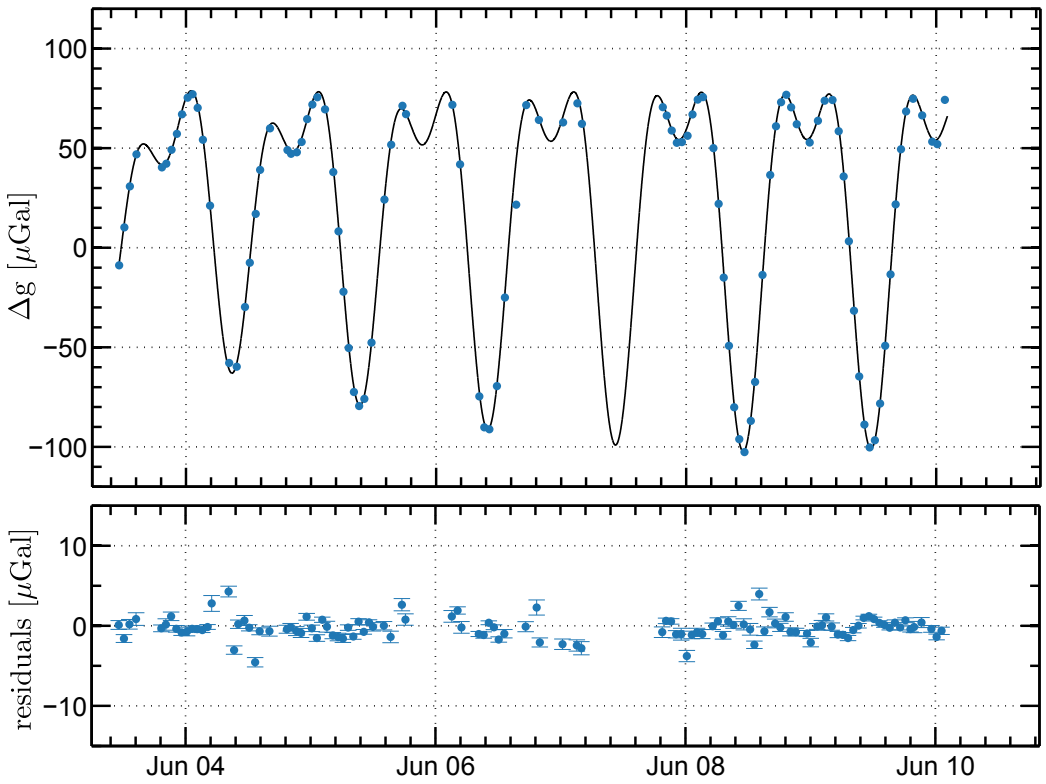

Figure 4.6: Gravity measurements performed with GAIN during the gravity comparison with the FG5X-220 in June 2013 (top) and the theoretical tide prediction (black). The gravity data are corrected for the atmospheric mass variations. The residuals after correcting the top data for the tidal effect (bottom). Each data point is averaged for 60 min. 1 µGal = 10^{-8} m/s^2.

2013. The FG5X-220 was again operated by the Institut für Erdmessung (IfE). The FG5X-220 [Micro-g LaCoste] is an improved version of the FG5 with an extended free-fall length up to 35 cm. The elevator system was redesigned to reduce the recoil during the impact of the corner cube [129]. The FG5X-220 was positioned over a gravity reference point at the ground floor of the mechanical workshop in the physics institute's building (Berlin Adlershof). That reference point was surveyed by the Bundesamt für Kartographie und Geodäsie (BKG) in 2010 [130].

The mechanical workshop has only an elementary air conditioning system. Temperature changes as high as 1 K occur on a time-scale of one hour. GAIN was positioned $\approx$ 2 m away from the FG5X-220. Joint gravity measurements for a period of more than 6 days were recorded. The FG5X-220 operated with its standard measurement procedure of 50 drops spaced by 10 s in the beginning of every hour. Those were combined to a measurement set, while GAIN performed a drop every 1.48 s. For this measurement, the GAIN apparatus was separated into its three main parts, the physics package including the vibration isolation, the laser system and the electronic rack. They were transported to the mechanical workshop and set up to full operation. During this phase a sudden malfunction in one of the tapered amplifiers in the original cooling module occurred. Therefore, the newly developed amplifier

module (see Section 3.2.4) was integrated in the setup, replacing the previous one.

The results of the gravity recording are shown in Figure 4.6. Each data point is averaged for 60 min to match the length of one measurement set for the FG5X-220. For a period of seven days an almost continuous gravity recording with several gaps was achieved. A similar performance, in terms of gravity data scatter, as in the gravity measurement in December 2012 was achieved. No increase in the standard deviation during the day time is present.

The residuals of the FG5X-220 together with GAIN's residuals are shown in Figure 4.7. They are both corrected by the tidal model and the effect of atmospheric pressure. Data taken by GAIN show no drift during the time of the comparison. The averaged gravity value recorded by the FG5 however shows a decrease of almost 5 µGal during the first 4 days and an increase of the same size during the last two days. Such a gravity signal is not visible in the GAIN residuals. This signal is most likely caused by the high temperature changes that cause mechanical strain in the FG5X-220 assembly or by small tilts of the floor of the workshop. The FG5X-220 usually operates on measurement pillars, positioned in a much more temperature stable environment. This also means that gravity signals smaller than 1 µGal present in GAIN can not be clearly distinct from a experimental drift in the order of 1 µGal in a comparison with a falling corner cube gravimeter.

The standard deviation of the gravity value obtained in an one hour measurement during the week days (from the 4th to the 6th of June) by the FG5X-220 is ≈ 4 µGal. During the weekend (the 7th and the 8th of June) the standard deviation of the FG5X-220 is reduced by a factor of two to ≈ 2 µGal. However, the standard deviation for GAIN shows an almost constant standard deviation of ≈ 1 µGal except for some outliers.

The stability expressed in terms of the modified Allan deviation is shown in Figure 4.11. No white noise ($1/\sqrt{\tau}$ scaling) is clearly present. Starting with an instability of 17.3×10^{-9} g after 3 s corresponding to $29.8 \times 10^{-9}\,\mathrm{g}/\sqrt{\mathrm{Hz}}$, the instability reaches a level of 5.8×10^{-10} g after 10^4 s and 1.2×10^{-10} g after 10^5 s. Compared to the instability during the gPhone comparison, the short term sensitivity is a factor of two (for time scales between 3 s and 10^2 s) and a factor of four (between 2×10^2 s and 10^4 s) higher. For longer averaging times however, the instability decreases further in contrast to the rising stability for this time scales in GAIN gravity data taken during the gPhone-98 comparison. The small increase in the short term sensitivity is most probably caused by the higher vibration noise level of the measurement site caused by a building construction site across the street and the traffic of people leaving and entering the nearby entrance. The improved performance for long averaging times is caused by the Raman intensity and direction stabilization (see Section 3.4.4) and the use of the new amplifier module (see Section 3.2.4). This two improvements were implemented before the measurement campaign with the FG5X-220.

The comparison between GAIN and the FG5X-220 falling corner cube gravimeter reveals the advantages of the active vibration isolation used in GAIN and the active control of critical experimental parameters. Even under the environmental conditions of a mechanical workshop located on the ground flour of a busy physics building GAIN shows low noise and drift free operation. The continuous high repetition rate gravity measurement of GAIN shows the advantage over a falling corner cube gravimeter, like the FG5X-220.

This section showed that to reveal GAIN's full performance a comparison with a gravimeter

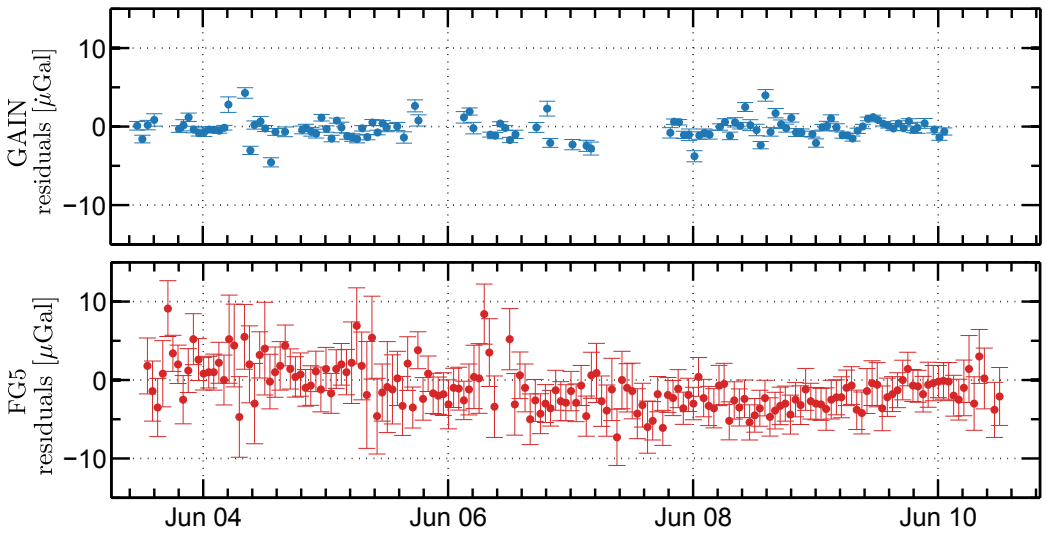

Figure 4.7: The gravity residuals during the comparison with the FG5X-220. GAIN residuals (blue) and FG5X-220 residuals (red) after correcting for the tidal and atmospheric effects. Each data point is averaged for 60 min. 1 µGal = 10^{-8} m/s^2.

with a higher precision than the FG5X-220 is needed. In addition, drift free operation or a precise knowledge of this drift is needed. A comparison with such a gravimeter, namely a superconducting gravimeter is presented in the next section.

4.1.3 Wettzell campaign: GAIN vs. superconducting gravimeter

The results of the comparison between GAIN and the FG5X in the previous section indicate that on the sensitivity level reached by GAIN, theoretical predicted gravity changes due to tidal effects are not accurate enough to distinguish small changes in gravity from instrumental drifts. In addition, the previous measurement locations are not suitable to enable the full performance of gravimeters due to their environmentally dynamical environment. To explore the full performance of cold atom gravimeters in terms of sensitivity and stability, a measurement campaign in the Geodetic Observatory Wettzell was carried out in October 2013.

Located in the Bavarian forest, the observatory records Earth's orientation in space and is used to determine positions located on the Earth. Besides, satellite laser ranging, very-long-baseline interferometry (VLBI) and a laser ring gyroscope, one superconducting gravimeter [SG-30,GWR Instruments, Inc] continuously measures the changes in the local gravity value. Completed by regular gravity measurements with absolute gravimeters and the low seismic noise environment, the observatory was the place of choice for the comparison with a superconducting gravimeter. Its measurement principle is shown in Figure 4.8 (a).

A superconducting hollow Niobium sphere is held against gravity by a magnetic field created by two superconducting coils and additional currents induced on the sphere surface. The currents in the superconducting coils and on the sphere surface are extremely stable, making drifts almost non-existent. The highly linear dependence of the sphere's displacement to grav-

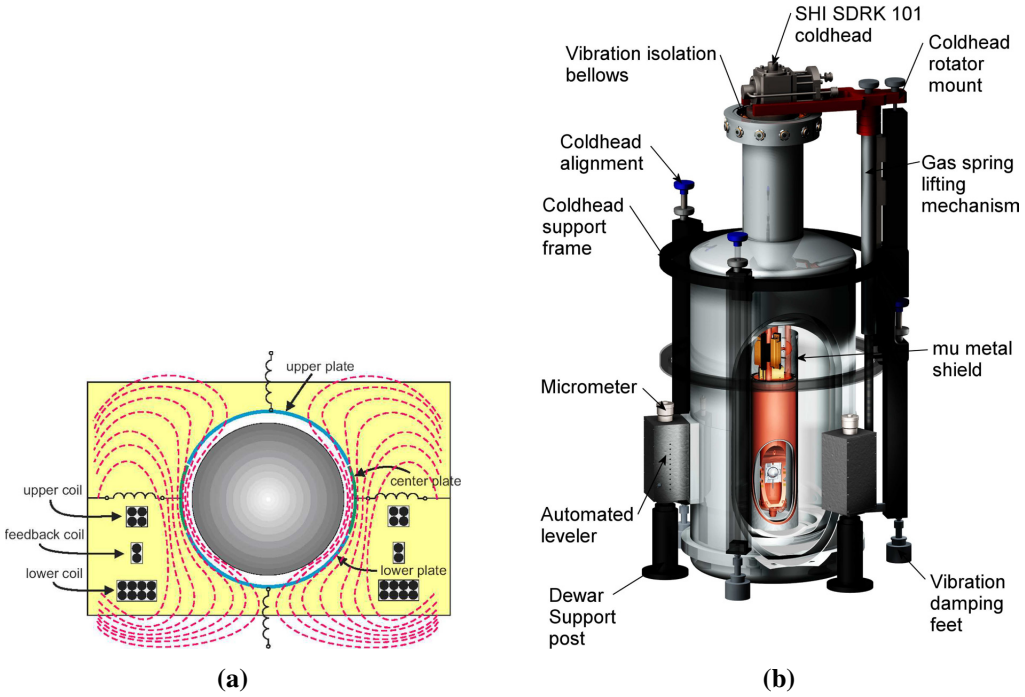

Figure 4.8: (a) The measurement principle of a superconducting gravimeter. A hollow Niobium sphere is held in a stable magnetic field. Changes in its position are read out by a capacitance sensor. (b) The assembled superconducting gravimeter [OSG,GWR Instruments, Inc]. The height of the instrument is 140 cm and the diameter is 42 cm [131]. (both Figures from the OSG Brochure [131])

ity changes is read out by a capacitive sensor. To increase the dynamic range of the SG-30 an additional superconducting coil is used as an actuator. The Niobium sphere is kept in a fixed position in a feedback loop by usage of the capacitance sensor's reading. The sensors voltage is low passed and is read out with a high precision multimeter. The conversion factor of this voltage into a change of gravity is based on absolute measurements of known gravitational signals. Earth's tides measured by the SG-30 can be compared to the theoretical models. The accuracy of this models, however, is limited. The scaling factor is therefore calibrated by a synchronous measurement with an absolute gravimeter. Such a measurement has the advantage of a simultaneous determination of the absolute gravitational value. The SG-30 in Wettzell has two sensors. One (lower) sensor is located underneath the second (upper) sensor. Their scaling factors were determined by previous measurement campaigns to $-739.0(11)\,\mathrm{nm/s^2/V}$ for the lower and $-678.4(10)\,\mathrm{nm/s^2/V}$ for the upper sensor.

The cryogenic cooled chamber of the SG-30 is pressure stabilized and can be transported if needed (see Figure 4.8 (b) for an impression of the instrument). Transporting the SG-30, however, leads to changes in the scaling factor that are not fully understood yet. Therefore the SG-30 is used for long term gravity recordings on a fixed location [115]. This allows for regular characterisation of the small but existing instrumental drift.

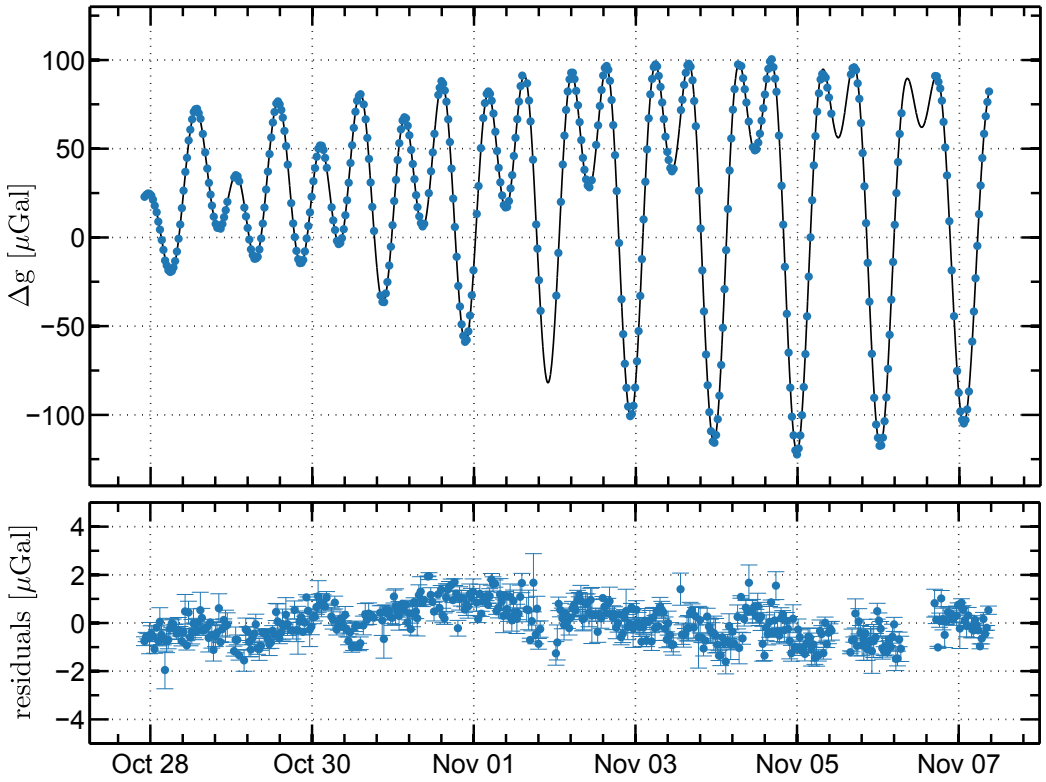

Figure 4.9: Gravity measurements performed with GAIN during the gravity comparison with the SG-30 in November 2013 at the Geodetic Observatory in Wettzell (top) and the theoretical tide prediction (black). The gravity data are corrected for the atmospheric mass variations. The residuals after correcting for the tidal effect (bottom). Each data point is averaged over 30 min. 1 µGal = 10^{-8} m/s^2

The gravity data recorded during this campaign is shown in Figure 4.9. More than 10 days of almost uninterrupted recording were obtained. After subtracting the gravity data for the tidal effects and the effect of atmospheric pressure a standard deviation of less than 2 µGal over the whole measurement period is reached. Small daily variations in the order of 1 µGal are visible. This behaviour is also reflected in the Allan deviation plot (dashed blue line in Figure 4.11). A sensitivity of $16 \times 10^{-9}\,\mathrm{g}/\sqrt{\mathrm{Hz}}$ for averaging times up to 4×10^3 s corresponding to white noise present in the gravity data. For longer averaging times the stability remains at 3×10^{-10} g.

The comparison of the data recorded by GAIN with the SG-30 data is shown in Figure 4.10 (top). The residuals of the SG-30 data corrected by tides and the effect of atmospheric pressure show oscillations at a time-scale of $\approx$ 12 h. An increase of the gravity data during the first 4 days by 2 µGal and a decrease in the following 4 days is visible in both instruments. These gravity variations present in both devices indicate that the parameters used for the calculation of the tidal effect are not ideal for the measurement site. This could also be the case for the oscillations occurring twice a day at the SG-30 data.

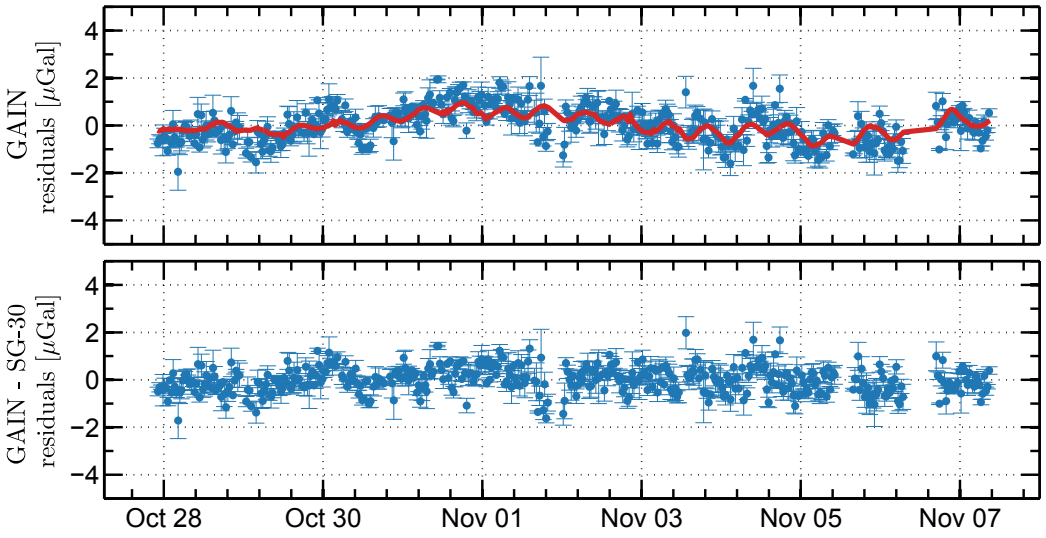

Figure 4.10: Top: GAIN's residuals (blue) and the SG-30 residuals (red) during the comparison with the SG-30 corrected for the tidal model and pressure. Bottom: GAIN's residuals after correcting by the SG-30 gravity signal. Each GAIN data point is averaged over 30 min.

To remove all common mode gravity variations and obtain the residual signal of the two instruments, the GAIN gravity data was corrected by the data from the SG-30. The remaining residuals between the two gravimeters are shown in Figure 4.10 (bottom). The previous small gravity variations are not present any more in this data and only variations less than 1 µGal are visible in the first 4 days. This is due room temperature changes with a period of 24 h that were suppressed during the period of the remaining data set [132]. The modified Allan deviation of the residuals of this data set is shown in Figure 4.11 (solid blue line). For this data the scaling factor of the SG-30 was determined by a linear regression of the gravity data to be $-740.4(3)\,\mathrm{nm/s^2/V}$ and $-680.6(3)\,\mathrm{nm/s^2/V}$ for the lower and for the upper sensor respectively. In addition a time delay of 20 s between GAIN and SG-30 was obtained by a correlation between the gravity data taken by the two instruments [132].

For averaging times up to 4×10^3 s the Allan deviation coincidence with the one obtained without the corrections. For longer averaging times however, the MDEV maintains to decrease with an almost white noise spectrum up to 4×10^{-11} g after 10^5 s. This is the best reported stability for an atomic gravimeter and demonstrates that at this level of stability, the modelling of tidal effects and small residual gravity signals can limit the achievable performance of GAIN and gravimeters in general.

The results of the gravity measurement campaign in the Geodetic Observatory Wettzell show a long term performance for GAIN with the best reported stability for a gravimeter based on atom interferometry. The sensitivity and stability surpass the stability of a corner cube gravimeter with a comparable degree of mobility and demonstrate that cold atom gravimeters can already be a competitive alternative to existing classical gravimeters. To further improve its performance the next sections briefly recalls the noise contributions limiting the sensitivity

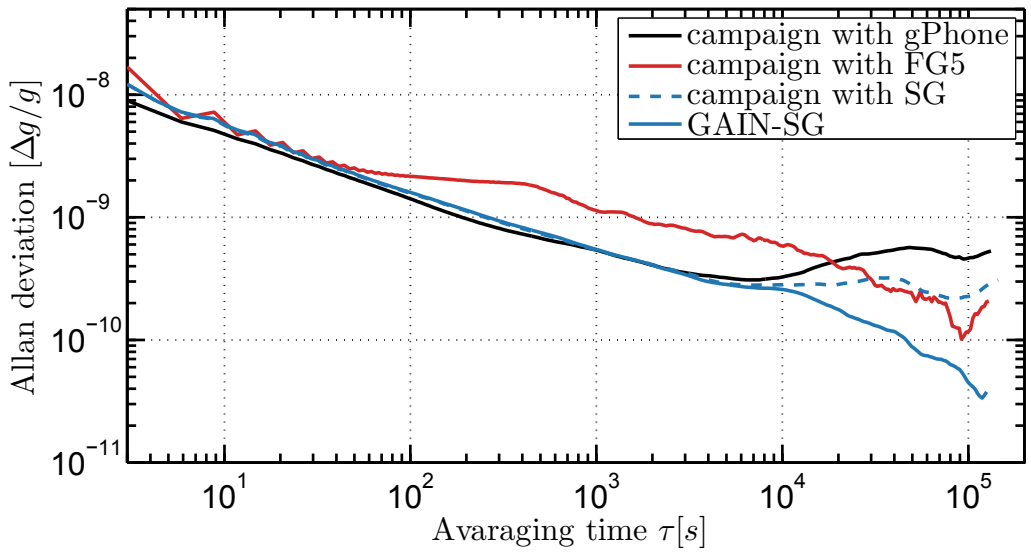

Figure 4.11: The modified Allan deviation (MDEV) of the gravity data taken during the campaigns. The Allan deviation for the gravity data taken during the gPhone comparison is shown in black. The MDEV for the FG5X-220 comparison is shown in red. For the SG-30 comparison the MDEV for the gravity data corrected by the tides and atmospheric pressure is shown in dashed blue, while the gravity data corrected by the SG-30 data (including the time delay and the improved scaling factor value) is shown in solid blue. See text for more details.

in GAIN and gives an overview over its systematic effects .

4.2 Sensitivity analysis

To understand the limiting contributions to the sensitivity of GAIN, an analysis of the present major noise sources is given in this section. The sensitivity for a measurement of local gravity is the ratio of the resolvable phase σ_Φ and the total interferometer phase $\Delta\Phi$ (see Equation 2.36).

$$\frac{\Delta g}{g} = \frac{\sigma_\Phi}{\Delta\Phi} = \frac{\sigma_\Phi}{\mathbf{k_{eff}} \cdot \mathbf{g} T^2} \tag{4.4}$$

The variance of the phase σ_Φ^2 is the sum of the individual variances of all noise sources contributing to the interferometer. With the typical noise sources present in cold atom experi-

ments, the phase variance can be written as

$$(\sigma_\Phi)^2 = \underbrace{\underbrace{\frac{1}{N_{\mathrm{at}}}}_{\text{atom shot noise}} + \underbrace{\frac{1}{N_{\mathrm{at}} n_{\mathrm{ph}}}}_{\text{photon shot noise}} + \underbrace{\sigma^2_{\mathrm{elec}}}_{\text{electronic detection noise}}}_{\text{detection noise } \sigma^2_{\mathrm{det}}} + \underbrace{\sigma^2_{\mathrm{ph}}}_{\text{Raman phase noise}} + \underbrace{\sigma^2_{\mathrm{vib}}}_{\text{vibration noise}} . \tag{4.5}$$

Here, the first term corresponds to the atomic projection noise of N_{at} atoms. The second term is the photon shot noise of n_{ph} detected photons per atom followed by the electronic noise of the detection system σ_{elec}. The two last terms are the Raman phase noise σ_{ph} and the vibration noise σ_{vib} [133]. These are the most dominant noise sources in our setup. The first three noise sources can be summarized together as detection noise σ_{det}. The first term $1/N_{\mathrm{at}}$ represents the fundamental detection noise limit for non entangled particles. A detection system with negligible photon shot noise and electronic noise has therefore a standard deviation of the detection noise $\sigma_{\mathrm{det}} = 1/\sqrt{N_{\mathrm{at}}}$ and is called atom shot noise limited and is ultimately limited by the number of atoms that contribute to the interferometer signal.

Detection noise

During the measurement campaign in Wettzell the main noise sources in GAIN were characterized. The short term detection noise can be estimated by measuring the standard deviation σ_{P} of the normalized atomic population exited in the $|\mathrm{F}=2\rangle$ state after a $\pi/2$-Raman pulse (obviously one can also use the population in the $|\mathrm{F}=1\rangle$ state) [87]. Vibration and Raman phase noise do not contribute to this single pulse. Sitting on the slope of the interferometer fringe the population noise σ_{P} translates into phase noise of the interferometer fringe σ_ϕ as shown in Figure 4.12. With a $\pi/2$-pulse only, σ_{P} is direct proportional to the detection noise σ_{det} of the interferometer via

$$\sigma_{\mathrm{det}} = \frac{2\sigma_{\mathrm{P}}}{A} \tag{4.6}$$

in *radian* or

$$\sigma_{\mathrm{det}} = \frac{2\sigma_{\mathrm{P}}}{A \cdot k_{\mathrm{eff}} \cdot T^2} \tag{4.7}$$

in m/s^2 as can be seen from Figure 4.12. Here A is the contrast of the interferometer defined as peak to peak amplitude of the fringe. The fringe contrast A during the Wettzell campaign ranged around 0.55 and this value is used for the following calculations and a time T between the pulses of 260 ms. In GAIN a standard deviation $\sigma_{\mathrm{P}} = 5.3 \times 10^{-3}$ per shot was experimen-

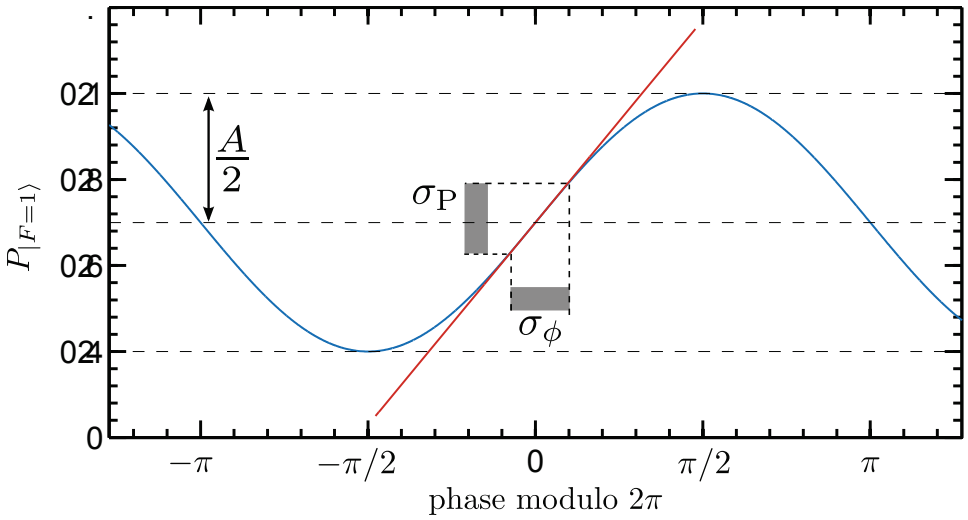

Figure 4.12: Relation between the population noise σ_P of the exited atoms and the interferometer phase noise σ_ϕ in an interferometer. By measuring on the slope of the fringe, the part of the fringe with an approximately linear relation between phase and population (where the red line and the blue fringe almost overlap), the detection phase noise scales inversely to the population noise given by the Equation 4.6.

tally determined during the campaign. This corresponds to

$$\sigma_{\text{det}} = 19.3\,\text{mrad/shot} \tag{4.8}$$

or 1.77 μGal/shot. If detection noise would be the only noise contribution in GAIN this would correspond to an Allan deviation of $2.2 \cdot 10^{-9}\,(\Delta g/g) \cdot 1/\sqrt{\tau}$. This is almost a factor of 8 lower then the Allan variance shown in Figure 4.11 and detection noise not a limiting factor in our setup. In our case about 10^5 atoms contribute to the detection signal [93]. This results in a shot noise limited probability $\sigma_{N_{\text{sn}}}$ of

$$\sigma_{N_{\text{sn}}} = \frac{1}{\sqrt{N_{\text{at}}}} = \frac{1}{\sqrt{10^5}} = 3.2 \times 10^{-3} \tag{4.9}$$

per shot. Thus, less than a factor of 2 lower then the detection noise in GAIN. Our detection scheme is almost shot noise limited and can be only improved by increasing the number of the detected atoms.

Raman phase noise

The influence of the Raman laser phase noise σ_{ph} on the interferometer phase noise is a combination of several noise sources. Phase noise from the frequency reference, phase noise of the frequency chain and noise added by the electronic feedback loop (see Section 3.2.5 and [78]). The sum of this noise sources can be calculated from the measured phase noise of the

Raman lasers scaled with the weighting function (see Section 2.4.2). An evaluation of σ_{ph} is performed by operating the interferometer in a Doppler insensitive configuration (Figure 3.13 (c)) while measuring the interferometer noise on the fringe slope. Since the momentum transfer in the Doppler insensitive configuration is 5 orders of magnitude smaller than in the Doppler sensitive case (see the end of Section 2.1). This is also the case for the vibration noise that scales with $\mathbf{k_{eff}}$ (see Section 2.4.3). A standard deviation of $\sigma_{\text{P}} = 1.1 \times 10^{-2}$ per shot with a contrast of $A = 0.55$ was measured on the slope of the interferometer fringe, corresponding to 40 mrad/shot. This noise is the sum of the Raman phase noise and the detection noise that was measured previously. The contribution of the Raman phase noise therefore is

$$\sigma_{\text{ph}} = \sqrt{\sigma_{\text{P}}^2 - \sigma_{\text{det}}^2} = 35\,\text{mrad/shot}, \tag{4.10}$$

or 3.2 μGal/shot. This is about a factor of 3 higher than the calculated results using the Raman laser phase noise and the interferometers weighting function performed in [78]. Most likely the degradation in the phase lock performance is caused by non optimized feedback parameters in the phase locking electronics. This noise dominates over the detection noise but is not limiting the gravimeter in its current state, as shown in the vibration noise analysis below.

Vibration noise

The sum of all noise sources σ_Φ in the interferometer is the slope of the fringe noise in the Doppler sensitive configuration (see Figure 3.13 (b)) and is the per/shot sensitivity in a gravity measurement. A standard deviation $\sigma_{\text{P}} = 4.0 \times 10^{-2}$ per shot with a fringe contrast $A = 0.55$ corresponds to 145 mrad/shot or 13.4 μGal/shot. Assuming that only the noise sources given in Equation 4.5 are present in the atom interferometer, the contribution of the vibration noise σ_{vib} is

$$\sigma_{\text{vib}} = \sqrt{\sigma_\Phi^2 - \sigma_{\text{det}}^2 - \sigma_{\text{ph}}^2} = 139.4\,\text{mrad/shot}, \tag{4.11}$$

or 12.9 μGal/shot. The vibration noise is clearly the most dominant noise source in GAIN and reducing its contribution will directly improve the performance of the interferometer. One approach for reducing the vibration noise is to improve the vibration isolation platform (see Section 3.1.3). This can be done either by a more sensitive seismometer, by an improved active feedback loop or by using the residual vibrations from the seismometer for post correction of the interferometer data [95]. The method of post correction was implemented in a recent measurement campaign and is presented in detail in the thesis of Christian Freier [117]. A second approach is to perform measurements in locations with lower levels of seismic noise [134]. The time resolved gravity values for these locations are however not always of interest for the geodetic community. In contrast, the vibration levels on a space station [135] or satellite [136] are extremely low, making these platforms an excellent candidate as operating environment for atom interferometry for measurements aiming at fundamental physics or space geodesy.

After the discussion of the major noise sources in GAIN, a summary of the systematic effects in the interferometer is given in the next section.

4.3 Systematic effects

The performed measurement campaigns demonstrated the high sensitivity and stability of GAIN. For subsequent measurements on the same location or for comparison of gravity values measured by other gravimeters, the absolute gravity value along with the its systematic uncertainty is needed. A summary of systematic effects that lead to a bias in the measured gravity value measured by GAIN is given in this section with focus on the effect of wavefront aberrations in the atom interferometer. A thorough discussion of the other systematic effects can be found in the thesis of Christian Freier [117].

4.3.1 Major contributions

The major systematic effects originate directly from the principle of the gravity measurement as can be seen from the equation used to determine this value:

$$\mathbf{g} \cdot \mathbf{k_{eff}} = |\mathbf{g}| \cdot |\mathbf{k_{eff}}| \cdot \cos\theta = \alpha_\omega. \tag{4.12}$$

It includes the absolute wavelength of the effective wave vector $\mathbf{k_{eff}}$, the absolute frequency of the chirp rate α_ω and the orientation of the wave vector and the orientation of gravity axis which enclose an angle θ. The following list includes an evaluation of these contributions. Additional systematic effects are summarized at the end of this section.

Orientation of the measurement axis θ

The orientation of the effective wave vector relative to the local gravity is performed in two steps. First, the two Raman beams are overlapped by coupling the reflected Raman beams back in to the fibre using the Tip/Tilt mirror as shown in Section 3.4.4. This methods allows for a relative alignment of the incident and reflected Raman beams in mutual orientation with an accuracy of some μrad. Second, the orientation of the effective wave vector with respect to gravity is performed by the method presented in [132], where the correlation between the measured tilt of the telescope and residual gravity is exploited to calculate the orientation with an accuracy better than 5 µrad. Using the equation $\Delta g/g = -\theta^2$ (see Section 3.4.4) a misalignment of 5 µrad corresponds to $\Delta g = 2.5 \times 10^{-11}$ g which is well below the targeted accuracy of 5×10^{-10} g.

Absolute frequency of the chirp rate α_ω

The chirp rate α_ω is derived in the experiment from a DDS that is referenced to the 10 MHz source [DLR 100, Spectra Dynamic]. This low phase noise 10 MHz source has to be referenced to an absolute frequency. We compare the 10 MHz output against a GPS disciplined oscillator (GPSDO). In the future a direct phase lock to the GPSO can be performed. GPSDOs reach a relative accuracy of less than 10^{-12} after 1 day [137], more than two orders of magnitude lower than our targeted accuracy.

Absolute wavelength of the effective wave vector $\mathbf{k}_{\text{eff}}$

The absolute value of the effective wave vector $\mathbf{k}_{\text{eff}} \approx 2f_{\text{ref}} \cdot (2\pi/c)$ was evaluated by performing spectroscopy on the cold atomic cloud in the magnetically shielded interferometry zone. By scanning the frequency of a probe laser pulse applied on the apex of the fountain (to eliminate the Doppler shift of the launched atoms) an offset of the reference laser frequency f_{ref} of -0.41 MHz with an uncertainty of 0.06 MHz was measured. This corresponds to a bias of $-10.7 \pm 1.6 \cdot 10^{-10}$ g [81, 138].

The uncertainty of the systematic effects given above is well below the GAIN's targeted accuracy of 5×10^{-10} g. This is not the case for the influence caused by wavefront aberrations of the non-perfect optical elements in the retroreflected beam path. This effect is the biggest uncertainty factor in modern atom gravimeters [139]. The next section presents a method that can be used to reduce the uncertainty caused by for wavefront aberrations well below the targeted accuracy of 5×10^{-10} g.

4.4 Wavefront aberrations

This section analyses theoretically and experimentally the error in a gravity measurement caused by wavefront aberrations in GAIN. This analysis can be used to preselect optical elements that cause the smallest error and also to correct for it at the same time. The error caused by wavefront aberrations of the Raman beams is a direct consequence of the working principle of atom interferometry. It originates from the Equation 2.31

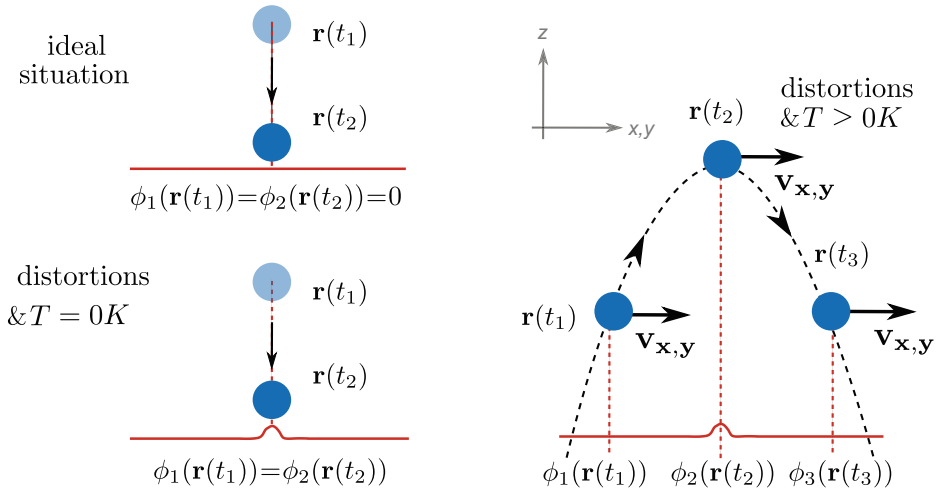

Figure 4.13: (left) Wavefront error caused by a finite cloud temperature and thus atoms with finite velocities. In the case of a planar or non planar effective wavefront an atom with a zero transverse velocity (in the xy plane) the phase imprinted to the atom by this wavefront during every interferometer pulse is the same. (right) The phase imprinted to an atom with a transverse velocity $\mathbf{v}_{\mathbf{x},\mathbf{y}}$ depends on its position and is different pulse.

$$\Delta\Phi = (\phi_1 - \phi_2^A) - (\phi_2^B - \phi_3), \tag{4.13}$$

where the interferometer phase $\Delta\Phi$ is the difference between the phases of the two interferometer paths A and B. This equation assumes that the interferometer phase is the same for all atoms participating in the interferometer sequence. This is only true for a plane Raman wavefront. For an arbitrary wavefront, the phase shift for an atom j depends on its actual position $\mathbf{r}_j$ within the plane perpendicular to the direction of the effective wavefront (see Figure 4.13). In this case the above equation becomes

$$\Delta\Phi_j = \left[\phi_1(\mathbf{r}_j(t_1)) - \phi_2^A(\mathbf{r}_j(t_2))\right] - \left[\phi_2^B(\mathbf{r}_j(t_2)) - \phi_3(\mathbf{r}_j(t_3))\right], \tag{4.14}$$

where t_i is the time of the i-th Raman pulse spaced by the interferometer time T.

For a finite cloud temperature, atoms move transverse to the wavefront during the interferometer sequence [139]. The atom's position during the three Raman pulses depends on each atom's individual velocity and initial position (see Figure 4.13). The error caused by wavefront aberrations depends therefore on the initial density distribution of the cloud, the clouds trajectory, the velocity distribution due to the finite cloud temperature and the detections process, which averages the atomic population over their spatial distribution in the detection area.

The effective wavefront in Equation 4.14 is the difference between the reflected and the incoming Raman beam. Since both beams enter the vacuum chamber from the same fibre collimator, aberrations present in both Raman beams cancel out. These aberrations include aberrations caused by the lens of the collimator and the top Raman window. Due to the large Raman beam diameter ($1/e^2$) of 29.5 mm the Rayleigh length is $\approx$ 1 km. Wavefront changes due to beam divergence are therefore neglected in our setup.

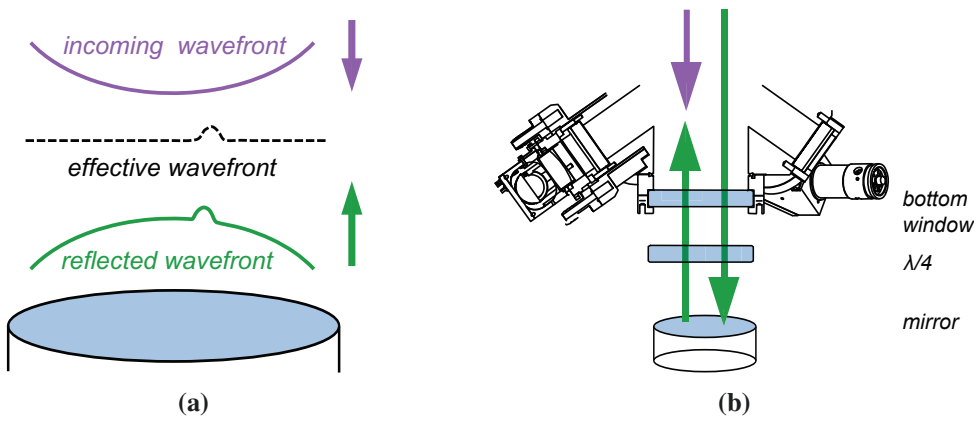

Figure 4.14: The origin of the wavefront aberrations in GAIN. (a) The effective wavefront is the difference between the reflected (green) and the incident (violet) wavefront. It is the sum of the wavefront aberrations caused by the individual optical elements that are only present in one of the Raman beams. (b) The optical elements present only in one of the beam paths are the bottom window, the $\lambda/4$ wave plate and the mirror for the retro-reflected Raman beam (green).

Only aberrations present in the reflected beam lead to aberrations in the effective wavefront. These are the aberrations caused by the bottom Raman window, the quarter-wave plate and the retro-reflecting mirror. Aberrations of the transmitted beam can originate from non planar surfaces of the optics and an inhomogeneous density inside the the optical element. The effective wavefront error $\delta\phi_{\text{eff}}$ therefore can be expressed as

$$\delta\phi_{\text{eff}} = 2\cdot\delta\phi_{\text{w}} + 2\cdot\delta\phi_{\lambda/4} + \delta\phi_{\text{m}}, \tag{4.15}$$

where $\delta\phi_{\text{w}}$, $\delta\phi_{\lambda/4}$ and $\delta\phi_{\text{m}}$ account for errors from window, $\lambda/4$ wave plate and mirror, respectively. The factor of two for the bottom window and the quarter-wave plate accounts for the double pass of the reflected Raman beam (before and after the reflection from the mirror) as can be seen from Figure 4.14 (a). Figure 4.14 (b) shows the optical elements that induce the wavefront aberrations in our setup.

4.4.1 Measuring wavefront aberrations

To calculate the cumulated, total effect of wavefront aberrations in our setup, the aberration of any given optical element has to be measured first. This measurement is performed with a Shack-Hartmann sensor [SHSCam XHR GE, Optocraft]. This sensor type measures the local wavefront curvature by an array of micro lenses that focuses the light on a CCD chip. The spatial deviation of the focused spots from the position of spots caused by a reference wavefront is proportional to the local wavefront curvature. The curvature is numerically calculated by a software provided by the manufacturer. The sensor has a 24 mm $\times$ 36 mm CCD chip, and an array of 240 $\times$ 160 micro lenses [140]. Wavefront aberrations caused by optical elements working in transmission, like windows or wave plates, can be measured by the Shack-Hartmann sensor in a differential measurement.

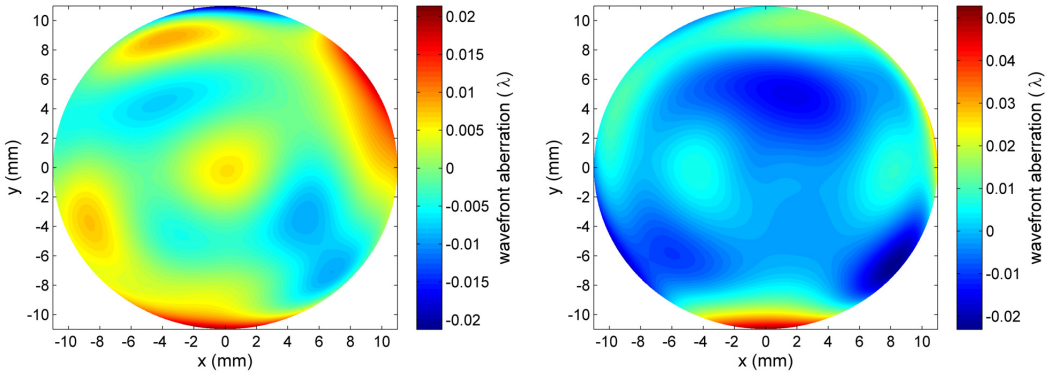

Figure 4.15: The wavefront aberration from two measured windows, called window no. 1 (a) and window no. 2 (b). The aberrations are represented by the first 36 Zernike polynomials and λ = 780 nm. The tilts in x and y direction (the average slope of the wavefront) are removed.

First, the wavefront of a laser beam is measured directly with the sensor. This measurement is then used as the reference wavefront for the measurement of the wavefront where the optical element to be tested is placed into the beam path. The wavefront obtained this way includes only aberrations caused by the optical element. To minimize the deformation of the micro lens array during the reference and original measurement its temperature is stabilized with a Peltier element integrated into the sensor. The accuracy of this differential method is specified to $\approx \lambda/200$ rms over a circular area of the whole CCD chip (24 mm diameter) [140].

The wavefront is decomposed into the orthogonal basis of Zernike polynomials by the sensor's software. The Zernike polynomials represent optical image errors like defocus, astigmatism, coma etc. and are widely used in the human eye medicine and optical testing [141]. The first 36 coefficients are used for the further calculation and reconstruction, since their numeration is defined by the ISO norm 24157 [142]. The reconstructed wavefront aberrations of two high quality windows named window no. 1 and window no. 2 [custom-made, Melles Griot] are shown in Figure 4.15.

4.4.2 Calculations of the effect of wavefront aberrations in an atom interferometer

To calculate the error in our gravity measurement caused by a given wavefront error an algorithm was developed by the author and implemented in MATLAB by Bastian Leykauf during his bachelor thesis [143]. In this simulation, test atoms in the plane of the wavefront (x-y plane in Figure 4.16) are created. They are initially equally spaced in momentum and position space. For the time of every Raman pulse the position of the test atoms is then calculated based on their classical trajectories. The error for the individual test atom is evaluated based on the Equation 4.14. Due to the active alignment of the Raman beams in our setup any tilt introduced by the test window will be cancelled. The corresponding Zernike coefficients are

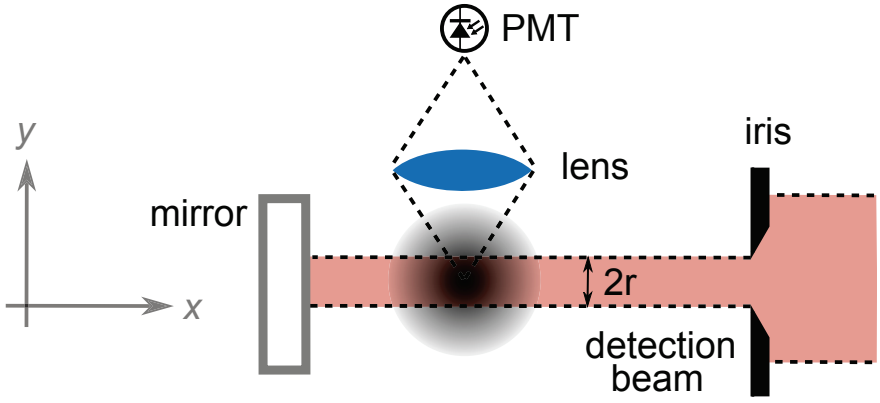

Figure 4.16: The optical detection setup in GAIN. The diameter of a originally 50 mm ($1/e^2$) beam can be changed by an adjustable iris. The beam passes the vacuum chamber and is retroreflected by a mirror. The florescence of the atoms illuminated by the beam is collected by a lens on a photo multiplier tube (PMT).

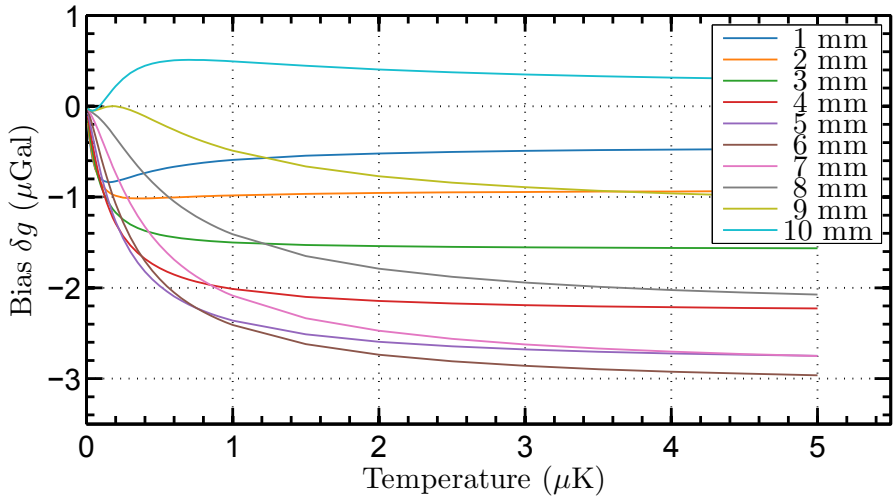

Figure 4.17: The calculated temperature dependence of the error in a gravity measurement induced the wavefront aberrations of window no. 1 in our gravimeter for different detection radii and a cloud radius ($1/e^2$) of 3 mm. For temperatures typically achieved in our setup ($\approx$ from 2 µK to 5 µK), the dependence is almost uniform.

thus set to zero for the following calculations. The atoms enter the detection zone 128 ms after the last Raman pulse. The phase shifts are weighted with their initial momentum and position distributions. We assumed them both to be Gaussian, although the velocity distribution of atoms loaded from optical molasses is sometimes better described by a Lorentzian distribution [134]. We calculated the phase shift for both, a Gaussian and a Lorentzian fit of the measured velocity distribution of our cloud and found only a negligible difference below 1 % between them.

Not all atoms in the detection area contribute to the interferometer signal. The atomic cloud is illuminated by the detection beam, with diameter r as shown in Figure 4.16. The diameter r is adjusted by an iris placed after the input fibre in the detection beam telescope. Without the iris, the original beam has a diameter of 50 mm ($1/e^2$). A beam with an almost uniform intensity up to a radius r of 12 mm can be created by changing the aperture of the iris. 12 mm is the maximum beam radius that can be directly imaged by our Shack-Hartmann sensor. As a simplification, we assume that only atoms in a circular area with the diameter of the detection beam are detected with uniform weighting.

Figure 4.17 shows the temperature dependence of the phase error caused by the wavefront of window no. 1 for various detection radii. The displayed error is twice as big as the error caused by the reconstructed wavefront in Figure 4.15 since the Raman beam passes the window twice. It clearly shows that the phase error strongly depends on the detection radius and only slightly on the temperature for values above 2.0 µK. The main reason for this is that for higher temperatures only atoms from the low tail of the corresponding velocity distribution remain in the detection zone and atoms with high velocities leave the detection zone and do

not contribute to the signal. The low temperature dependence is consistent with the results obtained in [139]. In their experiment an extrapolation of the wavefront error, obtained for reachable temperatures in a setup similar to ours, to zero temperature for a fixed detection zone using a fit to Zernike polynomials was not successful. To reach our targeted uncertainty below 0.5 µGal, cloud temperatures less than 200 nK are needed. This is almost one order of magnitude lower than temperatures achievable for rubidium with molasses cooling [144].

We utilize the strong detection radius dependence of the wavefront error to compare the numerical simulation with experimental data. Due to a small free space volume between the bottom window and the mirror in our setup we are able to insert one of the measured windows directly into the beam path of the Raman laser (see Figure 4.14 (b)). In doing so, we can directly measure the wavefront error induced by this window in the gravimeter as a function of the detection radius. For every set detection radius, we first perform a measurement of local gravity g with the procedure presented in Section 3.4.4 without and subsequently with the test window to obtain g_W. The gravity data are corrected for tidal effects and atmospheric pressure. The wavefront error or bias δg is given by the difference between both gravity values

$$\delta g = g_W - g. \tag{4.16}$$

For small detection radii only a small amount of atoms is detected, and the sensitivity of the gravity measurement is decreased. Therefore, the time for a single gravity measurement varies from 5 to 25 hours for window no. 1 and 16 to 72 hours for window no. 2, which was used in the second measurement. The radius of the detection beam is measured with the Shack-Hartmann sensor.

The measured wavefront bias δg for windows no. 1 and no. 2, together with the bias obtained by the numerical simulation are shown in Figure 4.18 and 4.19. For the simulation a cloud size of 3 mm ($1/e^2$ radius), a cloud temperature of 3 µK and a central position of the cloud centre

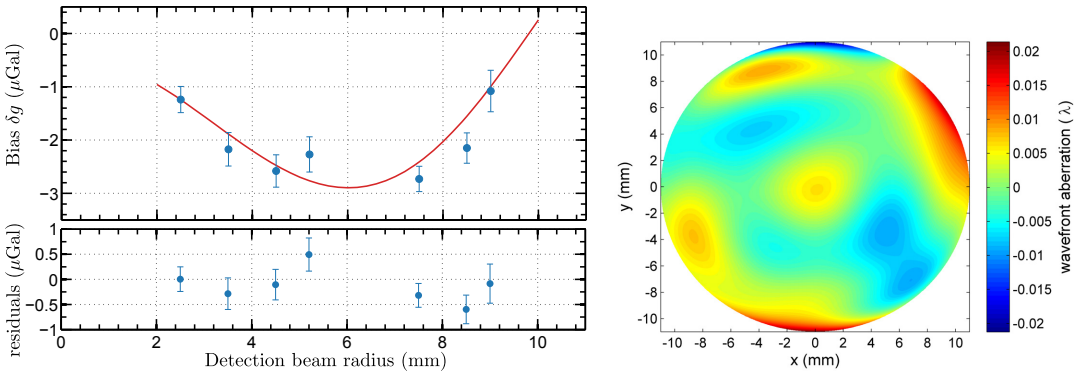

(a) **(b)**

Figure 4.18: (a) The measured bias δg of the gravity value (blue dots) caused by window no. 1 inserted in the beam path of our gravimeter compared to the results obtained from theory (red line). The residuals of the measured and the calculated values are shown below. (b) Wavefront aberrations from the corresponding window no. 1

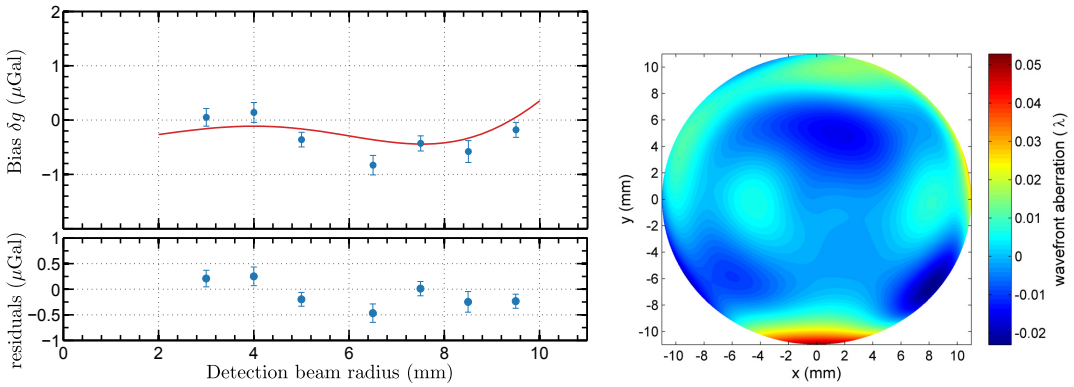

(a) **(b)**

Figure 4.19: (a) The measured bias δg of the gravity value (blue dots) caused by window no. 2 inserted in the beam path of our gravimeter compared to the results obtained from theory (red line). The residuals of the measured and the calculated values are shown below. (b) Wavefront aberrations from the corresponding window no. 2. Same scale as in Figure 4.18

in respect to the measured wavefront are assumed. The displayed uncertainty σ_δ for every data point is calculated from the uncertainty of the the two gravity measurements (σ for the gravity without and σ_W with the test window) via

$$\sigma_\delta = \sqrt{\sigma_W^2 + \sigma^2}. \tag{4.17}$$

The measurement is in good agreement with the simulation. No fit of any experimental parameters (cloud radius, cloud temperature and center position) was applied. Using window no. 1 in our setup and correcting the gravity value for the aberrations results in a standard deviation of 0.37 µGal between the measured and the calculated value (the standard deviation of the residuals in Figure 4.18), almost a factor of 10 smaller than the effect itself. For window no. 2 the standard deviation of 0.18 µGal is even smaller. Choosing window no. 2 over window no. 1 as the bottom window for a future gravimeter would result in a reduction of the wavefront error by a factor of 5, even without an applied correction.

The numerical results can be used for characterization of windows and wave-plates prior to mounting, selecting the windows with the smallest total absolute error from a given set. Assuming the same achievable standard deviation for the mirror and the wave-plate as the one for window no. 2, the total uncertainty caused by wave front aberrations in our gravimeter would be

$$\Delta_{WF} = \sqrt{(0.18\,\mu\text{Gal})^2 + (0.18\,\mu\text{Gal})^2 + (0.18\,\mu\text{Gal}/2)^2} = \sqrt{9/4}\cdot 0.18\,\mu\text{Gal} \tag{4.18}$$

or 0.27 µGal. However, based on measurements with two windows it is hard to predict the uncertainty of our method. For the following calculation we will assume a standard deviation

of 0.37 µGal (the higher deviation from the two windows measurements) for an optical element that is passed twice by the Raman beams (window or wave-plate) and the half for the mirror.

4.4.3 Wavefront aberrations in GAIN

Given the error for the measured gravity value and its uncertainty caused by given wavefront aberrations obtained by numerical calculation, we can calculate this error in our gravimeter based on the measured wavefront aberration of the optics in GAIN. This requires that the wavefront aberrations caused by the optical elements in the reflected Raman beam path (bottom window, wave-plate and mirror) are known. The wavefront aberrations of the wave-plate can be measured with the Shack-Hartmann sensor with the same differential method as the on used for the test windows. The reconstructed wavefront of the $\lambda/4$ wave-plate is shown in Figure 4.20 (a). For the retro-reflecting mirror a differential measurement with the Shack-Hartmann sensor is more complicated. Its aberrations can only be measured if a mirror with a known surface profile (with the required accuracy) is used for the reference measurement [140]. If such a mirror would be commercially available, it can be used itself as the retro-reflecting mirror in GAIN.

The mirror's surface profile is equal to its wavefront aberrations and can be measured using optical interferometers that scan the mirror surface [145]. They achieve a very high accuracy due to correlation measurements. They require just a small reference flat, which is available more easily. The surface profile of the retro reflecting mirror was measured with such a device with the help of Stefan Breuer, FBH, Berlin. Using an optical interferometer for surface profile measurements [NewView 6300, Zygo], the wavefront aberration of the retro reflecting mirror could be obtained. For the measurement, the mirror was mounted in the same lens tube as the one used on top of the Tip/Tilt stage in our atom interferometer (see Figure 3.3). The torque applied by the retaining ring was measured to match the one used in GAIN. The surface profile

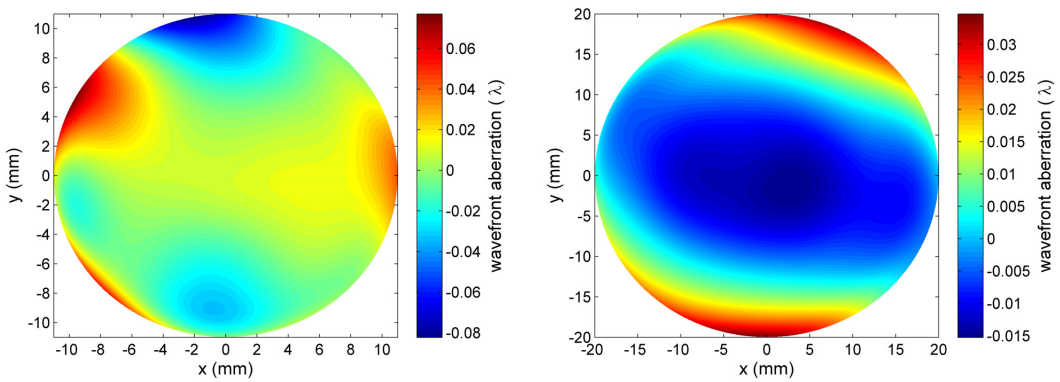

Figure 4.20: The measured wavefront aberrations by the optical elements in GAIN represented by the first 36 Zernike coefficients and $\lambda = 780\,\text{nm}$. The $\lambda/4$ wave plate (a) was measured by the Shack Hartman sensor. The mirror (b) was measured by an optical interferometer.

of the retro-reflecting mirror is shown in Figure 4.20 (b).

The calculated bias in GAIN caused by this wavefront aberrations is -2.2 ± 0.38 µGal for the $\lambda/4$ wave-plate and 0.4 ± 0.19 µGal for the mirror. With the wavefront aberrations of the mirror and the wave-plate, only the wavefront of the bottom window is unknown. Unfortunately, we are not able to measure the wavefront aberrations of the bottom window in our setup at this point. This would require us to open the vacuum, followed by a full baking out procedure afterwards and would cause several months of down time for the apparatus. Until then, a rough estimation of the aberrations of the window can be done.

Beside the two presented windows, the wavefront aberrations of three additional windows were measured in the Bachelor thesis by Alexander Stein, supervised by the author [146]. Their induced error on the gravimeter measurement was also calculated [143]. Given the assumption that these window aberrations have the same variance as the the windows already installed in our setup, an estimation of the wavefront aberration of the bottom window can be performed.

To do so, the average wavefront bias of the five windows -1 µGal, is taken as the bias for the bottom window. For the uncertainty of this wavefront bias, we assume a standard deviation equal to the highest wavefront bias measured in all the five windows. The uncertainty caused by the bottom window in this case is 2.2 µGal.

The bottom window is mounted to the vacuum chamber with a pressure difference of $\approx$ 1 bar between the vacuum side and the side exposed to atmospheric pressure. This pressure difference may bend the window resulting in additional aberrations. In a test setup, consisting of a short vacuum flange sealed with two windows (from the set of five used for wavefront measurement presented in this section), this effect was investigated [146]. This led to the assumption that the pressure difference caused by the vacuum causes an aberration dominated by a defocus. Based on this data a bias of -2.3 µGal was calculated.

This measurement was repeated by the author in October 2015. No such deformation caused by the pressure difference was measured in the sensitivity limits of the wavefront sensor. This effect is therefore not considered. The resulting wavefront error caused by three optical elements in our gravimeter is displayed in Table 4.1.

Optical element	**Bias** (10^{-10} g)	**Uncertainty** (10^{-10} g)
$\lambda/4$ wave plate	-22	$\pm$3.8
mirror	4	$\pm$1.9
bottom window	-10	$\pm$22
Total	**-28**	$\pm$**22.4**

Table 4.1: The wavefront effect in the gravimeter GAIN. The uncertainty is calculated based on measurements and methods presented in this chapter.

4.4.4 Future mitigation strategies and a summary of the systematic effects in GAIN

The previous section evaluated the effect of wavefront aberrations in GAIN. Based on the measured wavefront from the optics used in our setup the error caused by these elements can be estimated. The uncertainty of the bottom window dominates over the $\lambda/4$ plate and the mirror, that can be measured directly. However, new setups will profit by the presented method by preselecting the optical elements, prior their assembly.

To decrease the uncertainty even further, a better model of the detection area would be desirable. A spatial resolved detection of the atomic population in the plane of the Raman beams can dramatically improve the sensitivity of our method. Such a detection scheme using one or multiple CCD cameras imaging the fluorescence of the atomic cloud might be implemented in our setup.

An alternative approach was recently proposed by Dickerson et al. [80]. Atoms from a so called 'point source', an atomic cloud with a negligible initial size, link their final position during detection to their trajectory during the interferometer sequence. Such a correlation allows for an in situ measurement of the wavefront aberrations using spatial resolved imaging [80].

The major systematic effects in GAIN are summarized in Table 4.2. Besides the systematic effects already pointed out in Section 4.3.1 the following Table 4.2 includes additional contributions.

The switching of the MOT coils during the interferometer sequence causes a rapid change of their magnetic field. This field is picked up by the feedback coils in the vibration isolation, causing vibrations synchronous to the experiment cycle. The corresponding bias is shown in Table 4.2 (round brackets). A recently installed magnetic shield around the MOT chamber, effectively suppresses the synchronous vibrations [138] as can be seen in Table 4.2 (value without round brackets).

Effect	**Bias** (10^{-10} g)	**Unceratinty** (10^{-10} g)
Wave vector alignment	-1	$\pm$1
Frequency of the reference laser	-10	$\pm$5
Coriolis effect	0	$\pm$10
Self gravitation	19	$\pm$5
AC Stark	0	$\pm$5
Synchronous vibrations	0 (90)	$\pm$ 5(50)
Wavefront aberrations	-28	$\pm$22

Table 4.2: The main systematic effects in GAIN. The bias (this value has to be subtracted from the measured gravity value) and the corresponding uncertainty are shown. The value for the effect of synchronous vibrations is shown with the recently installed magnetic shield and without (in round brackets).

4.5 Summary and sensitivity estimation of a space based atom interferometer

Mobile gravity measurements with a mobile atom interferometer were performed. Its sensitivity surpasses the sensitivity of a gravimeter based on a falling corner cube. During a comparison with a superconducting gravimeter, without the limitations of tidal models, stable operation over 10 days where performed. This measurements show the high potential of atom interferometers for gravity measurements and tests of the UFF in space.

Space operation can increase the performance of atom interferometers by several orders of magnitude. With a pulse separation time of T =260 ms like presented in GAIN an increase by a factor of 10 to $T = 2.6$ s seams feasible and even higher free evolution times are proposed for space based atom interferometers in Section 1.4. With the same sensitivity like the one demonstrated in the Wettzell campaign and analysed in Section 4.2, an increase in sensitivity by a factor of $T^2 = 100$ can be achieved. This assumption is based on the fact, that the temperature of the cloud can be reduced to a degree, where its expansion is not limiting the detection noise due to loss of detected atoms. Such cooling techniques, where the expansion of cloud can be effectively reduced by switching on an optical or magnetic potential, were already demonstrated [147, 148].

With the low residual vibrations in microgravity [135, 136], the influence of vibrations on the interferometer noise can be neglected. In a gradiometer configuration for high sensitive measurements of Earth's geoid [92, 149] or in dual species configuration for a future test of the UFF [68], the detection noise become the dominant noise source [107]. With the already achieved detection noise of 19.3 mrad/shot during the Wettzell campaign (see Section 4.1.3), the potential sensitivity per interferometer becomes 1.77×10^{-11} g/shot.

This potential sensitivity demonstrates the benefits of space operation for cold atom interferometers. It has to be noted that this performance can be achieved in a compact device, without the need of a long interferometer zone. The small size of the device means also that the magnetic field have to be precisely controlled in a small volume instead in the long interferometer zone, like in ground based experiments [150]. The sensitivity can even be further improved by several orders of magnitude using higher atom numbers, large momentum beam splitters [151–153] or sub shot noise limited detection using entangled atomic sources [154].

Space based atom interferometers requires a high technological readiness for all components used. The next chapter briefly presents an atom interferometer, built to operate during a sounding rocket flight as a crucial technological step towards space operation of atom interferometers.

5 MAIUS: a matter wave interferometer on a sounding rocket

The previous chapter presented gravity measurements carried out by GAIN with unprecedented stability for atom interferometers. This performance can be further increased by several orders of magnitude when operating the atom interferometer on a space platform. To fully exploit the long interferometry time achievable in microgravity, the expansion of the atomic cloud has to be drastically reduced to a temperature even colder than the one used in GAIN. This is done by evaporative cooling of the atomic ensemble trapped in a magnetic field until most of the atoms populate the ground state of the trap [155]. Such a state of matter is called a Bose-Einstein condensate (BEC).

This chapter introduces the Matter Wave Interferometer in Microgravity MAIUS mission (German acronym for MAterienwellenInterferometer Unter Schwerelosigkeit) that will operate on a sounding rocket. MAIUS aims to explore atom interferometry with Bose-Einstein condensates with free evolution times T that are not possible on ground.

5.1 Introduction

MAIUS has the goal to perform atom interferometry for the first time in a space environment. This will be done on a sounding rocket launched from the Esrange Space Center (ESC), Sweden. The launch is scheduled for winter 2016. The two stage VSB-30 rocket allows for a microgravity time of approximately 6 minutes for the given mass of the MAIUS payload, and an apogee of 238 km [156]. The goals of the MAIUS mission are [157]:

1. Creation of the first ^{87}Rb Bose-Einstein condensate in space
2. Demonstration of a point source with ultra-low expansion velocities, corresponding to temperatures lower than 1 nK
3. First atom interferometer based on Bose-Einstein condensates in space
4. Observation of Bose-Einstein condensates after multiple seconds of free evolution
5. Atom interferometry on time scales of multiple seconds

A typical sequence for BEC production on an atom chip in the QUANTUS-2 drop tower apparatus, a prototype for the MAIUS payload, is shown in Figure 5.1. Pre cooled atoms are loaded from an atomic source (a 2D+ MOT that is not shown here) into a 3D MOT. The

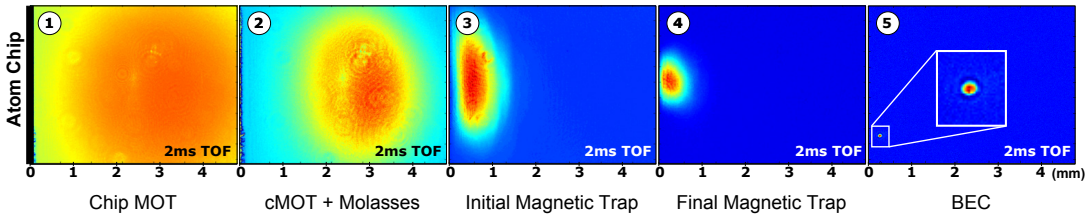

Figure 5.1: A typical sequence for BEC production on an atom chip. (1) The atoms are loaded into the 3D MOT. (2) The size of the atomic cloud is compressed and the atoms are cooled using optical molasses. (3) The atoms are trapped into the initial magnetic trap and transferred to the more efficient final magnetic trap (4), where the evaporation of the atoms to a BEC is performed (5). Figure adapted from [158].

atomic cloud in the 3D MOT is compressed by increasing the detuning of the trapping light and reducing the magnetic field gradient, cooled using optical molasses and transferred to an initial magnetic chip trap. Only atoms in a magnetic sensitive state with m_F=+1 or m_F=+2 can be trapped. Optical pumping with σ^+ light transfers the atoms into the m_F=+2 state. Afterwards the atoms are transferred to the final magnetic trap where RF-evaporation continuously removes the hottest atoms in the trap and reduces their temperature until most of the atoms are in the ground state and the BEC is formed.

After releasing the BEC from the trap, the residual expansion of the condensate is reduced by applying a magnetic lens. This is performed by turning on a magnetic trap for a short period reducing the kinetic energy of the atoms [147]. After the magnetic lens, the atoms in the condensate are still polarized in the m_F=+2 state and are transferred to a magnetic insensitive m_F=0 state using an adiabatic rapid passage [147] to reduce the sensitivity of the interferometer to magnetic fields. This state preparation is followed by the Mach-Zehnder atom interferometer sequence described in Section 2.3.1 using Bragg transitions [159].

A Bragg $\pi/2$-pulse splits the atomic wave packet in a coherent superposition between the two momentum states with equal probabilities. After a π-pulse the wave packet is spatially overlapped when a second $\pi/2$-pulse recombines the wave packet. The atomic population in the two external states depends on the phase difference between the two interferometer paths and is detected using absorption imaging instead of fluorescence imaging as used in GAIN (see Section 3.4.2)

To perform this sequence on a sounding rocket, a complete atom interferometer apparatus based on Bose-Einstein condensates was developed, assembled and integrated in a sounding rocket with an inner diameter of 500 mm by the MAIUS team. This includes the vacuum chamber, the electronics, the battery module and the laser system. These components were designed to operate after the harsh conditions during a sounding rocket launch. The contribution to MAIUS during this thesis included the design, assembly and integration of the MAIUS laser system. Afterwards the laser system was operated and optimized with MAIUS flight electronics for more than two years. This results were achieved in close collaboration with the members of the MAIUS Laser system team (M. Krutzik, H. Duncker, O. Hellmig, A. Wenzlawski and J. Grosse).

5.2 Payload

This section gives an overview over the MAIUS payload. A detailed description of the experiment design together with thermal simulations and the performed qualification steps can be found in the thesis of Jens Grosse [160] and Stephan Seidel [157].

The advantage of long microgravity times compared to laboratory environments comes at the price of very limited space for all subsystems, constraints on the overall mass, the lack of a stable temperature environment and demands for additional extremely high mechanical stability during launch. During the 44 s long boost phase vibrational loads of $\approx 1.8\,g_{RMS}$ and peak accelerations up to 13 g will be caused by the two motors to the rocket. The individual payload parts are attached to shock mounts to reduce this load [161].

To ensure a successful launch the payload parts have to perform acceptance vibration tests at a level of $5.4\,g_{RMS}$ for every axis. Individual components need to be qualified in vibration tests at an even higher load of $8.1\,g_{RMS}$. This tests have to be performed hard-mounted (without the shock mounts) and are a requirement from the launch provider.

Water cooling for the electronics and for the laser system is available only before lift-off. Due to aerodynamic friction the payload structure will increase its temperature by approximate 5 °C during the flight additional to the heat produced by the subsystems [160].

In spite of these conditions, all systems have to fit into the rocket and perform accurately during the limited time of the sounding rocket mission that starts after the boost phase of the rocket. This is particular challenging for the laser system due to the high mechanical loads

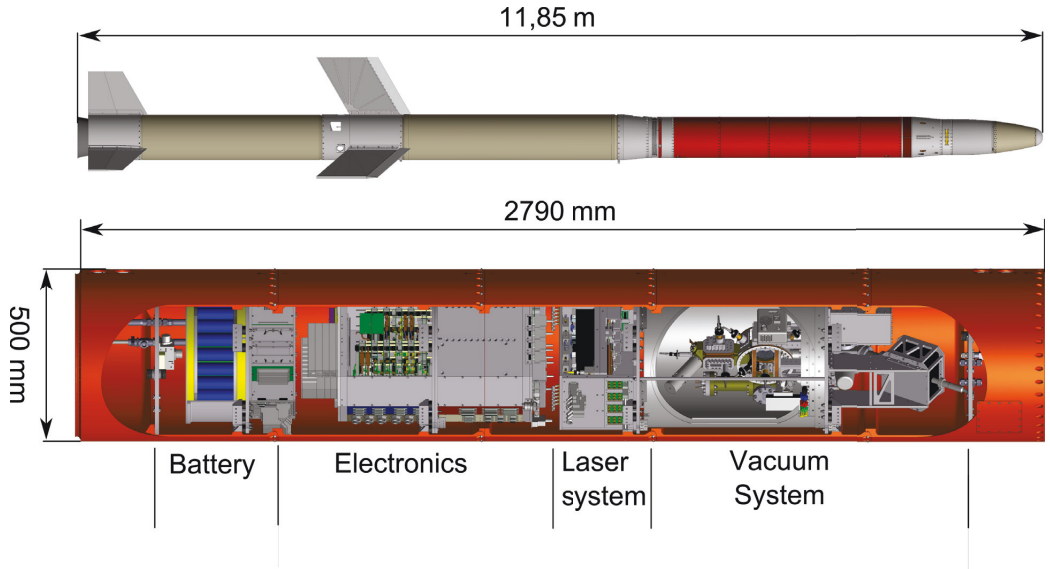

Figure 5.2: CAD drawing of the VSB-30 sounding rocket (top) and the MAIUS payload (bottom). The VSB-30 has two rocket motors to increase the microgravity time for the payload. The payload consists of the battery module, the electronics, the laser system and the vacuum system (from left to right). The inner diameter of the hull sections is 500 mm. Modified Figures from [160].

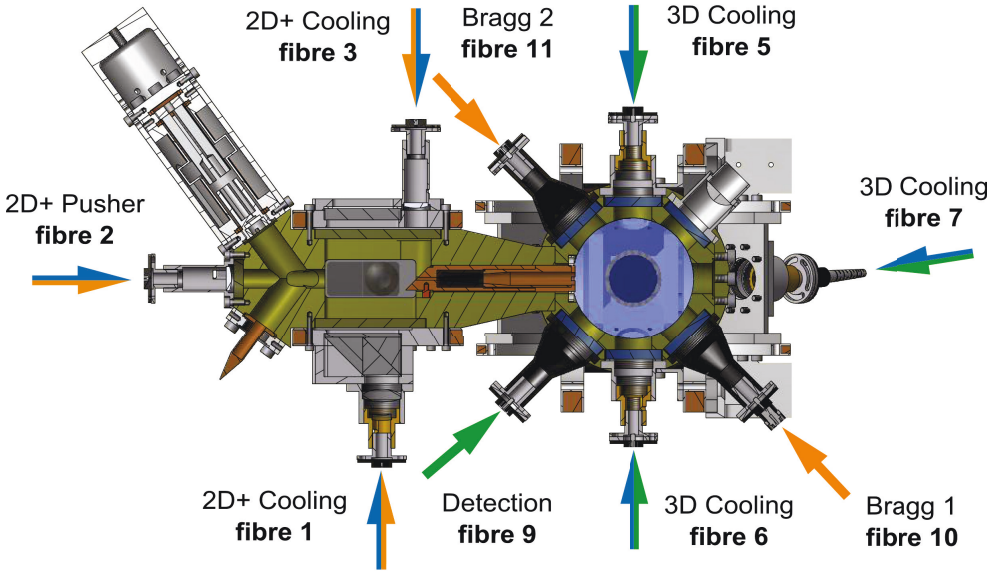

Figure 5.3: A CAD drawing of the MAIUS vacuum system (modified, original courtesy of Jens Grosse). The 2D+ MOT on the left side is connected to the 3D MOT on the right side (both made from titanium) via a differential pumping stage (copper tube that connects the two chamber parts). Magnetic field coils (not shown here) and beam collimators are rigidly attached to the chamber. The function of all collimators along with the corresponding fibre number in the laser system are shown. See the text below for more details and Section 5.3 for an in depth description of the laser system.

and temperature changes. A CAD drawing of the payload together with the assembled rocket is shown in Figure 5.2. The payload subsystems consist of the battery module, the electronics, the laser system and the vacuum system (from left to right).

The vacuum system is based on two parts. The 2D+ MOT chamber has a relatively high rubidium vapour pressure in the 10^{-7} mbar region. In the 2D+ MOT, rubidium atoms released from an oven are transversally laser cooled and trapped using a two-dimensional magnetic and optical field. In the longitudinal direction two counter propagating laser beams (called the pusher and retarder) reduce the beam velocity using molasses cooling. The laser cooled atomic beam in the 2D+ MOT is continuously guided to the 3D MOT chamber through a differential pumping stage.

The differential pumping stage, a tube with a low conductance, maintains a pressure difference of three order of magnitude between the 2D+ and the 3D MOT, which has a pressure of $\approx 10^{-10}$ mbar. This allows for a high atom loading rate in the 3D MOT through the 2D+ MOT (see Figure 5.3) while keeping a sufficient low pressure in the 3D MOT [162]. This reduces collisions of the atoms in the 3D MOT with the background atoms that would otherwise lead to a high atom number loss, making the production of a Bose-Einstein condensate impossible. The vacuum is maintained by an ion getter pump attached to a pumping tube near the 3D MOT

chamber, while two titanium sublimation pumps can be activated if needed.

The magnetic fields to trap and evaporate the atoms in the 3D MOT section are created by wire structures on the atom chip similar to the ones used for drop tower experiments [158]. The atom chip creates strong magnetic fields gradients close to its surface with modest currents. This reduces the size of the vacuum chamber and the overall power consumption, two crucial aspects in compact atom interferometers. The coating of the atom chip surface is high reflecting and serves as a mirror for two of the four 3D MOT beams. This so called mirror-MOT configuration [155] is necessary to cool and trap the atoms in the 3D MOT close to the surface of chip. Light is delivered through polarization maintaining (pm) fibres to the collimators that are directly attached to chamber. A CAD drawing with the position of the various telescopes for the vacuum system is shown in Figure 5.3. Optical fibres deliver frequency stabilized light needed to perform the complete experimental sequence to the telescopes from the laser system which is presented below.

5.3 Laser system

Based on the experimental sequence presented above, the MAIUS laser system needs to provide light for cooling and repumping of the atoms in the 2D+ and 3D MOT overlapped and distributed in a specific ratio through pm fibres. One additional fibre for the optical pumping and for the absorption detection of the atoms as well as two fibres deliver light for the Bragg interferometry (11 fibres in total). It has to be compact, reliable and fully functional after the vibration phase of the launch. A laser system that fulfils these requirements is presented in this section.

5.3.1 Micro-integrated laser sources

The MAIUS laser modules are based on a micro-integrated-optical bench (MIOB) in a master oscillator power amplifier (MOPA) setup. Here, a DFB diode laser is used as a master oscillator (MO) and its output is amplified in a tapered amplifier (PA). These modules are explicitly designed for atom interferometry experiments with rubidium on a sounding rocket. The collimation optics and optical isolators are integrated onto an optical bench to provide short beam paths and a high mechanical stability. The bench is made from the electrically insulating Aluminium nitrite (AlN), a ceramic with high thermal conductivity of $\approx 200\,\mathrm{W/mK}$, about half of that of copper. Along the optical elements the MIOB has on-board coaxial electrical connections for laser current, modulation and several thermistors for temperature stabilization on a footprint of only $80\,\mathrm{mm} \times 25\,\mathrm{mm}$ [163]. The laser modules are developed by the project partner Ferdinand-Braun-Institut, Leibniz-Institut für Höchstfrequenztechnik (FBH) [164].

The DFB diode with a line width (FWHM) of about 1 MHz is used as the master oscillator for the tapered amplifier. The output is collimated with a combination of two cylindrical lenses and passes a micro-isolator with 60 dB isolation to prevent feedback what might cause multi mode operation of the laser. After the isolator another combination of two cylindrical lenses is used to couple the light into the back facet of a tapered amplifier. The amplifier generates

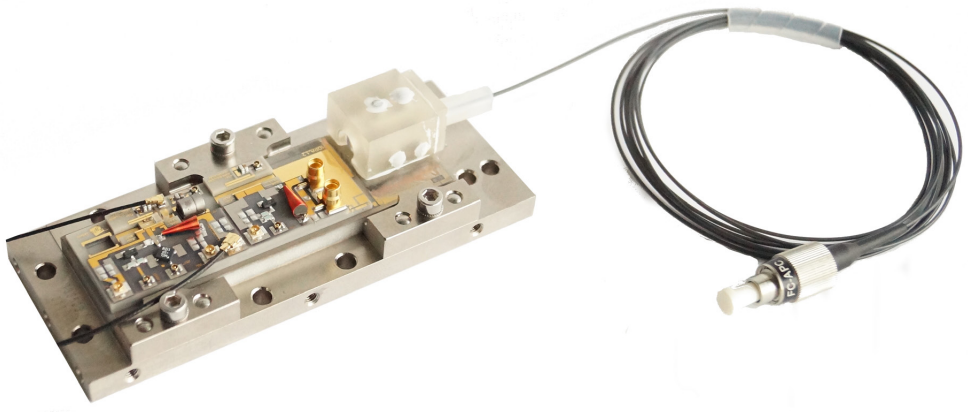

Figure 5.4: The diode laser module used in the MAIUS laser system. Light from a DFB diode is collimated using micro optics and passes an optical isolator. The output and is coupled into a pm fibre. The tapered amplifier, that is not integrated in this picture, can achieve a free space output power of up to 1 W. Module dimensions with the CCP are 104 mm $\times$ 42 mm with a mass of about 270 g.

an output power of $\approx$ 1 W at an injection current of 2000 mA for the amplifier section and 200 mA for the ridge-waveguide section (RW) that are driven individually [165]. The RW section acts a single lateral mode filter for the seed light to suppress higher modes at the TA output [166] .

The free space output of the amplifier is then collimated with two cylindrical lenses. Typical operation temperatures for the DFB diode and the module are around 36 °C. The output of the DFB diode rear facet is also collimated and passes a 30 dB micro-isolator. This light is used to monitor the output power of the DFB diode.

To couple the output of the tapered amplifier into an optical fibre a coupler made from Zerodur, a glass ceramic with a low coefficient of thermal expansion (cte) [167] is glued directly on the MIOB. The Zerodur couplers were developed and assembled for the MAIUS mission by project partners from the Institut für Laserphysik at the Hamburg University. A detailed overview of the Zerodur technology can be found in [167]. In front of the fibre coupler a polarization beam splitter cube is used to increase the polarisation extinction ratio (PER) of the light emitted by the amplifier. Figure 5.4 shows a mounted fibre coupled laser module used in MAIUS.

The DFB diode laser frequency can be tuned coarse and slow with the diode temperature and fine tuning is done with the injection current. The DFB diode laser temperature is stabilized to a fixed value and the frequency is tuned with the current only in our system. A thermistor directly mounted on the MIOB close to the DFB diode chip is used for temperature stabilization of the diode that is mounted on the MIOB. The MIOB itself is clamped on a structure made from copper called the conductively-cooled package (CCP) (see Figure 5.4). The CCP is placed on a Peltier element and a spacer made from a low thermal conductivity, high stiffness material [Ketron PEEK 1000, Quadrant], that prevents the CCP from bending

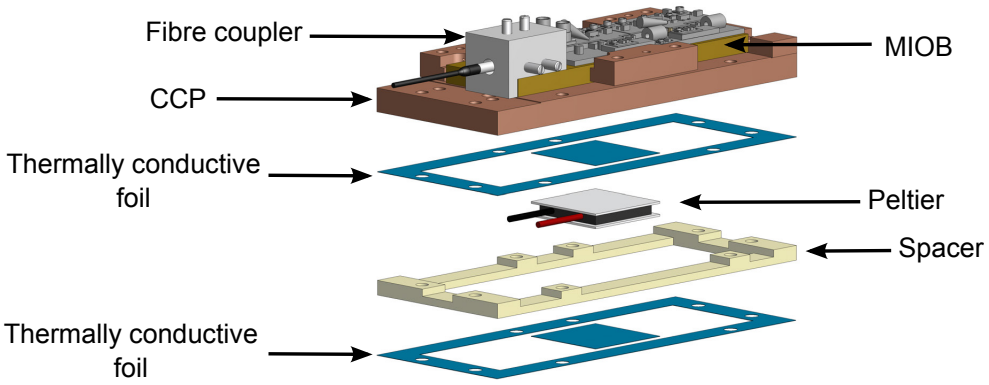

Figure 5.5: The mounting concept of the laser modules used in MAIUS. The micro-integrated-optical bench (MIOB) is clamped on the CCP. A Peltier element between the CCP that is screwed to a baseplate is used for temperature stabilization of the DFB diode. A spacer between the CCP and the baseplate prevents the MIOB from bending and thin thermally conductive foil ensures proper thermal contact of the Peltier.

when being mounted to a baseplate with screws made of Titanium Grade 5. These two materials were chosen due to their low thermal conductivity (0.25 W/mK for the PEEK 1000 and 6.8 W/mK for the Titanium Grade 5) to reduce the thermal connection between the baseplate and the CCP. To compensate for surface roughness of the CCP and the Peltier element to ensure proper thermal contact between them both, a 0.1 mm thin thermally conductive foil [U 90 KERATHERM, Kerafoil] is used. This thermal design results in an almost equal temperature of the stabilized DFB diode and the MIOB while providing mechanical stability. Figure 5.5 shows the mounting concept for the MAIUS laser modules.

To operate the MAIUS experiment, four laser modules are used (see Figure 5.6 (a)). One of them is a DFB MO laser only where the amplifier is not integrated since 10 mW ex-fibre is sufficient for the frequency stabilization. This laser is stabilized to an atomic transition in a rubidium gas cell and serves as a frequency reference for three MOPA modules, called science lasers. The laser system contains two additional MOPA modules (redundancy) that can be used as a replacement for the science lasers in case of malfunction before the launch. In this case the optical fibre connection of the malfunctioning laser is cut through and then connected with one of the redundancy lasers. This is done after opening the laser system housing using a fibre splicer.

5.3.2 Frequency stabilization

Depending on the optical beam profile of the amplifier output 350 mW - 500 mW optical power can be coupled into an pm fibre. Light from every module passes a fibre coupled optical isolator [IO-J-780, Thorlabs]. This reduces optical feedback from free space components in the free space switching and distribution module. An in-line photo diode [OZ optics] after

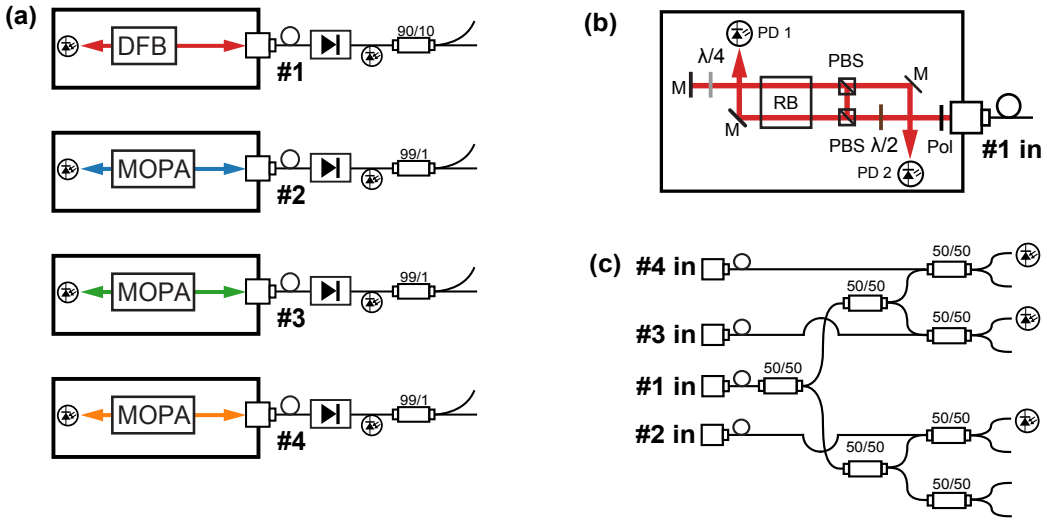

Figure 5.6: Four lasers are used to drive experimental sequences in MAIUS (a). One master laser (MO, #1) is stabilized to an optical transition in a rubidium cell in the spectroscopy bench (b). Light from the three science lasers (MOPA #2-4) is overlapped together with light from the MO in a fibre splitter system (c). The beat notes are detected on fast photo diodes and are used for offset frequency stabilization.

the isolator is used to monitor the output power. A pm fibre splitter [Gooch & Housego] with a splitting ratio of 1:99 for each of the science laser distributes the main part of the light to the switching and distribution module shown in Figure 5.7. The smaller fraction is used for laser frequency stabilization. For this purpose it is guided towards a fibre based splitter system [custom assembly, Evanescent Optics] together with light from the reference laser (MO #1 in Figure 5.6 (a)). Light from the reference laser is split with a 10:90 ratio.

The smaller fraction is guided for frequency stabilization to the spectroscopy bench made of Zerodur shown in Figure 5.6 (b). The reference laser is stabilized using Doppler-free frequency modulation spectroscopy (FMS) to the $|F = 3\rangle \rightarrow |F' = 3/4\rangle$ crossover transition of ^{85}Rb (see Section 3.2.2). The fibre coupled input is collimated using a Zerodur collimator and is split in two beams. The first beam passes a rubidium gas cell and is retro reflected on a mirror. With a $\lambda/4$ wave plate in front of the mirror the polarisation of the initial and the reflected beam are orthogonal and the reflected beam is separated on a polarisation beam splitter and detected on a photo diode [S5971, Hamamatsu] (PD 2 in Figure 5.6 (b)). This beam produces a Doppler free absorption signal. The second beam passes the gas cell in a single pass, and a second photo diode (PD 1) detects a Doppler broadened absorption signal, that can be used to support laser locking procedures.

The photo diode is directly soldered to a printed circuit board (PCB) which is fixed with adhesive to the spectroscopy bench. To convert the photo diode current generated by the incident laser light in to a voltage signal, a transimpedance amplifier circuit is used. A frequency of 6.25 MHz is used to modulate the DFB injection current (this value originates from the clock frequency that drives the electronic cards). The bandwidth of the photo diode is higher than

the modulation frequency of the laser to be limited only by the photon shot noise of the detected beam. To make this high bandwidth possible, a low noise, high bandwidth operational amplifier [OPA657, Texas Instruments] is integrated, and the feedback capacity is obtained by an numerical simulation of the circuits noise behaviour using a model presented in [168]. The numerical simulation results in a shot noise limited 3 dB detection bandwidth of 30 MHz for the used beam power of 50 μW.

The main fraction of the light from the reference laser (MO #1) is guided into the splitter system and is split into four ports (see Figure 5.6 (c)). Three of these ports are superimposed with light from the three science lasers (MOPA #2-4) and generate beat-notes by guiding the light onto fast photo diodes [Hamamatsu, G4176-03]. The photo-diodes are directly glued to FC/APC collimators [60FC-4-M4.5S-02, Schäfter + Kirchhoff] attached to the fibre connectors of the beat splitter assembly outputs. Figure 5.6 (c) shows the beat splitter assembly. The science lasers are offset-locked to the reference laser using the generated beat signals.

5.3.3 Switching and distribution

The science laser light needs to be switched and distributed to the 11 optical fibres attached to the physics package. In addition the duration and intensity of the interferometry beams need to be timed and controlled. This is performed in a switching and distribution module shown in Figure 5.7, that is already described in [167] and thus will be only recalled here

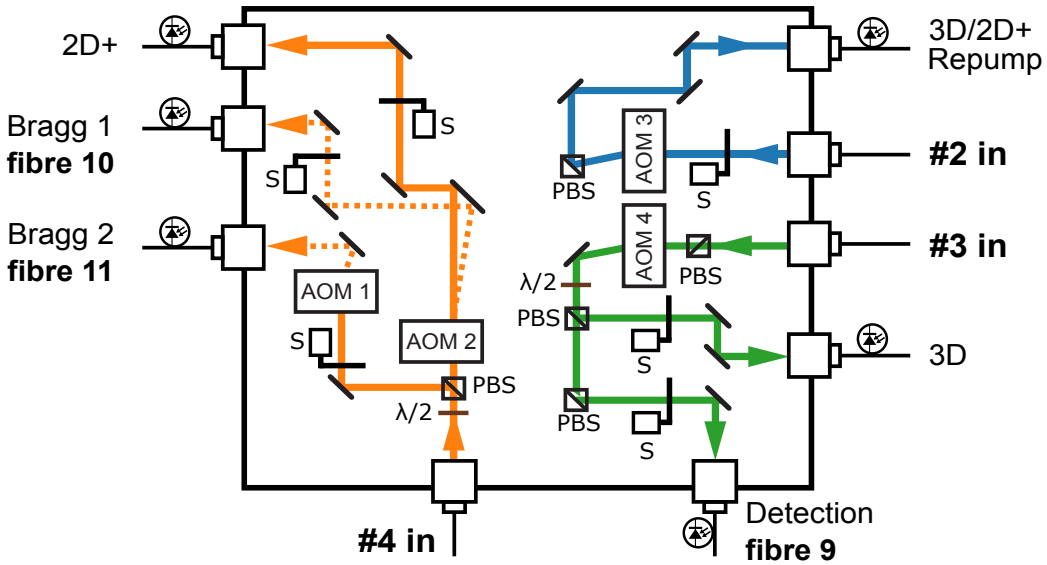

Figure 5.7: The MAIUS laser system switching and distribution module. Light from laser #2 is used as repumping light for the 2D+ and 3D MOT. Light from laser #3 is used for laser cooling in the 3D MOT and detection (fibre **9** used for detection is directly attached to the vacuum chamber). Light from laser #4 is split into two paths, both including an AOM. The 0-th diffraction order is used for the 2D+ MOT while the first diffraction orders of the two AOMs create the Bragg interferometry beams (fibres **10** and **11**).

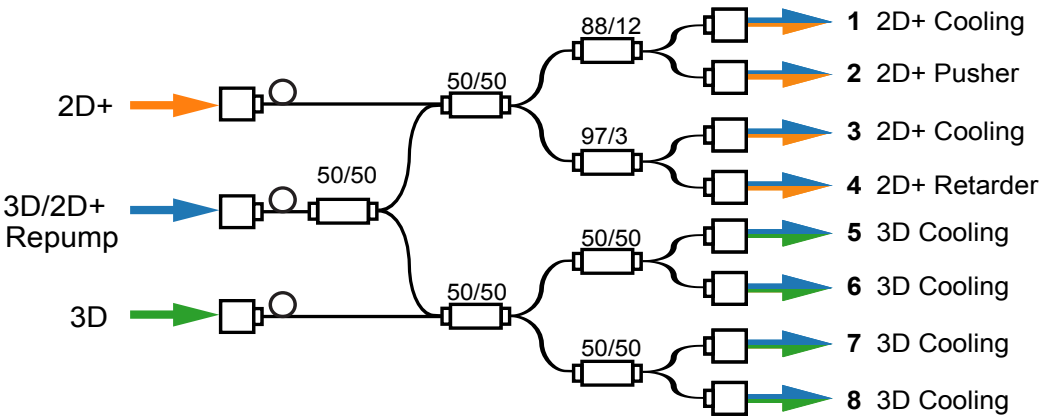

Figure 5.8: The fibre based distribution module overlaps the light from the science lasers used for laser cooling with repumping light in the desired intensity ratio for operation of the 2D+ MOT (fibres **1-4**) and the 3D MOT (fibres **5-8**).

briefly. The module is based on a Zerodur bench with a footprint of 210 mm $\times$ 180 mm. Light from each science laser (MOPA #2-4) is guided from Zerodur fibre collimators attached to the optical bench and is distributed over six pm fibre outputs using Zerodur couplers. Optical components like wave plate holders and mirrors are made of Zerodur and are directly glued to the board using a two component epoxy. Acousto-optical modulators (AOM) [3080-125, Crystal Technology, Inc] are used for fast switching and pulse shaping of the light while self-built optical shutters driven by a stepper motor [AM 1524-V-6-35-05, Faulhaber] are used for slow switching and total extinction of spurious stray light. Such a shutter is placed before every outputs coupler in the system (see Figure 5.7).

Light from laser #2 is used as repumping light for the 2D+ and 3D MOT. An AOM driven by 80 MHz (AOM 3 in Figure 5.7) is used for fast switching and the first diffraction order is coupled into a pm fibre. Light from laser #3 is used for detection and cooling in the 3D MOT. Therefore it is split into two paths with an adjustable ratio using a $\lambda/2$ wave plate and a polarizing beam splitter (PBS). The position of the wave plate is fixed with glue after initial adjustment. Light in both paths is switched using AOM 4 driven by a 80 MHz and coupled into pm fibres afterwards.

Light from the remaining laser #4 is used for 2D+ MOT cooling and for Bragg interferometry light. First, the light passes a combination of a $\lambda/2$ wave plate and a PBS and is split and passes an AOM each (AOM 1 and AOM 2). The zeroth diffraction order of AOM 1 is coupled into a pm fibre and is used for the 2D+ MOT cooling. On and off switching of the 2D+ MOT light, and thus the flux of the atomic beam to the 3D MOT is realized only with a shutter, since there is no need for fast switching. The first AOM diffraction order in every path is used for generation of the Bragg pulses. This is performed by driving the two AOMs with frequencies around 80 MHz and a difference of n·15 kHz [169], which corresponds to a multiple of the effective wave vector recoil for Bragg interferometry.

Intensity fluctuations in the fibres caused by thermal cycling by the on and off switching of

the AOMs cause fluctuations in the atom number of the 3D and 2D+ MOT. They also change the length for a π or $\pi/2$ Bragg pulse and have to be minimized for a stable operation of the experiment. To this end, the AOMs for the 3D+ MOT (AOM 4) and the repump and detection light (AOM 3) are kept in the on-state, while the shutters in front of the fibre couplers are closed. Before a light pulse is performed the AOMs are switched off followed by opening the shutters. A light pulse is then generated by the AOM, the shutter is closed afterwards and the AOM is switched on again. This procedure ensures, that the AOMs are in the on-state almost the whole sequence and their temperature is kept constant at $\approx 33\,^{\circ}\mathrm{C}$. This procedure can not be applied to the Bragg AOMs because the zeroth order of AOM 2 is needed for operation of the 2D+ MOT. Since the Bragg AOMs are used only for the short interferometry pulses the fibre coupling was maximized for pulsed operation.

Each of the six outputs in the switching and distribution module is monitored with the help of in-line photo diodes [OZ optics]. This allows for real time monitoring of the power levels and improves the diagnostics in the case of malfunction. Three of the six output fibres, one for detection (fibre **9**) and two for the Bragg pulses (fibres **10** and **11**) are directly guided to the physics package. The remaining three fibres, one for the 2D+ cooling, 3D cooling and 3D/2D+ repumping each are overlapped in a 3 to 8 fibre based splitter system (see Figure 5.8). This splitter system [custom assembly, Evanescent Optics] is designed to overlap the cooling and the repumping light and to distribute it to a final number of 8 fibres for the 2D+ and 3D MOT operation with a fixed intensity ratio.

The four beams for the 2D+ MOT, namely the two transverse cooling beams (fibres **1** and **3**), one pushing (fibre **2**) and one retarder beam (fibre **4**), have a ratio of 44%, 48.5%, 6% and 1.5% respectively. The polarization extinction ratio (PER) for every output fibre in the splitter system is specified to be greater than $-23\,\mathrm{dB}$. Four beams for the 3D MOT (fibres **5-8**) in the so called mirror-MOT configuration, where the atom chip surface serves as a retro-reflecting

fibre	usage	2D+	3D	3D/2D+ Repump
1	2D+ cooling	41 mW		4.31 mW
2	2D+ pusher	6 mW		0.62 mW
3	2D+ cooling	46 mW		4.43 mW
4	2D+ retarder	1.7 mW		0.17 mW
5	3D cooling		27.7 mW	2.59 mW
6	3D cooling		26.3 mW	2.53 mW
7	3D cooling		23.9 mW	2.43 mW
8	3D cooling		25.8 mW	2.65 mW
9	detection		7.1 mW	
10	Bragg 1	8 mW		
11	Bragg 2	35 mW		

Table 5.1: The individual output powers in each of the 11 MAIUS Laser system fibres. The output power was measured at the DFB diode current of 200 mA, a RW current of 200 mA and a PA current of 2000 mA. Date of the measurement was June the 17th 2015.

element for two 3D MOT beams [155] are used. They have a symmetric splitting ratio of 25%, 25%, 25% and 25% .

The laser system provides 94.7 mW and 9.5 mW fibre coupled light for cooling and repumping to the 2D+ MOT and 103.7 mW and 10.2 mW for the 3D MOT. Each Bragg interferometry beam has more than 8 mW of power and for the detection 7.1 mW are available. The individual light powers in each fibre are shown in Table 5.1. The power levels were measured at the diode laser module's working point (DFB diode current of 200 mA, RW current of 200 mA and PA current of 2000 mA).

5.3.4 Laser system assembly

The subsystems, namely the micro-integrated diode laser modules, the optical isolators, the Zerodur spectroscopy bench, the switching and distribution board, the fibre splitters and splitter assemblies together with the electronics for beat detection were integrated into one housing. This housing provides electrical interfaces to the electronic module, mechanical interfaces to the hull of the rocket and 11 pm fibres as the optical interface to the vacuum chamber.

The central structure is a water cooled base plate used as a heat sink. It was designed to limit the maximum temperature increase to 2.5 K during the flight, where water cooling is only available until lift off. For laboratory operation convection cooling is sufficient to operate the system without water cooling. All laser modules in the system are mounted to the top side (in the flight direction of the rocket) as shown in Figure 5.9 (a). The MIOB has integrated surface mount connectors. MML miniature coaxial connectors [MML type H2.5, H2.0 and

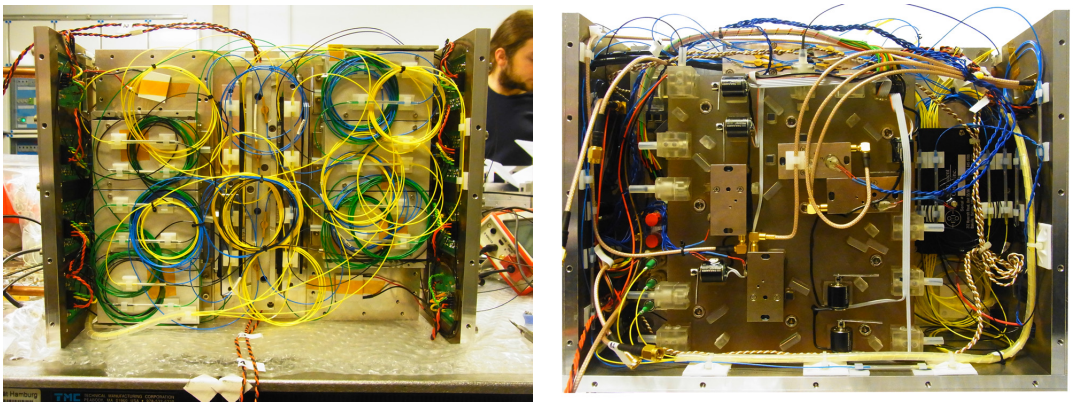

(a) **(b)**

Figure 5.9: The MAIUS laser system during assembly. (a) The laser modules are mounted on the top side of the heat sink (left and right). Every module is protected from falling objects by a cover that is also used to fix the optical fibres and the splice protection tubes. Four fibre coupled optical isolators are mounted in the central structure (in the middle between the laser modules). (b) The bottom side of the heat sink contains the switching and distribution board (in the middle), the spectroscopy bench (top left), the fibre splitter systems on top of each other (right) and the fibre collimators with the attached beat photo-diodes (bottom left).

H1.5, Radiall] are used to apply current to the laser diode and the ridge wave-guide and to connect the thermistors, while two small coaxial connectors [MMCX series, Huber+Suhner] are used for the PA current. Interface PCBs mounted behind the laser modules route each current to an SMA connector and the thermistors together with the Peltier element to a single D-SUB 9 connector.

The interface PCB board also features a large area photo diode [S1223, Hamamatsu] to monitor the power of the collimated rear output of each laser module. The coaxial cables are routed in two cable ducts on both sides of the laser module. This cable ducts are also used as a support structure for a front and top cover to protect the laser modules from dust and other falling objects during integration and inspection. The front cover is also used for mounting of the optical fibres together with the splice protection tubes. The output of the laser modules is spliced to the input port of the optical isolator and the outputs are routed to the bottom side of the heat sink. Figure 5.9 (a) shows the top side of the laser system.

On the bottom side, the switching board, the spectroscopy bench, both fibre splitter assemblies (one for distribution and one for frequency stabilization) and the RF components for beat signals are mounted. The two Zerodur boards are screwed to the heat sink on a rubber pad to prevent the Zerodur boards from cracking. SMA cables connect each beat photo diode to a Bias Tee and RF amplifiers, mounted on the bottom cover of the laser system. The high amount of wires for the in-line photo diodes, thermistors and shutters are routed to D-SUB crimp connectors located on the sides of the laser system housing. Using crimp connectors avoids soldering close to the optical elements and eases the integration process. All cables and fibres are fixed with cable straps or glue to prevent them from moving into one of the optical beam paths. Figure 5.9 (b) shows the bottom side of the laser system.

The assembled MAIUS laser system has dimensions of 340 mm×274 mm×227 mm and a total mass of 27 kg. The top and bottom plate can be removed to access all components. To mount the laser system to the inner hull of the rocket, an adapter plate is used. The assembled MAIUS laser system is shown in Figure 5.10 (in the rocket configuration the orientation of the laser system is reversed).

The assembled laser system was subjected to a vibration test at the acceptance level of 5.4 g_{RMS}. This test has to be performed and passed prior to the integration into the rocket structure. All components already successfully passed the qualification vibration test of 8.1 g_{RMS} hard-mounted to the shaker. The micro-integrated diode laser modules passed even a vibration test with 29 g_{RMS} [163].

For the vibration test, the MAIUS laser system was mounted with shock mounts (flight configuration) into a test hull. The test is composed of a resonance scan in the 5- 2000 Hz frequency band with an amplitude of 0.25 g and a sweep rate of 2 oct/min for each axis. This resonance scan is followed by the random vibration test corresponding to 5.4 g_{RMS} with a duration of 60 s. A second resonance scan identifies mechanical changes in the structure and completes the test procedure. After the vibration test the optical power of all fibre outputs have been compared to measurements performed before the transportation to the shaker facility and showed an average decrease of 1.2 %.

5.3.5 Integration into the MAIUS rocket payload

The MAIUS laser system was transported to the Institut für Quantenoptik, Leibniz Universität Hannover, where the vacuum system and the electronic module were constructed. The integration of the complete payload and its operation also takes place there. While the vacuum system was assembled and operated with a ground laser system and ground electronics, the integration of the laser system with the flight electronics was performed.

This includes a first operation of the individual flight electronic cards using a control interface in LabVIEW. The optimization of the parameters for operation with the laser system, and the assembly of the cards in the final configuration on a ground test bed. Before the laser system electronics were integrated into the rocket hull, a 3D MOT loaded from the 2D+ MOT using the MAIUS laser system was realized.

After the completed integration of the payload subsystems (see Figure 5.2) into the rocket hull, their combined operation started. After optimization, the first BEC with the complete flight payload (laser system, electronics and vacuum chamber) was created. The complete operation, including the experimental sequence was performed with the MAIUS flight software. An absorption imaging of a BEC created by this system is shown in Figure 5.11.

5.4 Summary and the next steps

The design, assembly and integration of a laser system for the MAIUS sounding rocket mission was presented. Its compact size and robustness will be used to perform atom interferometry

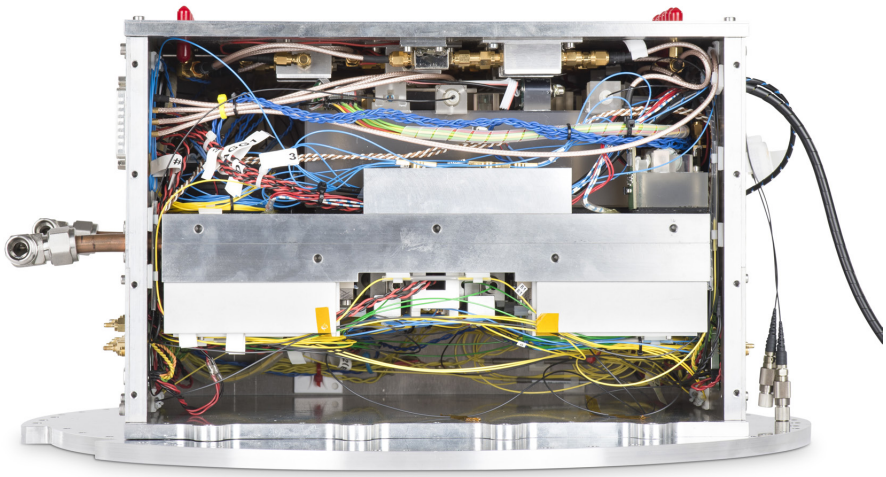

Figure 5.10: The assembled MAIUS laser system with one housing wall removed. The Zerodur bench for switching and distribution and the spectroscopy bench are mounted on top. The top side also houses the fibre splitter assemblies and the beat detection. The laser modules are mounted on the bottom side of the water cooled heat sink with the connectors located on the left side. The dimensions are 340 mm×274 mm×227 mm with a total mass of 27 kg.

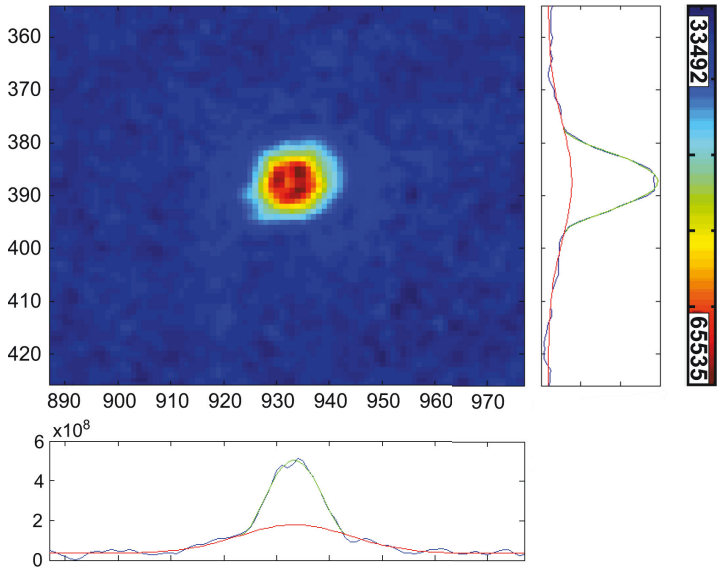

Figure 5.11: An absorption image of a Bose-Einstein condensate produced with the MAIUS payload in flight configuration. The x and the y axis correspond to the number of the individual pixels of the CCD camera. The optical density in arb.u. is colour coded (blue corresponds to low and red to high density). The integrated density per each axis is displayed in a line plot. A bimodal density distribution is visible. A Gaussian distribution of thermal atoms is shown as a red line and the Thomas-Fermi distribution, typical for a BEC, is shown as a green line. After conversion to atom density the generated BEC contains 2×10^4 atoms.

during a sounding rocket flight scheduled for winter 2016. In Mai 2016 the MAIUS payload was already integrated into the rocket hulls and operates with the flight electronics and the flight software. The automatized experimental sequence that optimizes the BEC creation and Bragg atom interferometry is optimized and implemented in the near future. The next steps include a final environmental test of the assembled rocket and the transportation to the launching side Esrange, Sweden.

To qualify the technology developed for the MAIUS mission, namely the micro-integrated diode laser modules and the Zerodur assembly technology, three sounding rocket payloads in total were designed, build and successfully operated on rocket flights during this thesis. The first payload that were launched on-board the TEXUS 51 sounding rocket contained a DFB diode laser and a spectroscopy bench equally to the one used in MAIUS. The module remained fully operational and showed a frequency stability suitable for atom interferometry over the complete time of the rocket flight. Two additionally payloads, one of which contained narrow linewidth diode lasers, were both successfully launched on the TEXUS 53 rocket 8 months after the TEXUS 51 mission.

This sounding rocket experiments paved the way for a success of the MAIUS mission and future space based missions in general aiming to test the foundations of general relativity like the Universality of Free Fall or the Local Position Invariance. This experiments are described

in the next chapter.

6 Precision spectroscopy in space

Chapter 4 demonstrated the high sensitivity and stability of a gravimeter based on atom interferometry. The performance demonstrated on Earth can even be further improved by multiple orders of magnitude by space operation. The weightlessness in the free falling reference frame of a space vehicle allows for extended free evolution times T where the sensitivity scales with T^2.

The previous Chapter 5 introduced MAIUS, an atom interferometer that will operate on a sounding rocket. To perform such experiments in space, the technology used in atom interferometers, for example the laser system has to be compact, robust and autonomously operating over the time frame of such a space mission. To test of the laser technology used in MAIUS before the actual start of the mission, will deliver useful information about the laser technology readiness.

Beside their use in atom interferometry, frequency stabilized laser can be used in space to test the postulates of the Einstein Equivalence Principle (EEP) (see Section 1.1). Lasers can be interpreted as clocks and the comparison of the "ticking rate"of such two different clocks in a changing gravitational potential represent a test of the Local Position Invariance.

In this chapter the FOKUS sounding rocket mission, the first frequency comparison between an optical and a microwave clock in space, will be presented. This experiment represents a pathfinder mission for a future LPI test in space. For this purpose a frequency stabilized laser, that can also be used as an optical frequency reference for atom interferometry in space, was realized and successfully operated in space using a developed automated locking scheme.

First an overview over the FOKUS project will be given, second the subsystems with focus on the optical frequency reference module will be introduced and third, a summary of the launch campaign in April 2015 including a presentation of the results is shown. Two additional sounding rocket payloads, namely FOKUS Reflight and KALEXUS are also presented. Each of this two payloads contained improved or new developed components and stabilization schemes to improve the performance of future experiments.

6.1 Gravitational redshift test with clocks

One of the consequences of general relativity (GR) is the existence of a gravitational redshift. The frequency difference $\Delta\nu$ between two clocks running at frequency ν (with a clock we associate in this context electromagnetic radiation in general) at two points with a gravitational potential difference ΔU is [31]

$$\frac{\Delta\nu}{\nu} = \frac{\Delta U}{c^2}. \tag{6.1}$$

Thus, tests of the gravitational redshift can be performed by measuring the change in relative frequency of an atomic clock in a changing gravitational potential, with an identical second one in rest. The most precise test of this kind is Gravity-Probe A performed in 1976 [170]. A hydrogen maser on a rocket, reaching a height of 10000 km was compared with a reference maser on ground. The predicted gravitational redshift was confirmed with an accuracy at the 7×10^{-5} level.

However, this test type is hard to perform on the fractional instability level of 2×10^{-18} after 10000 s reached by today's optical clocks [28], because it suffers from two major drawbacks. First, a continuous optical or microwave link on this level has yet to be demonstrated and second, this level of instability requires a precise knowledge of the relative position of the two clocks to each other. From Equation 6.1 follows, that a height difference of 1 cm on earth produces a relative frequency shift of 10^{-18}. Using the full potential of optical clocks for an LPI test requires to track the clock's position on the cm level. A differential measurement with two different clocks at the same position moving through a varying gravitational potential, does not have these limitations.

The third postulate of the EEP in Section 1.1, the Local Position Invariance (LPI), postulates that "clock's rates are also independent of their space-time positions"[8]. If the performed experiment is such a differential measurement between two clocks, the LPI implies that the gravitational redshift is identical for every clock independent of its internal structure. Clock comparisons between two different clocks at the same gravitational potential, are called "Null redshift tests"since no change in the clock comparisons is expected when GR holds. In the case of a violation of the GR a parameter β is introduced. The β parameter describes the deviation from general relativity and is predicted to depend on the clocks internal structure (nuclear and electron structure i.a.) by several alternative theories of gravity [12]. Equation 6.1 becomes

$$\frac{\Delta\nu}{\nu} = (1+\beta)\frac{\Delta U}{c^2}. \tag{6.2}$$

With two different clocks, both located at the same position and moving in a changing potential it becomes

$$\frac{\Delta\nu_1}{\nu_1} - \frac{\Delta\nu_2}{\nu_2} = (\beta_1 - \beta_2)\frac{\Delta U}{c^2}. \tag{6.3}$$

Here ν_1 and ν_2 are the frequencies of the two clocks and β_1 and β_2 the deviations from GR. Every change in the difference of relative frequencies directly indicates a violation of general relativity and does not requires a precise knowledge of the change in the gravitational potential at all. (This holds if both clocks are located so close to each other that the gravity difference between their positions is negligible). By measuring the difference frequency of the two clocks, the Equation 6.3 becomes

$$\frac{\Delta\nu_1}{\nu_1} - \frac{\Delta\nu_2}{\nu_2} \approx \frac{\Delta\nu_{12}}{\nu} = (\beta_1 - \beta_2)\frac{\Delta U}{c^2}, \tag{6.4}$$

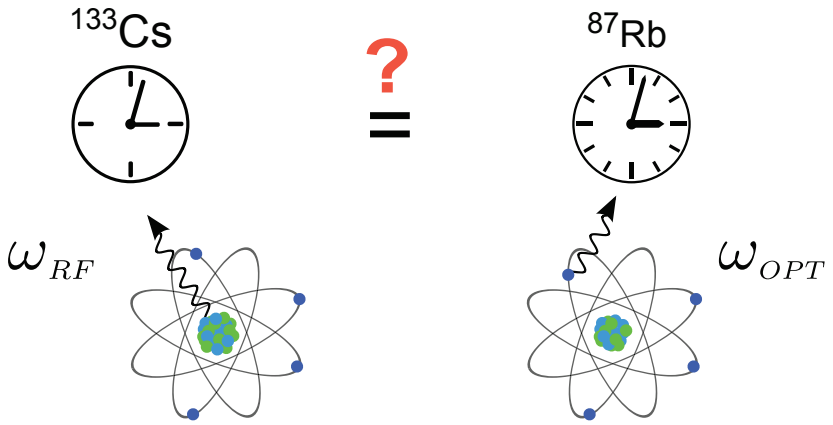

Figure 6.1: The clock comparison scheme for the FOKUS mission. A radio frequency transition ω_{RF} in ^{133}Cs is compared to an optical transition ω_{OPT} in ^{87}Rb. The two clock transitions are based on two different interactions. The radio frequency transition is based on a magnetic dipole transition while the optical frequency is based on the electric dipole transition.

where $\Delta\nu_{12}$ is the frequency difference of the two clocks. This conversion requires that the difference frequency of the two clocks can be directly measured ($\nu_1 \approx \nu_2 = \nu$). An instrument that can do exactly that even for two frequencies in the microwave and optical domain, namely a frequency comb, is introduced later in this chapter. The LPI can therefore be tested by measuring directly the frequency difference between two internally different nearby clocks in a changing gravitational potential.

The best Null test of the LPI to date is based on evaluating the frequency difference between caesium and rubidium fountains who contribute to the global time scale and are operating almost continuously for many years. Since the Earth is moving on an elliptical orbit around the sun, the gravitational potential is modulated with an amplitude of $\Delta U/c^2 \approx 1.6 \times 10^{-10}$ over a period of a year [171]. No annual variation of the frequency difference was found within the limits of statistical uncertainty of the clocks, leading to an upper limit of $(-2.7 \pm 4.9) \times 10^{-7}$ for the β_{12} value for hyperfine transitions in ^{87}Rb and ^{133}Cs [171].

According to Equation 6.4 this result can further be improved in two ways. First, one can use clocks with a higher precision (improving $\Delta\nu_{12}/\nu$) or second, one can use space missions with a highly elliptical orbit around the sun (increasing $\Delta U/c^2$). A prototype experiment of the second type was performed during this thesis. The clock comparison scheme is shown in Figure 6.1. A laser, stabilized to an optical transition is compared to a caesium microwave clock using a frequency comb, during a rocket flight. This first optical to microwave clock comparison in space is presented in detail in the following chapter.

6.2 Measurement principle

To perform a clock comparison in space, two different clocks and a frequency counter to count their frequency difference are needed. In the microwave domain up to 100 GHz, frequency

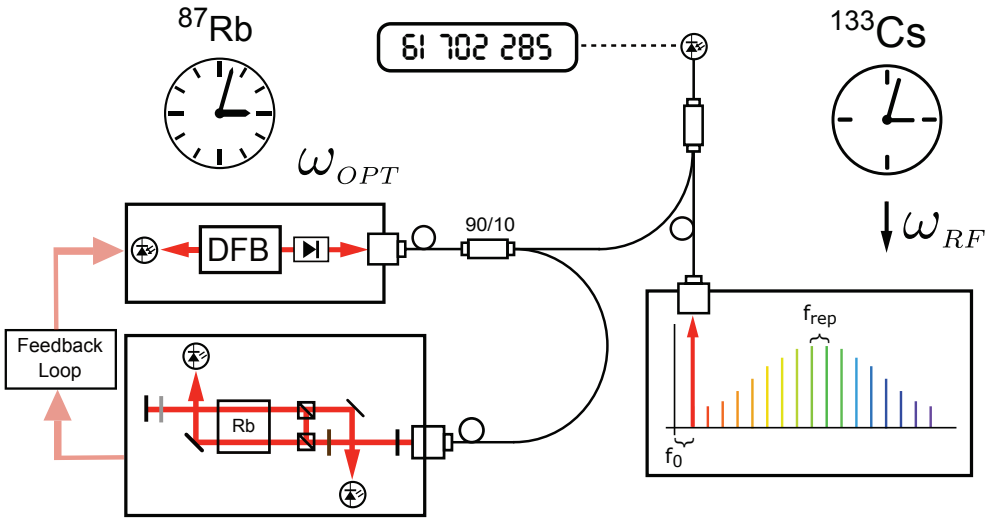

Figure 6.2: Experimental scheme for the first clock comparison, a null LPI test in space. (left) The frequency of a diode laser is stabilized to an atomic transition in a rubidium gas cell and the optical frequency is measured via a frequency comb. (right) The comb is referenced to a microwave clock based on a hyperfine transition in caesium.

counters based on semiconductor technology are available. However, optical frequencies going up to 1000 THz can not be counted directly. Only when compared with another known frequency close to the frequency to be measured, their difference frequency can be counted in the microwave domain. The prototype clock comparison experiment in space presented in this thesis called FOKUS (Fibre-Optical Comb-generator Under Microgravity, german acronym FaserOptischer Kammgenerator Unter Schwerelosigkeit) uses a frequency comb to compare the microwave clock with an optical frequency reference. The experimental scheme of the FOKUS experiment is presented in Figure 6.2.

A DFB diode laser is fibre coupled and a small fraction of the light is used to generate a Doppler free spectrum in a rubidium gas cell and is stabilized to one of the transitions using frequency modulation spectroscopy (FMS) [102]. The remaining light is combined with the comb output to generate a beat note. The frequency comb as well as the counter for the beat note are referenced to a microwave clock [SA.45s CSAC, Symmetricon]. The beat note is used as a direct measure of β_{12} with the relation given in Equation 6.4.

6.3 Sounding rocket payload for the TEXUS 51 mission

This section presents the individual parts of the FOKUS payload for the TEXUS 51 mission. The general working principle of a frequency comb and the fibre based frequency comb used in the payload are introduced, followed by a description of the rubidium module providing the optical reference for the test. The section ends with a qualification of the system performance. Figure 6.3 gives an overview of the complete FOKUS payload. A water cooled heat sink is

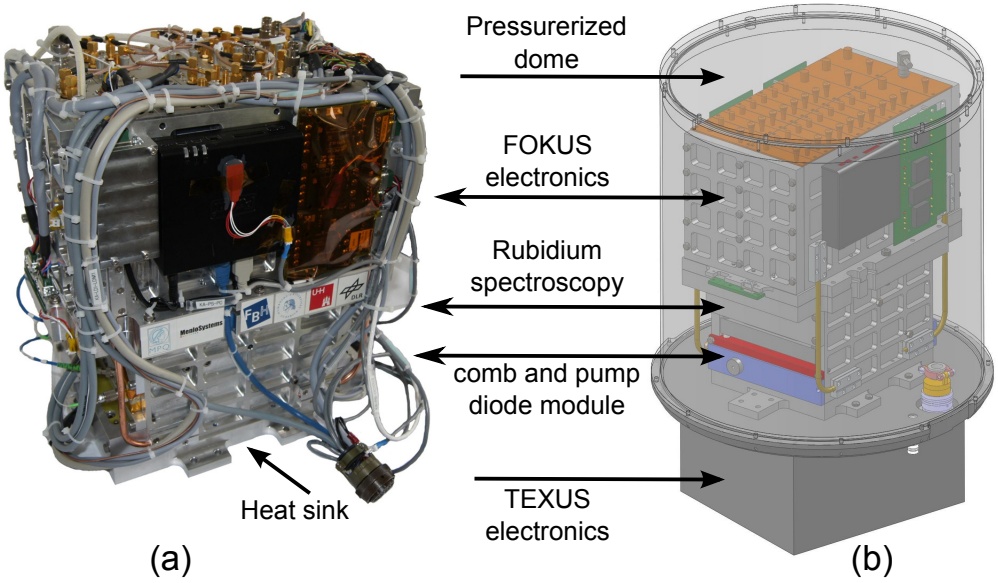

Figure 6.3: The assembled FOKUS payload **(a)** and the CAD drawing of the FOKUS payload **(b)** including the pressurized dome (half -transparent). About two thirds of the overall volume is assessed by the electronics. The fibre frequency comb module, the pump laser diodes and the rubidium spectroscopy module are positioned close to the water cooled heat sink (till lift off). The dimensions of the payload are 310 mm x 200 mm x 480 mm with a total mass of 23 kg. Pictures provided by Menlo Systems.

used for temperature stabilization of the fibre frequency comb and the pump diode module. The FOKUS electronics use about two thirds of the total payload volume. The rubidium spectroscopy module is located between the electronics and the frequency comb. The FOKUS frequency comb is described below.

6.3.1 Fiber frequency comb

Accurate frequency measurements are based on linking the frequency of interest to the frequency of the caesium hyperfine structure, since it is the definition of the second and thus of frequency. In the microwave domain, this task can be performed using frequency synthesisers. Measuring optical frequencies relied for a long time on so called “frequency chains ”, where an enormous amount of oscillators spanning the whole spectrum from RF to optical are linked to each other, by successively phase locking one oscillators frequency to a harmonic of the other. The later was created using non-linear conversion, resulting in harmonic, sum or difference frequency generation of the oscillators involved. These chains were dedicated for a specific optical frequency and could operate uninterrupted only for minutes [172] due to their high complexity.

The problem of the dedicated and high complex frequency chains has been solved by the rapid progress in mode locked femto-second pulse lasers in the 90s. A (Fourier limited) short

pulse in the time domain can be represented as a broad pulse in the frequency domain, linking the FWHM (full width at half maximum) pulse duration $\Delta\tau$ to the FWHM spectral pulse width Δf via

$$\Delta f \approx \frac{1}{\Delta\tau}. \tag{6.5}$$

If the pulse is realized inside a laser cavity with an optical length of L, than the pulse is composed of discrete frequencies spaced by the free spectral range of the cavity $FSR = c/2L$. If the phases of these modes are arbitrary, the laser operates in the chaotic continuous-wave regime, however if the modes have a particular fixed phase relationship they interfere and form a short and high intensity laser pulse, where the intensity and the inverse pulse duration scale with the number of modes involved. The frequency f of the n-th comb line can then be written as

$$f = f_0 + n \cdot f_{rep} \tag{6.6}$$

where f_{rep} is the spacing of the comb lines and f_0 the displacement of the first comb line from zero (modulo f_{rep}). Both parameters usually range from some MHz to some GHz and can be stabilized to a microwave source using phase locked loops. Titanium-sapphire laser or Ti:Sa-Laser quickly became the workhorse for creating frequency combs. Their high emission bandwidth of $\approx$ 100 THz makes a Ti:Sa-Laser perfectly suitable for mode locked operation, since high bandwidth ensures a high number of modes and thus short and high power pulses [173]. The solid state Korund (Al_2O_3) -crystal that is doped with Titanium ions (Ti^{3+}) offers another useful feature for mode-lock operation, an intensity dependent refractive index called Kerr effect [174]. The light in the crystal is focused stronger for high intensities, which can be used to obtain mode locked operation by placing an aperture behind the crystal. Low intensity cw operation experience a strong attenuation in the resonator and is thus suppressed and the high intensity mode-locked operation is initiated.

As stated before, the comb has two parameters, f_{rep} and f_0, that both can be referenced to a frequency in a microwave domain. The two parameters f_0 and f_{rep} can be locked mostly independently. The repetition rate f_{rep} can be directly detected by shining light on a fast photo diode. This signal appears as an RF signal comb with the a spacing f_{rep}. By filtering one RF comb line with a band pass filter, the rep rate can be phase stabilized to an RF reference by changing the optical cavity length via one of the cavity mirrors attached to a piezo actuator. Using a low locking band width of $\approx$ 100 Hz, the low phase noise of the comb at Fourier frequencies above 100 Hz is undisturbed and the low phase noise of the RF reference is transferred to the comb at Fourier frequencies below 100 Hz [175].

The offset frequency f_0, often also called as the carrier–envelope offset (CEO) frequency is the second free parameter of the comb. The offset is caused by the chromatic dispersion in the laser cavity [176]. It can not be detected like the repetition rate f_0 by a photo diode, because only the difference frequencies of the comb lines appear in the RF spectrum. However, a so called f - 2f interferometer offers a direct access to the offset frequency. If the comb spectrum is at least one optical octave wide, the low frequency part $f_0 + nf_{rep}$ can be frequency doubled

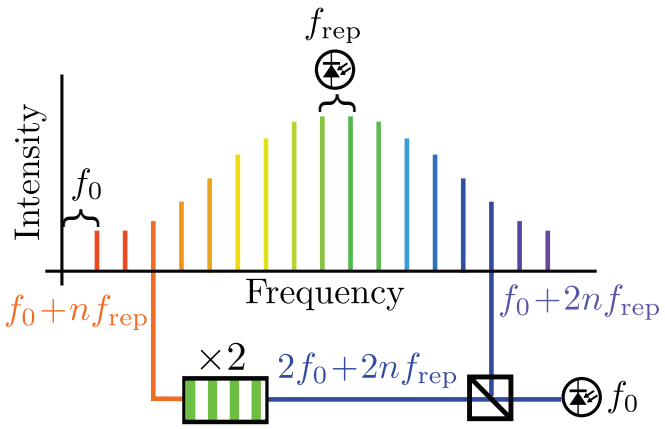

Figure 6.4: The working principle of a self referenced frequency comb. The repetition rate f_{rep} can be detected directly from the comb output on a photo diode. For the carrier envelope offset f_0 the low frequency part of the octave spanning comb is frequency doubled in a non linear crystal (2x in the Figure) and overlapped on a photo diode with the high frequency part. The beat signal contains now f_0 besides f_{rep} and higher harmonics that are filtered away.

to $2f_0+2nf_{rep}$ in a non-linear crystal and overlapped with the high frequency part f_0+2nf_{rep} on a photo diode. The resulting rf spectrum reveals the difference frequencies of both parts of the spectrum $2f_0+2nf_{rep}-f_0-2nf_{rep}=f_0$ and thus gives access to the offset frequency f_0. The offset frequency can then be phase locked to a rf reference by adjusting the dispersion in the laser cavity. This can be done by changing the pump current of the Ti:Sa-Laser or tilting a prism inserted in the cavity set-up for example. The needed spectral broadening of the pulse can be accomplished by sending the pulse through a highly non-linear medium. A convenient way is to use a so called Photonic-crystal fibre (PCF), that guides the light through a pattern of holes in a fibre, thus ensuring a very high intensity needed for the non-linear process of spectral broadening [177].

The frequency comb with stabilized repetition rate and offset frequency offers a ruler of equally spaced narrow frequency lines spanning a wide spectrum in the optical domain. Its stability and accuracy is determined only by the rf reference and allows for a direct measurement of optical frequencies [176]. The theoretical and practical work, that led to the first realisation of the frequency comb was awarded with the Nobel Prize in the year 2005 [178]. Despite its prevalent use in today's laboratories the Ti:Sa-Laser based frequency comb is still to sensitive to environmental parameters to be used in a space mission, due to its design based on free space optics. A fibre based frequency comb that is able to operate during a sounding rocket flight, that was used for the TEXUS 51 mission is presented below.

Fibre based set-ups are intrinsically stable and can be made compact and robust. Furthermore, the rapid progress in the telecommunication technology, that uses fibre optics for data transmission led to highly reliable optical components in the Telecom wavelength window reaching from $\approx$1260 nm to $\approx$1675 nm. These components are available of the shelf.

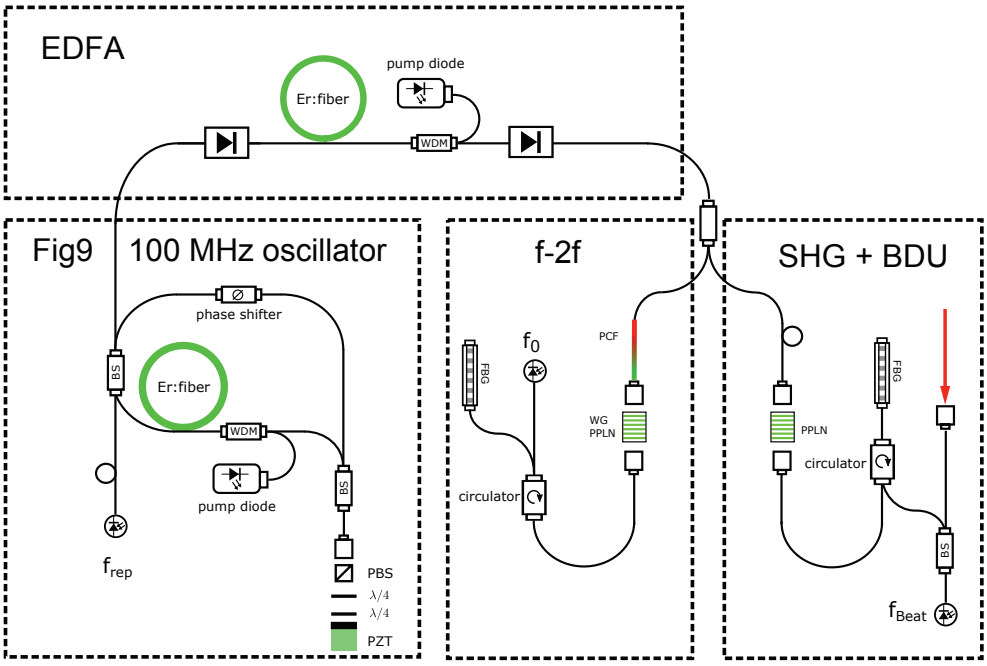

Figure 6.5: The FOKUS fibre frequency comb scheme. The Fig-9® oscillator operating at 100 MHz is amplified in an erbium doped fibre amplifier (EDFA). The repetition rate is directly detected on a fast photo diode. The carrier offset frequency is detected in a f-2f interferometer. For beat detection with laser light at 780 nm light from the oscillator is frequency doubled by second harmonic generation (SHG). See text for details. Scheme adapted from [179].

The comb oscillator is based on the Fig-9® design by Menlo Systems (US Patent [180]), a non-linear amplified loop mirror oscillator [179, 181]. A schematic overview of the frequency comb is shown in Figure 6.5. Due to a fibre amplifier in the loop, a non-linear phase shift is present in the loop. By appropriate polarisation control in the loop only a high intensity pulse is transmitted and the comb is mode locked. For more details see the US Patent [180].

The fibre system has a design repetition rate of 100 MHz and operates with the gain medium Erbium at a centre wavelength of 1560 nm. The frequency can be slowly tuned over a wide range by changing the temperature of the comb housing and thus the length of the cavity formed by the fibre loop. The necessary fast tuning for locking the oscillator length is performed in a short free space area where the retro reflector mirror is attached to a piezo element. Light from the pump diode is coupled into the fibre amplifier via wavelength-division multiplexing (WDM) couplers, while fibre splitter couple a fraction of the light for rep-rate detection and for further amplification in an erbium doped fibre amplifier. After the amplifier the obtained pulse power is sufficient for spectral broadening, needed for the f-2f interferometer, in an periodically poled Lithium-Niobate ridge wave guide. A small part of the light after the amplifier is split and frequency doubled in a second Lithium-Niobate wave guide generating light centred at 780 nm for beat detection with the Rb light. The setup is completely based on polarization maintaining components and is encapsulated in space-grade silicon rubber to

reduce vibrations and ensure good thermal coupling [179]. The complete comb module has dimensions of 220 mm x 142 mm x 25 mm. The separate modules for two butterfly pump diodes each have dimensions of 112 mm x 170 mm x 32 mm. The comb has a fibre input for cw-laser light coming from the rubidium module which is presented in the next subsection.

6.3.2 Rubidium spectroscopy module

While the frequency comb provides light referenced to an rf reference, the Rubidium module delivers light stabilized to an optical transition in rubidium. A distributed feedback (DFB) diode serves as the laser source. The laser module is the same as the one used in MAIUS (see Section 5.3.1).

The fibre coupled light passes a 90/10 polarization maintaining (pm) fibre splitter [Gooch & Housego]. The larger light fraction is used for beat detection with the frequency comb and the lower fraction of the light is guided to the spectroscopy bench. This spectroscopy module is a duplication of the module used in the MAIUS laser system (see Section 5.3.2). The rubidium cell is enclosed in one layer of mu metal foil. The module is shown in Figure 6.6

The laser diode current is modulated by an external 10 MHz signal generated by the same oscillator used for stabilization of the frequency comb. Since both, the pump and the probe beam are obtained from the same modulated laser, the error signal in this frequency modulation spectroscopy (FMS) method differs from the MTS signal, and shows strong absorption peaks

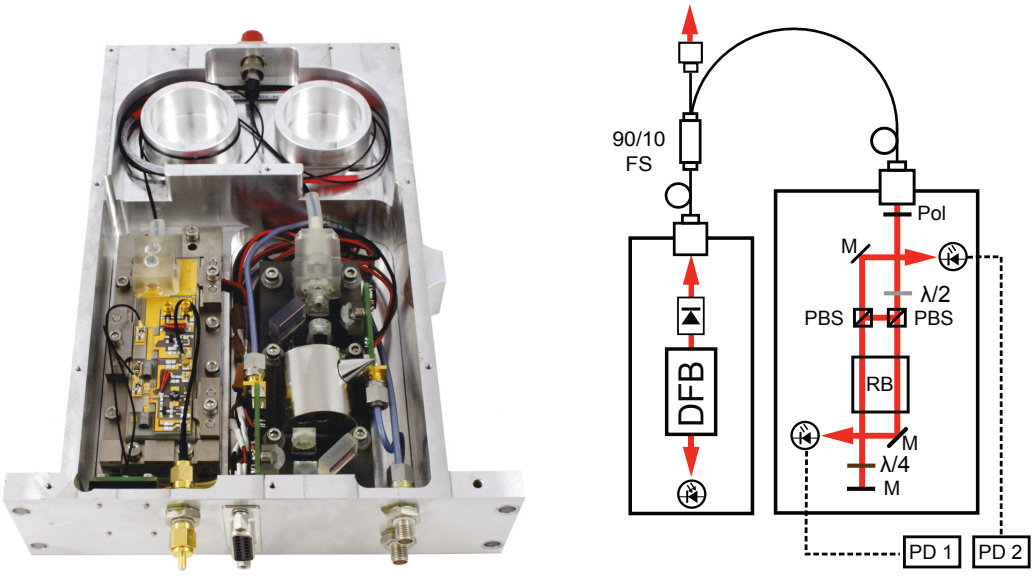

Figure 6.6: The FOKUS rubidium spectroscopy module with removed cover (left) and the optical scheme (right). The laser module on the left is fibre coupled and a small fraction of the light is guided to the spectroscopy optical bench on the right. The remaining light is used for the beat detection with the frequency comb via a fibre connector on the back side. The electronic interfaces are on the front side.

for the possible transitions and a Doppler broadened background. The photodiode signal is separated outside the spectroscopy module via a Bias-Tee, the DC-part of the signal is directly monitored while the AC-signal is amplified, filtered and mixed with a second 10 MHz signal with an adjustable phase. For a more detailed description of the microwave signal part, see Section 3.2.2 where a similarly method is described to demodulate an error signal. The error signal is fed to a PID circuit (lock-box) to stabilize the error signal and thus the laser frequency to a fixed value. The algorithm for the locking procedure to a desired transition was developed during the project and is presented next.

6.3.3 Electronics and control

The flight electronics to control the rubidium module and the frequency comb are adapted systems based on Menlo Systems Synchro platform [179]. They are mostly analogue electronics, for temperature control, low noise current drivers, PID lock-boxes, beat detection and frequency counting boards. Values that need to be controlled (temperature set points, current set points, PID feedback values etc.) are generated with DAC converters and values that are monitored are converted with ADCs. The FOKUS software (python based) runs on a rugged compact microcomputer [Pokini] based on the Intel Atom Z550 CPU, with a Windows operating system. To write and read values to and from the electronic boards a computer programmable logic device (CPLD) is used. The operating speed of the CPLD limits the data rate of the system to ≈ 3 Hz. Most of the data can be down streamed to the operators during flight, while all data send to the Pokini are stored on a internal SSD drive.

Digital feedback loops are used for rough control of the repetition rate and the CEO frequency and are switched to analogue ones when they are within their capture range. A similar approach would be desirable for stabilization of the rubidium frequency to a transition of choice. In contrast to the error signal of the rep rate and CEO, which are highly linear and feature only a single locking point in the operating range, the error signal generated by the FM spectroscopy has multiple locking points spaced very closely together (see Figure 6.7). In addition the laser's unlocked frequency is drifting on short time-scales (1-100 seconds) considerably more than the spacing of two neighbouring transitions and can exceed several 100 MHz for longer time-scales (from 100 seconds). To distinguish one locking point (one optical rubidium transition) from another a current scan with enough data points is one possible approach. However, after one scan that is wide enough to reach, detect and resolve multiple transitions ≈ 1000 data points are needed. Recorded with a rate of 3 Hz the rocket flight would be almost over before the scan is finished. The laser frequency drift during this time makes it a gamble to go to a calculated current value and stabilize to the desired transition.

To overcome this limitation and reduce the failure possibility of the mission a robust locking algorithm was developed during this thesis. The main idea is to utilize the natural abundance of ^{87}Rb and ^{85}Rb ($\approx 27.8\,\%$ and $\approx 72.2\,\%$ [79]) and their respective $F = 2 \rightarrow F'$ transitions which are spaced by ≈ 1200 MHz. Figure 6.7 shows the absorption and the FMS error signal of the transitions mentioned above. Between the two respective F=2 to F' transitions the Doppler broadened absorption signal, which is overlapped with the Doppler free absorption signal in the FMS method, appears a local transmission maximum and thus a moderate slope

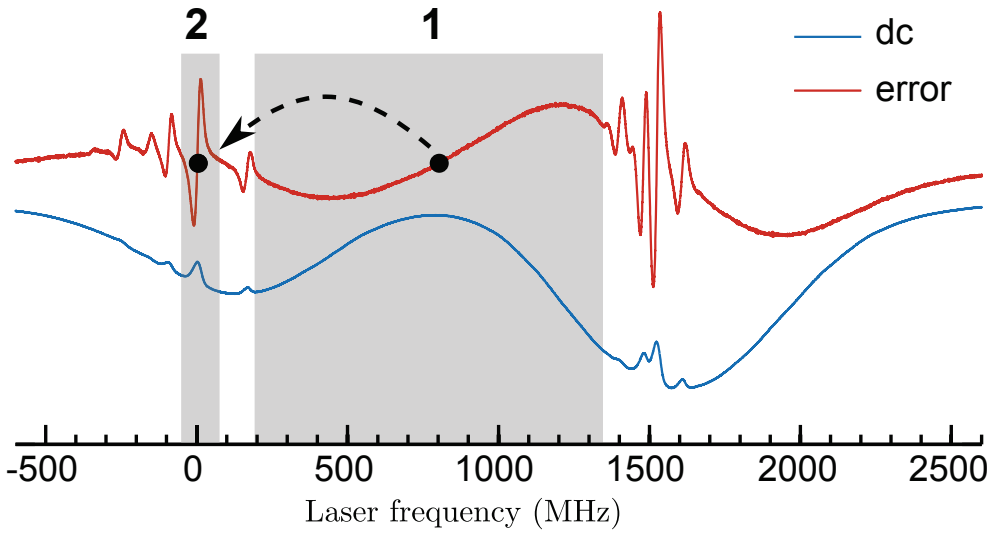

Figure 6.7: The FOKUS locking scheme developed for autonomous frequency locking during a rocket flight. A moderate slope with a wide locking range between the ^{85}Rb $F = 2 \rightarrow F'$ and the ^{87}Rb $F = 2 \rightarrow F'$ manifold is used for stabilizing the DFB laser to an intermediate locking point (**1**). Using a current jump the laser is stabilized to the steep slope of a Doppler free transition in ^{87}Rb (**2**). The grey shaded areas indicate the respective locking ranges.

in the FMS error signal. This slope ranges over the spacing between the two isotopes that corresponds to a high locking range. Laser frequency's being in this range can be locked to the middle of this slope by activating the PID feedback loop. This range of $\approx$ 800 MHz is more than the observed drift of the lasers frequency over months, for a fixed laser current so the laser can be locked to this point after a cold start of the system by automatically enable the PID loop after the temperature of the CCP has reached its set point. Despite the moderate slope, the locked laser shows a frequency variation less than 10 MHz which is stable enough for the next step of the locking scheme, a frequency jump.

The desired Doppler free transition can now be reliably reached by opening the PID loop, making a small predefined frequency step to the final transition and closing the PID loop again. The frequency jump is realized by a step in the injection current that can be calculated using the current to frequency conversion factor of the DFB laser. This conversion factor was experimentally determined to be -1.3 MHz per μA and the step to the F=2 to F'= CO 2/3 transition in ^{87}Rb was calculated based on this factor. The final current step is lower than the the calculated one, since the current step also results in a small jump of the diodes temperature which can not be stabilized fast enough during the time of the jump. The capture range to the F=2 to F'= CO 2/3 transition was experimentally determined to be $\approx$ 80 MHz resulting in a reliable locking scheme using only very low data rate and computing power. After it's implementation, this locking procedure was exposed to a test procedure including 50 locking attempts, and never failed to stabilize the lasers frequency.

6.3.4 Performance and qualification

Two rubidium spectroscopy modules were build for the TEXUS 51 sounding rocket mission, an engineering model (EM) and a flight model (FM). Despite their same mechanical and electrical interfaces, major changes have been implemented in the FM and various improvements over the EM were achieved. The main change included another laser module with a diode operating at 36 °C instead of 13 °C. The whole module is sandwiched between heat-producing elements (electronics on top and the comb module underneath) and the heatsink temperature increases by 6 K during the flight. The optimized diode allowed for safe operation of the module over the whole possible temperature range present in the lab as well as in the integrated payload. This was not the case for the laser diode used first due to the limited current of the temperature controller. The gas cell in the FM has a magnetic shield made of a foil with high magnetic permeability (μ-metal). This reduces the energy shift in rubidium due to the changing orientation of the rocket in respect to the earth's magnetic field and stray magnetic fields produced by the other payloads in the rocket which are not shielded. Small changes included an improved bandwidth of the spectroscopy photodiodes and optimized cable management that eases the assembly or reparation of the module parts.

Both, the EM and FM passed a vibration test to simulate the vibration loads during the rocket launch. The vibration levels were provided by Airbus DS and are listed in table 6.1. A rms value of 8.1 g was exposed on the rubidium module for 60 s per axis. Before and after a vibration test for every axis a resonance search at the level 0.5 g with a sweep rate of 2 oct/min was applied. During the vibration test the laser stayed locked on to a rubidium transition on every axis and no drop in output-power could be observed. This performance shows clearly that the used technologies are suitable to operate even under a harsh environment and can be qualified for operation on a sounding rocket. After the shaker test the FM was integrated into the FOKUS Payload and all measurements presented below are taken with it.

To characterize the performance of the FOKUS Payload multiple long term frequency measurements were performed. They were done mostly over night and show the frequency stability between the rubidium module and the frequency comb which is referenced to the microwave source. The corresponding modified Allan deviation (see Equation 4.3) is shown in Figure 6.8. Starting with a relative frequency instability of 6×10^{-11} after 1 second the Allan deviation decreases almost with a white frequency noise spectrum for averaging times up to 30 s and

Frequency band	Power spectral density
20–399 Hz	0.0045 g^2/Hz
400–599 Hz	0.0675 g^2/Hz
600–1299 Hz	0.0045 g^2/Hz
1300–2000 Hz	0.0675 g^2/Hz
Total	**8.104 g_{RMS}**

Table 6.1: Vibration levels applied during the qualification shaker test on every axis. (Requirement by Airbus DS.) Before and after a vibration test a resonance search was applied for every axis.

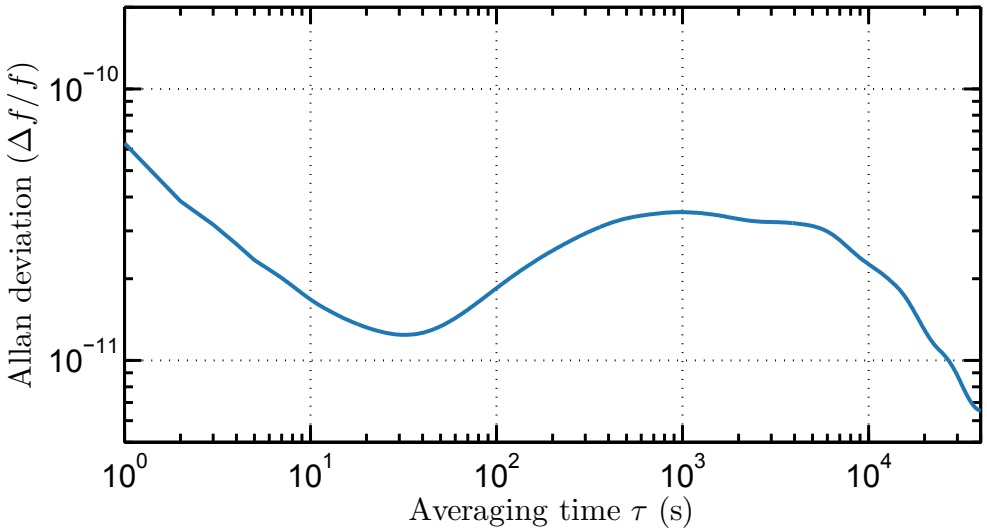

Figure 6.8: The modified Allan deviation of the relative beat frequency between the FOKUS comb and the stabilized DFB laser taken during a measurement in 2014. The stability is better than 10^{-10} for all averaging times.

increases from that point to a plateau around 1000 s to decrease again after 1×10^4 s. The frequency instability of this measurement is limited in the first 30 seconds by the instability of the combs microwave reference which is specified to be better than 1×10^{-10} in one second. The instability in the second part possibly results from environmental temperature drifts that cause drifts in the analogue electronics. This frequency instability is comparable with state of the art compact rubidium DFB diode laser systems which use the FMS technique for frequency stabilization [182].

The relative frequency instability is better than 1×10^{-10} over the whole measurement time and better than 1×10^{-11} after 3×10^4 s. This represents only a small fraction of 6 MHz, the natural linewidth in rubidium, a requirement for laser cooling. The performance of the module is therefore suitable as a frequency reference for experiments with cold rubidium atoms, such as MAIUS, STE QUEST and others (see Table 1.1). In contrast to lab based experiments, the FOKUS payload was built to operate during a flight on the TEXUS 51 sounding rocket campaign that is presented in the following section.

6.4 The TEXUS 51 launch campaign on Esrange

The launching site for the TEXUS 51 sounding rocket mission is called Esrange and belongs to the Swedish Space Centre (SSC). Located about 50 km up north from the small mining city Kiruna and lies above the polar circle. A 5600 km^2 big and mostly uninhabited tundra region north to the Esrange, serves as a safe landing area for the ballistic TEXUS and other sounding rocket missions. Besides a launch tower called Skylark (see Figure 6.9 b) where rockets with the VSB-30 motor can be launched. A second launch tower for the larger MAXUS type rockets

allows for additional launches. A balloon launch pad is also available during the whole year. Together with the the good flight connection via the Kiruna airport the Esrange is a perfect starting point for sounding rocket missions in whole Europe.

The TEXUS 51 campaign was originally scheduled for April 2013 as a double campaign together with TEXUS 50. After a successful launch of the rocket, the landing point of TEXUS 50 sounding rocket was outside the calculated impact area. An analysis of the Skylark launch tower unveiled a misalignment on the guide rails. The launch of the TEXUS 51 was cancelled while the rocket was ready to be launched. The campaign was resumed in April 2015. This campaign including launch procedure, flight sequence and the experimental results is presented in this section.

6.4.1 Mission overview

The TEXUS 51 sounding rocket mission consists of four independent experiments. Each of them has an independent power supply and communication module. The modules are integrated in their frames which form the rocket hull and are connected mechanically and electrically with each other. After attaching the recovery module that includes the parachute for a soft landing and modules for data transmission, two VSB-30 rocket motors are attached to rocket and the whole assembly is positioned in the Skylark launch tower. This whole procedure takes usually 3-4 days including multiple tests of the single payloads and complete system function tests.

Since TEXUS rockets have no guidance system, it's ballistic flight trajectory requires calm wind conditions for a safe launch and landing in the calculated impact area. The weather conditions in the impact area have to allow for a safe payload recovery right after impact to recover sensitive samples. The weather data for the next day are evaluated daily and depending on the results a launch is attempted. Scheduled originally for the 17th of April, the launch was postponed to the 23th of April due to non-optimal weather conditions.

Time (s)	Altitude (km)	Event
T + 0.0	0	lift off
T + 13.4	7.8	Motor first stage separation
T + 59.0	92.0	Motor second stage separation
T + 72.0	114.1	Start of zero-g
T + 260.9	258.0	Apogee
T + 442.0	89.0	End of zero-g
T + 623.4	2.4	Main parachute release
T + 633.0	2.4	Main parachute de-reefed
T + 883.9	0.62	Impact
T + 6900	0.62	Payload recovery

Table 6.2: TEXUS 51 flight sequence. Data provided by Kayser-Threde GmbH (now OHB System AG)

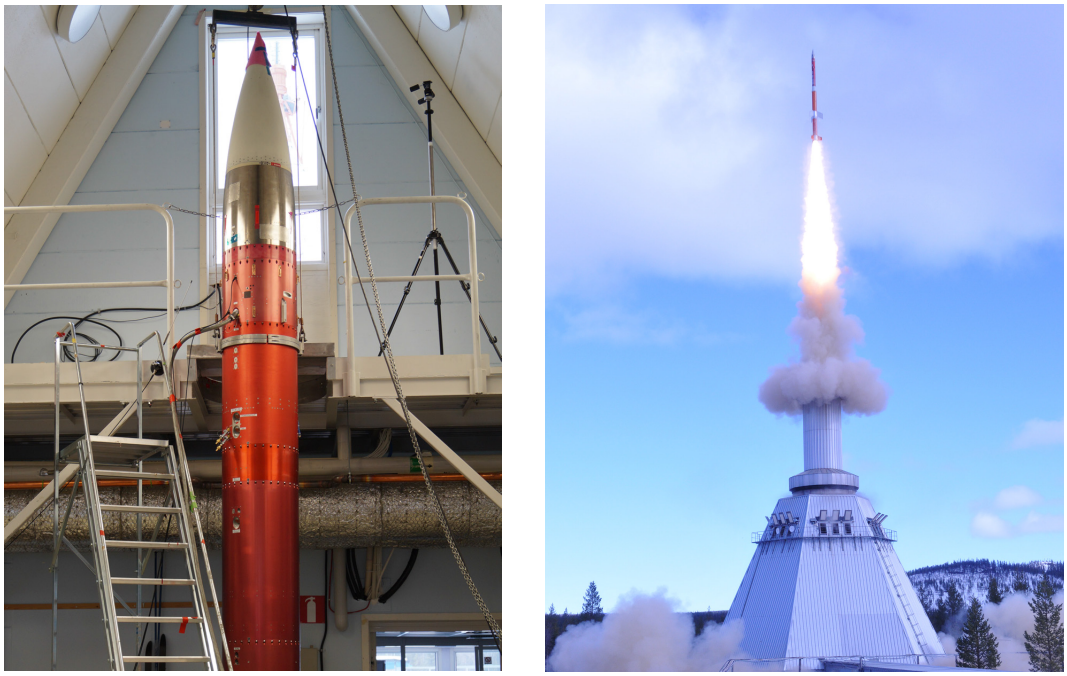

(a) **(b)**

Figure 6.9: (a) The assembled TEXUS 51 sounding rocket in the integration hall. The FOKUS payload is located in the middle. **(b)** The launch of the TEXUS 51 sounding rocket on the 23th of April 2015 at 9:35 local time at Esrange, Sweden. Picture provided by Airbus Defence and Space.

The launching sequence starts 4 h before lift off by turning on the power supplies of the payloads. The time after this sequence start can be scheduled individually by the operators and access to the payload via a late access panel is possible. This is however not the case for the FOKUS payload which is automatically switched on after the power up. After 40 min the temperatures of the rubidium and the comb module are stabilized, the repetition rate and the CEO are stabilized as well as the rubidium laser using the method presented in Section 6.3.3. From this point on the system status is monitored by the operators and the launch team (AIRBUS DS) and manual intervention is possible.

The point of no return is reached 4 min before lift off when the starting sequence is initialized. The lift off signal was given at 9:35 am local time followed by a peak thrust acceleration of 8.1 g resulting from the first motor stage which is then separated 13.4 s after lift off. This is followed by the ignition of the second stage and a de-spin procedure with a Yo-Yo system which reduces the spin from 2.8 Hz to 0.14 Hz. After the Yo-Yo de-spin the second stage is also separated and the zero-g phase (defined as the phase with a residual acceleration $< 10^{-4}$ g) starts 72 s after lift off. The zero-g phase lasts for 370 s. The rocket reaches an apogee of 258 km, followed by a spin-up phase. 487 s after lift off the rocket re-enters the earth's atmosphere and is decelerated first via a pilot parachute and then via the main parachute. The sequence of the rocket launch is presented in Table 6.2.

During the flight various parameters are recorded and a predefined sequence is performed. The sequences for the rubidium spectroscopy and the sequence for the comb are almost independent from each other. The rubidium laser is locked prior lift off. A manual initialization of the auto lock procedure can be done via a telemetry command. After the rocket vibrations are finished and the μ-g phase starts, the combs repetition rate and offset rate are automatically locked. With the comb and the DFB laser both stabilized, the beat between them is countable and its value is recorded for 248 s. Afterwards the rubidium laser is scanned for 100 s (corresponding to $\approx$ 300 data points) over a predefined current range that covers the ^{87}Rb F=2 to F' and the ^{85}Rb F=2 to F' manifolds and locked afterwards again. From this point the beat with the frequency comb is counted until the data transmission discontinues.

6.4.2 Results

The results of the rocket flight are presented in this section. Figure 6.10 shows the FMS error signal of the laser during the flight along with the absorption signal. The laser stayed stabilized on the rubidium transition during the lift off and the high vibration boost phases. Due to the low data rate of the on board computer of $\approx$ 3 Hz, noise in the error signal during this period can not be resolved. 333 s after the lift off the laser frequency is intentionally scanned over the rubidium transitions. One can clearly see the spectroscopic features in the error signal and the Doppler free absorption spectra in the absorption signal. After the scan the laser is locked again to the same transition as before the lift off and remains so for the remaining flight. This data shows the first Doppler free laser spectroscopy performed in space.

The frequency measurement between the rubidium laser and the frequency comb is presented in Figure 6.11. After about 86 s, the frequency comb is stabilized to the microwave

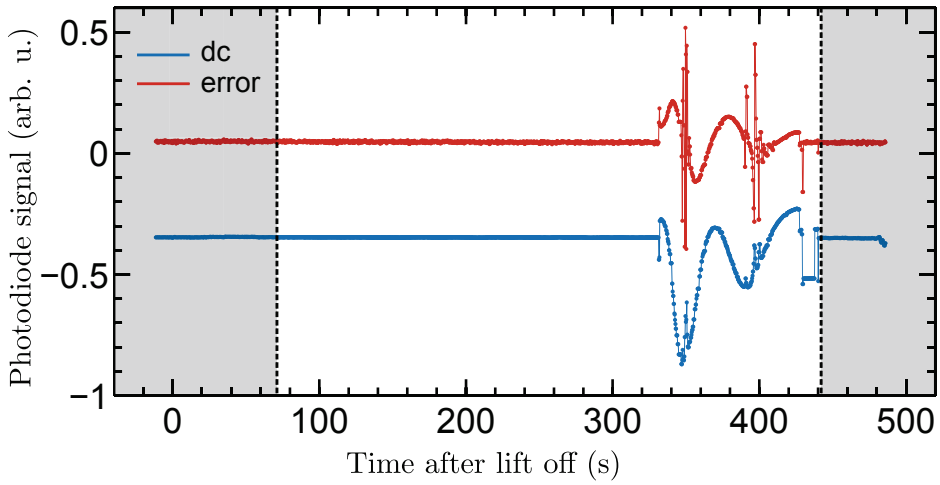

Figure 6.10: The error signal (red) and the absorption signal (blue) of the FOKUS spectroscopy module during the TEXUS 51 sounding rocket flight. The laser remained stabilized during the boost phase. 333 s after lift of, the laser is intentionally scanned over the rubidium transitions and relocked afterwards. The unshaded region represents time of microgravity.

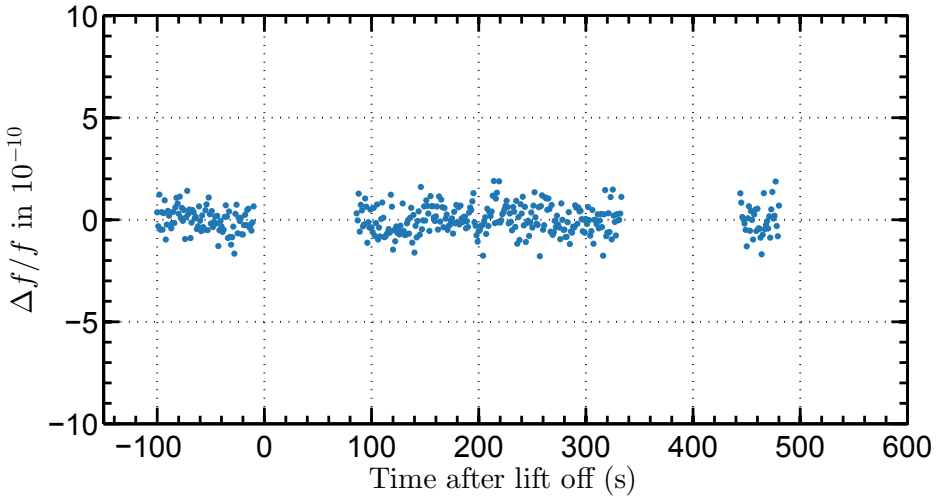

Figure 6.11: Beat frequency between the rubidium laser and the frequency comb during the TEXUS 51 sounding rocket flight. A linear frequency drift of 122 Hz/s is removed from the data.

reference and the beat frequency is counted. This is a prove that the rubidium laser stayed stabilized on the chosen transition during the lift off and the rockets boost phase (no relock durin this period was performed), since the F=2 to F'= CO 2/3 ^{87}Rb transition is the only one that lies in the range of the band pass filter before the frequency counter. During the frequency scan of the rubidium laser from 334 s to 443 s the beat frequency lies outside the band pass window and shows arbitrary values. After the relock procedure, the beat measurement continues. This data represents, to our knowledge, the first frequency measurement in the optical domain in space with a frequency comb and can be interpreted as a prototype test of the Local Position Invariance in space using optical frequencies. A linear frequency drift of 122 Hz/s is removed from the data shown in Figure 6.11. This is most probably caused by the increasing temperature of the whole payload during the flight that causes drifts in the laser electronics. However, since rocket trajectory is a parabola and thus an even function and a linear drift is an odd one, the linear drift does not affects evaluation of the frequency measurement for a test of the Local Position Invariance.

For evaluation of the frequency measurement towards an LPI test, the frequency data has to be compared to the predicted signal using the Equation 6.4 with $\frac{\Delta\nu_{12}}{\nu}$ being the relative frequency change during the flight presented above and ΔU being the change in the gravitational potential experienced during the flight. Data from the rocket flight including altitude were provided by OHB System AG. In the spherical approximation the earth's potential U can be written as

$$U = -\frac{GM}{r} = -\frac{GM}{R+h}, \tag{6.7}$$

with the gravitational constant G, Earth's mass M and Earth's radius R. With the knowl-

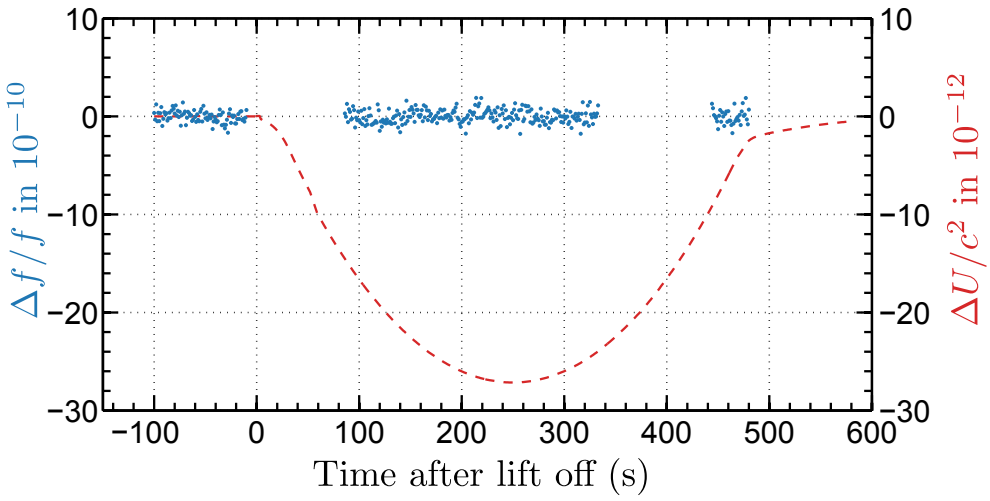

Figure 6.12: The analysis of the frequency measurement during the sounding rocket flight as an LPI test. The relative beat frequency data is shown in blue. The change in the gravitational potential ΔU as a function of the flight duration is shown as a red dashed line.

edge of the rockets altitude h the potential can be calculated. Figure 6.12 shows the gravitational potential for the flight together with the corresponding beat frequency data. Using least squares analysis of this data results in an upper limit for a violation of the LPI principle $(\beta_{\mathrm{Cs_{RF}}} - \beta_{\mathrm{Rb_{OPT}}}) = 0.186 \pm 0.260$ for the two clocks used (uncertainty is expressed in 1σ). The uncertainty of this measurement is orders of magnitude higher than state of the art LPI tests [171] with an upper limit of $(\beta_{\mathrm{Rb}} - \beta_{\mathrm{H}}) = (-2.7 \pm 4.9) \times 10^{-7}$.

But still, this is the first LPI Null test between two different species with two different transitions (optical and microwave), and can be improved far beyond the current limits by using state of art optical clocks and a larger change in the gravitational potential, which can only be achieved on a satellite mission. For example using atomic clocks for comparison at the 10^{-16} level (routinely achieved by optical lattice or ion clocks in the laboratory) on an high elliptical orbit ($\Delta U/c^2 \approx 10^{-7}$) would lead to an LPI test at the 10^{-9} level [179].

This section presented the first test of the Local Position Invariance in space. Using a fibre based frequency comb and a laser stabilized to a rubidium transition, an optical frequency measurement was performed during a sounding rocket flight. Despite the high statistical uncertainty of this measurement, caused by the microwave reference and the chosen the atomic species for stabilization, this is a pioneering experiment for future tests of general relativity. The techniques developed here will be useful in various future experiments including for example the test of the Universality of Free Fall with atom interferometry. Highly stable laser sources and frequency combs will play an important role in future atomic clocks, navigation and high precision spectroscopy. Two follow-up sounding rocket missions were realized during this thesis and are shortly presented in the next section.

6.5 Two sounding rocket payloads for the TEXUS 53 mission

Two additional payloads were designed, built and successfully launched on the TEXUS 53 sounding rocket mission. The first one is a re-flight of the original FOKUS payload, where the rubidium reference module was replaced by a new module that uses modulation transfer spectroscopy (MTS) instead FMS to improve the long term stability of the laser frequency. The second one named KALEXUS is a separate payload including two ECDLs autonomously stabilized to a potassium transition. The KALEXUS experiment was operated by Aline Dinkelaker and Max Schiemangk during the optimization phase and the rocket launch.

6.5.1 FOKUS Reflight

During the FOKUS project phase an opportunity for a second launch of the payload on-board TEXUS 53 opened up. No major changes could be done due to the tight schedule of only 6 months between the return of the FOKUS payload and delivery of the upgraded payload to the launch operator Airbus DS. For the FOKUS payload, a new rubidium reference module was built and a second beat detection unit for the potassium wavelength was designed and integrated. The previous reference oscillator for the frequency comb was replaced by a rubidium oscillator [Microsemi, XPRO]. This oscillator offers a short term stability of one order of magnitude better than the CSAC at the cost of a higher volume and power consumption. The short available implementation time left no time for a development of new electronics. It was therefore decided to use only the existing electronic interfaces in the FOKUS payload.

The new rubidium reference module utilizes modulation transfer spectroscopy (see Section 3.2.2) for laser frequency stabilization instead FMS. To this end a new Zerodur optical bench with two counter-propagating fibre inputs was constructed by the project partner Johannes Gutenberg-Universität Mainz. The rubidium gas cell glued on the bench is placed inside a μ-metal shield. Light from the DFB laser is split in two parts using a pm fibre splitter [Thorlabs, PMC780-90B-APC] with a 90:10 ratio where the major part is used as an optical output for the beat measurement with the frequency comb. The remaining part is used to perform spectroscopy. A pm fibre splitter [Gooche & Housego, FFP-DF3267B1P] with a 66:33 ratio, is used to generate the two optical paths needed for the MTS. A fibre coupled electro optical phase modulator (EOM) [Photline, NIR-MPX 800-LN-0.1] is spliced in the optical path of the pump beam to phase modulate the light. This fibre coupled phase modulator is based on a Lithium Niobate (LiNbO3) crystal wave guide resulting in a high modulation efficiency. A RF-power of ≈ 0 dBm for the 10 MHz modulation frequency is used without the need of an additional RF-amplifier like in the case of a free space modulator (see Section 3.2.2).

The high optical power in the modulated path compensates for the high insertion loss of 3.5 dB of the modulator, resulting in similar power levels in each path. The laser light in each path is detected by a high bandwidth photo diode (same circuit as in FOKUS) after passing the rubidium cell. The optical scheme and a photograph of this module is shown in Figure 6.13. Each photo diode signal is divided into a DC and AC signal by means of a Bias-T [Minicircuits, ZX85-12G+]. Since the FOKUS electronics provides one lock-box for the DFB laser a rf switch [Minicircuits, ZX80-DR230+] is used to transmit one of the PD signals driven

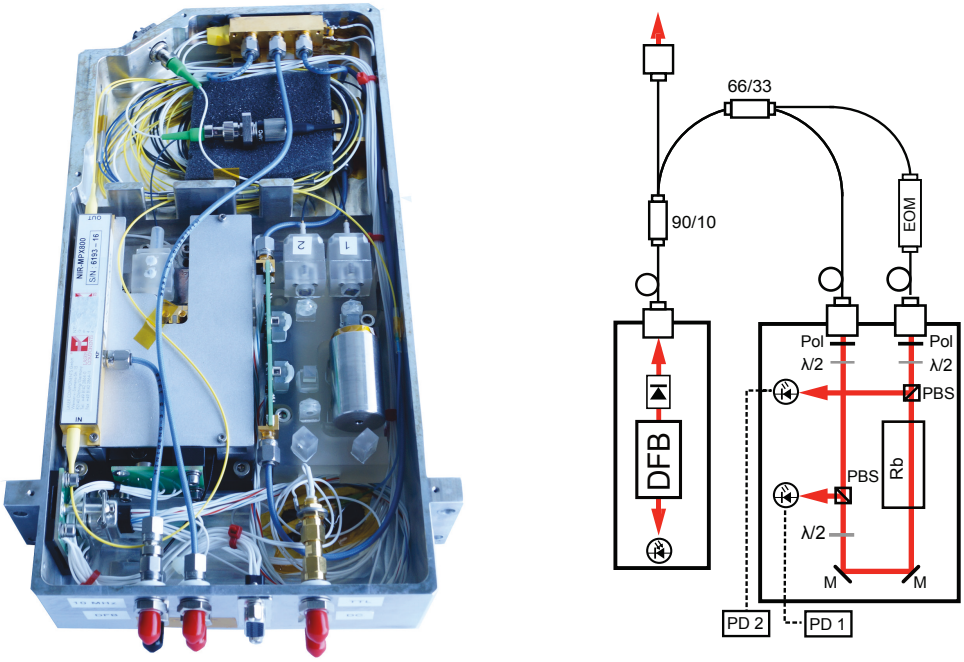

Figure 6.13: The FOKUS Reflight rubidium module with removed cover (left) and the optical scheme (right). A fibre coupled EOM is used to phase modulate the laser light in one of the optical paths. Light in each path is detected by a photo diode to generate a FMS (PD 1) or MTS (PD 2) error signal. An RF switch can be used to select one of the signals.

by a TTL signal generated by a spare digital output channel. The demodulated signal of the path which is modulated by the EOM provides a FMS error signal (PD 1 in Figure 6.13) while the other path provides a MTS error signal (PD 2 in Figure 6.13).

The MTS error signal has no Doppler broadened background with a slope over a wide frequency range that can be used as a first locking step as in the original FOKUS locking scheme. The FOKUS Reflight rubidium module contains a photo diode for each of the two optical paths. Only one error signal at the time can be demodulated, but fast switching between the two signals is easily performed using the RF switch. This is used in the locking scheme to stabilize the DFB diode laser to the MTS error signal. First, the laser is stabilized between the ^{85}Rb F=2 and the ^{87}Rb F=2 using the FMS error signal exactly like in the original FOKUS locking scheme. Than the frequency control loop is opened, followed by a previously determined current jump and a simultaneous switch to the MTS error signal. Then, the control loop is closed to stabilize the laser to the F=3 to F'=4 ^{85}Rb transition using the MTS method.

Prior to the integration into the FOKUS Reflight payload the performance of the rubidium reference module was evaluated in a direct frequency measurement with the FOKUS frequency comb at July the 13, 2015. The result of this measurement is shown in Figure 6.14 (solid blue line). The relative frequency stability after an averaging time of 1 s is 10^{-11} and a factor of five better than the stability of the original module (dotted line in Figure 6.14). This improvement

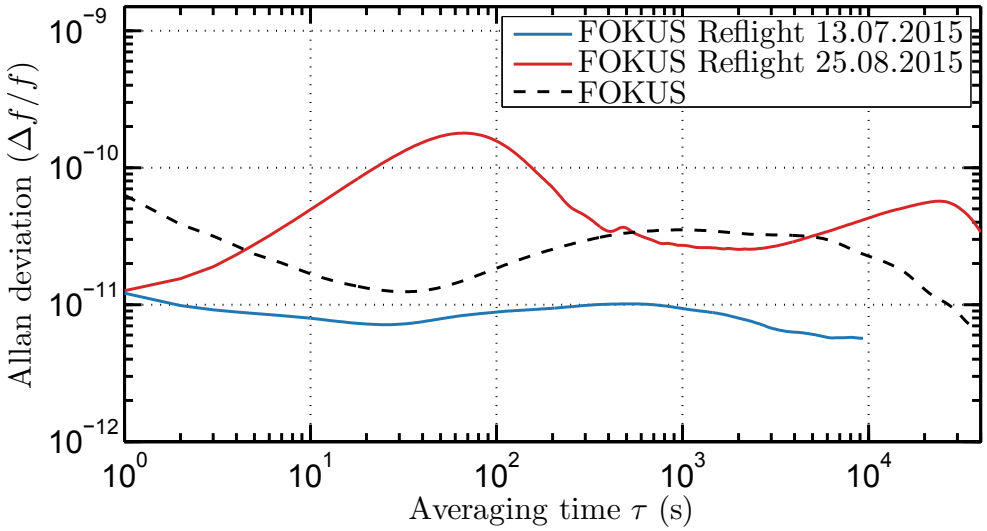

Figure 6.14: The stability of the beat frequency between the FOKUS Reflight rubidium reference and the frequency comb expressed in terms of the modified Allan deviation (MDEV). Data taken in a measurement before (blue solid line) and after (red solid line) a vibration test of the whole payload are shown. A decrease in the frequency stability after the vibration test is visible. The frequency stability of the original payload is shown as a dashed grey line.

is mostly caused by the more stable reference oscillator for the frequency comb. For longer averaging times the stability improves only slightly to 9×10^{-12} after 10 s and to 6×10^{-12} after 10^4 s. While this performance is limited by drifts, an improvement over the previous version for all time scales was achieved.

This module was integrated into the FOKUS payload and replaced the original spectroscopy module. The optical output is again connected to the frequency comb. A small spare volume under the spectroscopy module is used to mount a new developed beat detection unit for 767 nm light. This light is produced in a independent payload called KALEXUS is presented below in the Section 6.5.2.

After integration the whole payload was qualified in vibration test (see Section 6.3.4) and another frequency measurement was performed in August 2015. The stability in terms of the modified Allan variation is shown in Figure 6.14 as a solid red line. The MDEV after 1 s (the gate time of the counter) is with 10^{-11} the same as prior the vibration test. For longer averaging times the stability decreases to a maximum of 5×10^{-11} after 70 s and stays almost one order of magnitude lower than prior the vibration test. This decrease in stability was caused by an etalon in the optical setup formed between the presented measurements. Most probably by a displacement of optical elements in the beam path. This effect could not be removed due to the limited remaining time before the final transfer of the payload to Airbus.

6.5.2 KALEXUS

To fully exploit the potential of diode lasers for precision measurements in space, laser with a narrow linewidth such as ECDLs are needed. This laser type allows for low noise phase locking of two lasers (see Section 3.2.5 for an example) or even narrowing the line width even further by locking the laser to a stable reference resonator [183]. Line widths smaller than 1 Hz were achieved with this method. Such narrow line width laser are crucial for high resolution spectroscopy of narrow transitions in optical clocks. The laser linewidth also has an impact on the phase noise in an atom interferometer due to a propagation delay between the two interferometer beams. This was extensively analysed in [184]. The sounding rocket mission KALEXUS (German acronym for KAlium Laser Unter Schwerelosigkeit) uses two micro-integrated ECDLs. One of the ECDLs is stabilized to an optical transition in ^{39}K and the other one is offset locked to the first. A fibre optical switch is used to switch the spectroscopy laser during the flight as a demonstration of redundancy operation desired for long term satellite missions or mobile quantum sensors.

The optical scheme of the KALEXUS payload is shown in Figure 6.15. Two extended cavity diode lasers are used as light sources. The ECDLs are based on the same micro-integrated optical bench technology as the laser modules for MAIUS and FOKUS provided by the FBH. A ridge-waveguide (RW) chip with a length of 1 mm long and AR-coated rear facet is used

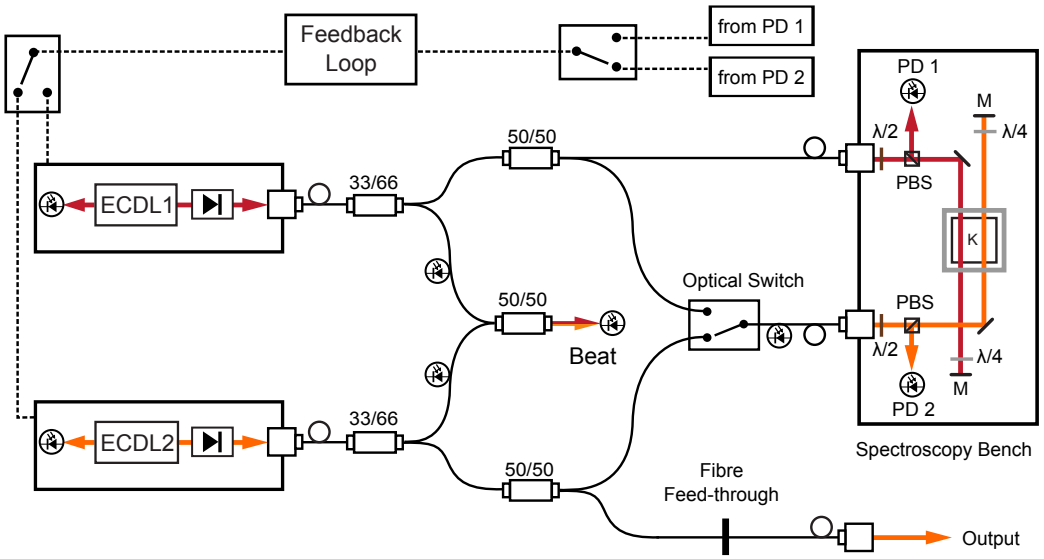

Figure 6.15: The optical schematic of the KALEXUS payload. The ECDLs are fibre coupled and light from each ECDL is split into two paths. One path of each ECDL is overlapped in a second fibre splitter and the light is detected on a fast photo diode for a measurement of the beat frequency between the two lasers. The remaining path of each ECDL can be routed to the spectroscopy bench using an optical switch while light from ECDL 1 has an additional permanent connection. An optical output from ECDL 2 is provided by a fibre feed-through for frequency measurement.

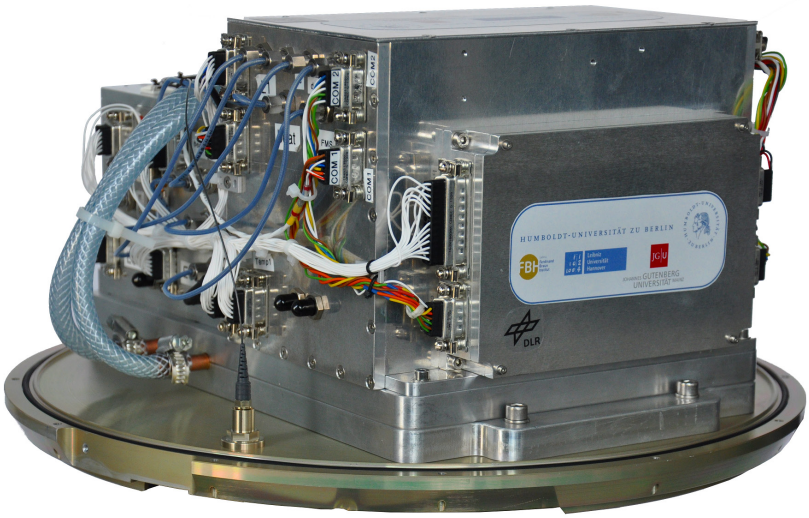

Figure 6.16: The assembled KALEXUS payload after the TEXUS 53 launch. The laser module, the spectroscopy module including all optical components (left) and the electronics module (right) are mounted on a water-cooled heat sink. An electronic board (the housing mounted on the side of the electronic module) generates all voltages used in the setup and provides an interface for communication with the operator. The optical fibre feed through can be seen in the front. The payload dimensions are 350 mm x 210 mm x 190 mm with a total mass of 16 kg (without the base plate).

as the gain medium. The rear facet output is focused on a volume holographic Bragg grating (VHBG) using a micro lens. The VHBG diffracts the incident light back into the gain medium and provides optical feedback required for a single mode operation. The VHBG is glued on a μ-TEC, that is used to tune the centre wavelength of the diffracted light. The length of the laser cavity with a free spectral length of ≈ 4 GHz is controlled by stabilizing the MIOB with a Peltier element placed under the CCP (see Section 5.3.1). The front output is collimated, passes a micro optical isolator with 30 dB isolation, and is coupled into a pm optical fibre using a Zerodur coupler resulting in 12 mW power ex fibre. The measured laser linewidth is $\approx$100 kHz (FWHM) and more details can be found in [163]. Two ECDLs are integrated in a laser module using the same mounting concept as in MAIUS 5.3.1 with an adapted electrical interface PCB.

Both laser outputs are guided to the spectroscopy module with FC/APC mating sleeves. Light from each ECDL is split into two paths by means of a pm fibre splitter and one output each is overlapped using an additional fibre splitter. One of the splitter outputs is collimated by means of a fibre collimator [60FC-4-M4.5S-02, Schäfter + Kirchhoff,]. The light is then directed onto a photo diode [G4176-03, Hamamatsu] followed by a Bias Tee [ZX85-12G+, Minicircuits] and is amplified by a RF amplifier [ZX60-3018G+, Minicircuits]. The remaining outputs are used for spectroscopy and for the optical interface with the FOKUS Reflight

frequency comb. Several in-line photo diodes are implemented in the optical paths for monitoring purposes. A vacuum fibre feed through [V-SF-PMC-780-5.2-NA012-APC/APC, Schäfter + Kirchhoff] is used to deliver light from ECDL 2 (see Figure 6.15) to the FOKUS Reflight payload.

The spectroscopy module contains an optical Zerodur bench with two independent inputs. The light from one of the ECDLs (ECDL 1 in Figure 6.15), is permanently connected to the optical bench, while a fibre coupled optical 1x2 switch [eol 1x2, Leoni] can select either light from ECDL 2 or light from ECDL 1 to be transmitted. After passing the potassium cell, each beam is retroreflected and passes thereby a $\lambda/4$ wave plate twice. After the second pass through the cell each beam is detected on a fast photo diode on a PCB board glued to the optical bench. Due to the lower vapour pressure in potassium compared to rubidium, a higher vapour pressure is needed for a sufficient absorption signal [185]. The potassium gas cell is heated by ohmic loss in a wire wrapped around the thermally insulated cell. An RF switch [ZX80-DR230+, Minicircuits,] directs one of the AC coupled photo diode outputs to a RF amplifier [ZFL-500LN+, Minicircuits].

The major electronic components used in KALEXUS were developed by Dr. Thijs Wendrich, University of Hannover and are the same as the one used in MAIUS. They include a current driver card with two channels, two cards for temperature control with two channels each, a frequency control card with one channel for generating the FMS error signal and three channels for offset locking (only one channel is used in KALEXUS). A photodiode input card reads out the in-line and diode rear output photodiode for monitoring purposes. A compact industrial minimized pc system [MOPSlcdLX 800, Kontron,] running Labview Real Time 2009 is used to control the electronic cards. Ethernet is used to access the pc from ground while an RS232 interface also allows communication during the flight via the rockets service module. The interfaces from and to the service module use optocoupler to galvanic isolate the payload. The payload works on a 24-20 V supply and all required voltages are generated inside the payload with DC-DC converters.

6.6 The TEXUS 53 launch campaign on Esrange

The TEXUS 53 launch campaign took place in January 2016, with a scheduled first countdown for January 17th. The two payloads, FOKUS Reflight and KALEXUS operated independently, while the frequency comb in FOKUS Reflight constantly measures the frequency of ECDL 2.

6.6.1 Mission overview and results

The KALEXUS Payload is located under the FOKUS Reflight module and one fibre feedtrough from each payload is connected using a mating sleeve attached to the outside of the pressurized dome of each payload. The connection was fixed with adhesive after the final integration into the rocket hull. The flight sequence for FOKUS Reflight is the same as for the original FOKUS flight with the exception of the locking scheme, which has an additional step for switching from the FMS to the MTS error signal (see Section 6.5.1).

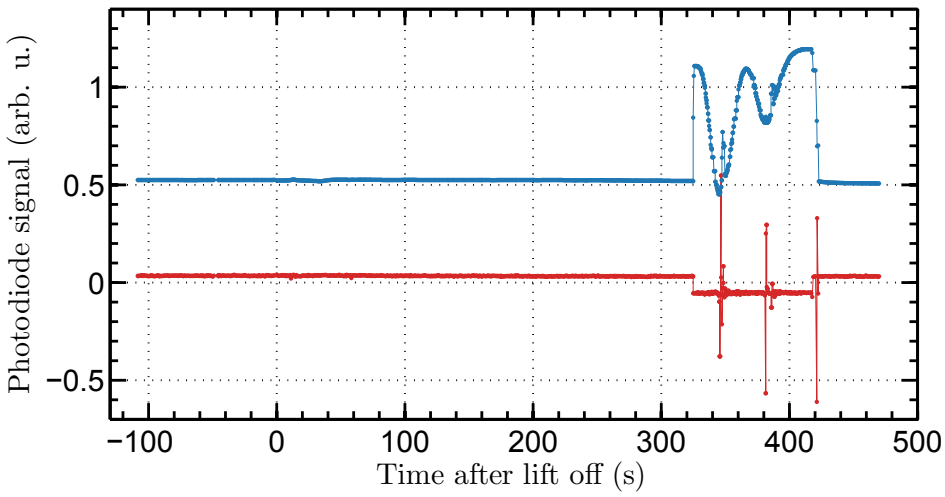

Figure 6.17: Spectroscopy data of the FOKUS Reflight rubidium module during the TEXUS 53 sounding rocket flight. The absorption is shown in blue and the MTS error signal in red. The laser remained frequency stabilized during the rocket's boost phase and could be relocked after an initiated scan over the rubidium transitions. The data rate corresponds to 3 Hz.

KALEXUS performs a more complex sequence. ECDL 1 is locked to an atomic transition first using the FMS method, and ECDL 2 is offset locked in respect to the first. Then the role of the FMS locked laser and the spectroscopy laser are interchanged. Afterwards the ECDL 1 is locked again to the potassium transition and the frequency of ECDL 2 is offset locked and recorded with the frequency comb. The two payloads operate independently and interchange no data during the flight. A detailed description of the payload and the complete KALEXUS mission including the sequence will be given in a future publication [186].

The results of the FOKUS Reflight mission on TEXUS 53 campaign are summarized in Figure 6.17. Like in the TEXUS 51 campaign, the DFB laser remained frequency stabilized during the rocket's boots phase. 325 s seconds after the lift off a scan of the DFB diode laser current was initiated for a period of 100 s. The laser could be relocked afterwards to the original optical transition. All data was recorded with a data rate of 3 Hz. 84 s after lift off the rep rate and the CEO of the frequency comb were both stabilized and the beat frequency with the FOKUS Reflight DFB laser and the KALEXUS ECDL 2 was counted. The comb remained stabilized until an automated power shut down after the end of the μg phase.

The frequency data of both payloads are shown in Figure 6.18. Due to an etalon effect probably caused by reflections on the fibre facets, the frequency shows strong oscillates in both measurements. For the FOKUS Reflight payload, the frequency oscillates with an amplitude of ≈ 0.2 MHz with no visible drift of the average frequency. For KALEXUS the oscillations are ≈ 1.0 MHz and thus a factor of five higher. In addition a frequency drift of ≈ 1.5 MHz in the first 100 seconds before launch are visible. They are probably caused by deactivating the water cooling and the on or off turning of other payloads. The MTS method used in FOKUS Reflight could have an advantage over the FMS method used in KALEXUS in terms

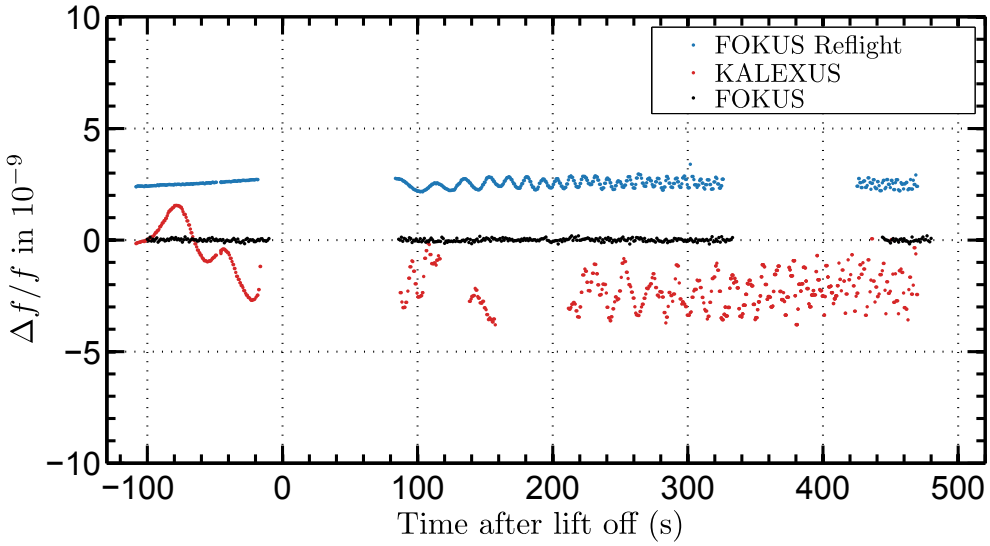

Figure 6.18: Relative frequencies measured during the TEXUS 53 sounding rocket flight. The relative frequency of the FOKUS Reflight laser is shown in blue and the relative frequency of the KALEXUS ECDL 2 is shown in red. The frequency oscillations due to an optical etalon are clearly visible in both data sets. Frequency data from the FOKUS laser on the TEXUS 51 mission are additionally shown in black.

of frequency drifts due to its intrinsically offset free error signal.

The fast oscillations in KALEXUS and FOKUS Reflight module are caused by unwanted etalon effects. This can be seen in the frequency data taken during the flight shown in Figure 6.18. Despite an extensive analysis prior the campaign this effect could not be removed before the begin of the campaign. A more detailed description of the KALEXUS flight sequence and an in depth analysis of the etalon will be carried out and published in the future [186].

After landing, the payload was recovered and switched on after re-thermalization one day after the recovery. Both payloads were operated without any detected malfunctions.

6.7 Summary

This chapter presented the first optical frequency measurement in space on-board a sounding rocket. A DFB diode laser was stabilized to an optical rubidium transition and its frequency was measured with a fibre based frequency comb. The laser remained frequency stabilized even during the rocket's boost phase. The technologies used for the realization of the rubidium module demonstrated a high technological maturity and are a test of the MAIUS core laser technologies. The successful FOKUS flight therefore increased the success possibility of the MAIUS mission. The presented laser systems can be easily adapted to various wavelengths using appropriate semiconductor materials and vapour cells. They can be therefore used for atom interferometers and atomic clocks based on different atomic species.

Besides this technology demonstration, the optical frequency measurement can be inter-

preted as a pathfinder experiment for a test of the Local Position Invariance using optical clocks in space. The resulting violation parameter $(\beta_{\mathrm{Cs_{RF}}} - \beta_{\mathrm{Rb_{OPT}}}) = 0.186 \pm 0.260$ for the two clocks used in the comparison confirms the LPI principle within the uncertainty. Future improvements of several orders of magnitude can be reached on a sounding rocket flight using high performance optical references.

Two other sounding rocket payloads, one including a DFB diode laser and one including narrow linewidth ECDLs were constructed and successfully operated on a joint sounding rocket flight. The frequencies of the stabilized lasers were compared with a frequency comb using an optical fibre link between the two individual payloads.

7 Summary and outlook

During this thesis a number of milestones towards a space based atom interferometer for a test of the Universality of Free Fall have been achieved. The results of the ground measurements performed with the mobile atom interferometer GAIN and the results of the sounding rocket missions are listed therefore separately.

7.1 Results of ground based atom interferometry

A mobile atom interferometer has been compared with state-of-the-art classical gravimeters during three gravity measurement campaigns. During the third gravity comparison with a superconducting gravimeter, a stability of 5×10^{-11} g was reached after 10^5 s, the best reported stability for a gravimeter based on atom interferometry. To enable the measurement campaigns a newly developed amplifier module was realized as a major modification of the previous laser system. The module uses only one tapered amplifier instead of two amplifiers in the previous module and still delivers only 7 % less fibre coupled output power. In addition it is more compact, stable and remained maintenance free during and after the measurement campaigns.

Additionally, the biggest contribution to the uncertainty in GAIN caused by wavefront aberrations in the optical beam path was analysed by a mathematical model and for the first time experimentally verified. A bias of $-28 \pm 22 \times 10^{-10}$ g was determined in our gravimeter and a mitigation strategy was proposed for future assemblies.

7.2 Results of the sounding rocket missions

A laser system for the MAIUS mission aiming for the demonstration of the first atom interferometer with a Bose–Einstein condensate in space on a sounding rocket was built. The laser system was qualified, put in operation and optimized. After the successful integration of all subsystems into the rocket structure the MAIUS payload currently produces BECs.

The laser technology used in MAIUS was successfully tested on two sounding rocket missions showing the high maturity of its key technologies. First, a compact spectroscopy module including a DFB laser and a rubidium gas cell was designed and built. It was integrated into a sounding rocket payload called FOKUS containing a fibre frequency comb. The relative frequency stability of the stabilized DFB laser is better than 6×10^{-11} for averaging times between 1 s and 10 000 s. This meets the stability requirements for MAIUS as well as atom interferometry based gravimeters aiming for a stability at the 0.1 μGal level. The payload was operated on the sounding rocket mission TEXUS 51. The laser remained frequency stabilized during the boost phase. A scan of the laser frequency was initiated, performing the first

Doppler-free spectroscopy in space and the laser was automatically relocked afterwards using a procedure specially developed for this mission. During the microgravity phase of 6 min the laser frequency was measured with the frequency comb. The first frequency measurement in the optical domain in space with a frequency comb was thereby performed. This measurement can be seen as a prototype test of the Local Position Invariance with optical clocks in space and the analysis of the data resulting in $|\beta_{\mathrm{Cs_{RF}}} - \beta_{\mathrm{Rb_{OPT}}}| = 0.186 \pm 0.260$ confirmed the LPI principle.

A second spectroscopy module using modulation transfer spectroscopy for frequency stabilization was built and integrated into the follow-up payload FOKUS Reflight. The frequency stability was improved by a factor of ≈ 5. A third autonomous payload with two narrow line width ECDLs was designed, assembled and put in operation. Both payloads operated during the sounding rocket mission on the TEXUS 53 and KALEXUS successfully demonstrated the maturity of narrow line width laser technology and redundancy concept, required for satellite missions aiming for high precision atom interferometry.

7.3 Outlook on atom interferometry with GAIN

Several improvements of the GAIN apparatus are being currently installed. First, a recent demonstration of launching two atomic clouds, one during the flight of the other, in the so called "juggling atomic fountain" sequence [187]. The time between the launches can be adjusted for the same velocity of both clouds with an adjustable distance between them in the launch direction. This way two clouds can be addressed simultaneously by the same Raman pulses, creating two separated interferometers. The phase difference between them is proportional to the gravity gradient. Raman noise and vibration noise are highly suppressed in this differential interferometer. The phase noise in the gradiometer will be dominated by detection noise only.

The second ongoing improvement in GAIN, the implementation of Raman sideband cooling, can be used to reduce the detection noise. This technique allows to cool the launched atoms to temperatures about one order of magnitude lower than currently achieved in GAIN. Temperatures as cold as 500 nK were achieved for ^{87}Rb using this technique [188]. The corresponding decreased expansion of the atomic cloud will increase the number of atoms in the detection zone. In addition the cooled atoms are polarized in only one magnetic sub-state instead of equally in all of the five sub-states, increasing the atom number aftter the selection process even more. The reduced detection noise will improve the performance in differential interferometers or during gravity measurements on low vibration sites.

Not long ago the residual vibrations of the retro reflecting mirror in GAIN were measured by the seismometer below it. This signal was used in a post-correction process to reduce the vibration noise in GAIN by more than a factor of 2 [138] and possibly even more by optimization in the near future.

This ongoing or already completed modifications alone will improve the short term sensitivity in GAIN. This will ease the analysis of systematic effects due to the decreased averaging time in addition to the colder atomic cloud. Further gravity comparison campaigns with clas-

sical as well as atomic gravimeters are planned and comparisons with both gravimeter types will profit from the mentioned implementations.

7.4 Outlook on space based tests of UFF and LPI

The demonstrated stability in GAIN, mainly limited by seismic noise, clearly shows the potential of atom interferometers for future tests of the Universality of the Free Fall using two different atomic species in space. The residual vibration noise can be highly suppressed in differential dual species measurements by post-processing algorithms. The current implementation of a gradiometer operation mode in GAIN will provide helpful insight in these methods.

The MAIUS mission is planned for winter 2016 and its success will be a major step for space based missions. MAIUS will perform atom interferometry in parameter regimes, i.e. temperatures and interferometry times inaccessible on ground. Two follow up sounding rocket missions are currently prepared and their sub-systems are being assembled. These two missions aim to perform dual species atom interferometry with rubidium and potassium BECs, alternately in the first and simultaneously in the second mission.

In a satellite, the sensitivity can be further increased by several orders of magnitude by the extended free evolution time. Several space missions dedicated to tests of UFF have been proposed that predict an improvement of the best quantum based tests by a factor of 10^6 and a factor of 10^2 with respect to classical tests. The technological maturity demonstrated in the sounding rocket missions presented in this thesis contributes to the realization of the first space based quantum test of the UFF.

With an optical clock and a RF reference with an accuracy both at the 10^{-16} level (this is realistic or already space qualified) replacing the ones used in the LPI test performed during this thesis can improve the best test performed on ground by a factor of 10^3. This requires a potential difference achievable on a trajectory from Earth to Mercury[179].

These tests of the foundations of general relativity could bring insight in a quantum theory of gravity and produce a deeper understanding of the laws of physics. Changing our view of the universe could be worth the effort.

A Rubidium 87 data

Parameter	Symbol	Value
Atomic mass	m	$1.443\,160 \times 10^{-25}$ kg
Boltzmann's constant	k_B	$1.380\,65 \times 10^{-23}$ J/K
Planck's constant	$\hbar$	$1.054\,571\,5 \times 10^{-34}$ Js
D_2 transition frequency	ω_0	$2\pi \cdot 384.230\,484\,46$ THz
Recoil velocity	v_r	5.8845 mm/s
Recoil energy	ω_r	$2\pi \cdot$ 3.7710 kHz
Wavelength (vacuum)	λ	780.241 209 6 nm
Natural line width (FWHM)	Γ	$2\pi \cdot$ 6.07 MHz

Table A.1: Rubidium 87 data and physical constants used for calculations in this thesis (from [79]).

Bibliography

[1] Steven Weinberg. A Model of Leptons. *Physical Review Letters*, 19(21):1264–1266, November 1967.

[2] Sheldon L. Glashow. Partial-symmetries of weak interactions. *Nuclear Physics*, 22(4):579–588, February 1961.

[3] Hansjorg Dittus, Claus Lämmerzahl, and Slava G. Turyshev, editors. *Lasers, Clocks and Drag-Free Control*, volume 349 of *Astrophysics and Space Science Library*. Springer Berlin Heidelberg, Berlin, Heidelberg, 2008.

[4] Claus Lämmerzahl and Hansjorg Dittus. *Lasers, Clocks and Drag-Free Control: Exploration of Relativistic Gravity in Space*, chapter Fundamental Physics, Space, Missions and Technologies, pages 3–25. Springer Berlin Heidelberg, Berlin, Heidelberg, 2008.

[5] P. Gill and H.Margolis and A. Curtis and H. Klein and S. Lea and S.Webster and P.Whibberley. Optical Atomic Clocks for Space. Technical Supporting Document, Version 1.7, 2008.

[6] C.M. Will. *Theory and Experiment in Gravitational Physics*. Cambridge University Press, 1993.

[7] B. Abbott et al. Observation of Gravitational Waves from a Binary Black Hole Merger. *Phys. Rev. Lett.*, 116(6):061102, feb 2016.

[8] Pasquale Maddaloni, Marco Bellini, and Paolo De Natale. *Laser-Based Measurements for Time and Frequency Domain Applications*. Taylor and Francis, first edition, 2013.

[9] D.J.W. Giulini, C. Kiefer, and C. Lämmerzahl. *Quantum Gravity: From Theory to Experimental Search*. Lecture Notes in Physics. Springer Berlin Heidelberg, 2003.

[10] C Wetterich. Crossover quintessence and cosmological history of fundamental "constants". *Physics Letters B*, 561(1-2):10–16, May 2003.

[11] Thibault Damour, Federico Piazza, and Gabriele Veneziano. Runaway dilaton and equivalence principle violations. *Physical review letters*, 89(8):081601, August 2002.

[12] Clifford M. Will. The Confrontation between General Relativity and Experiment. *Living Reviews in Relativity*, 9, 2006.

[13] F. Vetrano. Atom interferometry for gravitational wave detection. *Proceedings of the International School of Physics "Enrico Fermi"*, 188:605–629, 2014.

[14] V. Alan Kostelecký and Neil Russell. Data tables for Lorentz and CPT violation. *Reviews of Modern Physics*, 83(1):11–31, March 2011.

[15] S. Schlamminger, K.-Y. Choi, T. Wagner, J. Gundlach, and E. Adelberger. Test of the Equivalence Principle Using a Rotating Torsion Balance. *Physical Review Letters*, 100(4):041101, January 2008.

[16] James Williams, Slava Turyshev, and Dale Boggs. Progress in Lunar Laser Ranging Tests of Relativistic Gravity. *Physical Review Letters*, 93(26):261101, December 2004.

[17] Albert A. Michelson and Edward W. Morley. Lviii. on the relative motion of the earth and the luminiferous Æther. *Philosophical Magazine Series 5*, 24(151):449–463, 1887.

[18] S. Herrmann, A. Senger, K. Moehle, M. Nagel, E. Kovalchuk, and A. Peters. Rotating optical cavity experiment testing Lorentz invariance at the 10-17 level. *Physical Review D*, 80(10):105011, November 2009.

[19] M. E. Tobar, P. L. Stanwix, J. J. McFerran, J. Guena, M. Abgrall, S. Bize, A. Clairon, Ph. Laurent, P. Rosenbusch, D. Rovera, and G. Santarelli. Testing local position and fundamental constant invariance due to periodic gravitational and boost using long-term comparison of the SYRTE atomic fountains and H-masers. *Physical Review D*, 87(12):122004, June 2013.

[20] J. R. Maze, P. L. Stanwix, J. S. Hodges, S. Hong, J. M. Taylor, P. Cappellaro, L. Jiang, M. V. Gurudev Dutt, E. Togan, A. S. Zibrov, A. Yacoby, R. L. Walsworth, and M. D. Lukin. Nanoscale magnetic sensing with an individual electronic spin in diamond. *Nature*, 455(7213):644–647, October 2008.

[21] David M Toyli, Charles F de las Casas, David J Christle, Viatcheslav V Dobrovitski, and David D Awschalom. Fluorescence thermometry enhanced by the quantum coherence of single spins in diamond. *Proceedings of the National Academy of Sciences of the United States of America*, 110(21):8417–21, May 2013.

[22] Andrew D. Ludlow, Martin M. Boyd, Jun Ye, E. Peik, and P.O. Schmidt. Optical atomic clocks. *Reviews of Modern Physics*, 87(2):637–701, June 2015.

[23] B.N. Taylor. *International System of Units (SI) (rev. , 2008 Ed.)*. NIST special publication. DIANE Publishing Company, 2009.

[24] D. Wineland and Wayne Itano. Laser cooling of atoms. *Physical Review A*, 20(4):1521–1540, October 1979.

[25] Mark Kasevich, Erling Riis, Steven Chu, and Ralph DeVoe. rf spectroscopy in an atomic fountain. *Physical Review Letters*, 63(6):612–615, August 1989.

[26] R Wynands and S Weyers. Atomic fountain clocks. *Metrologia*, 42(3):S64–S79, jun 2005.

[27] T L Nicholson, S L Campbell, R B Hutson, G E Marti, B J Bloom, R L McNally, W Zhang, M D Barrett, M S Safronova, G F Strouse, W L Tew, and J Ye. Systematic evaluation of an atomic clock at 2 $\times$ 10(-18) total uncertainty. *Nat. Commun.*, 6:6896, January 2015.

[28] B J Bloom, T L Nicholson, J R Williams, S L Campbell, M Bishof, X Zhang, W Zhang, S L Bromley, and J Ye. An optical lattice clock with accuracy and stability at the 10(-18) level. *Nature*, 506(7486):71–5, February 2014.

[29] C J Campbell, A G Radnaev, A Kuzmich, V A Dzuba, V V Flambaum, and A Derevianko. Single-ion nuclear clock for metrology at the 19th decimal place. *Physical review letters*, 108(12):120802, March 2012.

[30] Ekkehard Peik and Maxim Okhapkin. Nuclear clocks based on resonant excitation of γ-transitions. *Comptes Rendus Physique*, 16(5):516–523, June 2015.

[31] Hans C. Ohanian and Remo Ruffini. *Gravitation and Spacetime*. Cambridge University Press, third edition, 2013. Cambridge Books Online.

[32] V. V. Flambaum and A. F. Tedesco. Dependence of nuclear magnetic moments on quark masses and limits on temporal variation of fundamental constants from atomic clock experiments. *Physical Review C*, 73(5):055501, May 2006.

[33] Brenton Young, Mark Kasevich, and Steven Chu. Precision atom interferometry with light pulses. In Paul R. Berman, editor, *Atom Interferometry*, pages 363 – 406. Academic Press, San Diego, 1997.

[34] B Barrett, A Bertoldi, and P Bouyer. Inertial quantum sensors using light and matter. *Phys. Scr.*, 91(5):053006, may 2016.

[35] Ch. J. Bordé. Atomic clocks and inertial sensors. *Metrologia*, 39(5):435–463, October 2002.

[36] DW Keith, CR Ekstrom, QA Turchette, and DE Pritchard. An interferometer for atoms. *Physical review letters*, 66(21):2693–2696, May 1991.

[37] O Carnal and J Mlynek. Young's double-slit experiment with atoms: A simple atom interferometer. *Physical review letters*, 66(21):2689–2692, May 1991.

[38] M. Kozuma, L. Deng, E. Hagley, J. Wen, R. Lutwak, K. Helmerson, S. Rolston, and W. Phillips. Coherent Splitting of Bose-Einstein Condensed Atoms with Optically Induced Bragg Diffraction. *Physical Review Letters*, 82(5):871–875, February 1999.

[39] Mark A Kasevich, D. S. Weiss, E. Riis, K. Moler, S. Kasapi, and Steven Chu. Atomic velocity selection using stimulated Raman transitions. *Physical review letters*, 66(18):2297–2300, 1991.

[40] Mark A Kasevich and Steven Chu. Atomic interferometry using stimulated Raman transitions. *Physical review letters*, 67(2):181–184, 1991.

[41] Achim Peters, Keng-Yeow Chung, and Steven Chu. High-precision gravity measurements using atom interferometry. *Metrologia*, 38:25, 2001.

[42] T. Farah, C. Guerlin, A. Landragin, Ph. Bouyer, S. Gaffet, F. Pereira Dos Santos, and S. Merlet. Underground operation at best sensitivity of the mobile lne-syrte cold atom gravimeter. *Gyroscopy and Navigation*, 5(4):266–274, 2014.

[43] Zhong-Kun Hu, Bu-Liang Sun, Xiao-Chun Duan, Min-Kang Zhou, Le-Le Chen, Su Zhan, Qiao-Zhen Zhang, and Jun Luo. Demonstration of an ultrahigh-sensitivity atom-interferometry absolute gravimeter. *Phys. Rev. A*, 88:043610, Oct 2013.

[44] M. Hauth, C. Freier, V. Schkolnik, A. Senger, M. Schmidt, and A. Peters. First gravity measurements using the mobile atom interferometer gain. *Applied Physics B*, 113(1):49–55, 2013.

[45] J. M. McGuirk, G. T. Foster, J. B. Fixler, M. J. Snadden, and M. A. Kasevich. Sensitive absolute-gravity gradiometry using atom interferometry. *Phys. Rev. A*, 65:033608, Feb 2002.

[46] T L Gustavson, A Landragin, and M A Kasevich. Rotation sensing with a dual atom-interferometer sagnac gyroscope. *Classical and Quantum Gravity*, 17(12):2385, 2000.

[47] Andreas Wicht, J.M. Hensley, Edina Sarajlic, and Steven Chu. A preliminary measurement of the fine structure constant based on atom interferometry. *Physica Scripta*, 2002:82, 2002.

[48] G. Rosi, F. Sorrentino, L. Cacciapuoti, M. Prevedelli, and G. M. Tino. Precision measurement of the Newtonian gravitational constant using cold atoms. *Nature*, 510(7506):518–521, June 2014.

[49] JasonM. Hogan, DavidM.S. Johnson, Susannah Dickerson, Tim Kovachy, Alex Sugarbaker, Sheng-wey Chiow, PeterW. Graham, MarkA. Kasevich, Babak Saif, Surjeet Rajendran, Philippe Bouyer, BernardD. Seery, Lee Feinberg, and Ritva Keski-Kuha. An atomic gravitational wave interferometric sensor in low earth orbit (agis-leo). *General Relativity and Gravitation*, 43(7):1953–2009, 2011.

[50] Peter W. Graham, Jason M. Hogan, Mark A. Kasevich, and Surjeet Rajendran. New method for gravitational wave detection with atomic sensors. *Phys. Rev. Lett.*, 110:171102, Apr 2013.

[51] W. Chaibi, R. Geiger, B. Canuel, A. Bertoldi, A. Landragin, and P. Bouyer. Low frequency gravitational wave detection with ground-based atom interferometer arrays. *Physical Review D*, 93(2):021101, January 2016.

[52] Pacôme Delva and Jérôme Lodewyck. Atomic clocks: new prospects in metrology and geodesy. *ArXiv e-prints*, August 2013.

[53] S. Droste, F. Ozimek, Th. Udem, K. Predehl, T. W. Hänsch, H. Schnatz, G. Grosche, and R. Holzwarth. Optical-requency Transfer over a Single-Span 1840 km Fiber Link. *Physical Review Letters*, 111(11):110801, September 2013.

[54] N. Poli, M. Schioppo, S. Vogt, St. Falke, U. Sterr, Ch. Lisdat, and G. M. Tino. A transportable strontium optical lattice clock. *Applied Physics B*, 117(4):1107–1116, October 2014.

[55] S. M. Brewer, J. S. Chen, D. R. Leibrandt, C. W. Chou, D. J. Wineland, J. C. Bergquist, and T. Rosenband. A high-accuracy mobile al^{+}; optical clock. In *2014 IEEE International Frequency Control Symposium (FCS)*, pages 1–1, May 2014.

[56] Kai Bongs, Yeshpal Singh, Lyndsie Smith, Wei He, Ole Kock, Dariusz Świerad, Joshua Hughes, Stephan Schiller, Soroosh Alighanbari, Stefano Origlia, Stefan Vogt, Uwe Sterr, Christian Lisdat, Rodolphe Le Targat, Jérôme Lodewyck, David Holleville, Bertrand Venon, Sébastien Bize, Geoffrey P. Barwood, Patrick Gill, Ian R. Hill, Yuri B. Ovchinnikov, Nicola Poli, Guglielmo M. Tino, Jürgen Stuhler, and Wilhelm Kaenders. Development of a strontium optical lattice clock for the SOC mission on the ISS. *Comptes Rendus Physique*, 16(5):553–564, 2015.

[57] ESA/HPF/DLR. 2011 GOCE geoid. ESA website, 2011.

[58] Jürgen Müller, Majid Naeimi, Olga Gitlein, Ludger Timmen, and Heiner Denker. A land uplift model in Fennoscandia combining GRACE and absolute gravimetry data. *Physics and Chemistry of the Earth, Parts A/B/C*, 53-54:54–60, January 2012.

[59] Ludger Timmen, Olga Gitlein, Volker Klemann, and Detlef Wolf. Observing Gravity Change in the Fennoscandian Uplift Area with the Hanover Absolute Gravimeter. *Pure and Applied Geophysics*, 169(8):1331–1342, September 2011.

[60] I. Dutta, D. Savoie, B. Fang, B. Venon, C. L. Garrido Alzar, R. Geiger, and A. Landragin. Continuous Cold-atom Inertial Sensor with 1nrad.s^{-1} Rotation Stability. *ArXiv e-prints*, page 4, April 2016.

[61] B. Canuel, F. Leduc, D. Holleville, A. Gauguet, J. Fils, A. Virdis, A. Clairon, N. Dimarcq, Ch. J. Bordé, A. Landragin, and P. Bouyer. Six-Axis Inertial Sensor Using Cold-Atom Interferometry. *Physical Review Letters*, 97(1):010402, July 2006.

[62] Jason Williams, Sheng-wey Chiow, Nan Yu, and Holger Müller. Quantum test of the equivalence principle and space-time aboard the International Space Station. *New Journal of Physics*, 18(2):025018, February 2016.

[63] D. Schlippert, J. Hartwig, H. Albers, L. Richardson, L. C. Schubert, A. Roura, P. Schleich, W. W. Ertmer, and M. Rasel, E.˙ Quantum test of the universality of free fall. *Phys. Rev. Lett.*, 112:203002, May 2014.

[64] Lin Zhou, Shitong Long, Biao Tang, Xi Chen, Fen Gao, Wencui Peng, Weitao Duan, Jiaqi Zhong, Zongyuan Xiong, Jin Wang, Yuanzhong Zhang, and Mingsheng Zhan. Test of Equivalence Principle at 10^{-8} Level by a Dual-species Double-diffraction Raman Atom Interferometer. *Phys. Rev. Letters*, 115(1)(013004):4, July 2015.

[65] J Hartwig, S Abend, C Schubert, D Schlippert, H Ahlers, K Posso-Trujillo, N Gaaloul, W Ertmer, and E M Rasel. Testing the universality of free fall with rubidium and ytterbium in a very large baseline atom interferometer. *New Journal of Physics*, 17(3):035011, March 2015.

[66] Jason M. Hogan, David M S Johnson, and Mark A Kasevich. Light-pulse atom interferometry. In E. Arimondo, W. Ertmer, W P Schleich, and E. M. Rasel, editors, *Proceedings of the International School of Physics Enrico Fermi Course CLXVIII on Atom Optics and Space Physics*, pages 411–447, Oxford, 2007. IOS Press.

[67] Fiodor Sorrentino, Kai Bongs, Philippe Bouyer, Luigi Cacciapuoti, Marella de Angelis, Hansjoerg Dittus, Wolfgang Ertmer, A. Giorgini, J. Hartwig, Matthias Hauth, Sven Herrmann, Massimo Inguscio, Endre Kajari, Thorben T. Könemann, Claus Lämmerzahl, Arnaud Landragin, Giovanni Modugno, Frank Pereira dos Santos, Achmin Peters, Marco Prevedelli, Ernst M. Rasel, Wolfgang P. Schleich, Malte Schmidt, Alexander Senger, Klaus Sengstock, Guillaume Stern, Guglielmo Maria Tino, and Reinhold Walser. A Compact Atom Interferometer for Future Space Missions. *Microgravity Science and Technology*, 22(4):551–561, September 2010.

[68] D N Aguilera, H Ahlers, B Battelier, A Bawamia, A Bertoldi, R Bondarescu, K Bongs, P Bouyer, C Braxmaier, L Cacciapuoti, C Chaloner, M Chwalla, W Ertmer, M Franz, N Gaaloul, M Gehler, D Gerardi, L Gesa, N Gürlebeck, J Hartwig, M Hauth, O Hellmig, W Herr, S Herrmann, A Heske, A Hinton, P Ireland, P Jetzer, U Johann, M Krutzik, A Kubelka, C Lämmerzahl, A Landragin, I Lloro, D Massonnet, I Mateos, A Milke, M Nofrarias, M Oswald, A Peters, K Posso-Trujillo, E Rasel, E Rocco, A Roura, J Rudolph, W Schleich, C Schubert, T Schuldt, S Seidel, K Sengstock, C F Sopuerta, F Sorrentino, D Summers, G M Tino, C Trenkel, N Uzunoglu, W von Klitzing, R Walser, T Wendrich, A Wenzlawski, P Weßels, A Wicht, E Wille, M Williams, P Windpassinger, and N Zahzam. STE-QUEST—test of the universality of free fall using cold atom interferometry. *Class. Quantum Gravity*, 31(11):115010, jun 2014.

[69] Philippe Laurent, Didier Massonnet, Luigi Cacciapuoti, and Christophe Salomon. The ACES/PHARAO space mission. *Comptes Rendus Physique*, 2015.

[70] Pau Amaro-Seoane, Sofiane Aoudia, Stanislav Babak, Pierre Binétruy, Emanuele Berti, Alejandro Bohé, Chiara Caprini, Monica Colpi, Neil J Cornish, Karsten Danzmann, Jean-François Dufaux, Jonathan Gair, Oliver Jennrich, Philippe Jetzer, Antoine Klein, Ryan N Lang, Alberto Lobo, Tyson Littenberg, Sean T McWilliams, Gijs Nelemans, Antoine Petiteau, Edward K Porter, Bernard F Schutz, Alberto Sesana, Robin Stebbins, Tim Sumner, Michele Vallisneri, Stefano Vitale, Marta Volonteri, and Henry Ward.

Low-frequency gravitational-wave science with eLISA/NGO. *Classical and Quantum Gravity*, 29(12):124016, June 2012.

[71] Alexander Milke, Deborah N. Aguilera, Norman Gurlebeck, Thilo Schuldt, Sven Herrmann, Klaus Doringshoff, Ruven Spannagel, Claus Lammerzahl, Achim Peters, Bernd Biering, Hansjorg Dittus, and Claus Braxmaier. A space-based optical Kennedy-Thorndike experiment testing special relativity. In *2013 Joint European Frequency and Time Forum & International Frequency Control Symposium (EFTF/IFC)*, pages 912–914. IEEE, July 2013.

[72] P. Kómár, E. M. Kessler, M. Bishof, L. Jiang, A. S. Sø rensen, J. Ye, and M. D. Lukin. A quantum network of clocks. *Nature Physics*, 10(8):582–587, June 2014.

[73] Novaspace. A300 ZERO-G USER GUIDE. Novaspace documentation, version UG-2013-01, 2013.

[74] ZARM. ZARM Drop Tower Bremen User Manual, Version: April 26, 2012 . Manual, 2012.

[75] DLR. TEXUS Sounding rockets for microgravity research. Brochure, 2014.

[76] Alexandre Garcia, Sidney Servulo Cunha Yamanaka, Alexandre Nogueira Barbosa, Francisco Carlos Parquet Bizarria, Wolfgang Jung, and Frank Scheuerpflug. Vsb-30 sounding rocket: history of flight performance. *Journal of Aerospace Technology and Management*, Vol.3(No.3):325–330, September 2011.

[77] Dmitry Budker, Derek F Kimball, and David P DeMille. *Atomic physics: an exploration through problems and solutions; 2nd ed.* Oxford Univ. Press, Oxford, 2008.

[78] M. Schmidt. *A mobile high-precision gravimeter based on atom interferometry*. PhD thesis, Humboldt-Universitaet zu Berlin, https://www.deutsche-digitale-bibliothek.de/item/GZGCAQYX2X6MG7KILSX7FLMEBFRBLX5Y, 2011.

[79] D.A. Steck. *Rubidium 87 D Line Data*, 2008. revision 2.0.1, 2 May 2008.

[80] Susannah M. Dickerson, Jason M. Hogan, Alex Sugarbaker, David M. S. Johnson, and Mark A. Kasevich. Multiaxis inertial sensing with long-time point source atom interferometry. *Phys. Rev. Lett.*, 111:083001, Aug 2013.

[81] M. Hauth. *A mobile, high-precision atom-interferometer and its application to gravity observations*. PhD thesis, Humboldt-Universitaet zu Berlin, 2015.

[82] Kathryn Moler, David Weiss, Mark Kasevich, and Steven Chu. Theoretical analysis of velocity-selective Raman transitions. *Physical Review A*, 45(1):342–348, January 1992.

[83] Christian J. Bordé. Matter-wave interferometers: A synthetic approach. In Paul R. Berman, editor, *Atom Interferometry*, pages 257 – 292. Academic Press, San Diego, 1997.

[84] Uwe Sterr, Klaus Sengstock, Wolfgang Ertmer, Fritz Riehle, and Jürgen Helmcke. Atom interferometry based on separated light fields. In Paul R. Berman, editor, *Atom Interferometry*, pages 293 – 362. Academic Press, San Diego, 1997.

[85] B. Dubetsky and Mark Kasevich. Atom interferometer as a selective sensor of rotation or gravity. *Phys. Rev. A*, 74(2):023615, aug 2006.

[86] Sheng-wey Chiow, Tim Kovachy, Hui-Chun Chien, and Mark Kasevich. 102hk Large Area Atom Interferometers. *Phys. Rev. Lett.*, 107(13), sep 2011.

[87] A. Peters. *High precision gravity measurements using atom interferometry*. PhD thesis, Stanford, 1998.

[88] P. Gillot, B. Cheng, S. Merlet, and F. Pereira Dos Santos. Limits to the symmetry of a Mach-Zehnder-type atom interferometer. *Physical Review A*, 93(1):013609, January 2016.

[89] Kyle S. Hardman, Carlos C. N. Kuhn, Gordon D. McDonald, John E. Debs, Shayne Bennetts, John D. Close, and Nicholas P. Robins. Role of source coherence in atom interferometery. *Phys. Rev. A*, 89(2):023626, feb 2014.

[90] P Cheinet, B Canuel, Franck Pereira Dos Santos, A Gauguet, F. Leduc, and Arnaud Landragin. Measurement of the sensitivity function in time-domain atomic interferometer. *IEEE*, pages 1–15, October 2005.

[91] J. Le Gouët, T.E. Mehlstäubler, J. Kim, S. Merlet, A. Clairon, A. Landragin, and F. Pereira Dos Santos. Limits to the sensitivity of a low noise compact atomic gravimeter. *Appl. Phys. B*, 92(2):133–144, June 2008.

[92] N. Yu, J.M. Kohel, J.R. Kellogg, and L. Maleki. Development of an atom-interferometer gravity gradiometer for gravity measurement from space. *Appl. Phys. B*, 84(4):647–652, jul 2006.

[93] A. Senger. *A Mobile Atom Interferometer for High Precision Measurements of Local Gravity*. PhD thesis, Humboldt Universität zu Berlin, 2011.

[94] T. Petelski. *Atom interferometry for precision gravity measurements*. PhD thesis, Florenz, 2005.

[95] S Merlet, J Le Gouët, Q Bodart, A Clairon, A Landragin, F Pereira Dos Santos, and P Rouchon. Operating an atom interferometer beyond its linear range. *Metrologia*, 46(1):87–94, February 2009.

[96] J.M. Hensley, A. Peters, and S. Chu. Active low frequency vertical vibration isolation. *Review of Scientific Instruments*, 70(6):2735, 1999.

[97] C. Freier. Measurement of Local Gravity using Atom Interferometry. Diploma thesis, Humboldt-Universitaet zu Berlin, 2010.

[98] Fabien Theron, Olivier Carraz, Geoffrey Renon, Nassim Zahzam, Yannick Bidel, Malo Cadoret, and Alexandre Bresson. Narrow linewidth single laser source system for onboard atom interferometry. *Appl. Phys. B*, 118(1):1–5, December 2014.

[99] Jon H. Shirley. Modulation transfer processes in optical heterodyne saturation spectroscopy. *Opt. Lett.*, 7(11):537, November 1982.

[100] D J McCarron, S A King, and S L Cornish. Modulation transfer spectroscopy in atomic rubidium. *Meas. Sci. Technol.*, 19(10):105601, October 2008.

[101] C. Wieman and T. W. Hänsch. Doppler-Free Laser Polarization Spectroscopy. *Phys. Rev. Lett.*, 36(20):1170–1173, May 1976.

[102] Gary C. Bjorklund. Frequency-modulation spectroscopy: a new method for measuring weak absorptions and dispersions. *Opt. Lett.*, 5(1):15, January 1980.

[103] X. Baillard, A. Gauguet, S. Bize, P. Lemonde, Ph. Laurent, A. Clairon, and P. Rosenbusch. Interference-filter-stabilized external-cavity diode lasers. *Opt. Commun.*, 266(2):609–613, October 2006.

[104] M. Gilowski, Ch. Schubert, M. Zaiser, W. Herr, T. Wübbena, T. Wendrich, T. Müller, E.M. Rasel, and W. Ertmer. Narrow bandwidth interference filter-stabilized diode laser systems for the manipulation of neutral atoms. *Opt. Commun.*, 280(2):443–447, December 2007.

[105] Heung-Ryoul Noh, Sang Eon Park, Long Zhe Li, Jong-Dae Park, and Chang-Ho Cho. Modulation transfer spectroscopy for ^{87}Rb atoms: theory and experiment. *Optics express*, 19(23):23444–52, November 2011.

[106] S Kraft, A Deninger, C Trück, J Fortágh, F Lison, and C Zimmermann. Rubidium spectroscopy at 778–780 nm with a distributed feedback laser diode. *Laser Phys. Lett.*, 2(2):71–76, February 2005.

[107] F. Sorrentino, Q. Bodart, L. Cacciapuoti, Y.-H. Lien, M. Prevedelli, G. Rosi, L. Salvi, and G. M. Tino. Sensitivity limits of a Raman atom interferometer as a gravity gradiometer. *Phys. Rev. A*, 89(2):023607, feb 2014.

[108] Malte Schmidt, A. Senger, M. Hauth, C. Freier, V. Schkolnik, and Achim Peters. A mobile high-precision absolute gravimeter based on atom interferometry. *Gyroscopy and Navigation*, 2(3):170–177, August 2011.

[109] C. Salomon, J. Dalibard, W. D. Phillips, A. Clairon, and S. Guellati. Laser cooling of cesium atoms below 3 μk. *EPL (Europhysics Letters)*, 12(8):683, 1990.

[110] S-Q. Shang, B. Sheehy, P. van der Straten, and H. Metcalf. Velocity-selective magnetic-resonance laser cooling. *Phys. Rev. Lett.*, 65(3):317–320, jul 1990.

[111] T Brzozowski et al. Time-of-flight measurement of the temperature of cold atoms for short trap-probe beam distances. *Journal of Optics B: Quantum and Semiclassical Optics*, 4(1):62–66, February 2002.

[112] Dian-Jiun Han, Steffen Wolf, Steven Oliver, Colin McCormick, Marshall T. DePue, and David S. Weiss. 3D Raman Sideband Cooling of Cesium Atoms at High Density. *Physical Review Letters*, 85(4):724–727, July 2000.

[113] A. Sugarbaker. *Atom interferometry in a 10 m fountain*. PhD thesis, Stanford, 2014.

[114] S. Dickerson. *Long time atom interferometry for precision test of fundamental physics*. PhD thesis, Stanford, 2014.

[115] W Torge and J Müller. *Geodesy*. de Gruyter, Berlin – Boston, 4 edition, 2012.

[116] M Vancamp and P Vauterin. Tsoft: graphical and interactive software for the analysis of time series and Earth tides. *Computers & Geosciences*, 31(5):631–640, June 2005.

[117] C. Freier. *in preparation*. PhD thesis, Humboldt-Universitaet zu Berlin, 2016.

[118] Shau-Yu Lan, Pei-Chen Kuan, Brian Estey, Philipp Haslinger, and Holger Müller. Influence of the Coriolis Force in Atom Interferometry. *Physical Review Letters*, 108(9):1–5, February 2012.

[119] Micro g LaCoste. gPhone gravity meter. Brochure, 2016.

[120] T M Niebauer, G S Sasagawa, J E Faller, R Hilt, and F Klopping. A new generation of absolute gravimeters. *Metrologia*, 32(3):159, 1995.

[121] J. Hinderer, D. Crossley, and R.J. Warburton. 3.04 Gravimetric Methods – Superconducting Gravity Meters. In Gerald Schubert, editor, *Treatise on Geophysics*, pages 65 – 122. Elsevier, Amsterdam, 2007.

[122] Thomas A Herring, editor. *Geodesy*, volume 3 of *Treatise on Geophysics*. Elsevier, New York, 2007.

[123] J. E. Faller. Measuring little g: A fertile ground for precision measurement science. *NIST Journal of Research*, 110, 2005.

[124] W. Riley and David A. Howe. Handbook of frequency stability analysis. Special Publication (NIST SP) - 1065, 2008.

[125] D.W. Allan and J.A. Barnes. A Modified "Allan Variance" with Increased Oscillator Characterization Ability. In *Thirty Fifth Annu. Freq. Control Symp.*, pages 470–475. IEEE, 1981.

[126] Peter G. Nelson. An active vibration isolation system for inertial reference and precision measurement. *Rev. Sci. Instrum.*, 62(9):2069, sep 1991.

[127] P Gillot, O Francis, A Landragin, F Pereira Dos Santos, and S Merlet. Stability comparison of two absolute gravimeters: optical versus atomic interferometers. *Metrologia*, 51(5):L15, 2014.

[128] Micro g LaCoste. Micro-g LaCoste FG5 User's Manual. Manual, 2007.

[129] Micro g LaCoste. FG5-X Absolute gravity meter. Brochure, 2016.

[130] Andreas Reinhold and Walter Hoppe. Technischer Bericht (G4-2010-5) Absolute und relative Schweremessungen in der Humboldt-Universität zu Berlin (Campus Adlershof) vom 10.-12.09.2010. Technical report, Bundesamt für Kartographie und Geodäsie, 2010.

[131] Inc GWR Instruments. Observatory Superconducting Gravimeter (OSG). Brochure, 2011.

[132] M. Hauth, C. Freier, V. Schkolnik, and A. Peters. Atom interferometry for absolute measurements of local gravity. *Proceedings of the International School of Physics "Enrico Fermi"*, 188:557–586, 2014.

[133] C. Jentsch. *Konzeption und Aufbau eines Experimentes zur quantenlimitierten Inertialsensorik mit lasergekuehlten Rubidiumatomen*. PhD thesis, Universitaet Hannover, 2004.

[134] T. Farah, P. Gillot, B. Cheng, A. Landragin, S. Merlet, and F. Pereira Dos Santos. Effective velocity distribution in an atom gravimeter: Effect of the convolution with the response of the detection. *Phys. Rev. A*, 90:023606, Aug 2014.

[135] Richard DeLombard, Kenneth Hrovat, Eric Kelly, and Kevin McPherson. Microgravity Environment on the International Space Station. NASA/TM—2004-213039, 2004.

[136] B.V. Tryggvason, W.M.B. Duval, R.W. Smith, K.S. Rezkallah, S. Varma, R.F. Redden, and R.A. Herring. THE VIBRATION ENVIRONMENT ON THE INTERNATIONAL SPACE STATION: ITS SIGNIFICANCE TO FLUID-BASED EXPERIMENTS. *Acta Astronaut.*, 48(2-3):59–70, jan 2001.

[137] M.A. Lombardi, A.N. Novick, and V.S. Zhang. Characterizing the performance of GPS disciplined oscillators with respect to UTC(NIT). In *Proc. 2005 IEEE Int. Freq. Control Symp. Expo. 2005.*, pages 677–684. IEEE, 2005.

[138] C Freier, M Hauth, V Schkolnik, B Leykauf, M Schilling, H Wziontek, H-G Scherneck, J Müller, and A Peters. Mobile quantum gravity sensor with unprecedented stability. *Journal of Physics: Conference Series*, 723(1):012050, 2016.

[139] Anne Louchet-Chauvet, Tristan Farah, Quentin Bodart, André Clairon, Arnaud Landragin, Sébastien Merlet, and Franck Pereira Dos Santos. The influence of transverse motion within an atomic gravimeter. *New Journal of Physics*, 13(6):065025, June 2011.

[140] Optocraft Optical Metrology. SHSLab Dokumentation . Manual, 2013.

[141] H.H. Hopkins. *Wave Theory of Aberrations*. Monographs on the physics and chemistry of materials. Clarendon Press, 1950.

[142] ISO 24157:2008. Ophthalmic optics and instruments – Reporting aberrations of the human eye. ISO norm, 2012.

[143] B. Leykauf. The effect of wavefront aberrations in light-pulse atom interferometry. Bachelor thesis, Humboldt-Universitaet zu Berlin, 2014.

[144] Andrew J. Kerman, Vladan Vuletić, Cheng Chin, and Steven Chu. Beyond optical molasses: 3d raman sideband cooling of atomic cesium to high phase-space density. *Phys. Rev. Lett.*, 84:439–442, Jan 2000.

[145] D. Malacara. *Optical Shop Testing*. Wiley Series in Pure and Applied Optics. Wiley, 2007.

[146] A. Stein. Praezise Wellenfrontmessungen an Laserstrahlen. Bachelor thesis, Humboldt-Universitaet zu Berlin, 2013.

[147] H. Müntinga, H. Ahlers, M. Krutzik, A. Wenzlawski, S. Arnold, D. Becker, K. Bongs, H. Dittus, H. Duncker, N. Gaaloul, C. Gherasim, E. Giese, C. Grzeschik, T. W. Hänsch, O. Hellmig, W. Herr, S. Herrmann, E. Kajari, S. Kleinert, C. Lämmerzahl, W. Lewoczko-Adamczyk, J. Malcolm, N. Meyer, R. Nolte, A. Peters, M. Popp, J. Reichel, A. Roura, J. Rudolph, M. Schiemangk, M. Schneider, S. T. Seidel, K. Sengstock, V. Tamma, T. Valenzuela, A. Vogel, R. Walser, T. Wendrich, P. Windpassinger, W. Zeller, T. van Zoest, W. Ertmer, W. P. Schleich, and E. M. Rasel. Interferometry with bose-einstein condensates in microgravity. *Phys. Rev. Lett.*, 110:093602, Feb 2013.

[148] Tim Kovachy, Jason M Hogan, Alex Sugarbaker, Susannah M Dickerson, Christine A Donnelly, Chris Overstreet, and Mark A Kasevich. Matter wave lensing to picokelvin temperatures. *Physical review letters*, 114(14):143004, April 2015.

[149] Olivier Carraz, Christian Siemes, Luca Massotti, Roger Haagmans, and Pierluigi Silvestrin. A Spaceborne Gravity Gradiometer Concept Based on Cold Atom Interferometers for Measuring Earth's Gravity Field. *Microgravity Sci. Technol.*, 26(3):139–145, oct 2014.

[150] Susannah Dickerson, Jason M Hogan, David M S Johnson, Tim Kovachy, Alex Sugarbaker, Sheng-wey Chiow, and Mark A Kasevich. A high-performance magnetic shield with large length-to-diameter ratio. *The Review of scientific instruments*, 83(6):065108, June 2012.

[151] T Kovachy, P Asenbaum, C Overstreet, C A Donnelly, S M Dickerson, A Sugarbaker, J M Hogan, and M A Kasevich. Quantum superposition at the half-metre scale. *Nature*, 528(7583):530–3, December 2015.

[152] Pierre Cladé, Saïda Guellati-Khélifa, François Nez, and F. Biraben. Large Momentum Beam Splitter Using Bloch Oscillations. *Physical Review Letters*, 102(24), June 2009.

[153] Holger Müller, Sheng-wey Chiow, Sven Herrmann, and Steven Chu. Atom Interferometers with Scalable Enclosed Area. *Physical Review Letters*, 102(24), June 2009.

[154] Onur Hosten, Nils J. Engelsen, Rajiv Krishnakumar, and Mark A. Kasevich. Measurement noise 100 times lower than the quantum-projection limit using entangled atoms. *Nature*, 529(7587):505–508, January 2016.

[155] W Hänsel, P Hommelhoff, T W Hänsch, and J Reichel. Bose-Einstein condensation on a microelectronic chip. *Nature*, 413(6855):498–501, oct 2001.

[156] Andreas Stamminger, Josef Ettl, Jens Grosse, Marcus Hörschgen-Eggers, Wolfgang Jung, Alexander Kallenbach, Georg Raith, Wolfram Saedtler, Stephan Seidel, John Turner, and Markus Wittkamp. MAIUS-1 - Vehicle, Subsystems Design and Mission Operations. In *Proc. 22nd ESA Symp. Eur. Rocket Balloon Program. Relat. Res.*, volume SP-730, pages 183–190. ESA Communications, sep 2015.

[157] Seidel S.T. *Eine Quelle für die Interferometrie mit Bose-Einstein-Kondensaten auf Hoehenforschungsraketen*. PhD thesis, University Hannover, 2014.

[158] Jan Rudolph, Waldemar Herr, Christoph Grzeschik, Tammo Sternke, Alexander Grote, Manuel Popp, Dennis Becker, Hauke Müntinga, Holger Ahlers, Achim Peters, Claus Lämmerzahl, Klaus Sengstock, Naceur Gaaloul, Wolfgang Ertmer, and Ernst M Rasel. A high-flux BEC source for mobile atom interferometers. *New J. Phys.*, 17(6):065001, jun 2015.

[159] DM Giltner, RW McGowan, and SA Lee. Atom interferometer based on Bragg scattering from standing light waves. *Physical review letters*, 75(14):2638–2641, October 1995.

[160] J. Grosse. *Thermal and Mechanical Design and Simulation for the first High Precision Quantum Optics Experiment on a Sounding Rocket*. PhD thesis, University Bremen, 2016.

[161] Jens Grosse, Stephan Seidel, Markus Krutzik, Marco Scharringhausen, and Tim van Zoest. Thermal and mechanical design of the MAIUS atom interferometer sounding rocket payload. In *AIAA SPACE 2014 Conference and Exposition, SPACE Conferences and Exposition*. ESA Communications, okt 2014.

[162] K. Dieckmann, R. J. C. Spreeuw, M. Weidemüller, and J. T. M. Walraven. Two-dimensional magneto-optical trap as a source of slow atoms. *Physical Review A*, 58(5):3891–3895, November 1998.

[163] Erdenetsetseg Luvsandamdin, Christian Kürbis, Max Schiemangk, Alexander Sahm, Andreas Wicht, Achim Peters, Götz Erbert, and Günther Tränkle. Micro-integrated

extended cavity diode lasers for precision potassium spectroscopy in space. *Optics express*, 22(7):7790–8, April 2014.

[164] FBH. MICRO-INTEGRATED MASTER OSCILLATOR POWER AMPLIFIER USER GUIDE, Release 04.02, 2013-04-29, Issue 01. Manual, 2013.

[165] Max Schiemangk, Kai Lampmann, Aline Dinkelaker, Anja Kohfeldt, Markus Krutzik, Christian Kürbis, Alexander Sahm, Stefan Spieß berger, Andreas Wicht, Götz Erbert, Günther Tränkle, and Achim Peters. High-power, micro-integrated diode laser modules at 767 and 780 nm for portable quantum gas experiments. *Applied optics*, 54(17):5332–8, June 2015.

[166] Jun Jun Jun Jun Lim, S. Sujecki, Lei Lei Lang, Zhichao Zhichao Zhang, D. Paboeuf, G. Pauliat, G. Lucas-Leclin, P. Georges, R. MacKenzie, P. Bream, S. Bull, K.-H. Hasler, B. Sumpf, H. Wenzel, G. Erbert, B. Thestrup, P.M. Petersen, N. Michel, M. Krakowski, and E.C. Larkins. Design and Simulation of Next-Generation High-Power, High-Brightness Laser Diodes. *IEEE J. Sel. Top. Quantum Electron.*, 15(3):993–1008, 2009.

[167] Hannes Duncker, Ortwin Hellmig, André Wenzlawski, Alexander Grote, Amir Jones Rafipoor, Mona Rafipoor, Klaus Sengstock, and Patrick Windpassinger. Ultra-stable, Zerodur-based optical benches for quantum gas experiments. *Applied optics*, 53(20):4468–74, July 2014.

[168] Philip C. D. Hobbs. *Building Electro-Optical Systems: Making It all Work*. Building Electro-Optical Systems: Making It all Work, second edition, 2019.

[169] P A Altin, M T Johnsson, V Negnevitsky, G R Dennis, R P Anderson, J E Debs, S S Szigeti, K S Hardman, S Bennetts, G D McDonald, L D Turner, J D Close, and N P Robins. Precision atomic gravimeter based on Bragg diffraction. *New J. Phys.*, 15(2):023009, feb 2013.

[170] R. F. C. Vessot, M. W. Levine, E. M. Mattison, E. L. Blomberg, T. E. Hoffman, G. U. Nystrom, B. F. Farrel, R. Decher, P. B. Eby, C. R. Baugher, J. W. Watts, D. L. Teuber, and F. D. Wills. Test of relativistic gravitation with a space-borne hydrogen maser. *Phys. Rev. Lett.*, 45:2081–2084, Dec 1980.

[171] Steven Peil, Scott Crane, James Hanssen, Thomas Swanson, and Christopher Ekstrom. Tests of local position invariance using continuously running atomic clocks. *Physical Review A*, 87(1):010102, January 2013.

[172] H Schnatz, B Lipphardt, J Helmcke, F Riehle, and G Zinner. First phase-coherent frequency measurement of visible radiation. *Phys. Rev. Lett.*, 76(1):18–21, January 1996.

[173] SA Diddams, DJ Jones, J Ye, ST Cundiff, JL Hall, JK Ranka, RS Windeler, R Holzwarth, T Udem, and TW Hansch. Direct link between microwave and optical

frequencies with a 300 THz femtosecond laser comb. *Phys. Rev. Lett.*, 84(22):5102–5, May 2000.

[174] W. Demtröder. *Experimentalphysik 2*. Experimentalphysik / Wolfgang Demtröder. Springer Berlin Heidelberg, 2008.

[175] T. Udem and F. Riehle. Frequency Combs applications and optical frequency standards. *Riv. del Nuovo Cim.*, 30(12):564–602, 2007.

[176] D. J. Jones. Carrier-Envelope Phase Control of Femtosecond Mode-Locked Lasers and Direct Optical Frequency Synthesis. *Science (80-.).*, 288(5466):635–639, April 2000.

[177] R Holzwarth, T Udem, TW Hansch, JC Knight, WJ Wadsworth, and PS Russell. Optical frequency synthesizer for precision spectroscopy. *Phys. Rev. Lett.*, 85(11):2264–7, sep 2000.

[178] Nobelprize.org. Nobel Media AB 2014. Web. 30 Jun 2016. The 2005 Nobel Prize in Physics. Press Release, 2005.

[179] M. Lezius et al. Space-born Frequency Comb Metrology. *Submitted for publication in Optica*, 2016.

[180] W Haensel, R Holzwarth, R Doubek, and M Mei. Laser with non-linear optical loop mirror. US Patent 8873601 , 10 2014.

[181] N. Kuse, J. Jiang, C.-C. Lee, T. R. Schibli, and M.E. Fermann. All polarization-maintaining Er fiber-based optical frequency combs with nonlinear amplifying loop mirror. *Opt. Express*, 24(3):3095, feb 2016.

[182] Christoph Affolderbach and Gaetano Mileti. A compact laser head with high-frequency stability for Rb atomic clocks and optical instrumentation. *Review of Scientific Instruments*, 76(7):073108, July 2005.

[183] Ch. Salomon, D. Hils, and J. L. Hall. Laser stabilization at the millihertz level. *J. Opt. Soc. Am. B*, 5(8):1576, aug 1988.

[184] J. Le Gouët, P. Cheinet, J. Kim, D. Holleville, A. Clairon, A. Landragin, and F. Pereira Dos Santos. Influence of lasers propagation delay on the sensitivity of atom interferometers. *The European Physical Journal D*, 44(3):419–425, June 2007.

[185] L Mudarikwa, K Pahwa, and J Goldwin. Sub-Doppler modulation spectroscopy of potassium for laser stabilization. *J. Phys. B At. Mol. Opt. Phys.*, 45(6):065002, mar 2012.

[186] A. Dinkelaker et al. Autonomous frequency stabilization of two extended cavity diode lasers at the potassium wavelength on a sounding rocket. *in preparation*, 2016.

[187] Ronald Legere and Kurt Gibble. Quantum Scattering in a Juggling Atomic Fountain. *Physical Review Letters*, 81(26):5780–5783, December 1998.

[188] A. Kerman. *Raman sideband cooling and cold atomic collisions in optical lattices*. PhD thesis, Stanford, 2002.

Publications

1 Print

- **Autonomous frequency stabilization of two extended cavity diode lasers at the potassium wavelength on a sounding rocket**
  A. Dinkelaker, M. Schiemangk, **V. Schkolnik**, A. Kenyon, K. Lampmann, T. Wendrich, O. Hellmig, A. Wenzlawski, P. Windpassinger, E.M. Rasel, A. Wicht, M. Krutzik and A. Peters, *in preparation for submission to Applied Optics* (2016)

- **Optical frequency combs for space applications**
  M. Giunta, M. Lezius, C. Deutsch, T. Wilken, Theodor W. Hänsch, A. Kohfeldt, A. Wicht, **V. Schkolnik**, M. Krutzik, H. Duncker, O. Hellmig, K. Lampmann, A. Wenzlawski, P. Windpassinger, K. Sengstock, A. Peters, R. Holzwarth, *CLEO: 2016, OSA Technical Digest, paper STh4H.5* (2016)

- **A compact and robust diode laser system for atom interferometry on a sounding rocket**
  V. Schkolnik, O. Hellmig, A. Wenzlawski, J. Grosse, A. Kohfeld, K. Döringshoff, A. Wicht, P. Windpassinger, K. Sengstock, C. Braxmaier, M. Krutzik and A. Peters, *Submitted for publication in Applied Physics B, under review* (2016)

- **Mobile quantum gravity sensor with unprecedented stability**
  C. Freier, M. Hauth, **V. Schkolnik**, B. Leykauf, M. Schilling, H. Wziontek, H-G. Scherneck, J. Müller and A. Peters, *Journal of Physics: Conference Series* **723**, p.012050 (2016)

- **Space-born frequency comb metrology**
  M. Lezius, T. Wilken, C. Deutsch, M. Giunta, O. Mandel, A. Thaller, **V. Schkolnik**, M. Schiemangk, A. Dinkelaker, M. Krutzik, A. Kohfeldt, A. Wicht, A. Peters, O. Hellmig, H. Duncker, K. Sengstock, P. Windpassinger, K. Lampmann, T. Hülsing, T. W. Hänsch and R. Holzwarth, *Submitted for publication in Optica, under review* (2016)

- **The effect of wavefront aberrations in atom interferometry**
  V. Schkolnik, B. Leykauf, M. Hauth, C. Freier and A. Peters, *Applied Physics B* **120**, p.311 (2015)

- **Atom interferometry for absolute measurements of local gravity**
  M. Hauth, C. Freier, **V. Schkolnik**, A. Peters, H. Wziontek and M. Schilling, *Proceedings of the International School of Physics "Enrico Fermi"* **188**, p.557 (2014)

- **A frequency comb and precision spectroscopy experiment in space**
  T. Wilken, M. Lezius, T. W. Hänsch, A. Kohfeldt, A. Wicht, **V. Schkolnik**, M. Krutzik, H. Duncker, O. Hellmig, P. Windpassinger, K. Sengstock, A. Peters, and R. Holzwarth, *CLEO: 2013, OSA Technical Digest, paper AF2H.5.* (2013)

- **GAIN - a portable atom interferometer for on site measurements of local gravity**
  M. Hauth, C.Freier, V. Schkolnik, and A. Peters, *Frontiers in Optics 2013, OSA Technical Digest, paper LM4H.2.* (2013)

- **A mobile high-precision absolute gravimeter based on atom interferometry**
  M. Schmidt, A. Senger, M. Hauth, C. Freier, **V. Schkolnik**, and A. Peters, *Gyroscopy and Navigation* **2**, p.170 (2011)

- **Degenerate quantum gases in microgravity**
  J. Rudolph, N. Gaaloul, Y. Singh, H. Ahlers, W. Herr, T. Schulze, S. Seidel, C. Rode, **V. Schkolnik**, W. Ertmer, E. Rasel, H. Müntinga, R. Thorben, A. Resch, S. Herrmann, C. Lämmerzahl, T. van Zoest, H. Dittus, A. Vogel, A. Wenzlawski, K. Sengstock, N. Meyer, K. Bongs, M. Krutzik, W. Lewoczko-Adamczyk, M. Schiemangk, A. Peters, M. Eckart, E. Kajari, S. Arnold, G. Nandi, W. Schleich, R. Walser, T. Steinmetz, T.W. Hänsch and J. Reichel, *Microgravity Science and Technology* **23**, p.287 (2011)

2 Oral Presentations

Only those presentations are listed where the author of this thesis is first author and presenter.

- Deutsche Physikalische Gesellschaft (DPG), Annual Meeting, Hannover, Germany (2016)
- Deutsche Physikalische Gesellschaft (DPG), Annual Meeting, Berlin, Germany (2014)
- Frontiers of Matter Wave Optics (FOMO 2014), Crete, Greece (2014)
- Deutsche Physikalische Gesellschaft (DPG), Annual Meeting, Heidelberg, Germany (2015)
- International Astronautical Conference (IAC), Jerusalem, Israel (2015)

3 Poster Presentations

Only those presentations are listed where the author of this thesis is first author and presenter.

- Deutsche Physikalische Gesellschaft (DPG), Annual Meeting, Hannover, Germany (2016)
- Young Atom Opticians Conference (YAO), Hannover, Germany (2011)

- Deutsche Physikalische Gesellschaft (DPG), Annual Meeting, Hannover, Germany (2013)
- International School of Physics "Enrico Fermi", Summer Course on "Atom Interferometry", Varenna, Italy (2013)
- International Association of Geodesy (IAG), Potsdam (2013)
- Frontiers of Matter Wave Optics (FOMO 2014), Crete, Greece (2014)
- Deutsche Physikalische Gesellschaft (DPG), Annual Meeting, Berlin, Germany (2014)
- Deutsche Physikalische Gesellschaft (DPG), Annual Meeting, Heidelberg, Germany (2015)

List of Figures

List of Tables

List of Abbreviations

GR	General Relativity
EEP	Einstein equivalence principle
UFF	Universality of Free Fall
LPI	Local Position Invariance
LLI	Local Lorentz Invariance
AOM	acousto-optic modulator
ECDL	extended cavity diode laser
ESC	Esrange Space Center
DFB	distributed feedback
MIOB	micro-integrated-optical bench
CCP	conductively-cooled package
PER	polarization extinction ratio
EOM	electro-optic modulator
FMS	frequency modulation spectroscopy
MTS	modulation transfer spectroscopy
VHBG	volume holographic bragg grating
TEXUS	Technologische Experimente unter Schwerelosigkeit
PM	polarization-maintaining
DDS	direct digital synthesis
PFD	phase frequency detector
ADEV	Allan deviation
MDEV	modified Allan deviation
BEC	Bose–Einstein condensate
PMT	photomultiplier tube
MOPA	master oscillator power amplifier
PA	power amplifier
MO	master oscillator
RW	ridge waveguide
MOT	magneto-optical trap

Acknowledgments

During this work I received support from a lot of people and it is time to express my deep thankfulness. I would like to thank:

In the first place my supervisor Achim Peters who gave me the opportunity to work in his group during my thesis. His support and guidance backed by his profound knowledge motivated me to successfully participate in a number of fascinating projects that broadened my horizon. He gave me confidence to form and realize my ideas always aiming for the highest standards.

The members of the GAIN team Matthias Hauth and Christian Freier for the longstanding cooperation in the lab and during the measurement campaigns that would not have been possible without them. They were a never ending source of motivation and working with them was always a pleasure. Bastian Leykauf for proof-reading my thesis.

Matthias Lezius, Christian Deutsch, Tobias Wilken and Michele Giunta from Menlo Systems for sharing their comprehensive knowledge with me and the time we spent together prior and during the challenging sound rocket campaigns. The other members of the FOKUS and KALEXUS team, Hannes Duncker, Ortwin Hellmig, Anja Kohfeldt, Max Schiemangk, Aline Dinkelaker and Kai Lampmann for the smooth collaboration across whole Germany. Thomas Hülsing and Enrico Noack from Airbus for their extremely professional assistance.

The MAIUS team, especially Stephan Seidel, Hauke Müntinga, Holger Ahlers, Dennis Becker, Maike Diana Lachmann, Jens Grosse and André Wenzlawski. Markus Krutzik, Klaus Döringshoff and Andreas Schell for a huge load of inspiration, motivation, proof-reading my thesis and fruitful and inspiring discussions inside and outside the lab.

Klaus Palis, Matthias Schoch and Eugen Dischke for their help in designing electronics and making it all work. Thorsten Rausche, his team of the mechanical workshop and Christoph Kaiser for realizing my constructions and guiding me through the design phase. All colleagues from the QOM and NANO group and the members of the laser metrology group at the FBH. In particular Christoph Grzeschik, Moritz Nagel, Evgeny Kovalchuk, Regina Rheinländer, Andreas Wicht and Christian Kürbis.

My family and friends for believing in me and their support.

Aiste who accompanied me through ups and downs during the time of this thesis.

Selbständigkeitserklärung

Hiermit erkläre ich, die vorliegende Arbeit selbständig und nur unter Verwendung der angegebenen Quellen und Hilfsmittel angefertigt zu haben. Ich habe mich anderweitig nicht um einen Doktorgrad beworben und besitze einen solchen auch nicht. Die dem Verfahren zugrunde liegende Promotionsordnung der Mathematisch-Naturwissenschaftlichen Fakultät der Humboldt-Universität zu Berlin habe ich zur Kenntnis genommen.

Berlin, den 07.07.2016 Vladimir Schkolnik